

ALMA MATER STUDIORUM
UNIVERSITÀ DEGLI STUDI DI BOLOGNA

Dipartimento di Fisica e Astronomia

Dottorato di Ricerca in Astronomia
Ciclo XXVIII

Tesi di Dottorato

**Accretion of mass and angular momentum
onto the discs of spiral galaxies**

CANDIDATO:
Gabriele Pezzulli

RELATORE:
Filippo Fraternali

COORDINATORE:
Lauro Moscardini

Esame finale anno 2015

Contents

1	Introduction	1
1.1	Mass accretion	1
1.1.1	Observational overview	1
1.1.2	The theoretical context	5
1.2	Angular momentum assembly	9
1.2.1	Global angular momentum content	9
1.2.2	The angular momentum distribution	13
1.3	Thesis outline	15
2	The radial growth rate of stellar discs	17
2.1	Introduction	18
2.2	Star formation in exponential discs	20
2.2.1	A simple model	20
2.2.2	Theoretical <i>caveats</i>	20
2.2.3	Mass and radial growth rates	22
2.2.4	Predicted properties of SFRD profiles	22
2.3	Sample and data	23
2.3.1	Sample definition	23
2.3.2	Stellar mass surface density	24
2.3.3	Star formation rate surface density	26
2.4	Analysis	26
2.4.1	Fit of exponential discs	28
2.4.2	Fit of the star formation rate surface density	29
2.4.3	A note on the fitting strategy	30
2.4.4	Notes on systematics	31
2.5	Results	33
2.5.1	Inside-out growth	33
2.5.2	Mass and radial growth rates	34
2.6	Implications for the evolution of scaling relations of disc galaxies	36
2.6.1	The mass-radial growth connection	36
2.6.2	A comparison with a simple theoretical prediction	36
2.6.3	Evolutionary effects	39
2.7	Summary	40
2.A	The effect of the return fraction	41
2.B	The choice of the weights	44
2.C	The tentative double disc of NGC 3621	44

2.D	Λ CDM scaling relations with an evolving density contrast	46
2.E	Atlas	47
3	Accretion, radial flows and abundance gradients in spiral galaxies	65
3.1	Introduction	65
3.2	A minimal model for the evolution of galaxy discs	68
3.2.1	Exponential discs obeying the Kennicutt-Schmidt law	68
3.2.2	Effective accretion rate surface density	70
3.2.3	Metallicity evolution with independent annuli	71
3.2.4	Independent-annuli chemical evolution of exponential discs	72
3.3	Angular momentum, accretion and radial flows	74
3.3.1	General context and basic equations	74
3.3.2	The general mass flux decomposition	75
3.3.3	Particular cases	76
3.3.4	Application to the minimal galaxy evolution model	77
3.4	Chemical evolution with radial flows	79
3.4.1	The method of characteristics	79
3.4.2	Application to the minimal model	81
3.4.3	Origin of the steepening effect	82
3.4.4	The role of boundary conditions	82
3.4.5	Calibration from observed gradients	85
3.5	Inside-out models with radial flows	86
3.5.1	Structural constraints to inside-out growth	86
3.5.2	Accretion and radial flows in an inside-out model	88
3.5.3	Abundance gradients in inside-out models with radial flows	90
3.5.4	The effect of the inside-out growth parametrization	91
3.6	Application to NGC 628	92
3.7	Summary	93
3.A	Angular momentum and radial flows in fountain-driven accretion	95
3.B	Angular momentum accretion on a disc from random orbits	98
3.C	The effect of the IGM metallicity	101
4	Angular momentum and entropy in models of rotating coronae	105
4.1	Introduction	105
4.2	Isothermal equilibria	108
4.2.1	Basic equations	108
4.2.2	Dimensionless variables	110
4.2.3	A class of simple truncated models	111
4.2.4	Coronal structure for a given angular momentum distribution	112
4.2.5	Asymptotic analysis near the origin	113
4.2.6	The exponential angular momentum distribution	115
4.2.7	Truncated exponential angular momentum distributions	117
4.2.8	A tentative Milky-Way-like scaling	119
4.3	Baroclinic equilibria	121
4.3.1	A constructive approach to the general baroclinic equilibrium	121
4.3.2	Construction of the density and pressure fields	122

4.3.3	Entropy, hydrostatic potential and the choice of boundary conditions	123
4.3.4	Geometry and rotation	124
4.3.5	A class of models rotating on spheres	126
4.3.6	A self-similar family of rotating coronae in a logarithmic potential	127
4.4	Rotating equilibria from angular momentum and entropy distributions	130
4.4.1	Problem statement	130
4.4.2	An inductive reconstruction algorithm	131
4.4.3	Asymptotic analysis near the vertical axis	133
4.4.4	Regularization in the proximity of the equatorial plane	134
4.5	Summary	135
5	Conclusions	137
	Acknowledgements	141
	Bibliography	143

Chapter 1

Introduction

Energy dissipation and angular momentum conservation are universally recognized as the key ingredients for the formation of discs in every astrophysical context. It is therefore likely that the assembly of galaxy discs is due, at least in a large fraction, to the energy loss of dissipative gaseous material, with a significant amount of net angular momentum in the direction perpendicular to the plane of the forming disc. Accretion can come either from hot gas, condensing after the radiative loss of part of its thermal energy, or from gas that was cold from the beginning and dissipates part of its kinetic energy (either in shocks or in turbulent cascades) as a consequence of its impact onto the disc.

In Sec. 1.1 of this Introduction we give a general overview of the current understanding of mass accretion onto the discs of spiral galaxies, from an observational and a theoretical point of view. In Sec. 1.2 the angular momentum that must be associated to mass accretion is briefly discussed, with equal attention for well understood aspects and open issues, from a global and a local perspective.

Finally, in Sec. 1.3, we state the aim of this Thesis and we give an outline of the work presented in the following Chapters.

1.1 Mass accretion

1.1.1 Observational overview

Indirect evidence from chemical evolution

The first clear observational indications that the discs of spiral galaxies need continuous accretion of metal-poor gas from the intergalactic medium, came from the study of the chemical enrichment of the interstellar medium due to stellar evolution and nucleosynthesis. Theoretical predictions can be readily obtained for the metallicity evolution of a galaxy, or galactic region, in the absence of mass exchange with the surrounding medium (the *closed-box* scenario, e.g. Tinsley 1980). Early studies (e.g. van den Bergh 1962; Pagel & Patchett 1975) immediately realized that the metallicity distribution of long-lived stars in the solar neighbourhood, as computed under this hypothesis, is remarkably different from the observed one, in the sense that there are much less metal-poor stars with respect to predictions (the so-called

G-dwarf problem), while a much better agreement is found when continuous accretion of metal-poor gas from the intergalactic medium (IGM) is accounted for (e.g. Larson 1972; Tinsley 1980 and references therein). Our understanding of the chemical evolution of the solar neighbourhood has become significantly more complex, after the recent discovery of the impact of stellar migration on the local metallicity distribution of stars (e.g. Edvardsson et al. 1993; Sellwood & Binney 2002a), but still requires continuous accretion of metal-poor gas from the IGM (e.g. Schönrich & Binney 2009), which is now recognized as a key ingredient for the metallicity evolution of spiral galaxies in general (e.g. Pagel 2009; Matteucci 2012 and references therein).

Besides stellar metallicities, independent chemical evidence in favour of accretion comes from the chemical composition of the interstellar medium (ISM) of the Milky Way (e.g. Vilchez & Esteban 1996) and of external spiral galaxies (e.g. Moustakas et al. 2010; Sánchez et al. 2014). These measurements can be difficult, since they rely on the detection of faint *auroral lines* (e.g. Pagel 2009) or, as an alternative, on not trivial calibrations (e.g. Pilyugin 2007; Kobulnicky & Kewley 2004; Marino et al. 2013). In the Milky Way, good proxies for ISM abundances can be obtained from the photospheric abundances of Cepheid stars, which are very young and therefore a fair tracer of the composition of the ISM (e.g. Luck & Lambert 2011; Genovali et al. 2015). On the other hand, theoretical predictions can be easily made for gas-phase abundances. The closed-box model predicts them to increase with the gas mass fraction (i.e. gas over gas plus stars). Since the gaseous mass surface density in spiral galaxies declines less rapidly than the stellar one (van der Kruit & Freeman 2011), the consequent prediction is that the metallicity of the ISM should be a declining function of radius, which is in qualitative agreement with observations. The predicted abundance gradients, however, are too shallow with respect to the observed ones and therefore metal-poor gas accretion is needed (e.g. Phillipps & Edmunds 1991, though see Skillman 1998).

Chemical evolution arguments have been also recently applied to the evolution of galaxies as a whole. While global models have a limited accuracy due to their very crude assumptions (for instance, that the whole galaxy can be described by one single metallicity), they have the advantage to be applicable to large samples and therefore offer the possibility of looking for statistically significant correlations. Star forming galaxies have been found to lie on a tight mass metallicity relation (Tremonti et al. 2004; Gallazzi et al. 2005), with more massive galaxies being more metal-rich. Since more massive galaxies also have the smallest gas fraction (Evoli et al. 2011), this is in qualitative agreement with the closed-box predictions. However, a quantitative comparison again shows inconsistency: lower metallicities are generally found, with respect to a closed-box, the effect being the strongest for galaxies with the lowest stellar mass (Tremonti et al. 2004; Dalcanton 2007). This metal deficiency is predicted, on very general theoretical grounds, as a consequence of gas exchanges between the galaxy and its environment (Edmunds 1990). Indeed, the mass metallicity relation has been explained fairly well by models including both inflows and outflows (e.g. Lilly et al. 2013; Peng & Maiolino 2014). Furthermore, the scatter of the relation has been discovered to correlate with the star formation rate (Mannucci et al. 2010) and even better with the gaseous content of galaxies

(Bothwell et al. 2013), so that a three parameter relation exists (the so-called *fundamental metallicity relation*), which is also found to be remarkably invariant with redshift (Belli et al. 2013).

Star formation and the gas consumption problem

Irrespective of chemical evolution, a strong indication that the discs of spiral galaxies need continuous gas accretion from the IGM comes from their gas content and star formation rates. At the present time, spiral galaxies typically form stars at a rate such that, in the absence of substantial replenishment, the present reservoir of cold gas within star forming discs would be exhausted on short timescales (of the order of a few Gyr) (Kennicutt 1983; Bigiel et al. 2011; Kannappan et al. 2013). Interestingly, spiral galaxies that are actively forming stars today show similar levels of star formation during the majority of their evolution (Leitner 2012) and nonetheless their content of cold gas has not been varying much during the same amount of time (Zafar et al. 2013). Since stars form out of cold gas, this is possible only admitting that the cold gas reservoir is continuously replenished. This simple argument can be made quantitative, considering that the amount of cold gas and the star formation rate of spiral galaxies are strictly related to each other (Kennicutt & Evans 2012 and references therein). When this relation is taken into account, the accretion history and the star formation history of a whole galaxy or of individual regions can be reconstructed backwards in time, turning out to be related to each other and both mildly declining with increasing time (Fraternali & Tomassetti 2012).

Considerations about gas consumption likely provide the most clean view to quantify accretion across the evolution of spiral galaxies. Nonetheless, we stress that the chemical arguments that we have discussed above always retain a crucial importance. Chemical evolution, in fact, provides the key additional information that the accreting gas has to be metal-poor (e.g. Tosi 1988b). This has the important implication that metal-rich material ejected by stars and returned to the ISM, despite possibly giving a contribution to the total accretion rate (Leitner & Kravtsov 2011), cannot give account for the whole amount of gas needed to explain the observed properties of star-forming galaxies (e.g. Sánchez Almeida et al. 2014 and references therein).

Imprints of gas accretion on gaseous discs

The amount, structure and kinematics of cold (potentially star-forming) gas in and around spiral galaxies is most directly investigated by means of radio observations of the 21 cm emission line of neutral hydrogen (see Sancisi et al. 2008 for a review). A very common property of the discs of spiral galaxies is the presence of large amounts of cold gas, extending much farther out than the optical stellar disc (e.g. Broeils & Rhee 1997). The gaseous outskirts of spirals are often characterized by morphological and kinematical disturbances (e.g. Briggs 1990; Schoenmakers 1999; García-Ruiz, Sancisi & Kuijken 2002). The origin of these features is unclear. It has been argued, on dynamical arguments, that some of these structures cannot be long-lived and are rather likely to be erased by shear on a few orbital times (Baldwin,

Lynden-Bell & Sancisi 1980). If they are transient phenomena, they could be the manifestation of relatively frequent interaction or accretion events.

Dwarf galaxies constitute a particularly interesting scientific case for accretion: due to their low masses, they are expected to show the most dramatic (and therefore easily detectable) dynamical response to the impact of infalling material. Interestingly, morphological and kinematical distortions are commonly found in low-mass galaxies (Lelli, Verheijen & Fraternali 2014a); furthermore, asymmetries have been shown to be quantitatively related to recent starbursting events (Lelli, Verheijen & Fraternali 2014b), as expected if they were both a consequence of recent accretion.

Complementary evidence comes again from chemistry: Sánchez Almeida et al. (2015) found a spatial connection, in starbursting dwarf galaxies, between recent intense star formation events and a drop in gas phase metallicity, which could be easily explained if accretion of metal-poor gas has occurred very recently (less than one rotational period). Similarly, Reichard et al. (2009) found a connection between low gas-phase metallicity and lopsidedness, as expected if the asymmetries were due to accretion.

The origin of the cold gas

In principle, galaxies can acquire the gas that is needed to sustain star formation either from direct accretion of cold gas or from the cooling of hot gaseous haloes surrounding the disc (e.g. Sánchez Almeida et al. 2014).

Clearly, the most direct evidence for cold gas accretion on spiral galaxies would be the detection of cold gas outside of them, in the process of being accreted. Several galaxies are known to have HI-rich companions and it is possible that some of them will interact and eventually merge with the central galaxy; however, the accretion rate due to these events is insufficient to sustain the current level of star formation in spirals (Di Teodoro & Fraternali 2014). Some accretion can in principle come from purely gaseous clouds (without stars). It has long been known that the Milky Way is surrounded by the so-called *high-velocity clouds* (HVCs, Oort 1970). These clouds of cold, dense, metal-poor gas have a very different kinematics with respect to the Galactic disc, suggestive of an infall motion towards the Milky Way, and for this reason they have been considered the first direct evidence for accretion of cold gas from the IGM. Similar clouds have also been found very close to other spiral galaxies (e.g. van der Hulst & Sancisi 1988); however, there is no sign of HI complexes with similar properties at larger galactocentric distances (Fraternali 2009), contrary to what expected if HVCs originated in the IGM. A purely internal origin of HVCs (Bregman 1980) has been excluded as well, because of the low metallicity of these clouds (van Woerden & Wakker 2004), but it is possible that they arise from the interaction of the circumgalactic medium with gas ejected from the disc (Fraternali et al. 2015). Nevertheless, the accretion rate associated to HVCs does not seem to be enough to sustain the observed star formation rate of the Milky Way (Putman, Peek & Joungh 2012), though the contribution of ionized gas is still debated (Lehner & Howk 2011). It is therefore possible that an important contribution to accretion comes from very diffuse gas, with column densities below the sensitivity of current instruments ($N_{HI} \sim 10^{19} \text{ cm}^{-2}$, e.g. Oosterloo et al. 2007).

Diffuse gas can be probed in absorption, along the sightlines to distant quasars. It

is well known that the intergalactic space is permeated by relatively cold ($T \sim 10^4 K$) gaseous clouds with column densities as low as $\log(N_{HI}/\text{cm}^{-2}) = 12.5$ (the so-called *Ly- α forest*), though a large fraction of this gas may be unrelated to star forming galaxies (Penton, Stocke & Shull 2004). Nonetheless, studies based either on the Ly- α absorption line (e.g. Prochaska et al. 2011) or on absorption from low-ionization metal species (in particular MgII, e.g. Churchill et al. 2013) have provided evidence for the presence of cold gas in the circumgalactic medium of galaxies (i.e. within their virial radius). Unfortunately, it cannot be established, in most cases, whether this gas is actually infalling onto the galaxies or not. For geometrical reasons, a very clean test can be done only for those absorptions that are detected in the stellar spectrum of the galaxy itself; indeed, many outflows have been discovered in this way (Rubin et al. 2014), while inflowing motions are more difficult to detect (Rubin et al. 2012). The key information, however, comes again from metallicity: outflows, in fact, should be metal-enriched, while inflowing gas has to be metal-poor. Lehner et al. 2013 studied an HI-selected sample of Lyman-limit systems, with $16 < \log(N_{HI}/\text{cm}^{-2}) < 19$, and provided convincing evidence that their metallicity distribution is bimodal, with possibly outflowing metal-rich gas and possibly inflowing metal-poor material being found with approximately the same frequency, though a clear physical explanation for the spatial coexistence of these two markedly different phases still needs to be fully investigated. It is finally important to notice that, even admitting that some gas is really cold and inflowing, it is likely, given its very low density, that it will be ablated away during the interaction with the hot gas that is also present around massive galaxies, being therefore incorporated into the hot halo itself (Binney 2004). If this is the case, or if no cold accretion occurs at all, additional mechanisms should be invoked to explain the condensation of cold gas out of the hot medium (e.g. Kaufmann et al. 2009; Marinacci et al. 2010a).

1.1.2 The theoretical context

Hierarchical structure formation

Cosmology gives us a fairly clear understanding of the general assembly of structures in our Universe (e.g. Mo, van den Bosch & White 2010 and references therein), at least concerning the dark matter, which is believed to dominate the matter content of the Universe (Planck Collaboration 2014) and to interact (with itself and everything else) almost exclusively through gravitation (e.g. Randall et al. 2008). The formation of a highly non-uniform matter distribution out of an initially almost uniform one is due to the amplification, driven by gravitational instability, of primordial gaussian isentropic fluctuations imprinted on the cosmological background well before recombination. The amplitude of fluctuations is distributed in Fourier space in such a way that low mass structure are assembled earlier than the more massive ones (*hierachical* structure formation).

Given its small contribution to the total matter content of the Universe, ordinary matter (“baryons”) is expected to fall into the potential wells of the dark matter and to passively follow similar assembly paths; a significant gravitational role of baryons is expected only at late stages and in the central regions of dark mat-

ter haloes (*adiabatic contraction*, Blumenthal et al. 1986). Therefore, as long as gravity is the dominant force acting on them, baryonic structures should form in a hierarchical fashion as well. The most massive known baryonic structures (galaxy clusters) are indeed the youngest observed ones (e.g. Allen, Evrard & Mantz 2011 and references therein); however, the same is not true for galaxies, with the more massive being older than the less massive (*downsizing*, Cowie et al. 1996). This clearly indicates that physics other physical processes, in addition to gravitation, become very important at galaxy mass scales.

Virialization and galaxy formation

The simple linear analysis of gravitational instability ceases to be valid when the overdensity associated to a growing perturbation becomes comparable to the background density. This roughly corresponds to the *turn-around* time, when the effects of self-gravity overtake the Hubble flow and the mass enclosed within the perturbation separates from the general expansion, starting to collapse towards its centre. The subsequent evolution is usually understood in terms of idealized models of gravitational collapse (e.g. Gunn & Gott 1972; Cole & Lacey 1996). The evolution of dark matter and baryons becomes very different at this stage.

Since dark matter is collisionless (does not interact with itself or other particles other than through gravitation), its settlement into a virialized structure is a long and complex process involving, for each ‘shell’ of given initial radius, several passages through the centre and through other shells (*shell crossing*, e.g. Fillmore & Goldreich 1984), implying abrupt changes of the gravitational potential, which favour the onset of violent relaxation (Lynden-Bell 1967). Furthermore, dark matter is dissipationless (cannot give up its energy to other particles and in particular to the electromagnetic field), therefore it conserves its total energy and its final equilibrium can be relatively easily predicted, for a given cosmology, as a function of its mass M and its formation epoch. In particular, its size (the *virial radius*) scales with $M^{1/3}H^{-2/3}$, where H is the Hubble constant at the time of virialization (e.g. Mo, Mao & White 1998), while the proportionality constant depends on the cosmological parameters (e.g. Eke, Cole & Frenk 1996).

Baryons, on the other side, can be described as a collisional fluid. They cannot undergo shell crossing and any baryonic ‘shell’ will instead violently collide with the previously collapsed material. Depending on the geometry and clumpiness of accretion, the kinetic energy of the infall will either be instantaneously converted into thermal energy by means of a large-scale *virial shock*, or it will feed turbulent motions that are rapidly thermalized in a series of smaller shocks (Voit et al. 2003). In the absence of dissipative processes (see below), the baryons will thus reach, on a timescale close to the free-fall time, the equilibrium configuration of a hot ionized halo (*corona*) of large size (comparable to the virial radius) and large temperature (the *virial temperature*), proportional to the depth of the dark matter potential well. However, baryons are also dissipative: they can lose part of their energy, transferring it to the electromagnetic field through *radiative* processes, therefore cooling, losing pressure support and collapsing down to radii much smaller than the virial radius. If, during or after the collapse, the conditions for further fragmentation and star formation are met, a galaxy forms at the very centre of the dark matter halo (White

& Rees 1978).

Cold and hot mode accretion

As discussed in Rees & Ostriker (1977), the key quantity that determines galaxy formation is the gas cooling time, which is in turn determined by the density (governed by cosmology and by the non-linear collapse theory) and by its temperature, through the cooling function. The cooling function has a highly non linear shape ¹, a property that has been proposed by Rees & Ostriker (1977) as the origin of the masses and sizes of the galaxies that we observe today.

If the cooling time is much larger than the Hubble time, the gaseous hot halo (*corona*) will effectively have a non-dissipative behaviour: cooling will not be effective and, consequently, galaxy formation will be prevented. As an opposite limiting case, if the cooling time is shorter than the free-fall time, shock-heating does not even occur: in fact, any hypothetical shock-heated gas would cool and collapse to the centre so rapidly that it would not be able to sustain the shock front itself (Binney 1977), a scenario known today as *cold mode* accretion. In the intermediate range, a shock will develop and a galaxy will progressively form out of the cooling of the corona (*hot mode* accretion).

Analytic calculations (e.g. Birnboim & Dekel 2003) suggest that the boundary between cold mode and hot mode accretion is set, at each time, by the halo mass, with low mass galaxies accreting via cold mode and massive galaxies via hot mode. Since the halo mass increases with time due to mergers and diffuse accretion, massive galaxies likely switched from cold mode accretion at early epochs to hot mode at later times. For the most massive galaxies, a stage should be reached when cooling is so inefficient that accretion and consequently star formation are halted.

The detailed distinction between cold mode and hot mode accretion can be more complex than the simple sketch given above, considering that realistic accretion does not occur in a spherically symmetric fashion, but along filaments (Dekel & Birnboim 2006). In some hydrodynamical cosmological simulations (Dekel et al. 2009) such filaments are able to penetrate deeply into the halo, directly bringing cold gas to the central galaxy, while in others (Nelson et al. 2013) they are mostly ablated away by thermal conduction, during the interaction with the hot halo surrounding the galaxy. Similarly, minor mergers can in principle transfer both the stars and the cold gas of relatively small galaxies to a bigger one; however, while the stellar component will be distorted by tidal interactions and finally incorporated into the central object (e.g. Ibata et al. 2001), the gaseous component can undergo ram-pressure stripping and ablation, ending in the hot halo rather than in the cold ISM of the central galaxy (e.g. Bland-Hawthorn et al. 2007).

Missing baryons

The hot mode accretion scenario predicts that some fraction of the baryons associated to massive dark matter haloes resides in hot coronae. As a consequence, the

¹This results from a combination of different radiative processes including brehmsstrahlung, hydrogen and helium recombination and, for a non-primordial composition, collisionally excited emission lines of other species.

baryonic mass in the other phases (stars and cold gas) should be less than the total amount of baryons for a given dark matter halo. This fact is indeed confirmed by observations and is known as the *missing baryons problem* (e.g. Nicastro, Mathur & Elvis 2008). The designation as a “problem” is justified by the fact that the direct detection of hot coronae surrounding galaxies is quite challenging, especially for spiral galaxies, and it has been achieved so far in just a few cases (e.g. Anderson & Bregman 2011; Dai et al. 2012; Bogdán et al. 2013a). Furthermore, the determination of the total mass of hot haloes depends on assumptions on their structure and there is still no consensus on whether they comprise the whole theoretical baryonic budget or not (Anderson & Bregman 2010).

Not all the missing baryons are necessarily expected to reside within haloes. Some of them may have been expelled, in the form of winds, from either star formation or AGN *feedback*. An indication in this direction is given by the halo mass - stellar mass relation, as derived either from abundance matching (e.g. Behroozi, Conroy & Wechsler 2010) or with more direct methods, including satellite kinematics and weak gravitational lensing (Dutton et al. 2010). Apparently, the stellar mass of galaxies of every morphological type never exceeds $\sim 30\%$ of the baryonic mass nominally associated to their dark matter haloes and even lower fractions are found for massive ellipticals and for low-mass galaxies in general. When cold gas is accounted for, the detected baryonic mass increases significantly, especially for low-mass galaxies (Papastergis et al. 2012), but it is still very far from the nominal value, implying that the remaining is either hot or truly missing gas. Since the potential wells of low-mass galaxies are not deep enough to retain hot gas, the latter possibility is the most likely. A possible explanation is that the baryons “missing” from low-mass haloes have been removed by feedback at early times (Silk, Wyse & Shields 1987). Note that early feedback, originated in low-mass haloes, may even prevent some gas to enter the virial radius of more massive structures formed at later times (*preventive feedback*, Lu, Mo & Wechsler 2015). Processes like this may be related to the same mechanisms driving the so-called *re-ionization* of the Universe (e.g. Benítez-Llambay et al. 2015).

Quenching and morphology

We conclude this overview by quickly addressing the important open question of why galaxies with a given mass (and therefore similar halo temperatures and cooling times) form stars effectively or not, depending on the morphology (with spirals forming stars at much higher rates than ellipticals with similar masses).

This effect may be related the morphology-density relation (Dressler et al. 1997); indeed, quenching of star formation in galaxies may be partly (though not entirely) due to environmental effects (Peng et al. 2010). An alternative could be that, for some reason, feedback is particularly effective for ellipticals (McNamara & Nulsen 2007). Finally, an explanation can be looked for in the physics of heating and cooling; in this case, either ellipticals have an additional source of heating, capable to counteract the cooling rate of the hot gas (e.g. by dynamical heating due random motions of the stars, Posacki, Pellegrini & Ciotti 2013), or, conversely, spirals dispose of an additional cooling mechanism for the hot gas. One possibility in the latter direction is the scenario of *supernova-driven gas accretion* (Marinacci et al. 2010a),

a form of *positive feedback*, where the cooling of the coronal gas is triggered by the interaction with cold clouds ejected by the disc as a consequence of multiple supernova explosions.

1.2 Angular momentum assembly

1.2.1 Global angular momentum content

Tidal torques and the Fall relation

The origin of angular momentum in galaxies has been a hotly debated topic around the middle of the last century. It was unclear, for instance, whether it could be the manifestation of a primordial vorticity field (von Weizsäcker 1948). Theoretical efforts became more focused after convincing arguments were given by Peebles (1969) for the fact that gravitationally bound structures in our Universe acquire their angular momentum during their collapse, as a consequence of the coupling of their quadrupole moment with the tidal field of the surrounding density distribution (*tidal torques*).

A prediction of the tidal torque theory, applied to the current cosmological paradigm, is that the spin parameter of dark matter haloes $\lambda = l\sqrt{|\epsilon|}/GM$ (l and ϵ being the specific angular momentum and specific energy, respectively) should be distributed as a lognormal (Barnes & Efstathiou 1987), with $\langle \lambda \rangle = 0.035$ and a dispersion of 0.23 dex (Macciò, Dutton & van den Bosch 2008).

Because of the virial theorem, the specific energy $|\epsilon|$ of a dissipationless dark matter halo should scale with its mass divided by its virial radius (see Sec. 1.1.2). If coupled with the narrow range of predicted spin parameters, this implies that the specific angular momentum l of dark matter haloes should scale with their mass M as $M^{2/3}$. This relation can be easily scaled down to galaxies, reading:

$$l_{\star} \propto f_l f_{\star}^{-2/3} M_{\star}^{2/3} \quad (1.1)$$

where f_{\star} and f_l are the mass and specific angular momentum of a galaxy, respectively, in units of those of the host dark matter halo (Romanowsky & Fall 2012). In the simplistic view that these coefficients do not vary from one galaxy to another, galaxies are expected to follow a power law relation of the form:

$$l_{\star} \propto M_{\star}^{\alpha} \quad (1.2)$$

with $\alpha \sim 2/3$. We will refer to (1.2) as to the *Fall relation*, for reasons that will become immediately clear in the following.

Morphology and angular momentum

In a pioneering work, Fall (1983) studied the link between mass and angular momentum of galaxies, looking for an observational confirmation of the theory above. He found that spirals and ellipticals galaxies followed two relations of the type (1.2), both with a slope very close to the theoretical value $\alpha \sim 2/3$, but with a normalization offset of a factor ~ 6 at disfavour of ellipticals. This finding has been recently

confirmed by Romanowsky & Fall (2012). These authors propose that two distinct universal relations hold for discs and spheroids, with a common slope $\alpha \sim 0.6$ and different normalizations (lower for spheroids than for discs). Since spiral and lenticular galaxies are constituted of a disc a spheroid (the *bulge*), the position of these objects in the (M_*, l_*) should be a function of the bulge-to-disc ratio, in nice agreement with observations. While the common slope of the proposed relations is very close to the theoretical prediction, the different normalizations of discs and spheroids suggest that angular momentum assembly followed very different paths for the two kinds of objects.

For about one decade, the attention of the community was focused on how to explain the high angular momentum content of spirals. The reason is that, in the first hydrodynamical cosmological simulations, baryons were found to transfer a substantial fraction of their angular momentum to the dark matter halo through dynamical friction (Navarro & White 1994; Navarro & Steinmetz 1997), a fact known as the *angular momentum catastrophe*, or *global angular momentum problem* (not to be confused with the local one, see next Section). The situation appears much ameliorated in more recent simulations (e.g. Guedes et al. 2011), possibly due to the increase of numerical resolution (which beats down the efficiency of dynamical friction, Kaufmann et al. 2007), though other effects are generally believed to contribute (Fall 2002; Piontek & Steinmetz 2011). In particular, energy injected into the gas by supernova explosions (*star formation feedback*) can prevent the formation of gaseous clumps, further reducing the efficiency of dynamical friction (Sommer-Larsen, Gelato & Vedel 1999), or selectively expel the low-angular momentum gas from the halo, therefore enhancing the average specific angular momentum of the remaining material (Governato et al. 2010, see also next Section).

Of course, once the solution of the global angular momentum for spirals is achieved (by any means), the problem is turned back on how to explain the relatively low specific angular momentum content of ellipticals (and spheroids). Several possibilities have been investigated, based either on physical arguments (Romanowsky & Fall 2012) or on hydrodynamical cosmological simulations (Genel et al. 2015; Pedrosa & Tissera 2015), including biased collapse, repeated mergers and AGN feedback, though no explanation appears to be particularly compelling.

A major conundrum

Irrespective of morphology and normalization, the most puzzling problem, in our opinion, is how to explain the slope of the Fall relation or even why it is a power-law at all. In fact, as we have already pointed out, the general theoretical relation (1.1) reduces to the observed form (1.2) only if the mass and angular momentum fractions f_* and f_l are approximately constant with M_* . However, studies on the stellar mass-halo mass relation (see Sec. 1.1.2) indicate that at least f_* is not constant and even a strongly non-linear function of M_* . If not compensated by some fine-tuned variation of f_l , this effect should introduce a strong distortion in the Fall relation, in sharp contrast with observations. Despite the prominence of the paradox, no significant effort has still been done, to our knowledge, to unravel it. We point out, however, the work by Dutton & van den Bosch (2012), who, though without addressing the problem directly, provide potentially useful insight on the interplay between f_* and

f_i , based on both theory and observations.

Other scaling relations

Spiral galaxies are known to follow a relatively simple universal structure of galaxy discs (a radially declining exponential, Freeman 1970) and a regular rotation pattern (flat rotation curve, Begeman, Broeils & Sanders 1991). This allows the theoretical derivation of additional scaling relations and in particular the mass-size and the mass-velocity relations (Mo, Mao & White 1998), together with their evolution with time.

In contrast with the Fall relation, the mass-size and the mass-velocity relation involve either structure or kinematics separately and for this reason their observational counterparts have been studied in much more detail, in the Local Universe (e.g. Tully & Fisher 1977; McGaugh 2012; Shen et al. 2003; Courteau et al. 2007) and, more recently, at high redshift (e.g. Barden et al. 2005; Miller et al. 2012; Fathi et al. 2012).

Much insight can in principle be gained from the comparison between theory and observations. For instance a possible tension appears to be present between the predicted and observed slopes of the mass-velocity relation (also known as *Tully-Fisher relation*, from the pioneering work by Tully & Fisher 1977), which is now known to hold with a very small scatter and on a large mass dynamic range, especially when the cold gaseous mass is taken into account (*baryonic Tully-Fisher relation*, McGaugh 2012). Furthermore, current observations are compatible with no evolution of the Tully-Fisher relation out to $z \sim 1$ (Miller et al. 2011) and with small or no evolution at higher redshift (Miller et al. 2012), though observational uncertainties are still too large to discriminate between different scenarios. The current understanding of the evolution of the mass-size relation is also very similar in this respect (Trujillo et al. 2006).

When comparing theory with observations, it is however very important to keep in mind that the conversion of simple models (like the one by Mo, Mao & White 1998) into testable predictions relies on simplifying assumptions, most notably about the values of f_* and f_i ², which, as we have already discussed, are unlikely to be constant from one galaxy to another. Furthermore, the physics of shock heating and radiative cooling is naturally expected to introduce a time delay between accretion on the halo and accretion on the star forming disc, suggesting that a simple causal connection between the disc mass and the halo mass, evaluated at the same time, may not be an appropriate assumption (and similarly for the angular momentum). This in turn suggests that more refined parametrizations (for instance, explicitly taking the cooling time into account) would be of some help in putting theory and observations on a simple common ground.

At the same time, there are other independent empirical relations that, on the contrary, suggest a tight connection between galaxies and their haloes. For instance, Kravtsov (2013) claims evidence for the effective radii of galaxies being ~ 70 times smaller than the virial radii of the host haloes, irrespective of morphology. Another very important example is the relation between the mass and the star formation

² m_d and j_d/m_d , respectively, in the notation of Mo, Mao & White (1998).

rate of star forming galaxies (the *main sequence*, e.g. Elbaz et al. 2011): the ratio of star formation rate over stellar mass (*specific star formation rate*) appears to be roughly independent on stellar mass and increasing with redshift (Speagle et al. 2014). While the latter fact is obvious, considering the decline of star formation rate and the corresponding growth of stellar mass in the Universe (e.g. Wilkins, Trentham & Hopkins 2008), the former has been interpreted as an evidence for a direct connection between dark matter accretion and star formation (e.g. Lilly et al. 2013).

Inside-out growth

There is at least one theoretical prediction that is general enough to be relatively straightforwardly tested against observations. According to the tidal torque theory, material with higher specific angular momentum falls into dark matter haloes at later times. In the case of cold mode accretion, this directly implies later accretion onto the galaxy discs. For hot mode accretion, the high-angular momentum rotating gas will be stored in the outer regions of the corona, with lower density and longer cooling timescales. Therefore, in any case, the outskirts of spiral galaxies, which have the highest angular momentum content, are expected to form later. This implies that spiral galaxies should grow in size while they grow in mass (*inside-out* growth). Similarly to what we have seen for gas accretion (Sec. 1.1.1), this idea was originally introduced in the theory of galaxy evolution on the basis of chemical evolution arguments and it was found of great help in explaining the abundance gradients of spiral galaxies (e.g. Larson 1976; Matteucci & Franco 1989). However, more direct methods are now available to observationally constrain inside-out growth.

A very interesting indication is the detection of negative radial gradients in the ages of resolved stellar populations, which can be derived either by means of integral field spectroscopy (González Delgado et al. 2014) or, for very nearby galaxies, of resolved colour-magnitude diagrams (e.g. Gogarten et al. 2010; Barker et al. 2011). Note, however, that, similarly to what happens for the metallicity distribution of the stars in the solar neighbourhood (Sec. 1.1.1), the information on spatially resolved ages can be contaminated by the effect of stellar radial migration. Focusing on the spatial distribution of very young stars, one can in principle overcome this problem, though obtaining information only on the evolution at very recent times (e.g. Muñoz-Mateos et al. 2007).

A strong indication in favour of inside-out growth also comes from the study of scaling relations at different redshifts (see above). In fact, considering that the present-day largest galaxies are also the most massive ones (Shen et al. 2003), if galaxies had been growing in mass while keeping a constant size, then galaxies of a given observed stellar mass should be *larger* at high redshift than today. On the contrary, there is consensus on the fact they are either *smaller* or approximately of the same size (e.g. Trujillo et al. 2006).

We will come back on these and related topics in more detail in Chapter 2.

1.2.2 The angular momentum distribution

Detailed angular momentum conservation

Mestel (1963) argued that, within a protogalactic cloud, the timescale for viscous transport is always longer than the free-fall time. This implies that, during the collapse, the angular momentum distribution (that is, the amount of mass per unit specific angular momentum $\psi \equiv dM/dl$) will be conserved (*detailed angular momentum conservation*). While the total mass and the average specific angular momentum, which we have been talking about so far, are just the first two moments of ψ , the whole function in principle encloses an uncountably larger amount of additional information on the initial conditions out of which galaxies have formed.

To a first approximation (i.e. assuming an exponential radial mass distribution, with a flat rotation curve), the angular momentum distribution of discs is easily seen to follow the simple functional form:

$$\psi \equiv \frac{dM}{dl} \propto l \exp(-l) \quad (1.3)$$

with l is expressed in suitable units. A distribution of the kind of (1.3) was used by Mestel (1963) to infer the properties of the original protogalactic cloud.

A very similar idea was developed by Fall & Efstathiou (1980) to predict the structure and kinematics of dark matter halos from those of observed galaxy discs. Besides detailed angular momentum conservation, this work was based on the additional hypothesis that baryons and dark matter shared the same angular momentum distributions at the time of gravitational collapse. This assumption is justified by the fact that, before collapse, baryons and dark matter were subject to the same tidal torques, while non-gravitational interactions (and in particular non-gravitational torques) were most probably negligible at those epochs (see Sec. 1.1.2).

The local angular momentum problem

We are not aware of any purely theoretical derivation of the angular momentum distribution of dark matter haloes within the tidal torque theory. However, N-body simulations have now reached the resolution needed to address the problem numerically, which has been done by Bullock et al. (2001) and Sharma & Steinmetz (2005). Both these works have found $\psi(l)$ to have a finite limit (or a very mild divergence) for small values of l and a decline (with slightly different functional forms) with increasing l .

As first discussed, for the case of dwarf galaxies, by van den Bosch, Burkert & Swaters (2001), this distribution is very different from the one of observed discs, which is instead characterized by a peak at a finite value of l (cfr. also the simple estimate (1.3)). This problem is sometimes referred to as the *local angular momentum problem* (not to be confused with the global problem discussed in Sec. 1.2.1). In numerical simulations, the local angular momentum problem is manifested in the form of simulated galaxies with a too large bulge-to-disc ratio, or too slow rotation in the inner regions, with respect to real discs (van den Bosch 2001).

Compared to dark matter (and therefore to the supposed initial state of the baryons), galaxies lack both very low and very large angular momentum material

and, correspondingly, they are more rich in intermediate angular momentum material. As pointed out by Mo, van den Bosch & White (2010), this is the opposite of what expected as a consequence of ‘viscous’ evolution (Lynden-Bell & Pringle 1974) or, more in general, by any ‘esothermic’ process, that is a process implying either dissipation or dynamical heating (Lynden-Bell & Kalnajs 1972). This challenges the otherwise appealing idea that the exponential structure of disc is a product of secular evolution (Lin & Pringle 1987), indicating that the process responsible for the angular momentum distribution of discs has to be ‘endothermic’ instead (that is, it requires a source different from the mechanical energy of the disc).

The most popular solution to both the global and the local angular momentum problem is selective feedback (Governato et al. 2010, see Sec. 1.2.1), which implies a large amount of energy injection into the gas in the inner regions. This solution was originally proposed for dwarf galaxies, which are suspected to be prone to significant mass ejections for independent reasons (see Sec. 1.1.2). However, some problems are encountered with the application of the same idea to massive galaxies, which can have very low bulge-to-disc ratios as well: in fact, unphysically large energy injection would be required to push baryons out of the deeper potential wells of these galaxies. Nonetheless, Brook et al. (2012) have proposed that realistic discs can be produced also in this case, for the following reason. If a powerful outflow falls short of the escape speed, it will be reaccreted at very large radii. Along its orbit, it will pass through and likely interact with the hot gas. Locally, the hot gas rotates slower than the disc (larger temperature implies a larger pressure support against gravity) but at very large distances it will contain significant amount of angular momentum. If part of the angular momentum of the hot gas is transferred to the outflow, the latter will have, at the moment of reaccretion, a larger specific angular momentum than it had at ejection. This helps to alleviate the local angular momentum problem and to produce a final angular momentum distribution for the disc that is similar to the observed one.

At least three extensions can be envisaged, in our view, for this promising scenario. First, if turbulence is continuously fed in the corona by feedback-injected energy, it will last for much longer than the free fall time (originally considered by Mestel (1963) in its argument for detailed angular momentum conservation), possibly mediating some angular momentum redistribution within the hot gas before its condensation onto the disc. Second, in addition to the interaction with the hot medium, the mere re-accretion of outflowing material onto the disc already implies that mass elements with different angular momentum are put in contact with each other: from the point of view of the angular momentum distribution, this results in the production of material with intermediate values of specific angular momentum, at the expense of the extreme ones, precisely in the direction needed to solve the local angular momentum problem. Note that this mechanism does not require extremely large distances to be reached, nor (as a consequence) extremely large outflow velocities. Third, even without any feedback, the cooling of the corona onto the disc already violates the hypothesis of detailed angular momentum conservation (because of the already mentioned velocity difference between the two), again giving a contribution in the desired direction (the thermal content of the corona would be the energy source sustaining the process, in this case).

1.3 Thesis outline

The aim of this Thesis is the development of novel methods for the study of the mass and angular momentum assembly of the discs of spiral galaxies. We will give the preference to those descriptions that allow theoretical predictions to be easily derived, mostly by means of analytic techniques, and the comparison with observations to be straightforward and of transparent interpretation.

We first consider the growth of galaxy discs from the global point of view. As discussed in Sec. 1.2, this problem is very complex, but the robust theoretical prediction can be made that galaxy discs should grow in size while they grow in mass (inside-out growth). In Chapter 2, we show how a comparison between simple observables (the spatial distributions of the stellar mass and of the star formation rate) can be used to derive a direct measurement of the specific mass and radial growth rates of stellar discs. We apply our method to a sample of 35 nearby spiral galaxies and discuss our results in the light of theoretical expectations and of other work on the subject. Finally, we discuss the consequences of our findings for the study of the evolution of the scaling relations of disc galaxies with cosmic time.

We then focus on the local problem of how the accretion of mass and angular momentum on galaxy discs is distributed in space. This is much more complex, because of the larger amount of degrees of freedom involved. However, simple dynamical considerations, based on angular momentum conservation, can be used to predict the dynamical consequences of accretion, in particular the onset of radial gas flows within the disc, with a measurable effect on observables like chemical abundance gradients. In Chapter 3 we present some new and general, mostly analytic, techniques that can be used to infer the spatially resolved accretion profile and the local angular momentum of the accreting material from the structural and chemical properties of observed discs. We apply our methods to the Milky Way and to one external nearby spiral galaxy and discuss theory and observations in the context of some possible accretion mechanisms.

Finally, we make one step towards the physical understanding of the likely source of both the mass and the angular momentum of the discs of massive spiral galaxies. According to the hot-mode accretion scenario described in Sec. 1.1.2, this should be, at least at low redshift, an extended *corona* of shock-heated gas. As discussed in Sec. 1.2.2, the corona is expected to retain memory of its angular momentum distribution at the moment of collapse, which, in our view, offers a very promising link between the theories of structure formation and galaxy formation. In Chapter 4, we present analytic methods to predict structure and kinematics of the corona from its angular momentum distribution and discuss the implications in terms of observational constraints and theoretical expectations. We also consider the more general case of a baroclinic equilibrium in an arbitrary axisymmetric potential: we describe a novel parametrization of the general solution, as well as particular cases, and we show how structure and kinematics can be reconstructed, for these equilibria, from the joint angular momentum/entropy distribution, with potential applications to the study of the evolution of galactic coronae with time.

Finally, we give in Chapter 5 an overview of our work and of our findings.

Chapter 2

The radial growth rate of stellar discs[†]

Abstract

We start our investigation of the mass and angular momentum assembly of the discs of spiral galaxies by addressing the problem from the global point of view. As discussed in Chapter 1, a robust prediction of galaxy formation theory is that galaxies should grow in size while they grow in mass. The significant levels of star formation always found in the discs of spiral galaxies clearly indicate that these structures are still growing in mass at the present time. It is therefore very interesting to look for direct signatures of a possible ongoing growth in size (*inside-out growth*). In this Chapter, we present a new and simple method to measure the instantaneous mass and radial growth rates of the stellar discs of spiral galaxies, based on their star formation rate surface density (SFRD) profiles. Under the hypothesis that discs are exponential with time-varying scalelengths, we derive a universal theoretical profile for the SFRD, with a linear dependence on two parameters: the specific mass growth rate $\nu_M \equiv \dot{M}_*/M_*$ and the specific radial growth rate $\nu_R \equiv \dot{R}_*/R_*$ of the disc. We test our theory on a sample of 35 nearby spiral galaxies, for which we derive a measurement of ν_M and ν_R . 32/35 galaxies show the signature of ongoing inside-out growth ($\nu_R > 0$). The typical derived e-folding timescales for mass and radial growth in our sample are ~ 10 Gyr and ~ 30 Gyr, respectively, with some systematic uncertainties. More massive discs have a larger scatter in ν_M and ν_R , biased towards a slower growth, both in mass and size. We find a linear relation between the two growth rates, indicating that our galaxy discs grow in size at ~ 0.35 times the rate at which they grow in mass; this ratio is largely unaffected by systematics. Our results are in very good agreement with theoretical expectations if known scaling relations of disc galaxies are not evolving with time.

[†]Based on G. Pezzulli, F. Fraternali, S. Boissier & J.C. Muñoz-Mateos, 2015, MNRAS, 451, 2324.

2.1 Introduction

The theory of cosmological tidal torques (Peebles 1969) predicts the mean specific angular momentum of galaxies to be an increasing function of time. If applied to spiral galaxies, in which stars are mostly distributed on a rotating, centrifugally supported, disc, the theory suggests that the outer parts, with higher specific angular momenta, should form later than the inner ones (Larson 1976, the so-called *inside-out* formation scenario), also implying that spirals should grow in size while they grow in mass. Apart from this quite general prediction provided by cosmology, the details about how stellar discs form and grow in mass and size are not known from first principles and significant observational effort is still required to shed light on the missing links from structure formation to galaxy formation.

An invaluable input for modelers comes from some simple observed properties of the discs of spiral galaxies, that still wait for a comparatively simple theoretical explanation: among them, the exponential radial structure of galaxy discs (Freeman 1970), though sometimes broken at galaxy edges (e.g. Pohlen & Trujillo 2006; Erwin, Pohlen & Beckman 2008), and the fact that they obey simple scaling relations, including the Tully-Fisher relation between rotational velocity and mass (Tully & Fisher 1977, see also the ‘baryonic Tully-Fisher relation’, McGaugh 2012; Zaritsky et al. 2014), the Fall relation between angular momentum and mass (Fall 1983; Romanowsky & Fall 2012) and a more scattered mass-size relation (e.g. Shen et al. 2003; Courteau et al. 2007), which can also be seen as a corollary of the other two.

Observations of galaxies at different redshifts indicate that stellar discs have an exponential structure since very early epochs (Elmegreen et al. 2005; Fathi et al. 2012), while it is less clear whether scaling relations are truly universal or they evolve with cosmic time. For example, direct measurements of the mass-size relation for disc galaxies at various redshifts has led to claims for little or no evolution (e.g. Ravindranath et al. 2004; Barden et al. 2005; Ichikawa, Kajisawa & Akhlaghi 2012) as well as significant or strong evolution (e.g. Mao, Mo & White 1998; Buitrago et al. 2008; Fathi et al. 2012). The interpretation and comparison of these pioneering studies is made non trivial by inhomogeneities among observations at different redshifts, as well as differences in sample definitions and analysis techniques (see e.g. Lange et al. 2015); also, several subtle issues have been shown to significantly bias the results, most notably the selection effect due to cosmological dimming (e.g. Simard et al. 1999) and the evolution of M/L ratios due to evolving stellar populations (e.g. Trujillo et al. 2006). The related problem of the possible evolution of the Tully-Fisher relation, which also involves kinematic measurements, is even more complex and controversial (e.g. Vogt et al. 1997; Mao, Mo & White 1998; Miller et al. 2011; Miller et al. 2012 and references therein).

Since these issues are of extreme importance for our understanding of galaxy evolution, more observational effort is desirable, possibly dealing with multiple independent probes, to unveil the growth of the exponential discs of spiral galaxies. In addition to the crucial, but often challenging, comparison of galaxy properties at different redshifts, indirect information can be gained on the size growth of galaxy discs from the study of their properties in the Local Universe. Efforts in this direction can be split in two categories. The first is the exploitation of fossil signals of

the past structure of the disc: most notably, chemical enrichment (e.g. Boissier & Prantzos 1999; Chiappini, Matteucci & Romano 2001; Mollá & Díaz 2005; Naab & Ostriker 2006), and properties of stellar populations, including colour gradients (e.g. Bell & de Jong 2000; MacArthur et al. 2004; Wang et al. 2011), spectrophotometry (e.g. Muñoz-Mateos et al. 2011; González Delgado et al. 2014) and colour-magnitude diagrams (e.g. Williams et al. 2009; Gogarten et al. 2010; Barker et al. 2011). The second possibility is to look for the *instantaneous* signal of the growth process while it is in act. Spiral galaxies are not just passively evolving stellar systems, but keep forming stars at a sustained rate throughout their evolution (e.g. Aumer & Binney 2009; Fraternali & Tomassetti 2012; Tojeiro et al. 2013). Therefore, the radial distribution of newly born stars is a crucial ingredient for the structural evolution of a stellar disc and it can be used as a clean and direct probe of its growth.

Thanks to the deep UV photometry of the Galaxy Evolution Explorer (GALEX, Martin et al. 2005), radial profiles of the star formation rate surface density (SFRD) of nearby galaxies can now be traced out to considerable galactocentric distances and low levels of star formation activity. SFRD profiles, as traced by the UV light emitted by young stars, often turn out to be quite regular and, in many cases, remarkably similar to exponentials (Boissier et al. 2007, see also Goddard, Kennicutt & Ryan-Weber 2010). This supports the idea that star formation is tightly linked with whatever process is responsible for the maintenance and evolution of the exponential structure of galaxy discs. A closer inspection of the aforementioned SFRD profiles reveals, in many galaxies, some deviations from the exponential shape, in the form of a central downbending or depletion (see also Muñoz-Mateos et al. 2011). This is also clearly seen in the SFRD of the Milky Way, as traced, for example, by the distribution of Galactic supernova remnants (Case & Bhattacharya 1998). Indeed, star formation becoming progressively less effective towards the centre of galaxies is not very surprising, within the inside-out formation scenario: in the inner regions, the bulk of gas accretion and conversion into stars occurs quite early and relatively little residual star formation is expected to be in place there at late epochs, while the outskirts are still in their youth. Ultimately, the observed properties of SFRD profiles of spiral galaxies are in qualitative agreement with the inside-out paradigm and therefore they are good candidates to enclose the signal of radial growth. Our aim here is to give a simple quantitative description of this signal and a method to derive a measurement of the instantaneous mass and radial growth rates of the discs of spiral galaxies from the amplitude and shape of their SFRD profiles.

An earlier attempt in this direction has been done by Muñoz-Mateos et al. (2007). They assumed that surface densities of both stellar mass and star formation rate can be approximated with exponential profiles, though with different scalelengths, implying exponential profiles for the specific star formation rate (sSFR) as well, with sSFR increasing with radius for inside-out growing galaxies. This parametrization was applied to a sample of nearby spiral galaxies and the results were compared with the predictions of simple structural evolution models, providing constraints on the inside-out process.

Here we make a step forward, proposing a method that is both simpler and more powerful. Rather than modeling both stellar mass and SFRD with exponentials, we assume that just stellar discs are exponential at any time, with time-varying

scaleglengths. This naturally brings us (Sec. 2.2) to predict a universal shape for the SFRD profile with the observed properties outlined above, namely an inner depletion and an outer exponential decline. Furthermore, our theoretical profile has a very simple (linear) dependence on the disc mass and radial growth rates; hence, these parameters can be directly derived from observations in a model-independent way. We apply our method to a sample of nearby spiral galaxies described in Sec. 2.3, discuss our analysis in Sec. 2.4 and present our results in Sec. 2.5. In Sec. 2.6 the consequences of our findings are discussed on the issue of whether known scaling relations for galaxy discs are evolving with time or not. In Sec. 2.7 we draw our conclusions.

Appendices include: additional explanations to justify some of our choices (App. 2.A and 2.B), a detailed analysis of the interesting peculiar case of NGC 3621 (App. 2.C), additional calculations useful to put our work in a cosmological context (App. 2.D) and, finally, an Atlas (App. 2.E) with the details of our analysis for individual objects in our sample.

2.2 Star formation in exponential discs

2.2.1 A simple model

Let us assume that the mass surface density Σ_\star of the stellar disc of a spiral galaxy is well described, at any time, by an exponentially declining function of radius R , identified by a radial scalelength R_\star and a mass M_\star ¹, both allowed to vary with time t :

$$\Sigma_\star(t, R) = \frac{M_\star(t)}{2\pi R_\star^2(t)} \exp\left(-\frac{R}{R_\star(t)}\right) \quad (2.1)$$

Just taking the partial time derivative of (2.1) we get a very simple prediction for the star formation rate surface density $\dot{\Sigma}_\star$ as a function of time and galactocentric radius:

$$\dot{\Sigma}_\star(t, R) = \left(\nu_M(t) + \nu_R(t) \left(\frac{R}{R_\star(t)} - 2 \right) \right) \Sigma_\star(t, R) \quad (2.2)$$

where Σ_\star is given by (2.1), while the quantities ν_M and ν_R are defined by:

$$\nu_M(t) := \frac{d}{dt} (\ln M_\star(t)) = \frac{\dot{M}_\star(t)}{M_\star(t)} \quad (2.3)$$

$$\nu_R(t) := \frac{d}{dt} (\ln R_\star(t)) = \frac{\dot{R}_\star(t)}{R_\star(t)} \quad (2.4)$$

We discuss them more thoroughly in Sec. 2.2.3.

2.2.2 Theoretical *caveats*

At least two *caveats* should be kept in mind when considering the elementary inference outlined in Sec. 2.2.1.

¹Throughout the Chapter, when referring to a spiral galaxy, we will use the symbol M_\star to denote the stellar mass of its disc component alone.

First, by identifying $\dot{\Sigma}_*$ with $(\partial\Sigma_*/\partial t)$, we have implicitly neglected any contribution coming from a possible net radial flux of stars, that is a term:

$$\frac{1}{R} \frac{\partial}{\partial R} (2\pi R \Sigma_* u_{R,*})$$

where $u_{R,*}$ is the net radial velocity of stars. While radial migration of stars is widely recognized to be a fundamental ingredient of galaxy evolution, it has also been shown (Sellwood & Binney 2002b; Roškar et al. 2012) that its main working mechanism is basically a switch in the radial position of two stars in different circular orbits (the so-called *churning*, Schönrich & Binney 2009). This process produces no dynamical heating, no *net* radial flow of stars and no change in the mass distribution of the disc. Of course, some minor contribution to radial migration are also expected from other processes: breaks to our approximation can be expected in some cases, mostly in the inner regions, where dynamical processes might be associated with the formation of bars, rings and pseudobulges (e.g. Sellwood 2014) and at the outer edge, where radial migration has been proposed to induce changes in the outer structure of discs (Yoachim, Roškar, & Debattista 2012). More complex effects are also possible due to the interplay between stellar dynamics, gas dynamics and star formation; quite different approaches to this problem can be found, for example, in Schönrich & Binney (2009), Kubryk, Prantzos & Athanassoula (2013) and Minchev, Chiappini & Martig (2014).

Second, since stellar populations, during their evolution, return a substantial fraction of their mass to the ISM (Tinsley 1980), it is not necessarily trivial to connect the time derivative $\dot{\Sigma}_*$ to observed values of SFRD. In the following, we will adopt the instantaneous recycling approximation (IRA) and assume that a constant *return fraction* \mathcal{R} of the mass of a stellar population is instantaneously given back to the ISM. Accordingly, our $\dot{\Sigma}_*$ represents the *reduced* star formation rate surface density and it is equal to the observed SFRD multiplied by a factor $(1 - \mathcal{R})$, although we will often omit the attribute *reduced*, for brevity. More detailed studies (e.g. Leitner & Kravtsov 2011) show that the majority of the returned mass is released within ~ 1 Gyr from the birth of a population; hence, our approximation will be valid in those galaxies, or galaxy regions, where star formation has not been varying abruptly on timescales shorter than ~ 1 Gyr. As we show in Appendix 2.A, such abrupt changes can, in principle, be taken into account by replacing \mathcal{R} with an *effective return fraction* \mathcal{R}_{eff} , which is higher or lower than \mathcal{R} for abrupt quenching or starbursting events, respectively. These may be due, for instance, to tidal or ram pressure stripping or, viceversa, to significant recent accretion events. Similar effects can sometimes be observationally inferred in low surface brightness regions or in low surface brightness galaxies as a whole (Boissier et al. 2008) and may also be related to the phenomenology of extended UV (XUV) discs (Thilker et al. 2007a). Unfortunately, in general, neither the magnitude nor the direction of the needed correction can be known *a priori*. However, these possibilities should be kept in mind when considering peculiar features in the observed SFRD profiles of some individual objects.

2.2.3 Mass and radial growth rates

The quantities ν_M and ν_R , defined in (2.3) and (2.4), shall be called *specific mass growth rate* and *specific radial growth rate*. The word *specific* refers to the fact that they represent the mass and radial growth rates \dot{M}_* and \dot{R}_* , *normalized* to the actual value of mass M_* and scalelength R_* , respectively. However, since in the following we will deal only with specific quantities, we will often omit this attribute and refer to them just as mass and radial growth rates, for brevity.

While ν_M is always positive, ν_R can in principle take both signs, positive values being expected in the case of inside-out growth. At any time, the inverse of ν_M and ν_R can be interpreted as instantaneous estimates of the timescales for the growth of the stellar mass and scalelength, respectively (or for disc shrinking, in the case $\nu_R < 0$).

We notice that ν_M is strictly related to another physical quantity, namely the specific star formation rate (sSFR). More precisely, following the terminology of Lilly et al. (2013), ν_M coincides with the *reduced specific star formation rate* of the disc, where the word *reduced* (which we will omit from now on) refers to the fact that we are including the effect of the return fraction \mathcal{R} . Since our ν_M refers to the disc alone, it should not be confused with the sSFR of a whole spiral galaxy, which is evaluated including also the other stellar components, like the bulge. While the bulge can give a non-negligible contribution to the total stellar mass, it usually harbours little or no star formation: hence, the sSFR of a whole galaxy and of its disc alone can differ significantly (Abramson et al. 2014). Also, ν_M should not be confused with the *local* sSFR ($\dot{\Sigma}_*/\Sigma_*$), which is, in general, a function of galactocentric radius (e.g. Muñoz-Mateos et al. 2007).

The analogous quantity for the stellar scalelength, the (specific) radial growth rate ν_R , has been studied much less (and, as far as we know, not even clearly defined until now). To provide a simple method for its measurement is the main aim of this Chapter. Since ν_M and ν_R have the same physical dimensions and refer to the two basic properties of an exponential disc, we are also interested to measure both quantities at the same time and to attempt a comparison between them. This is indeed a natural outcome of our method (Sec. 2.2.4) and will bring us to the most interesting consequences of our results (Sec. 2.6).

2.2.4 Predicted properties of SFRD profiles

Our simple model predicts that, if a galaxy is observed at some particular time, its SFRD should follow a radial profile of the form:

$$\dot{\Sigma}_*(R) = \frac{M_*}{2\pi R_*^2} \left(\nu_M + \nu_R \left(\frac{R}{R_*} - 2 \right) \right) \exp \left(-\frac{R}{R_*} \right) \quad (2.5)$$

In Fig. 2.1 the predicted shape of the SFRD profile is drawn out, in dimensionless units, for some representative situations, which differ for the sign of the radial growth parameter ν_R . To achieve a fully dimensionless description of the model, we use here, as a parameter, the dimensionless ratio ν_R/ν_M , which has the same sign of ν_R , since, as pointed out in Sec. 2.2.3, ν_M is always positive. Also, with our adopted dimensionless units, the curves in Fig. 2.1 compare with each other as model discs

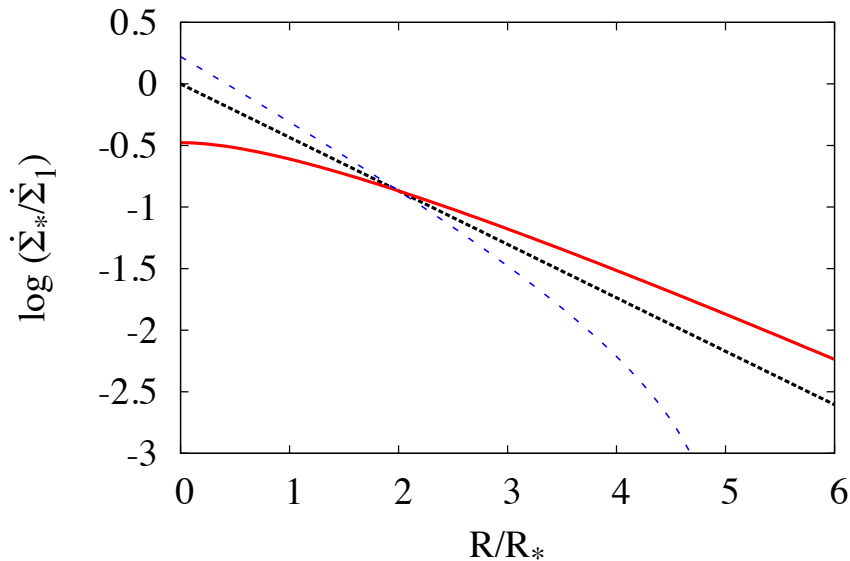


Figure 2.1: Predicted shape of the SFRD profile, in dimensionless units, for some illustrative values of the radial growth rate ν_R : absence of radial growth ($\nu_R = 0$, dotted black line), inside-out growth ($\nu_R = 1/3 \nu_M$, solid red line) and disc shrinking ($\nu_R = -1/3 \nu_M$, dashed blue line). The radius is in units of R_* , the SFRD is normalized to $\dot{\Sigma}_1 \equiv \nu_M M_*/2\pi R_*^2$, so that the comparison refers to discs with the same stellar mass, scalelength and *global* sSFR.

that share the same mass, scalelength and *global* sSFR ν_M , but differ in the spatial distribution of star formation, depending on the presence (and the direction) of an evolution of the scalelength with time.

In the absence of radial evolution ($\nu_R = 0$), the scalelength of the stellar disc is constant with time, stars always form with the same spatial distribution and the SFRD profile is an exponential as well, with the same scalelength of the already present stellar disc. In the case of disc shrinking ($\nu_R < 0$) star formation is enhanced, with respect to the previous case, in the inner regions, but it abruptly drops in the outskirts (reaching a vertical asymptote at $R/R_* = (2 + \nu_M/|\nu_R|)$). Conversely, for inside-out growth ($\nu_R > 0$), the SFRD shows the characteristic depletion in the central regions, while it is enhanced in the outskirts, where it ultimately gently declines with increasing radius, with an asymptotic behaviour, at large radii, similar to the one of the stellar mass distribution.

2.3 Sample and data

2.3.1 Sample definition

To define our sample, we started from the one studied by Muñoz-Mateos et al. (2011), which consists of 42 nearby spiral galaxies observed both by *Spitzer* and by GALEX, in the context of the SINGS survey (Kennicutt et al. 2003). For these and other nearby galaxies, radial profiles have been derived and published by Muñoz-Mateos

et al. (2009b) and Muñoz-Mateos et al. (2009a), for multi-wavelength emission ranging, for most galaxies, from FIR to FUV. Such a broad range is useful to trace both the stellar mass and the star formation rate, corrected for the effect of dust extinction. Muñoz-Mateos et al. (2009a) give radial profiles for the extinction in the UV, as inferred from TIR/UV flux ratios.

For this work, we made use of the radial profiles of the emission in the FUV GALEX band, corrected for extinction in the FUV (A_{FUV}). We also used profiles of emission in the $3.6 \mu\text{m}$ IRAC band, which we assume to be a good tracer of the stellar mass surface density. Some contamination may arise from the $3.3 \mu\text{m}$ PAH line, hot dust and AGB stars; however, these contributions are only expected to be important at the small scales of individual star-forming regions and just a mild effect persists at larger scales (Meidt et al. 2012). Furthermore, dust extinction at this wavelength is negligible and the M/L is quite insensitive to variations in age and metallicity, if compared to the optical bands (Meidt et al. 2014).

From the original sample of 42 galaxies, we excluded 5 galaxies (NGC 3049, NGC 3938, NGC 4254, NGC 4321, NGC 4450) for which FUV measurements were lacking because the GALEX FUV detector was turned off for technical reasons, one galaxy (NGC 7552) which was not present in the Muñoz-Mateos et al. (2009a) sample and another one (NGC 4625) for which the A_{FUV} radial profile was constituted of only one point. Therefore we ended up with a final sample of 35 galaxies. We have considered some possible additional criteria to further restrict our sample. Since our main goal is the study of the slow, continuous, evolution of the regular exponential structure of discs, galaxies that are suspected to be undergoing violent transient events, like interactions or mergers, could be excluded from the analysis. Furthermore, since we make a quantitative analysis of azimuthally averaged radial profiles, we could exclude those galaxies for which the geometrical parameters involved in the average (inclination and position angle) are not known with good accuracy or are suspected to be varying with radius. At least 3 galaxies (NGC 1097, NGC 1512, NGC 5194) have a nearby companion and for at least one (NGC 1512) the adopted position angle reproduces the outer isophotes better than the inner ones. However, it is not clear whether such selections could be done in a completely unbiased way. Also considering that our sample is relatively small, we decided to homogeneously analyse the whole set of 35 galaxies. Nonetheless, the aforementioned *caveats* should be kept in mind while considering our results. We adopt morphological classifications, distances and inclinations (as derived from axis ratios) from Muñoz-Mateos et al. (2011); these properties can also be found here in Table 2.1.

2.3.2 Stellar mass surface density

To get the stellar mass distribution, we made use of the high resolution (6 arcsec) radial profiles at $3.6 \mu\text{m}$ from Muñoz-Mateos et al. (2009b). To convert from surface brightness to mass surface density, we used the conversion formula:

$$\frac{\Sigma_{\star}}{\text{M}_{\odot} \text{pc}^{-2}} = 1.9 \times 10^7 \cos i \frac{I_{3.6\mu\text{m}}}{\text{Jy arcsec}^{-2}} \quad (2.6)$$

Table 2.1: Basic properties of galaxies in our sample. Morphological classification, distances and inclinations (derived from axis ratios) are as in Muñoz-Mateos et al. (2011).

Galaxy	RA (J2000) <i>h m s</i>	Dec (J2000) <i>° ' "</i>	Morphological Type	Type T	Distance (Mpc)	$\cos i$
NGC 0024	00 09 56.5	-24 57 47.3	SA(s)c	5	8.2	0.224
NGC 0337	00 59 50.1	-07 34 40.7	SB(s)d	7	25	0.621
NGC 0628	01 36 41.8	15 47 00.5	SA(s)c	5	11	0.905
NGC 0925	02 27 16.9	33 34 45.0	SAB(s)d	7	9.3	0.562
NGC 1097	02 46 19.1	-30 16 29.7	SB(s)b	3	15	0.677
NGC 1512	04 03 54.3	-43 20 55.9	SB(r)a	1	10	0.629
NGC 1566	04 20 00.4	-54 56 16.1	SAB(s)bc	4	17	0.795
NGC 2403	07 36 51.4	65 36 09.2	SAB(s)cd	6	3.2	0.562
NGC 2841	09 22 02.6	50 58 35.5	SA(r)b	3	14	0.432
NGC 2976	09 47 15.5	67 54 59.0	SAC pec	5	3.6	0.458
NGC 3031	09 55 33.2	69 03 55.1	SA(s)ab	2	3.6	0.524
NGC 3184	10 18 17.0	41 25 28.0	SAB(rs)cd	6	8.6	0.932
NGC 3198	10 19 54.9	45 32 59.0	SB(rs)c	5	17	0.388
IC 2574	10 28 23.5	68 24 43.7	SAB(s)m	9	4.0	0.409
NGC 3351	10 43 57.7	11 42 13.0	SB(r)b	3	12	0.676
NGC 3521	11 05 48.6	-00 02 09.1	SAB(rs)bc	4	9.0	0.464
NGC 3621	11 18 16.5	-32 48 50.6	SA(s)d	7	8.3	0.577
NGC 3627	11 20 15.0	12 59 29.6	SAB(s)b	3	9.1	0.462
NGC 4236	12 16 42.1	69 27 45.3	SB(s)dm	8	4.5	0.329
NGC 4536	12 34 27.1	02 11 16.4	SAB(rs)bc	4	15	0.421
NGC 4559	12 35 57.7	27 57 35.1	SAB(rs)cd	6	17	0.411
NGC 4569	12 36 49.8	13 09 46.3	SAB(rs)ab	2	17	0.463
NGC 4579	12 37 43.6	11 49 05.1	SAB(rs)b	3	17	0.797
NGC 4725	12 50 26.6	25 30 02.7	SAB(r)ab pec	2	17	0.710
NGC 4736	12 50 53.1	41 07 13.6	(R)SA(r)ab	2	5.2	0.813
NGC 4826	12 56 43.8	21 40 51.9	(R)SA(rs)ab	2	7.5	0.540
NGC 5033	13 13 27.5	36 35 38.0	SA(s)c	5	13	0.467
NGC 5055	13 15 49.3	42 01 45.4	SA(rs)bc	4	8.2	0.571
NGC 5194	13 29 52.7	47 11 42.6	SA(s)bc pec	4	8.4	0.804
NGC 5398 ^a	14 01 21.6	-33 03 49.6	(R')SB(s)dm pec	8.1	16	0.607
NGC 5713	14 40 11.5	-00 17 21.2	SAB(rs)bc pec	4	27	0.893
IC 4710	18 28 38.0	-66 58 56.0	SB(s)m	9	8.5	0.778
NGC 6946	20 34 52.3	60 09 14.2	SAB(rs)cd	6	5.5	0.852
NGC 7331	22 37 04.1	34 24 56.3	SA(s)b	3	15	0.352
NGC 7793	23 57 49.8	-32 35 27.7	SA(s)d	7	3.9	0.677

(a) In the original sample, this galaxy was referred to as TOL 89, which is the name of an HII region embedded within it.

which is the one derived by Leroy et al. (2008), though written in different units and modified for a K-band mass-to-light ratio equal to 0.8, instead of 0.5². This ratio is subject to several uncertainties (e.g. Bell et al. 2003); our choice was made to maximize consistency with the previous work by Muñoz-Mateos et al. (2007). We discuss the consequences of this and other systematics in Sec. 2.4.4.

2.3.3 Star formation rate surface density

To derive the SFRD profiles, we took the low resolution (48 arcsec) radial profiles in the FUV band from Muñoz-Mateos et al. (2009a) and corrected them for extinction using the A_{FUV} radial profiles at the same resolution. In that work, two estimates of A_{FUV} are provided, based on two slightly different dust attenuation prescriptions by Buat et al. (2005) and by Cortese et al. (2008), the latter containing a refinement to take additional dust heating from old stars into account. In this work we used extinction profiles from the Buat et al. (2005) prescription. We made this choice to maximize simplicity and reproducibility of our analysis (this recipe does not require additional information on K-band photometry). Muñoz-Mateos et al. (2009a) showed that the two prescriptions differ significantly only for early-type galaxies (ellipticals and lenticulars), which are absent in our sample. We verified that our conclusions are not modified when changing the adopted prescription.

The extinction corrected profile $\mu_{\text{FUV,corr}}$ (expressed in the AB magnitude system) was converted into a SFRD by making use of the formula:

$$\frac{\dot{\Sigma}_{\star}}{M_{\odot} \text{ pc}^{-2} \text{ Gyr}^{-1}} = (1 - \mathcal{R}) \cos i 10^{-0.4\mu_{\text{FUV,corr}} + 10.413} \quad (2.7)$$

which is again consistent with Muñoz-Mateos et al. (2007). For the return fraction, we adopted $\mathcal{R} = 0.3$, which is intermediate between possible values for different IMF choices (Leitner & Kravtsov 2011; Fraternali & Tomassetti 2012). Also the systematics associated with (2.7) is discussed in Sec. 2.4.4.

2.4 Analysis

For each galaxy in the sample, we performed our analysis in two steps. First, we made an exponential fit to the radial profile of the stellar mass surface density of the disc (see Sec. 2.3.2), deriving the values for the disc mass M_{\star} and scalelength R_{\star} . Then, keeping these parameters fixed, we fitted our theoretical profile (2.5) to the SFRD data (see Sec. 2.3.3). This second fit is the test bed for our theory. If successful, it provides our measurement of the two disc growth parameters: the specific mass growth rate ν_{M} and the specific radial growth rate ν_{R} .

A more extended description of the two steps is given in Secs. 2.4.1 and 2.4.2. They are depicted, for each individual galaxy, in an Atlas, which can be found in

²The formula of Leroy et al. (2008) was based on their measured linear 3.6 μm -to-K-band flux conversion and on an assumed K-band mass-to-light ratio. Changing the latter from 0.5 to 0.8 is equivalent to introducing an additional factor 1.6 in the 3.6 μm -to-stellar mass conversion.

NGC 0628

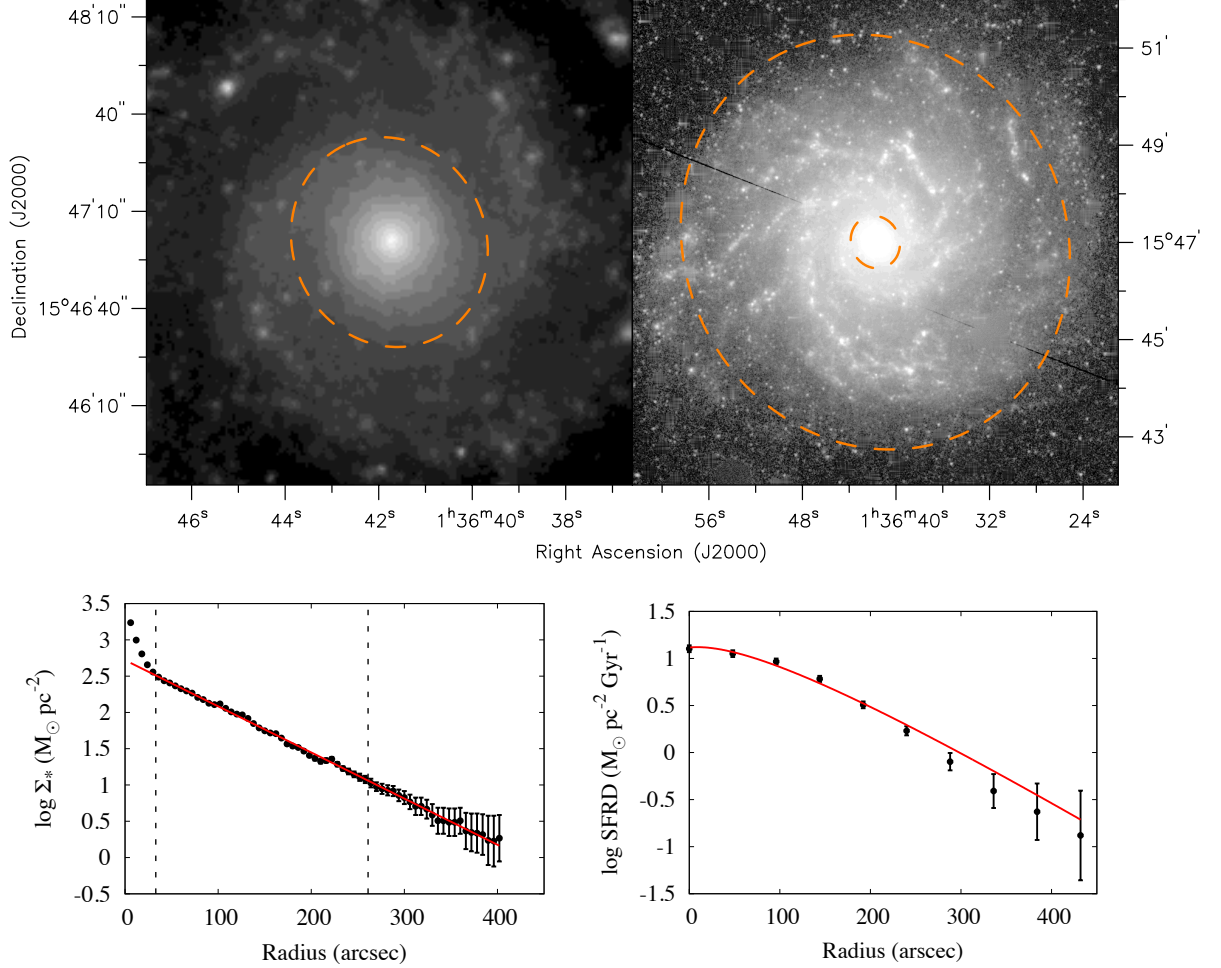


Figure 2.2: Our analysis for the galaxy NGC 628. *Upper panels* Selection of the domain where the emission at $3.6 \mu\text{m}$ is dominated by the light from the stars in the the disc: *left* the inner ellipse at 33 arcsec, out of which the spiral structure appears, *right* the outer ellipse at 261 arcsec, out of which the contribution from noise becomes significant. Note that the two images have very different scale and contrast. The inner ellipse is also shown in the right panel, to make the whole selected region visible at once. *Lower-left panel* Exponential fit to the stellar mass surface density, as traced by the emission at $3.6 \mu\text{m}$. The vertical dashed lines mark the limits of the domain that we have selected for this fit; in this case, the best-fitting exponential also extends further out in the outskirts. *Lower-right panel* Fit of our theoretical SFRD profile to the one obtained from extinction-corrected FUV light; a visual comparison with Fig. 2.1 is already enough to recognize this as an inside-out growing galaxy.

Appendix 2.E. A representative example, for the galaxy NGC 628, is reported here for illustrative purposes (Fig. 2.2).

All our fits were performed with a standard Marquardt-Levenberg algorithm. We also repeated the whole analysis with a different method (see Sec. 2.4.3) and verified that our results are robust with respect to the fitting strategy.

2.4.1 Fit of exponential discs

In order to extract the disc parameters from the radial profiles described in Sec. 2.3.2, we performed a simple exponential fit, for each galaxy, on a radial domain where the NIR emission is dominated by the disc component.

Such a domain was identified, on a case-by-case basis, considering the shape of the $3.6 \mu\text{m}$ profile with the aid of the direct visual inspection of the 2D maps at the same wavelength. For details about how these maps were obtained the reader is referred to Regan et al. (2004), Dale et al. (2005) and Muñoz-Mateos et al. (2009b). For each galaxy, the minimum and the maximum radius of our selected domain are the semi-major axes of two concentric ellipses, with centre and orientation equal to the ones used in the derivation of the profiles. The inner ellipse was chosen to exclude the central bright component, if present, like a bulge, a bar, or a central ring; the detection of spiral arms has been used in some cases as an evidence for the prominence of the disc component in a given region. In 4 cases (NGC 2403, IC 2574, NGC 4236, NGC 4826) we have found that the adopted centre of the ellipses did not coincide with the peak of the $3.6 \mu\text{m}$ emission; for these galaxies, an inner ellipse was selected with a semi-major axis equal or greater than twice the observed offset. The outer ellipse was most of the times selected to exclude those external regions where a contribution to the emission coming from the noise was found to be significant; for our data, this happens at a typical value of $\log(I_{3.6 \mu\text{m}}/\text{Jy arcsec}^{-2}) \sim -6.5$.

In 5 galaxies (NGC 3521, NGC 3621, NGC 4736, NGC 5055, NGC 7331) we found a significant flattening of the $3.6 \mu\text{m}$ profile well above the noise level and we excluded the outer region from the exponential fit for these objects. The most striking case is NGC 4736, where the effect is probably related to the presence of a prominent outer ring. In 3 of the above cases (NGC 3521, NGC 3621, NGC 5055) the change of slope occurs very near to the outermost radius where a regular spiral pattern can be seen. In the remaining two objects (NGC 3521 and NGC 7331) the flattening is associated with an abrupt change in the geometry of the $3.6 \mu\text{m}$ emission, with the isophotes becoming remarkably large and irregular in the outer regions. We ignore the physical origin of this effect; nonetheless, these peculiarities should be kept in mind in the interpretation of our results for these objects.

In most cases, our fits were performed weighting each point according to the nominal error, quoted in the original profiles. However, this is not necessarily always the best choice. Real galaxies are not expected to precisely follow an exponential, since transient perturbations like spiral arms, which are by definition ubiquitous in spiral galaxies, can sometimes overimpose oscillations on an underlying regular disc. This effect can become particularly important in the presence of spiral arms with a small pitch angle, tending to dominate the emission in a limited radial range. If, for a given galaxy, points with small error bars happen to be preferentially located

in a region dominated by spiral structure, the formal best-fitting profile will be biased to reproduce transient features, potentially missing the overall structure of the disc. For 7 galaxies (NGC 1097, NGC 1512, NGC 3031, NGC 3184, NGC 3351, NGC 4569, NGC 7793) we have found that an unweighted fit provided a better description of the overall structure of the profiles in the considered radial range. One example (NGC 3031) is discussed in more detail in Appendix 2.B, to better illustrate the reasons of our choice.

Although the whole procedure is slightly subjective, we verified that it gave a better account to the observed properties of our galaxies, in the domain of interest, with respect to a more complex global analysis, involving more components and parameters. This approach is the most suitable for our purposes, since we are just interested to reliably derive the disc parameters, rather than to get a detailed structural decomposition of the whole galaxy. We verified that the parameters that we found were stable with respect to small variations in the selection of the inner and outer radii.

An example of our domain selection and disc-fitting procedure is given in Fig. 2.2 (upper panels and lower-left panel) for the case of NGC 628; similar images and plots for the other galaxies can be found in the Atlas.

2.4.2 Fit of the star formation rate surface density

In the second step of our analysis, we fitted equation (2.5) to the observed SFRD profiles, keeping fixed the structural parameters M_* and R_* found in the previous step.

The SFRD profiles have a worse spatial resolution, and hence a more limited number of independent points, with respect to the mass surface density profiles. As a consequence, the results of the SFRD fits are more sensitive to changes in the adopted radial domain. In order to limit the dependence of our analysis on subjective choices, we decided to always perform the fit on the whole available domain. Not to exclude any point from the inner regions is equivalent to assume that the bulk of star formation is everywhere associated with the disc component. In other words, we neglected possible star formation activity directly occurring in the bulges, which is quite reasonable since these structures are known to be dominated by old stellar populations. Neither we put outer limits to our domain, implying that we did not try to model possible transient star formation episodes that might dominate the UV emission in the outer regions, nor any kind of structural irregularity and, most noticeably, the possible presence of warps, which are generally expected in the periphery of discs (e.g. Briggs 1990). All the SFRD fits were performed weighting points with their nominal errors, which were derived just propagating the errors in the μ_{FUV} and A_{FUV} profiles. In Fig. 2.2 (lower-right panel) the best-fitting SFRD profile is reported for the galaxy NGC 628; similar plots are reported for all galaxies in the Atlas.

In considering this part of the analysis, it should be kept in mind that, while the parameters ν_{M} and ν_{R} , in the theoretical SFRD profile (2.5), are allowed to change in the fitting process, the global slope is strongly constrained by the parameter R_* , which is held fixed to the value previously obtained from the structural fit (Sec.

2.4.1). Hence, notwithstanding the presence of 2 free parameters, we are by no means able to reproduce arbitrary profiles and the fact that we can recover the majority of SFRD distributions shall be regarded as a success of the model and gives us confidence on the meaningfulness of the resulting best-fit parameters.

In 5 cases (NGC 1512, NGC 3521, NGC 3621, NGC 4736, NGC 5055) we clearly detect an outer flattening in the radial profiles of both SFRD and stellar mass surface density. This can be considered as an indication for the existence of a distinct, relatively long-lived, outer star forming component. More detailed studies would be necessary to clarify this point. However, we notice here that three of these galaxies (NGC 1512, NGC 3621, NGC 5055) have been classified by Thilker et al. (2007b) as having a Type 1 XUV disc. We also notice that sometimes (e.g. for NGC 3621) the spatial coincidence between the two breaks is perfect, while in other cases (NGC 3521 and NGC 5055) the SFRD flattening occurs at larger radii, maybe challenging the idea of a common origin of the two structures. A unique case is the one of NGC 7331, which has a very prominent flattening of the stellar mass distribution, but an almost exponential SFRD profile, which our model is unable to account for; we refer the reader to Thilker et al. (2007b) and Ludwig et al. (2012) for more specific studies on this peculiar object and its surroundings. Finally, we report one case (IC 4710) where a quite marked downbending is found, at the same radius, in both profiles. This is not a very secure result, since the break occurs out of our chosen outer ellipse (see Sec. 2.4.1); if confirmed, it may be an example of radial migration in the presence of an outer cut-off in star formation efficiency, as described e.g. by Yoachim, Roškar & Debattista (2012) (see also Sec. 2.2.2).

Despite our choice of analyzing the whole sample in a homogeneous fashion, we recognize that more specific choices may be appropriate for those objects showing extreme behaviours in their SFRD profiles. As an example, we discuss In Appendix 2.C one possible alternative analysis for the very peculiar case of NGC 3621.

2.4.3 A note on the fitting strategy

Our choice of separating the analysis in two steps (Secs. 2.4.1 and 2.4.2) is motivated by the fact that the structural parameters (M_* , R_*) physically describe the mass distribution of stellar discs and hence, in principle, they are best measured on the basis of available data for Σ_* alone, irrespective of the distribution of newly born stars. Also, once such a measurement has been achieved, the fact that the SFRD profiles can be reproduced without a further tuning of (M_* , R_*) provides a valuable test for the validity of our theory.

However, we also investigated whether our results would change if our 4 parameters (M_* , R_* , ν_M , ν_R) were allowed to vary simultaneously to reproduce both the stellar mass and the SFRD radial profiles. To this purpose, we ran, for each galaxy, a Monte Carlo Markov Chain based on the combined likelihood of both our datasets (Secs. 2.3.2 and 2.3.3). We then compared the resulting radial growth rates with the ones derived with our preferred strategy, finding an excellent agreement, with a median absolute difference of just 2×10^{-4} Gyr $^{-1}$. We found some discrepancy in just 4 cases, 2 of which within 2σ (NGC 1097 and NGC 7793) and the other 2 within 3σ (NGC 3184 and NGC 3351). Note that all these objects belong to the group for

which an unweighted fit was found to provide a better description of the overall disc structure (see Sec. 2.4.1), while the effect of oscillations induced by spiral structure was not taken into account in the MCMC experiment. This probably explains even the moderate discrepancies for this small subset. Furthermore, it shows that our partially subjective choice of the weights, discussed in Sec. 2.4.1, has a very limited impact on our general results.

2.4.4 Notes on systematics

We distinguish between two kinds of systematics, those affecting individual galaxies in a different way and those affecting the whole sample more or less homogeneously.

To the first group belong distance and inclination. Distance uncertainties affect the physical values of the derived mass and scalelengths, while the inclination uncertainty mainly affects the determination of the mass. Inclination also affects the normalization of both the stellar mass and the SFRD profiles, but it does it exactly in the same way; it is easily seen that this implies a vanishing net effect on the estimates of ν_M and ν_R , which are also, even more obviously, completely independent on the adopted distance. The important consequence of this is that our method allows us to measure the specific mass and radial growth rates of discs with greater accuracy than the mass and scalelength themselves, a fact that we will further exploit in Sec. 2.6.

The second group of systematics comprises the mass-to-light ratio, the calibration of the FUV-to-SFRD conversion and the return fraction \mathcal{R} . Apart from second order effects, like possible variations of the mass-to-light ratio and the IMF with radius or morphological type, the main uncertainty coming from these systematics is a common multiplicative factor for both the growth parameters, ν_M and ν_R , for the whole sample, or, in other words, a possible global rescaling of all the derived timescales. As examples of global systematics, we consider in some more detail the effect of the IMF and of the return fraction. In our calibrations, we have implicitly adopted a Salpeter IMF. To switch, for instance, to the more popular Kroupa (2001) IMF, we should divide the M/L ratio and hence all stellar mass surface densities by a factor 1.6 (see footnote 2, Sec. 2.3.2), while multiplying all star formation rate surface densities by a factor 0.63 (Kennicutt & Evans 2012). The net result on the sSFR (and hence on the estimates of ν_M and ν_R) is less than 1 %. This is due to the fact that in both cases the impact of the IMF is essentially driven by a common change in normalization associated to the contribution of very low mass stars. The effect of the return fraction \mathcal{R} is stronger: for instance, changing our adopted $\mathcal{R} = 0.3$ into $\mathcal{R} = 0.48$ (which is the largest of the values suggested by Leitner & Kravtsov 2011) would imply a reduction of all growth rates by a factor 1.35 and an equal increase of all timescales. Unfortunately, the return fraction is a quite uncertain parameter, since it is significantly affected not only by the IMF, but also by the details of the final-to-initial mass relation, which is very difficult to determine observationally. However, we stress that the dimensionless ratio between ν_R and ν_M is unaffected by any of the systematics we have discussed so far. The importance of this fact will be highlighted in Sec. 2.6.

Table 2.2: Best fit structural (M_* and R_*) and growth (ν_M and ν_R) parameters for galaxies in our sample. Formal fitting errors are reported, not including contributions due to distance, inclination and calibrations of conversion fomulae. Compared with stellar mass and scalelength, the growth parameters ν_M and ν_R are less affected by systematic effects (see Sec. 2.4.4). Out of 35 studied galaxies, 32 have a positive radial growth rate ν_R .

Galaxy	M_* ($10^9 M_\odot$)	R_* (kpc)	ν_M (10^{-2} Gyr^{-1})	ν_R (10^{-2} Gyr^{-1})
NGC 0024	3.01 ± 0.13	1.62 ± 0.02	5.85 ± 1.03	2.51 ± 0.52
NGC 0337	27.7 ± 2.3	2.15 ± 0.06	11.6 ± 3.5	4.95 ± 1.72
NGC 0628	43.7 ± 1.4	3.64 ± 0.05	8.22 ± 0.36	2.87 ± 0.21
NGC 0925	11.3 ± 0.8	3.97 ± 0.11	10.3 ± 0.5	0.799 ± 0.381
NGC 1097	68.2 ± 8.1	6.32 ± 0.23	8.74 ± 1.04	-2.05 ± 0.75
NGC 1512	14.7 ± 2.2	2.22 ± 0.09	3.80 ± 0.81	1.22 ± 0.45
NGC 1566	78.0 ± 5.3	3.30 ± 0.07	8.21 ± 0.83	2.90 ± 0.44
NGC 2403	7.19 ± 0.22	1.51 ± 0.02	9.91 ± 0.25	2.93 ± 0.16
NGC 2841	92.8 ± 3.4	3.69 ± 0.05	1.62 ± 0.08	0.612 ± 0.045
NGC 2976	2.25 ± 0.21	0.802 ± 0.028	5.88 ± 0.57	2.04 ± 0.33
NGC 3031	48.3 ± 2.5	2.54 ± 0.03	1.99 ± 0.20	0.750 ± 0.118
NGC 3184	17.2 ± 1.6	2.42 ± 0.08	6.00 ± 0.80	1.50 ± 0.55
NGC 3198	32.0 ± 1.8	3.65 ± 0.07	8.05 ± 0.81	3.30 ± 0.42
IC 2574	1.21 ± 0.07	3.01 ± 0.08	12.0 ± 1.1	3.71 ± 0.70
NGC 3351	45.3 ± 3.4	2.86 ± 0.05	3.62 ± 0.17	0.384 ± 0.109
NGC 3521	54.2 ± 2.3	1.85 ± 0.03	4.75 ± 0.56	1.95 ± 0.29
NGC 3621	24.8 ± 1.0	1.74 ± 0.02	9.84 ± 2.05	4.18 ± 1.04
NGC 3627	58.2 ± 2.5	2.36 ± 0.03	4.66 ± 0.36	1.24 ± 0.21
NGC 4236	1.83 ± 0.10	2.77 ± 0.07	11.4 ± 0.5	4.70 ± 0.27
NGC 4536	27.0 ± 1.7	3.90 ± 0.09	11.2 ± 0.4	1.17 ± 0.24
NGC 4559	42.7 ± 1.4	4.47 ± 0.05	10.6 ± 1.0	4.10 ± 0.51
NGC 4569	78.3 ± 3.3	4.38 ± 0.05	2.07 ± 0.11	-0.02940 ± 0.0781
NGC 4579	87.6 ± 2.2	3.56 ± 0.03	1.70 ± 0.24	0.357 ± 0.155
NGC 4725	117 ± 11	5.45 ± 0.18	2.17 ± 0.25	0.831 ± 0.155
NGC 4736	22.8 ± 3.1	1.13 ± 0.05	4.75 ± 1.06	1.18 ± 0.52
NGC 4826	51.0 ± 1.3	1.96 ± 0.01	1.55 ± 0.21	-0.0850 ± 0.1068
NGC 5033	23.5 ± 2.6	3.91 ± 0.15	10.2 ± 0.7	2.09 ± 0.42
NGC 5055	57.4 ± 3.8	2.50 ± 0.05	4.87 ± 0.63	1.45 ± 0.34
NGC 5194	77.5 ± 6.1	2.75 ± 0.07	7.56 ± 0.55	1.26 ± 0.38
NGC 5398	4.86 ± 0.22	1.95 ± 0.03	8.77 ± 0.19	3.57 ± 0.10
NGC 5713	54.8 ± 6.6	1.94 ± 0.06	11.0 ± 3.6	4.54 ± 1.80
IC 4710	2.71 ± 0.22	2.13 ± 0.08	7.61 ± 1.69	1.97 ± 1.04
NGC 6946	46.6 ± 2.2	2.67 ± 0.05	8.31 ± 0.54	0.765 ± 0.529
NGC 7331	123 ± 13	2.64 ± 0.08	10.5 ± 3.8	5.02 ± 1.88
NGC 7793	5.10 ± 0.23	1.26 ± 0.02	9.10 ± 0.73	2.58 ± 0.46

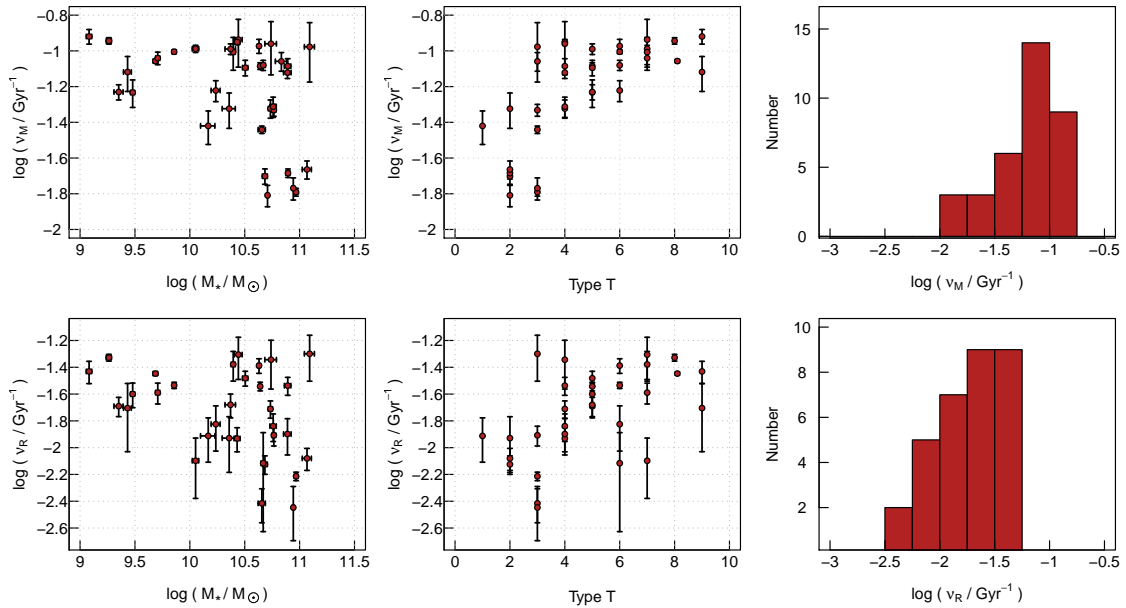


Figure 2.3: The specific mass and radial growth rates ν_M (top) and ν_R (bottom) as a function of disc stellar mass (left) and morphological type (middle) and the relative histograms (right). Lower panels contain only the 32/35 galaxies with $\nu_R > 0$. Error bars are formal fitting uncertainties. The distributions of ν_M and ν_R have some similarities (see text), but ν_R values are systematically lower by ~ 0.5 dex.

2.5 Results

The results of our analysis are listed in Table 2.2. The quoted errors are just the formal fitting ones; in particular, they do not take into account systematic uncertainties, which, as discussed in Sec. 2.4.4, might be important for the structural parameters M_* and R_* , but have a limited impact on the growth parameters ν_M and ν_R .

2.5.1 Inside-out growth

While our analysis is able to reveal both positive and negative radial growth rates, we find that 32 galaxies, out of 35, show $\nu_R > 0$. Of the remaining 3 galaxies with a formally negative radial growth rate, two (NGC 4569 and NGC 4826) have more than 100% uncertainty in ν_R and hence are consistent with evolution of the stellar scalelength in one sense or the other, or with no evolution. Incidentally, we point out that both these galaxies are known to have peculiar properties: NGC 4569 is an anemic spiral in the Virgo cluster, probably significantly affected by ram pressure stripping (Boselli et al. 2006), while NGC 4826 is likely to have undergone a strongly misaligned merger, as suggested by the presence of a counter-rotating gaseous disc in the outskirts (Braun et al. 1994). For only one galaxy in our sample, NGC 1097, we clearly find the signature of a shrinking of the disc. It is interesting to notice, *a posteriori*, that this galaxy has a very disturbed morphology. This is likely due

to a strong interaction with the companion NGC 1097A ³. This object is listed as a peculiar elliptical in the RC3 catalogue (de Vaucouleurs et al. 1991), though with ‘uncertain’ classification. In the GALEX Atlas (Gil de Paz et al. 2007), NGC 1097A is clearly visible as a clump northwest of the prominent bar of NGC 1097, bright in NIR and NUV, faint in FUV and surrounded by an extended, FUV bright, disc-like structure, all properties common, in the GALEX Atlas, to the bulges of spiral galaxies. This is suggestive that the whole system may be a galaxy pair in an advanced stage of merging. We also noted that NGC 1097 is the object with the largest derived disc scalelength (6.32 kpc) and we verified that this result is not changed if we exclude from the exponential fit the whole radial range occupied by NGC 1097A. NGC 1097 has also been suggested to have undergone other significant interactions in the recent past (Higdon & Wallin 2003). If our interpretation of a strong interaction state, likely a merger, for this system, is correct, then there is no surprise that it behaves differently from the regular evolution of isolated galaxies.

From these considerations, we can conclude that our findings are in excellent agreement with the general predictions of the inside-out growth scenario for the evolution of spiral galaxies.

2.5.2 Mass and radial growth rates

In Fig. 2.3 the mass and radial growth rates of the galaxies in our sample are plotted against disc stellar mass and morphological type. Since we are using logarithmic units, radial growth rates (lower panels) are reported only for those 32/35 galaxies with $\nu_R > 0$ (see Sec. 2.5.1). Error bars represent formal fitting errors only. In particular, errors on distance and inclination are not taken into account in these plots. As discussed in Sec. 2.4.4, these additional errors can affect stellar masses, but not ν_M and ν_R , which are only subject to a common multiplicative uncertainty due to global calibration issues. We also give in Fig. 2.3 the histograms for the distributions of ν_M and ν_R , binned in logarithmic intervals of 0.25 dex width.

From the upper panels of Fig. 2.3 we see that the specific mass growth rates (or specific star formation rates, or sSFR) of the discs of our galaxies assume a relatively narrow range of values, with most of our points clustered around $\nu_M \sim 0.1 \text{ Gyr}^{-1}$, which corresponds to a mass growth timescale of $\sim 10 \text{ Gyr}$. This is in substantial agreement with the typical sSFR of star-forming galaxies in the Local Universe (e.g. Elbaz et al. 2011) and in particular with the relative constancy of the sSFR of the discs of spiral galaxies (Abramson et al. 2014), although a more detailed comparison would require more statistics and a careful treatment of global systematics (Sec. 2.4.4), which is beyond the scope of this work (see e.g. Speagle et al. 2014 about subtle issues concerning the homogenization of measurements of this kind). We find that a small group of 6 galaxies (NGC 2841, NGC 3031, NGC 4569, NGC 4579, NGC 4826, NGC 4725) have a particularly low sSFR, with $\log(\nu_M/\text{Gyr}^{-1}) < -1.5$. We have already recognized two of them (NGC 4569 and NGC 4826) as objects with peculiar properties and a close to vanishing radial growth rate (see Sec. 2.5.1), but we cannot tell whether these peculiarities have a direct physical connection with the

³Note that NGC1097A cannot be seen in our Atlas, since it has been masked out from our 3.6 μm map.

Table 2.3: Basic statistics for our derived specific mass and radial growth rates (cfr. Fig. 2.3). Note that discs with higher masses have lower median values and a higher scatter for both ν_M and ν_R .

	$M_\star < 10^{10} M_\odot$	$M_\star > 10^{10} M_\odot$	All
$\log(\nu_M/\text{Gyr}^{-1})$			
Median	-1.05	-1.12	-1.09
Scatter	0.13	0.25	0.20
$\log(\nu_R/\text{Gyr}^{-1})$			
Median	-1.56	-1.87	-1.70
Scatter	0.18	0.37	0.35

low measured values of ν_M . However, we can see from the upper-mid panel that the whole group of 6 slowly-evolving galaxies are also among the galaxies of the earliest types in our sample. This may be interpreted as an indication of downsizing (e.g. Cowie et al. 1996): galaxies with high mass and early types are more likely to have completed most of their evolution in ancient epochs and hence to be growing with only mild rates nowadays. Also, galaxies of high mass and early-type might be more subject to star-formation quenching, the origin of which and its connection with morphology is still matter of investigation (e.g Martig et al. 2009; Pan et al. 2014).

In the lower panels of Fig. 2.3 we can see the distribution of the radial growth rates, which are the main novelty of this work. When plotted against disc mass, the radial growth rate ν_R shows a quite similar distribution with respect to the one of ν_M , but systematically shifted downwards by ~ 0.5 dex. This suggests that our galaxies are growing in size, on average, at about 1/3 of the rate at which they are growing in stellar mass. The histogram of ν_R reveals a distribution that is similarly asymmetric, though less strongly peaked, with respect to the one of ν_M . More than 50% of our galaxies are in the two bins around $\log(\nu_R/\text{Gyr}^{-1}) = -1.5$, that is 0.5 dex below the peak of the ν_M distribution, corresponding to a typical radial growth timescale of ~ 30 Gyr. Since the radial growth rate of galaxy discs has been studied much less than the sSFR, it is less obvious to compare our findings with the ones of previous studies. However, we notice the typical timescale reported above is compatible with a radial growth of $\sim 25\%$ in the last ~ 7 Gyr, very similar to what found by Muñoz-Mateos et al. (2011). Our typical ν_R is also consistent with the results from the detailed study of resolved colour-magnitude diagrams for M 33 (Williams et al. 2009), while NGC 300 seems to have been growing at about half of this rate (Gogarten et al. 2010). However, our estimates strictly refer to the current time and caution is mandatory in extrapolating these instantaneous measurements to a significant fraction of the past history of these galaxies.

Apart from the global vertical shift, the distributions of galaxies in the upper-left and bottom-left panels of Fig. 2.3 have a quite well defined common shape. In both cases, there is a horizontal upper envelope, close to the peak of the distribution, and a continuous increase of the scatter with increasing disc mass. Such a scatter is asymmetric and biased towards low values of ν_M and ν_R , with the result that, on

average, more massive discs appear to grow at a slower rate, both in mass and size, than the less massive ones. This effect is quantified in Table 2.3, where the median mass and radial growth rates are reported, together with the associated scatter, for two subsamples with a derived disc mass lower or greater than $10^{10} M_{\odot}$. It is not easy to understand, with our relatively small sample, if some simple physical property can be invoked to explain the scatter at high disc masses. However, we performed some simple checks and did not find any particular correlation between the position of galaxies in our plots and special properties, including the presence of a bar, an XUV disc, a break in the exponential profile, or indications of a warp or an interaction. We are therefore tempted to interpret the effect as intrinsic.

2.6 Implications for the evolution of scaling relations of disc galaxies

2.6.1 The mass-radial growth connection

Among our derived quantities, the mass and radial growth rates are the least affected by systematic uncertainties (see Sec. 2.4.4). Hence, the most reliable of our results are those that we can derive plotting ν_M and ν_R against each other. This is also important to understand whether the shift, that we found in Sec. 2.5.2, of a factor ~ 3 between ν_M and ν_R is significant only at a statistical level or if it reflects an evolutionary property of individual galaxies.

Indeed, this experiment (Fig. 2.4) reveals that the two growth rates are related to each other much more strongly than they are, individually, with mass or morphological type (cfr. Fig. 2.3).

The fact that masses and sizes of galaxies grow in an interlinked way is not very surprising on its own. Hence, rather than fitting a straight line to the points in Fig. 2.4, we prefer to seek for some simple physical explanation that can give a quantitative account to our finding.

2.6.2 A comparison with a simple theoretical prediction

Let us assume that mass and size of the discs of spiral galaxies are connected by a power-law (e.g. Courteau et al. 2007, Lange et al. 2015):

$$R_{\star} = AM_{\star}^{\alpha} \quad (2.8)$$

Furthermore, let us assume that the coefficients A and α are not evolving with time, so that the relation (2.8) defines not only the present locus, but also the evolutionary track of stellar discs. Then, from (2.8) and taking the definitions (2.3) and (2.4) into account, it immediately follows that the specific mass and radial growth rates should be linked by the very simple linear relation:

$$\nu_R = \alpha \nu_M \quad (2.9)$$

or, in logarithmic units:

$$\log \nu_R = \log \alpha + \log \nu_M \quad (2.10)$$

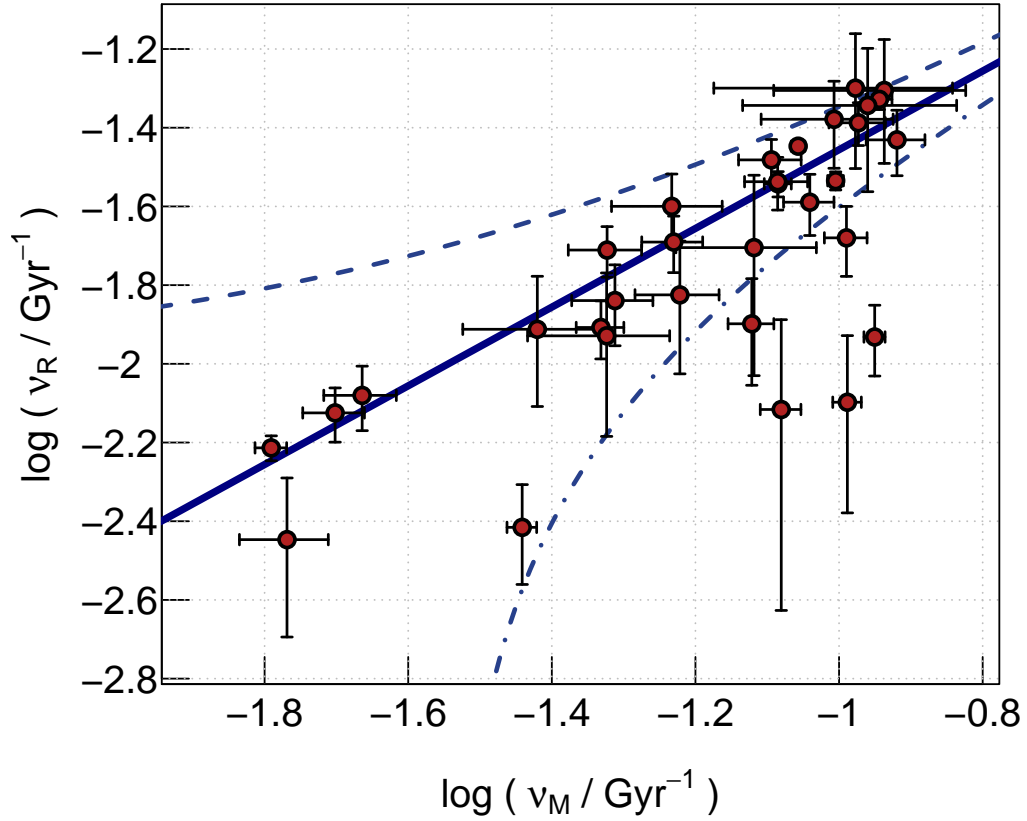


Figure 2.4: The relation between the specific mass growth rate and the specific radial growth rate of galaxy discs. The points are the results of our measurements, the lines are predictions of some simple models. The solid line is the expectation if known scaling relations of disc galaxies are not evolving with time, the dashed line and the dot-dashed line are for scaling relations evolving on a timescale of 100 Gyr, in one sense or the other (see text for details). A more rapid evolution is excluded by our results.

Independently on the value of α , equation (2.10) implies that (ν_M, ν_R) points should lie, in a double logarithmic plot like Fig. 2.4, on a line of unitary slope; this is indeed the slope of the solid line drawn in Fig. 2.4, which gives a quite good account for the distribution of our datapoints. This is already suggestive that our results are consistent with the existence of a non-evolving, power-law, mass-size relation for the discs of spiral galaxies.

Of course, for our simple scenario to be fully predictive, not only the slope, but also the intercept, of such a straight line should be predicted as well, which is accomplished by specifying the expected value for α . To do this, we just combine two well-known scaling relations for disc galaxies, the Tully-Fisher relation (McGaugh 2012), between the rotation velocity V and the mass M of a spiral galaxy:

$$V \propto M^{0.25} \quad (2.11)$$

and the Fall relation (Romanowsky & Fall 2012), between specific angular momentum l and mass:

$$l \propto M^{0.6} \quad (2.12)$$

which we have discussed in detail in Chapter 1. Since exponential discs belong to a structurally self-similar family, one also has:

$$R_* \propto \frac{l}{V} \quad (2.13)$$

Substituting (2.12) and (2.11) into (2.13) we get a power-law mass-size relation of the form (2.8), with $\alpha = 0.35$. This is not far from the value 0.32 empirically derived by Courteau et al. (2007) as an average slope for the mass-scalelength relation of disc galaxies in the Local Universe (since it was derived in the I-band, residual effects cannot be excluded arising from M/L variations). Shallower slopes are frequently found by studies based on half-light radius rather than disc scalelength (see e.g. Lange et al. 2015); this is in qualitative agreement with expectations if we consider an obvious morphological effect (more massive galaxies tend to have more prominent bulges and hence a smaller ratio between half-light radius and scalelength).

To define our simple model, we just retained the value $\alpha = 0.35$, derived from the Tully-Fisher and the Fall relations as explained above, and we adopted it to draw the solid line in Fig. 2.4. Hence we see that the majority of our data-points lie on a locus that can be independently predicted, without any free parameter, just assuming that known scaling relations for disc galaxies hold and are not evolving at the present time. Since these simple hypotheses are completely independent from the way our results were derived, the agreement between the two is very unlikely to occur by chance, or to be due to biases of any kind, and we therefore interpret this finding as an indication for the validity of both our method and the hypotheses themselves.

We can also consider what effect residual systematics on ν_M and ν_R could have on our findings. As discussed in Sec. 2.4.4, the effect is an unknown common multiplicative factor for ν_M and ν_R . In the diagram shown in Fig. 2.4, this implies a collective motion of all points along a line of unitary slope, or, equivalently, a mapping of the theoretical line into itself. Therefore, our conclusions are robust at least against the most obvious systematic uncertainties.

A word of caution is appropriate, however, against possible overinterpretation of our model and result. In fact, the Tully-Fisher relation is known to hold better for the whole baryonic content of spiral galaxies (McGaugh 2012), while we have implicitly applied it just to the stellar mass of the disc. On the other side, the Fall relation seems to hold better when the disc component is considered separately from the bulge. Hence, it can be argued that, in deriving our predictions, we have mixed non-homogeneous empirical evidence. A more detailed analysis, taking this aspect into a proper account, would be interesting, but is beyond the scope of this work.

2.6.3 Evolutionary effects

In the previous Section we have seen that our results are compatible with the Tully-Fisher and Fall relations to be not evolving with time. To quantify this statement, we put here an upper limit on how fast a possible evolution can be in order to be still compatible with our results. For simplicity, we focus our attention on the evolution in normalization, although a similar analysis could be performed for the slope evolution as well.

If, in (2.8), we allow the normalization A to change with time, then (2.9) simply modifies into:

$$\nu_R = \nu_A + \alpha\nu_M \quad (2.14)$$

where:

$$\nu_A(t) := \frac{d}{dt}(\ln A)(t) = \frac{\dot{A}(t)}{A(t)} \quad (2.15)$$

is the specific growth rate of the normalization coefficient A . Of course, when equation (2.14) is compared with our observations in the Local Universe, ν_A has to be intended as evaluated at the present time.

The dashed and dot-dashed lines in Fig. 2.4 show the predictions of two models with a very mild evolution in normalization, in one sense or the other: $\nu_A = \pm 0.01 \text{ Gyr}^{-1}$. It is clearly seen that the predicted distribution of galaxies in the (ν_M, ν_R) plane is extremely sensitive to the parameter ν_A , making this diagram a new and powerful observational tool to constrain the evolution of scaling relations of galaxy discs. Also, since the two additional lines are both inconsistent with the empirical distribution, we quantitatively infer that, even admitting that scaling relations are evolving with time, they are doing so on timescales that are larger than $(\nu_{A, \max})^{-1} = 100 \text{ Gyr}$, hence much larger than the Hubble time.

Strictly speaking, the statement above mainly refers to the mass-size relation (2.8). In fact, although the Tully-Fisher relation (2.11) and the Fall relation (2.12) are the backbone of the simple model sketched in 2.6.2, it may be considered not trivial to draw out conclusions concerning them individually, since they both involve kinematics, while we did not directly make use of kinematical data. However, our results indicate that an evolution of the Tully-Fisher relation, if present, has to be accompanied and finely balanced by an opposite evolution of the Fall relation. Furthermore, we stress that our firm upper limit ($|\nu_A| < \nu_{A, \max} = 10^{-2} \text{ Gyr}^{-1}$) only refers to ν_A evaluated at the present time and hence it can only be compared with theoretical predictions and observational determinations of the recent evolution of A .

It is interesting to compare our results with the predictions of simple cosmologically motivated models. Following Mo, Mao & White (1998), if the mass and angular momentum of discs are a fixed fraction of the ones of the dark matter haloes and if the latter are still growing today⁴, then a mass-size relation for discs should hold, of the form (2.8), with $\alpha = 1/3$, which is very close to our preferred value $\alpha = 0.35$ and, as we assumed, it is constant with time. On the other hand, the normalization A should scale as $H^{-2/3}$, where H is the Hubble constant. For a flat Universe made of matter and a cosmological constant, a simple calculation yields:

$$\nu_A = -\frac{2}{3} \frac{d \ln H}{dt} = \Omega_m H = 2.15 \times 10^{-2} \text{ Gyr}^{-1} \quad (2.16)$$

where, in the last equality, we assumed a matter density parameter $\Omega_m = 0.3$ and a Hubble constant $H = 70 \text{ km s}^{-1} \text{ Mpc}^{-1}$. The estimate above is twice than our upper limit $\nu_{A, \text{max}}$ and it is therefore incompatible with our empirical findings. More refined models for the assembly of dark matter haloes give predictions that are even worse, by a further factor 2 (see Appendix 2.D)⁵. The tentative indication is therefore that baryonic processes may be very important, in shaping the scaling relations of disc galaxies, at least at low redshift. It is remarkable, however, that these likely complex processes can conspire with the evolution of dark matter haloes to give rise to results as simple as the observed ones.

On the other hand, our results show no tension with observations of scaling relations at moderate redshift. Recent results indicate that the Tully-Fisher relation is compatible with small or no evolution at least up to $z \sim 1$ (Miller et al. 2011), while, to our knowledge, no similar studies are available yet concerning the Fall relation. Concerning the mass-size relation, we can mention the representative findings of Trujillo et al. (2006), which are compatible (within errors) both with the model by Mo, Mao & White 1998 discussed above and with no evolution up to $z \sim 1$. To tell the difference between different scenarios, more precise measurements at moderate redshift would be needed. In the meanwhile, a sensitive local diagnostics like the one that we have proposed here can serve as a valuable complement to pioneering observational campaigns in the distant Universe.

2.7 Summary

In this Chapter, we have developed, from very simple assumptions, a model that predicts a universal shape for the radial profile of the star formation rate surface density (SFRD) of spiral galaxies. This model accounts for the basic properties of observed profiles and naturally includes a parametrization of the growth of the stellar discs. As a consequence, we have devised a novel method to measure the instantaneous mass and radial growth rates of stellar discs, based on their SFRD

⁴In this case, the ‘virialization redshift’ of Mo, Mao & White (1998) is $z = 0$.

⁵Mo, Mao & White (1998) also considered that a halo can have stopped accreting material at a ‘virialization redshift’ $z > 0$. Simple scalings can be applied, in this case, only to those galaxies that have stopped forming stars accordingly, while stellar discs growing in quiescent haloes at $z = 0$, if they exist, are clearly governed by processes other than cosmological.

profiles. We have applied our method to a sample of 35 nearby spiral galaxies ⁶. Our main results are:

- (i) For most of the galaxies in our sample, the SFRD profile is satisfactorily reproduced by our model, in such a way that we could measure the mass and radial growth rates ν_M and ν_R of their stellar discs.
- (ii) Virtually all galaxies show the signature of inside-out growth ($\nu_R > 0$).
- (iii) Typical timescales for the mass and radial growth of our stellar discs are of the order of ~ 10 Gyr and ~ 30 Gyr, respectively, with some uncertainty due to systematic effects.
- (iv) The mass and radial growth rates appear to obey a simple linear relation, with galaxy discs growing in size at ~ 0.35 times the rate at which they grow in mass. Compared with the individual timescales given above, this dimensionless ratio is very robust against systematic uncertainties.
- (v) The distribution of galaxies in the (ν_M, ν_R) plane is a sensitive diagnostics for the evolution of scaling relations of galaxy discs.
- (vi) Our results are in very good agreement with a simple model, without free parameters, based on the universality of the Tully-Fisher relation and the Fall relation, suggesting that they are not evolving with time. Possible residual evolution is constrained to occur on timescales that are much larger than the age of the Universe.

APPENDICES

2.A The effect of the return fraction

The assumption of a constant return fraction breaks whenever the instantaneous recycling approximation does. In general, at a given observed time t_0 , the time derivative of the stellar mass surface density Σ_* is related to the instantaneous star formation rate surface density SFRD through the equation:

$$\frac{\partial \Sigma_*}{\partial t}(t_0) = \text{SFRD}(t_0) - \int_{t_{\text{birth}}}^{t_0} \frac{\partial \mathcal{R}}{\partial t}(t_0 - t') \text{SFRD}(t') dt' \quad (2.17)$$

where t_{birth} denotes the birth time of the considered galaxy, or disc, or disc annulus, and \mathcal{R} is the time dependent return fraction. The detailed dependence of \mathcal{R} on time changes with the chosen IMF, but it can be suitably approximated by:

$$\mathcal{R}(t) = \mathcal{R}_\infty \times \begin{cases} t/t_R & (0 < t < t_R) \\ 1 & (t > t_R) \end{cases} \quad (2.18)$$

⁶An application to the Milky Way will be presented in Sec. 3.5.4 of Chapter 3.

where \mathcal{R}_∞ is the asymptotic value of the return fraction (the one that we simply denote with \mathcal{R} in the manuscript), and t_R is of the order of 1 Gyr. Putting (2.18) in (2.17) one gets:

$$\frac{\partial \Sigma_\star}{\partial t}(t_0) = \text{SFRD}(t_0) - \mathcal{R}_\infty < \text{SFRD} >_{t_R}(t_0) \quad (2.19)$$

where

$$< \text{SFRD} >_{t_R}(t_0) := \frac{1}{t_R} \int_{t_0-t_R}^{t_0} \text{SFRD}(t') dt' \quad (2.20)$$

is the star formation rate surface density averaged in the last $t_R \sim 1$ Gyr.

Equation (2.19) can also be rewritten:

$$\frac{\partial \Sigma_\star}{\partial t}(t_0) = (1 - \mathcal{R}_{\text{eff}}(t_0)) \text{SFRD}(t_0) \quad (2.21)$$

with:

$$\frac{\mathcal{R}_{\text{eff}}(t_0)}{\mathcal{R}_\infty} = \frac{< \text{SFRD} >_{t_R}(t_0)}{\text{SFRD}(t_0)} \quad (2.22)$$

Equation (2.21) clarifies that the *effective return fraction* \mathcal{R}_{eff} is the quantity that shall be used in the definition of the *reduced* star formation rate surface density (used in our applications and in others) if the effect of non instantaneous recycling is taken into account.

On the other hand, equation (2.22) shows that \mathcal{R}_{eff} is largely insensitive to the long term star formation history of a given region (and hence, in particular, to the total stellar mass) and it rather depends on the details of its recent star formation history. In particular, $\mathcal{R}_{\text{eff}} \simeq \mathcal{R}_\infty$ whenever the star formation rate of the considered annulus has not varied much during the last $t_R \sim 1$ Gyr, irrespective of the previous evolution, and it is significantly lower (greater) than \mathcal{R}_∞ only when a significant starburst (abrupt quenching) has occurred on such a short timescale.

For example, a recent starburst or quenching event, occurring on a timescale $t_A < t_R$, could be approximately modeled as:

$$\text{SFRD}(t') = \text{SFRD}(t_0) \times \begin{cases} \sigma & (t_0 - t_R < t' < t_0 - t_A) \\ 1 & (t_0 - t_A < t' < t_0) \end{cases} \quad (2.23)$$

with $\sigma < 1$ for a starburst and $\sigma > 1$ for quenching. In this case, the prediction for \mathcal{R}_{eff} is:

$$\frac{\mathcal{R}_{\text{eff}}(t_0)}{\mathcal{R}_\infty} = \sigma + (1 - \sigma) \frac{t_A}{t_R} \quad (2.24)$$

Even if events of both kinds are likely to be occurring in some cases, their description would require a detailed study on a case-by-case basis. In fact, opposite situations (starburst or quenching) have opposite effects on the estimate of \mathcal{R}_{eff} and the magnitude of such effect is sensitive to the details of the phenomenon itself (in the example above, the timescale t_A and the intensity σ), implying that no reasonably general priors can be imposed without introducing a bias on the results.

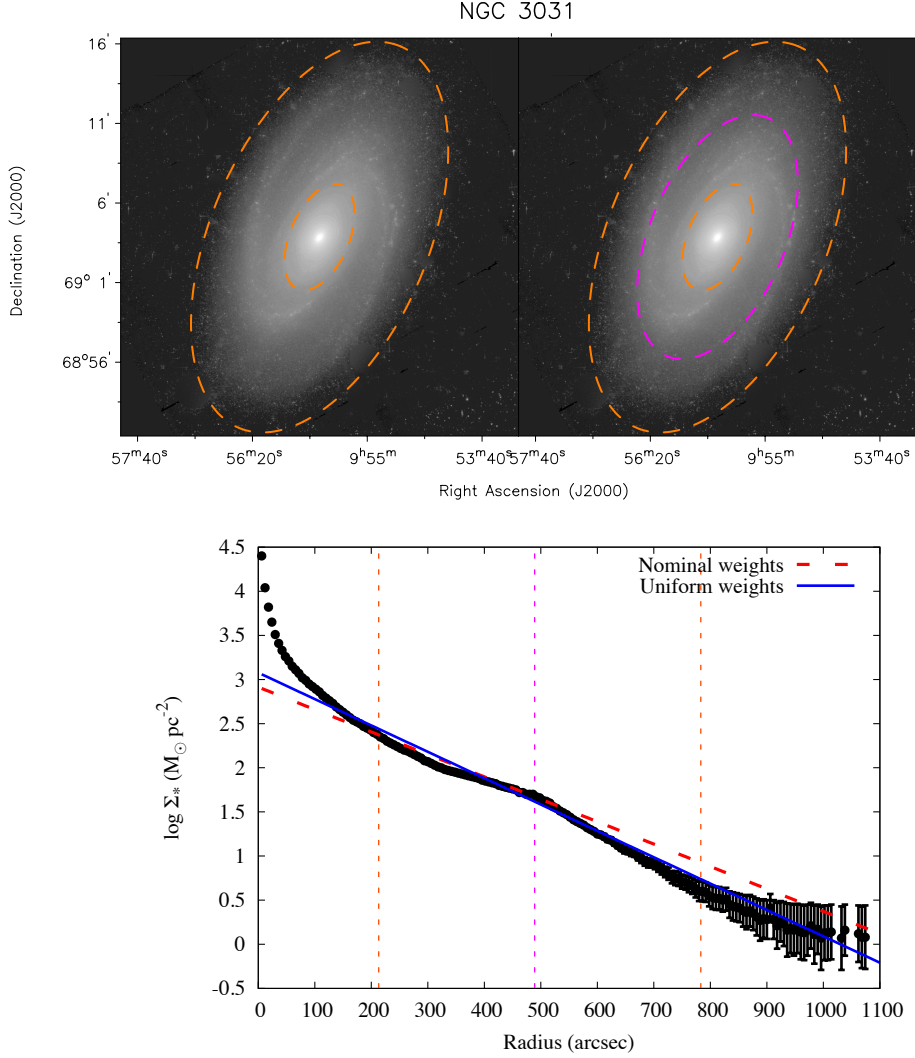


Figure 2.5: The combined effect of radially-varying measurement errors and spiral structure for NGC 3031. *Upper panels:* the map of the $3.6 \mu\text{m}$ emission (the two images have the same scale and contrast); *lower panel:* the stellar mass surface density profile, with the best fit exponentials obtained using error-based weights (red dashed line) and uniform weights (blue solid line). In all panels, the orange lines mark the disc-dominated region selected for the fit. The magenta line and ellipse mark the radius where a bump occurs in the profile of Σ_* . A prominent couple of spiral arms clearly dominate the emission at this very same radius.

2.B The choice of the weights

To illustrate our choice of the weights in fitting the stellar mass surface density profiles, we report in Fig. 2.5 (lower panel) the best-fitting exponential disc for NGC 3031 using both nominal weights and uniform weights. The two fits are quite different and in particular they have different stellar scalelengths: $R_{\star} = 170.9$ arcsec and $R_{\star} = 145.4$ arcsec, respectively. The nominally weighted fit better reproduces the inner region, where the errors are the smallest, out to a radius of ~ 500 arcsec, where the profile clearly shows a bump. The presence of this feature has the obvious effect of making the inner portion of the profile shallower than the outer one, which results in a larger derived best-fitting scalelength. The physical origin of this occurrence can be found by looking at the $3.6 \mu\text{m}$ map of this galaxy, which is shown in Fig. 2.5 (upper panel). The same image is reported here twice, with the same scale and contrast. In the left panel, ellipses are overlaid to mark the region selected for the fit (see the Atlas for a clearer view of this selection). The right panel also displays the ellipse at 489 arcsec; this is the radius where the bump in the profile occurs and it is marked by a vertical dotted magenta line in the lower panel of Fig. 2.5 as well. The comparison between all the panels of Fig. 2.5 clarifies that the bump in the profile is due to the presence, at that radius, of a prominent couple of spiral arms with a small pitch angle.

In our view, such a perturbation is the probable reason why the observed profile is deviating from an exponential. A proper analysis should take this effect into account, in addition to random deviations due to measurement errors. Related to this, we should point out that, in this context, simple quantitative proxies for the quality of the fits, like, for instance, the reduced χ^2 , are not necessarily as informative as usually assumed, simply because deviations from an exponential profile, in spiral galaxies, are not only due to measurement errors, but to physical oscillations as well. A correct Bayesian analysis, in a situation like this, would be the definition of a more sophisticated model, with additional parameters to describe spiral structure, to be explored with an MCMC sampling using a likelihood based on nominal errors. However, a realistic modelization of spiral structure in galaxies is beyond the scope of our work. In our opinion, a uniform weighting, if performed only when necessary and on a carefully selected radial range, can be considered a fairly good choice for our purposes and avoids over-weighting regions that are dominated by transient perturbations.

2.C The tentative double disc of NGC 3621

NGC 3621 is probably the most extreme case, in our sample, of a spiral galaxy with a stellar disc apparently described by two exponentials with different scalelengths. Furthermore, its SFRD profile shows a change of slope as well, in the same sense (flattening) of the stellar profile and at the very same radius $R \sim 225$ arcsec. NGC 3621 is also known for a remarkable flattening of the metallicity profiles of both the gas (Bresolin, Kennicutt & Ryan-Weber 2012) and the stars (Kudritzki et al. 2014), occurring around $R_{25} \sim 290$ arcsec.

These indications of a double-component nature led us to repeat our analysis,

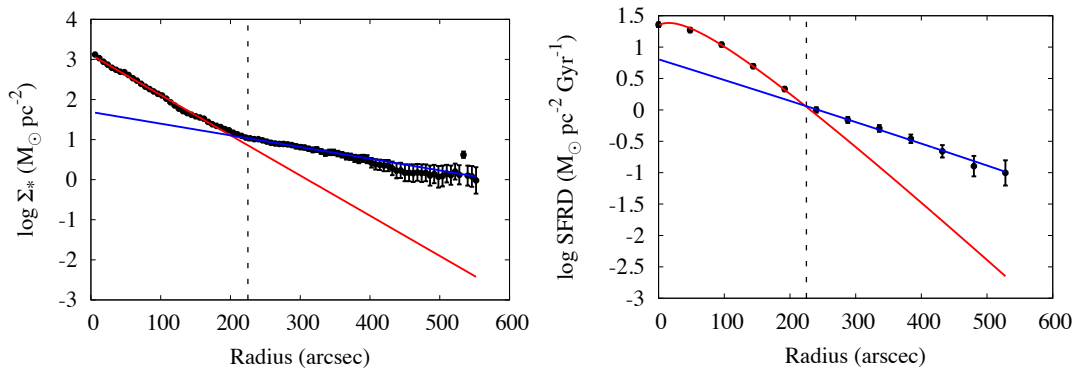


Figure 2.6: The double-disc analysis for NGC 3621. The radial profiles of the surface density of stellar mass (*left panel*) and star formation rate (*right panel*) are fitted with the theoretical model for the evolution of exponential discs (Sec. 2.2, 2.4), but the two regions inside and outside $R = 225$ arcsec are analyzed independently. The best fit parameters are reported in Table 2.4. The two components are apparently evolving towards the constitution of one single smooth disc on a timescale of ~ 30 Gyr (see text for details).

Table 2.4: Double-disc analysis of NGC 3621: best-fit parameters

	M_\star ($10^9 M_\odot$)	R_\star (kpc)	ν_M (10^{-2} Gyr^{-2})	ν_R (10^{-2} Gyr^{-2})
<i>Inner disc</i>	24.9 ± 1.1	1.74 ± 0.02	7.03 ± 0.15	2.67 ± 0.08
<i>Outer disc</i>	11.0 ± 1.3	5.99 ± 0.26	9.84 ± 0.19	-1.62 ± 0.36

described in Sec. 2.4, separately for the two regions inside and outside our observed transition radius. As shown in Fig. 2.6, this experiment gives a result of very good quality⁷. The best-fit parameters are reported in Table 2.4⁸. While the structural parameters of the inner disc are equal (by construction) to the estimates from the single-disc analysis (cfr. Table 2.2), the mass and radial growth rates are both smaller, compared with the single-disc estimates, and their ratio is nearer to the theoretical value (Sec. 2.6.2).

Interestingly, the inner disc, which has the smaller scalelength R_\star , has a positive specific radial growth rate ($\nu_R > 0$), while the opposite is true for the outer disc. If sustained in time, this trend goes in the direction of smoothing out the difference in the slopes of the two stellar mass profiles, possibly bringing the two discs towards a common scalelength on a timescale:

$$t_{\text{smooth}} = \frac{\ln\left(\frac{R_{\star,\text{out}}}{R_{\star,\text{in}}}\right)}{\nu_{R,\text{in}} - \nu_{R,\text{out}}} = 28.8 \text{ Gyr} \quad (2.25)$$

⁷We recall that the slope of SFRD profiles is not a free parameter, being fixed by the independently derived value of R_\star .

⁸Note that M_\star here has just the formal meaning of the parameter of equation (2.1): the actual masses of the two discs are smaller, since both of them have a limited radial extent.

An impressively similar timescale is the one independently obtained from the specific mass growth rates:

$$t'_{\text{smooth}} = \frac{\ln\left(\frac{M_{\star,\text{out}}}{M_{\star,\text{in}}}\right)}{\nu_{\text{M,in}} - \nu_{\text{M,out}}} = 29.1 \text{ Gyr} \quad (2.26)$$

This coincidence is not trivial at all (not even the sign of t_{smooth} and t'_{smooth} is *a priori* obvious) and implies that the two discs are also tending to a common normalization. This tentatively reinforces the idea that the two components are slowly evolving towards the constitution of a single smooth structure (though, of course, it may well be that the process will stop before its completion due to some form of star formation quenching).

2.D Λ CDM scaling relations with an evolving density contrast

Besides the dependence on the Hubble constant, the normalization A of the mass-size relation is also proportional to $\Delta_{\text{vir}}^{-1/3}$, where Δ_{vir} is the density contrast of collapsed structures, with respect to the critical density, at the time of virialization. This dependence is often neglected, since Δ_{vir} is generally regarded to as a universal constant⁹. Eke, Cole & Frenk (1996) suggested that this assumption may be inaccurate in the presence of a cosmological constant. The resulting dependence of Δ_{vir} on redshift has been parametrized analytically by Bryan & Norman (1998). Taking this effect into account, we obtain the following refined prediction for ν_A :

$$\begin{aligned} \nu_A &= -\frac{2}{3} \frac{d \ln H}{dt} - \frac{1}{3} \frac{d \ln \Delta_{\text{vir}}}{dt} \\ &= \left(1 + \frac{2\Omega_\Lambda(41 + 39\Omega_\Lambda)}{8\pi^2 - 82\Omega_\Lambda - 39\Omega_\Lambda^2}\right) \Omega_m H \\ &= 4.18 \cdot 10^{-2} \text{ Gyr}^{-1} \end{aligned} \quad (2.27)$$

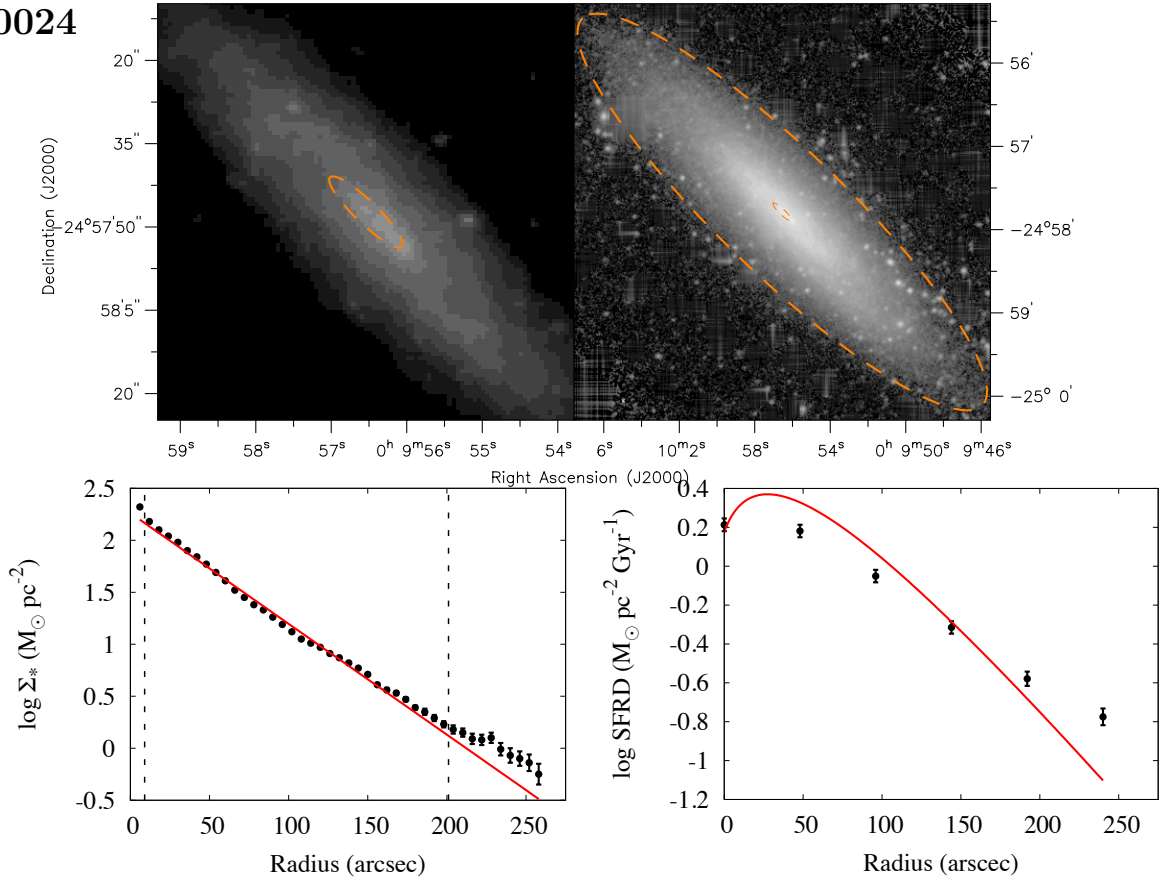
where $\Omega_\Lambda = 1 - \Omega_m = 0.7$ is the density parameter of the cosmological constant. The predicted value of ν_A is therefore, in this case, 4 times larger than our upper limit.

⁹This is, for instance, the basis of the “ R_{200} ” parametrization for the virial radii of dark matter haloes.

2.E Atlas

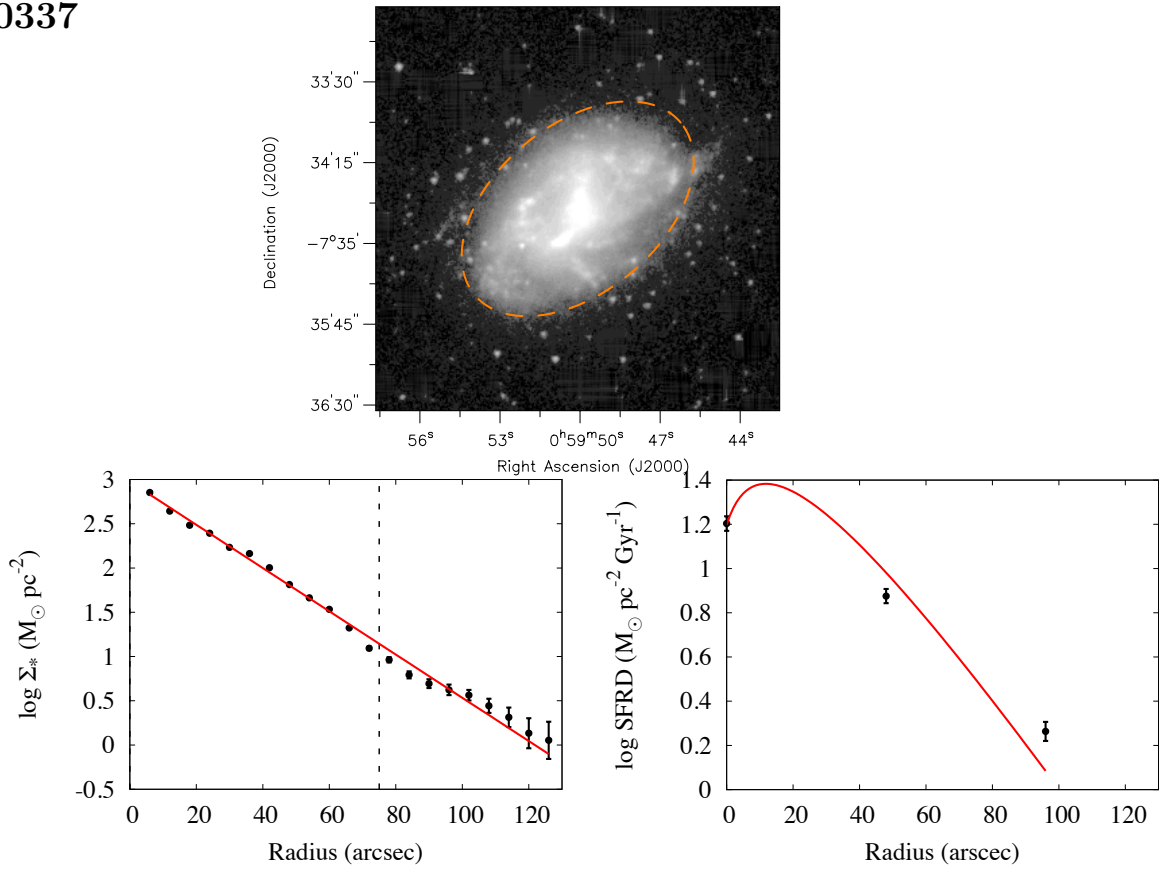
This Atlas contains the details of our analysis for individual objects in our sample. For each galaxy, the upper panels are maps of the emission at $3.6 \mu\text{m}$. Overlaid ellipses correspond to the limits of the radial range where the exponential fit to the $3.6 \mu\text{m}$ profile was performed (lower-left panel). The lower-right panel shows the observed SFRD profile, together with the best-fitting theoretical model.

NGC 0024



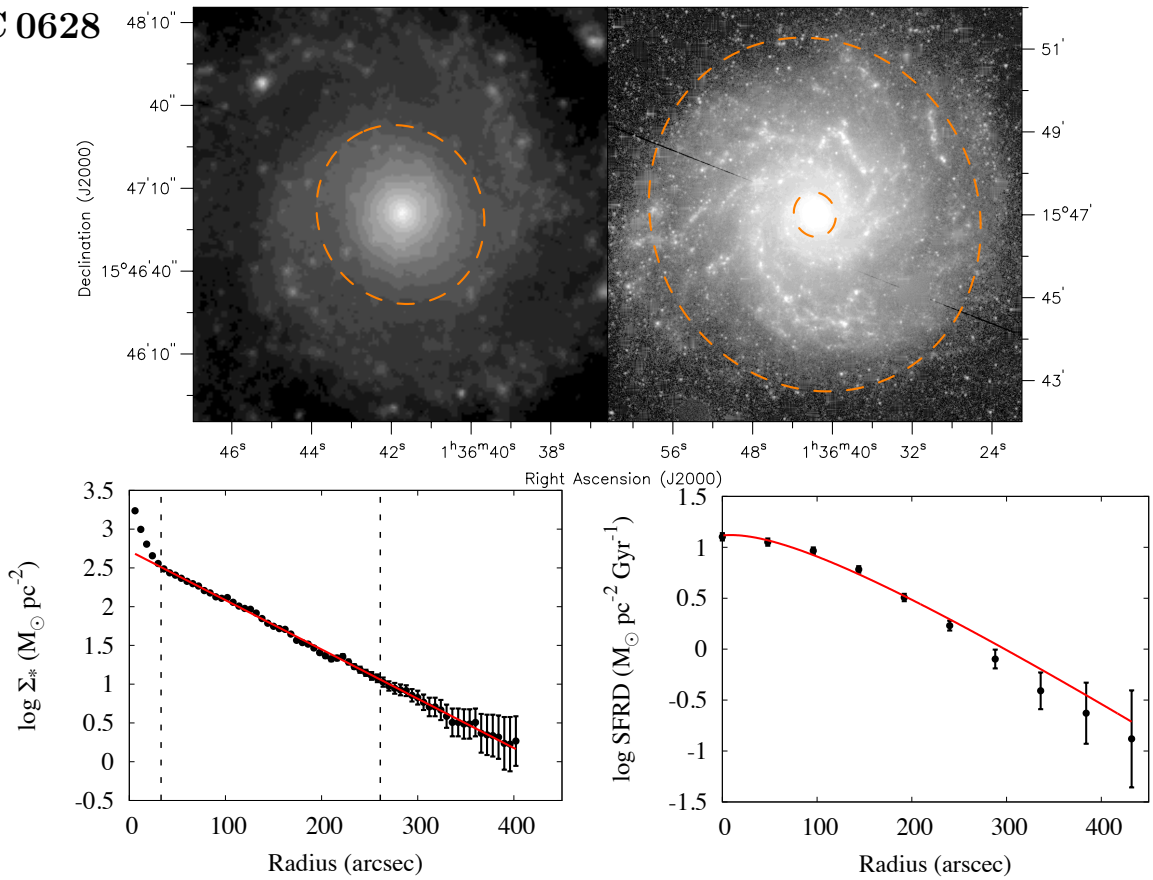
NGC 0024. $3.6 \mu\text{m}$ fit range: 9–201 arcsec. Special caution may be due for this object, which is the most inclined in our sample ($i = 77^\circ$).

NGC 0337



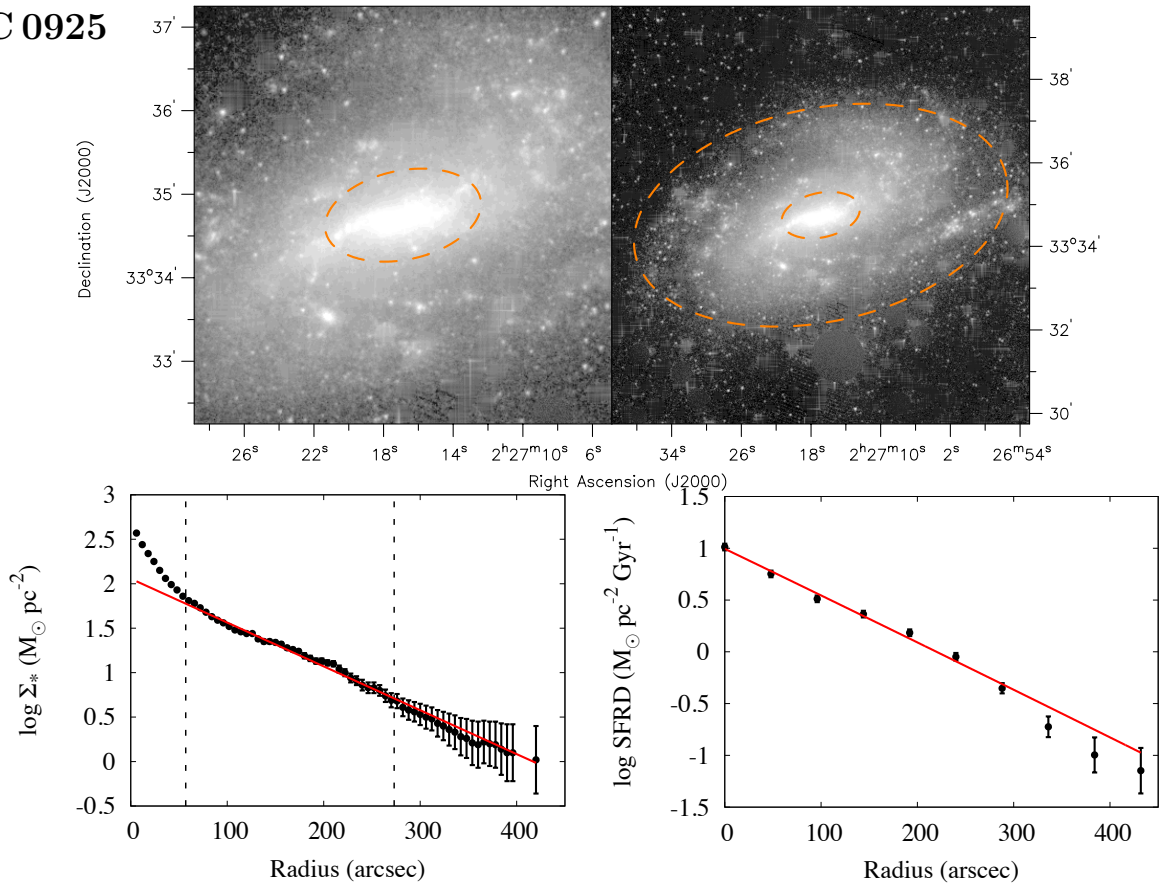
NGC 0337. $3.6 \mu\text{m}$ fit range: 0–75 arcsec. This is the most distant galaxy in our sample ($D = 25$ Mpc) and therefore the one with the worst spatial resolution.

NGC 0628



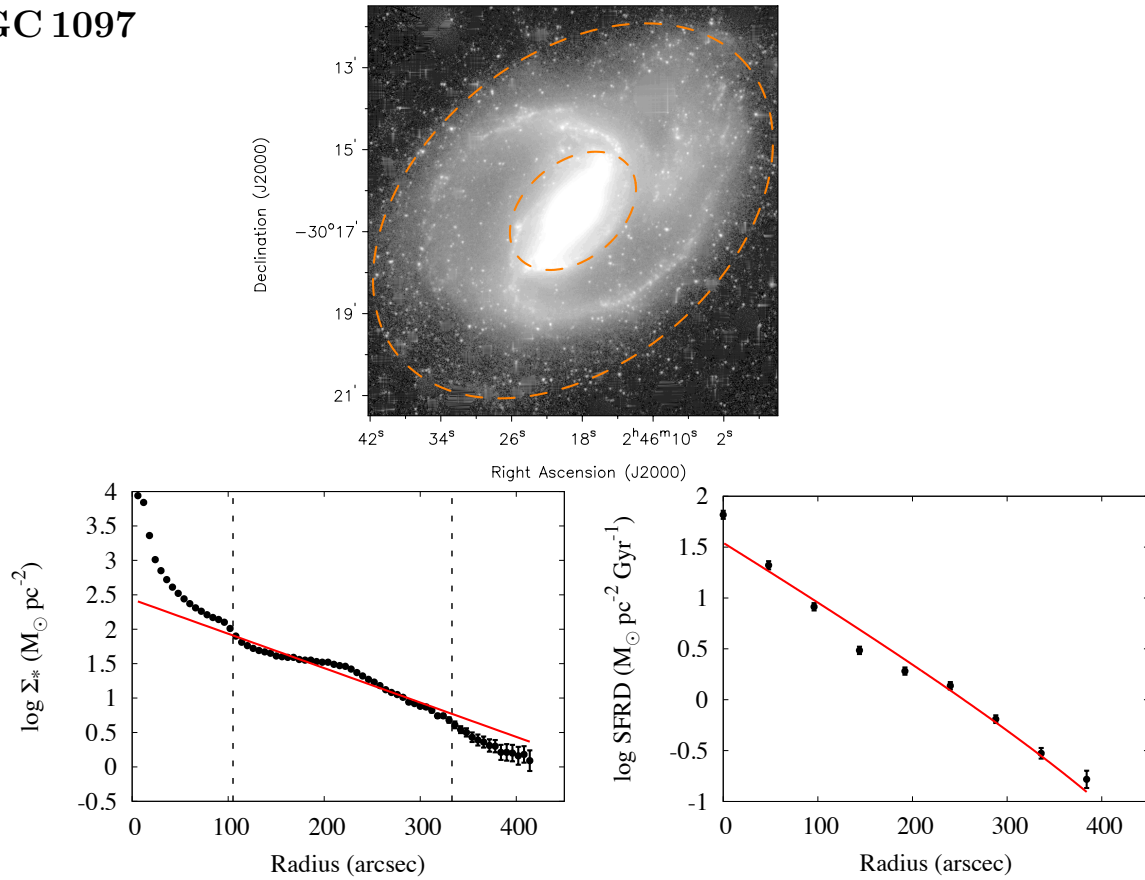
NGC 0628. $3.6 \mu\text{m}$ fit range: 33–261 arcsec.

NGC 0925



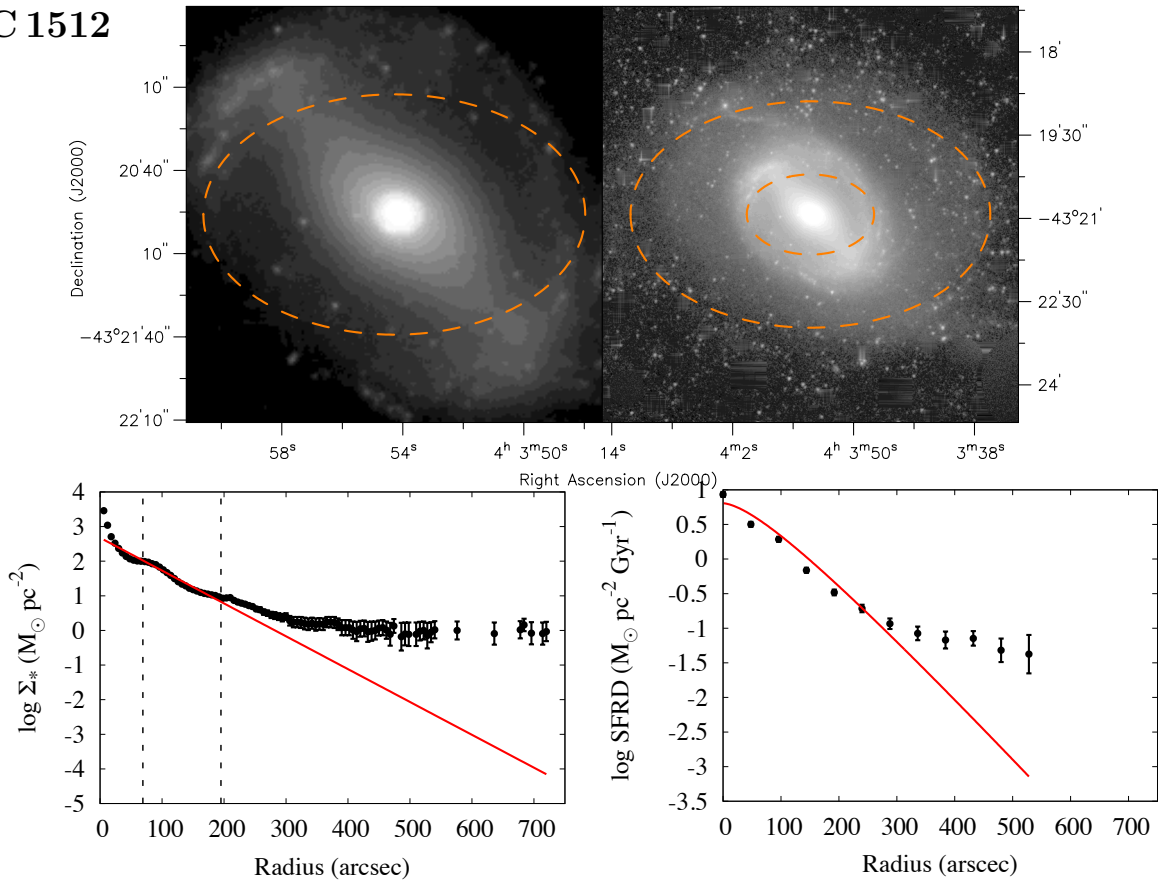
NGC 0925. $3.6 \mu\text{m}$ fit range: 57–273 arcsec.

NGC 1097



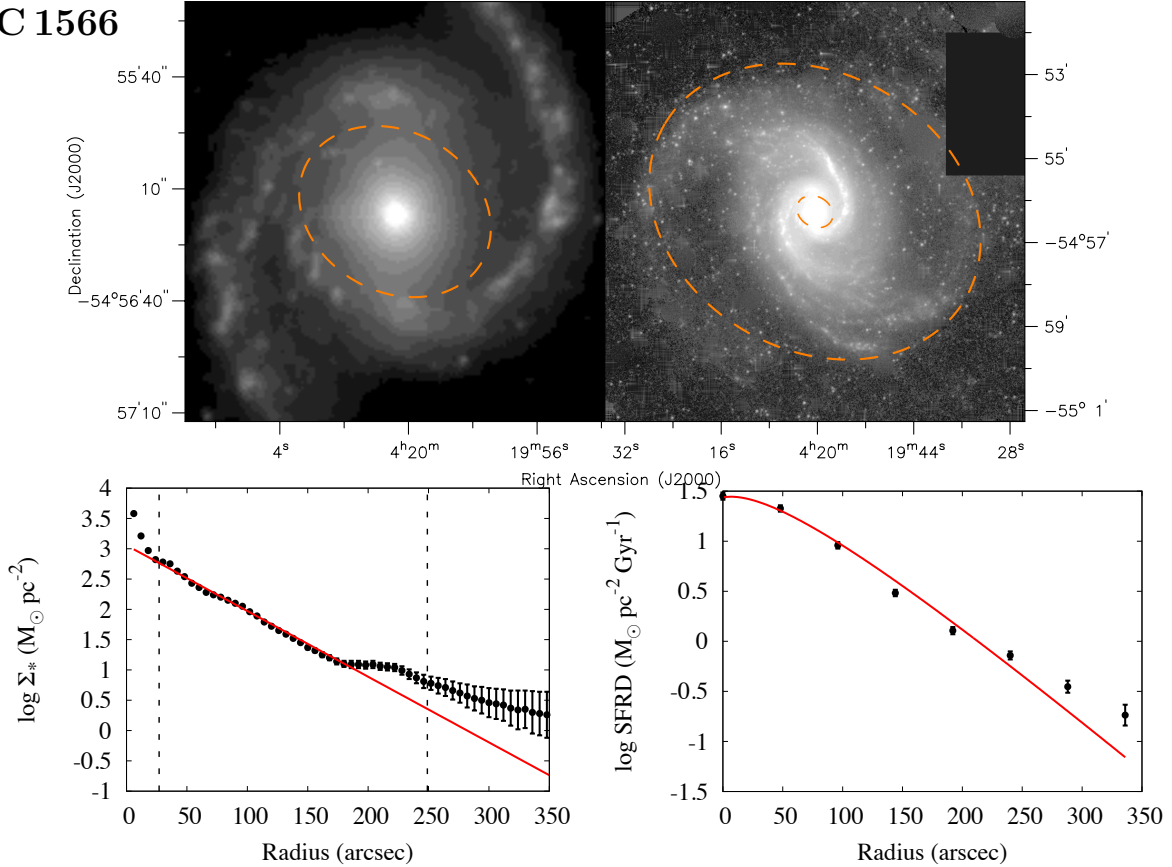
NGC 1097. $3.6 \mu\text{m}$ fit range: 105–333 arcsec; unweighted. Note that NGC 1097A (lying north-west of the bar) has been masked out from the map. This system is very likely to be a pair in an advanced phase of merging (see main text for details).

NGC 1512



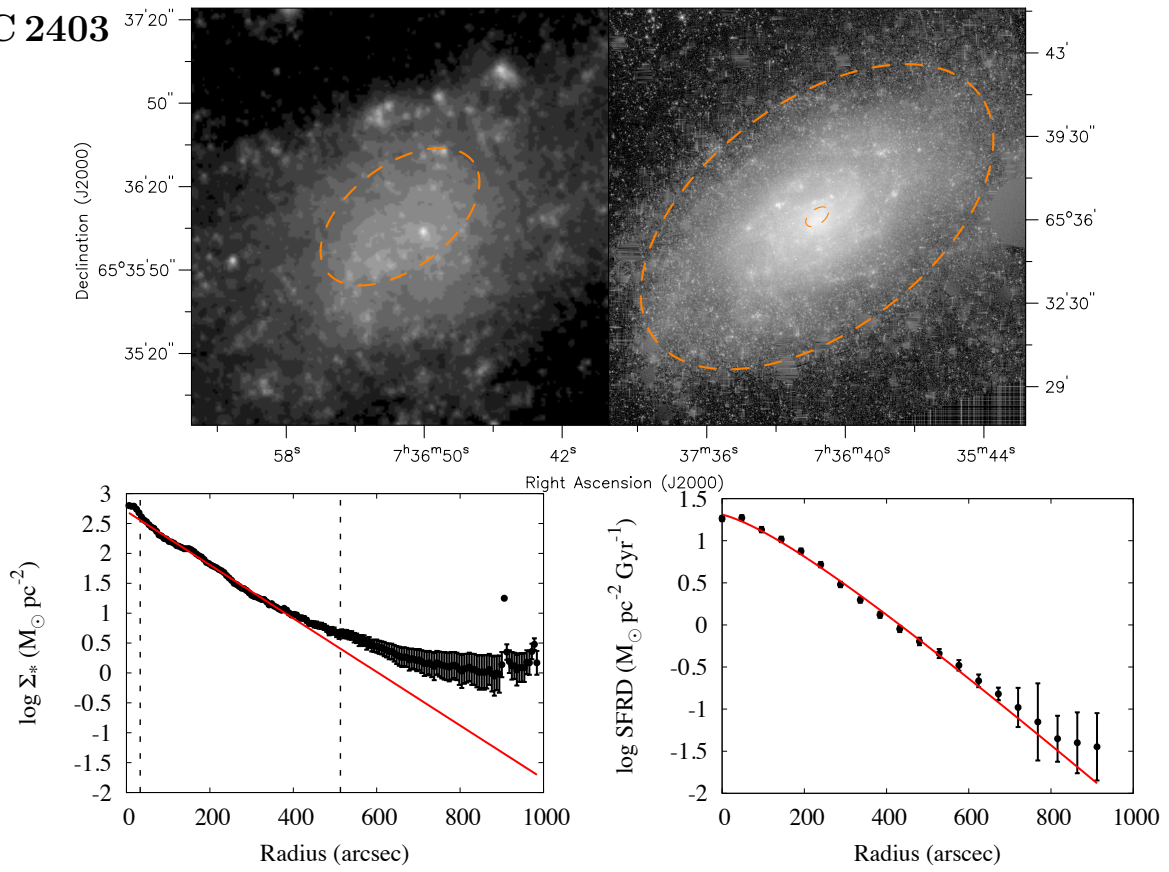
NGC 1512. $3.6 \mu\text{m}$ fit range: 69–195 arcsec; unweighted. The extended outer flattening, visible in both profiles, may be related to some interaction with NGC 1510 (out of the image, in the south-west direction).

NGC 1566



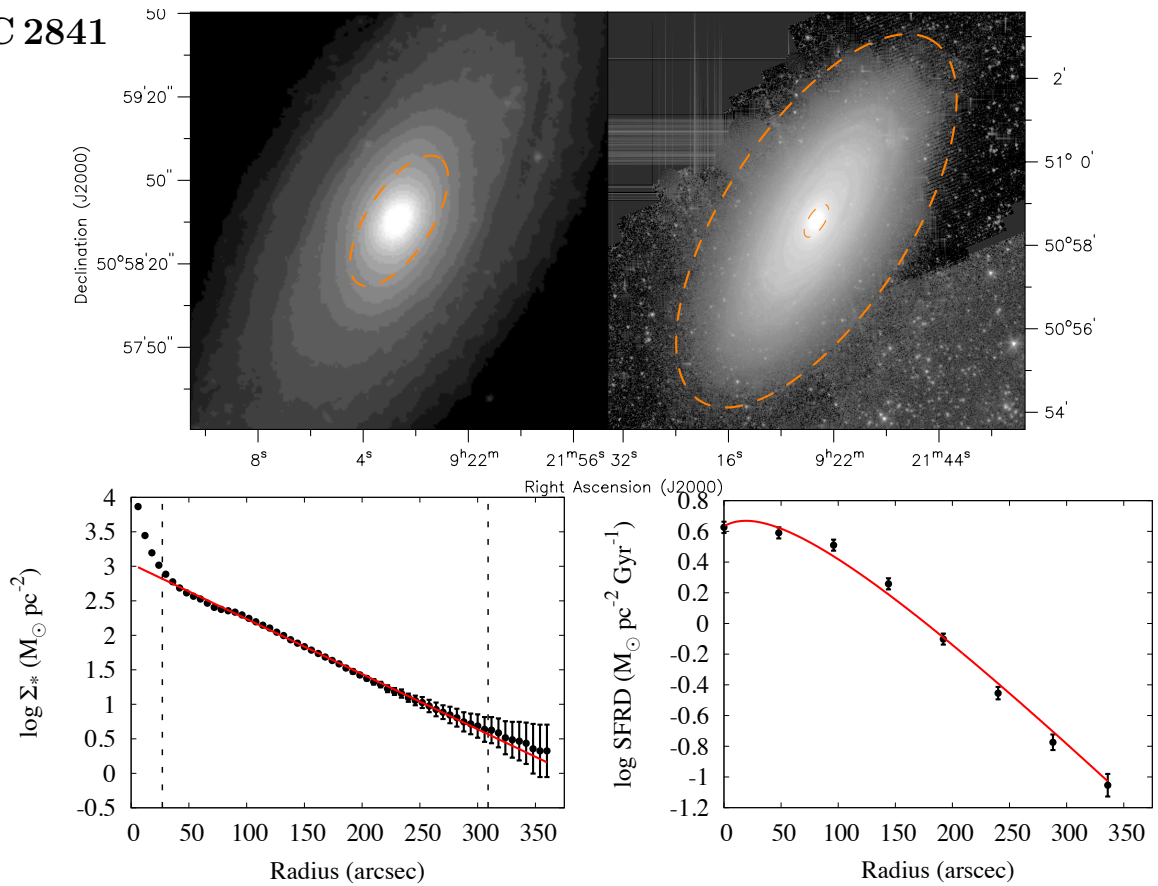
NGC 1566. $3.6 \mu\text{m}$ fit range: 27–249 arcsec. Two very prominent arms may be related to the step-like shape of the outer $3.6 \mu\text{m}$ profile.

NGC 2403



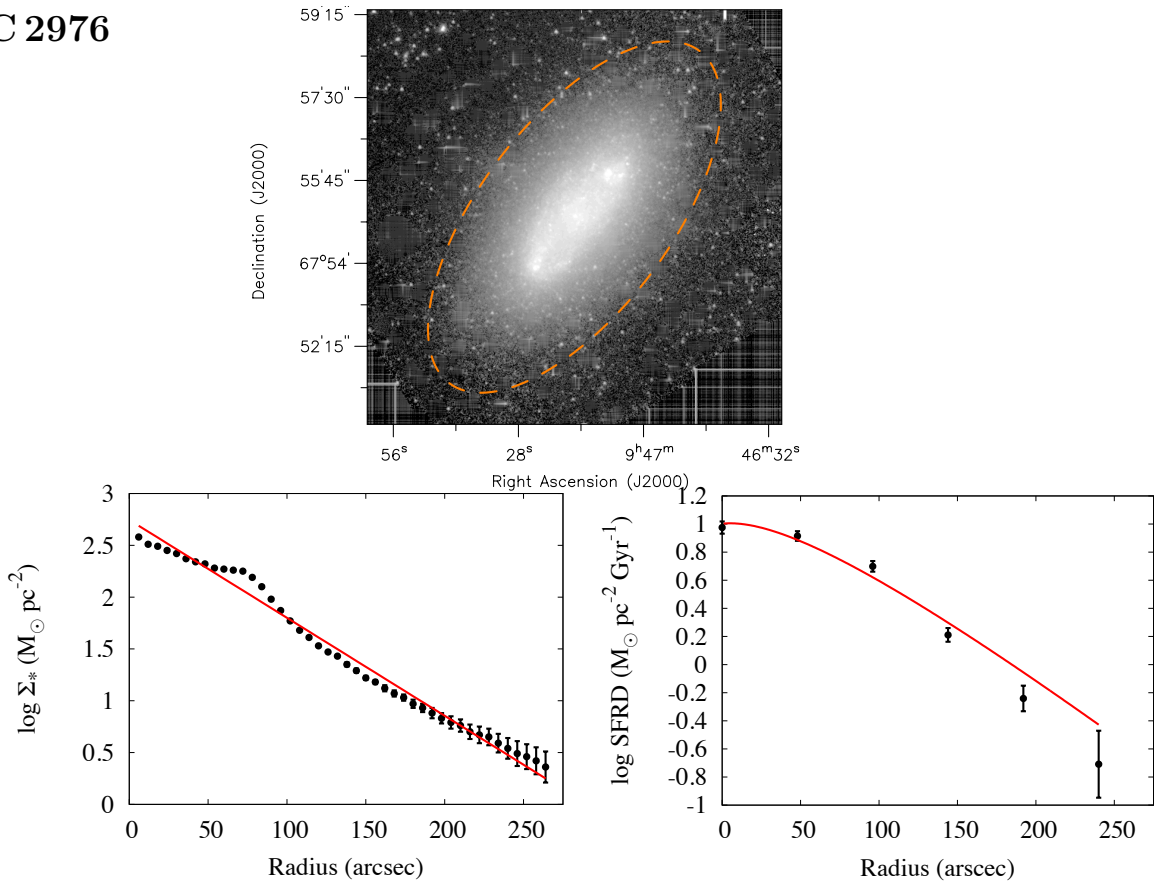
NGC 2403. $3.6 \mu\text{m}$ fit range: 33–513 arcsec. The inner ellipse is chosen to compensate for a small offset in the adopted centre.

NGC 2841



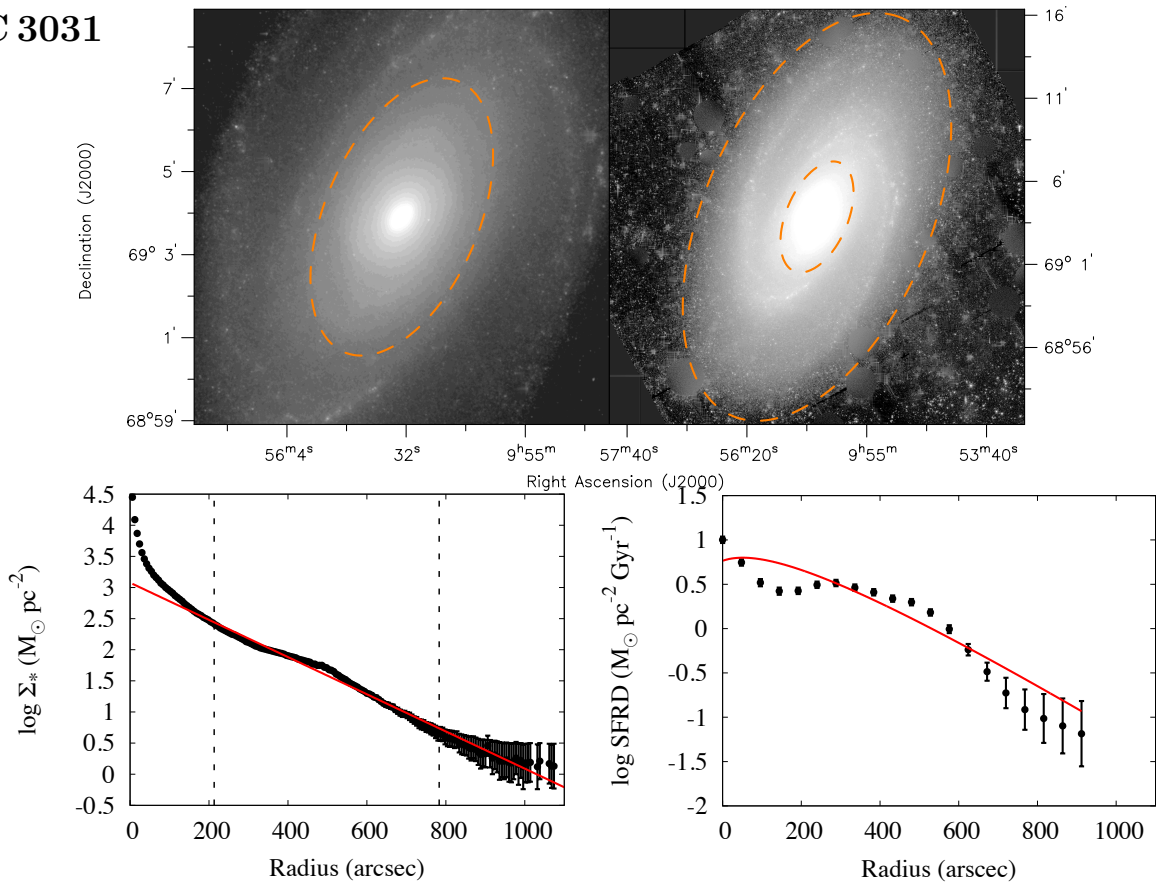
NGC 2841. $3.6 \mu\text{m}$ fit range: 27–309 arcsec.

NGC 2976



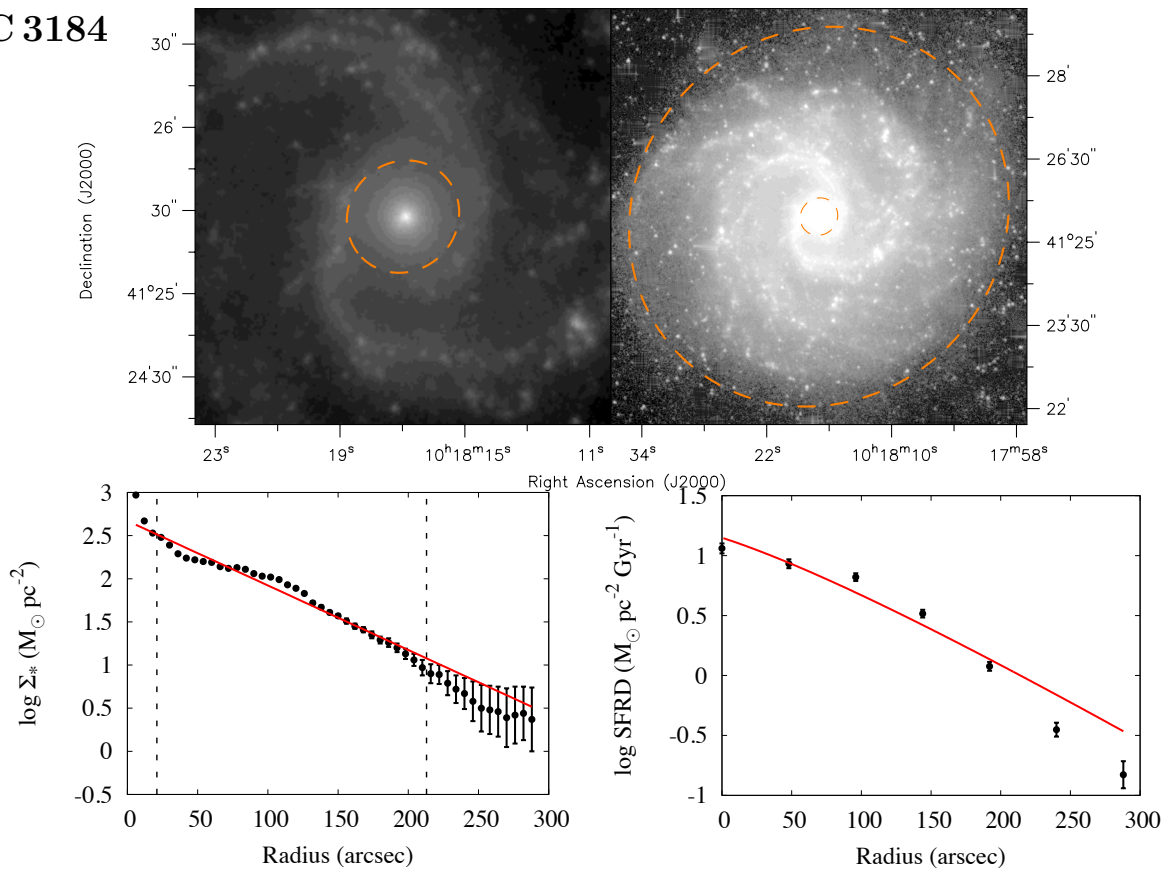
NGC 2976. 3.6 μm fit range: 0–264 arcsec, which is the whole available domain. A normal weighted fit gives a good account to the overall profile notwithstanding the presence of a prominent bump.

NGC 3031



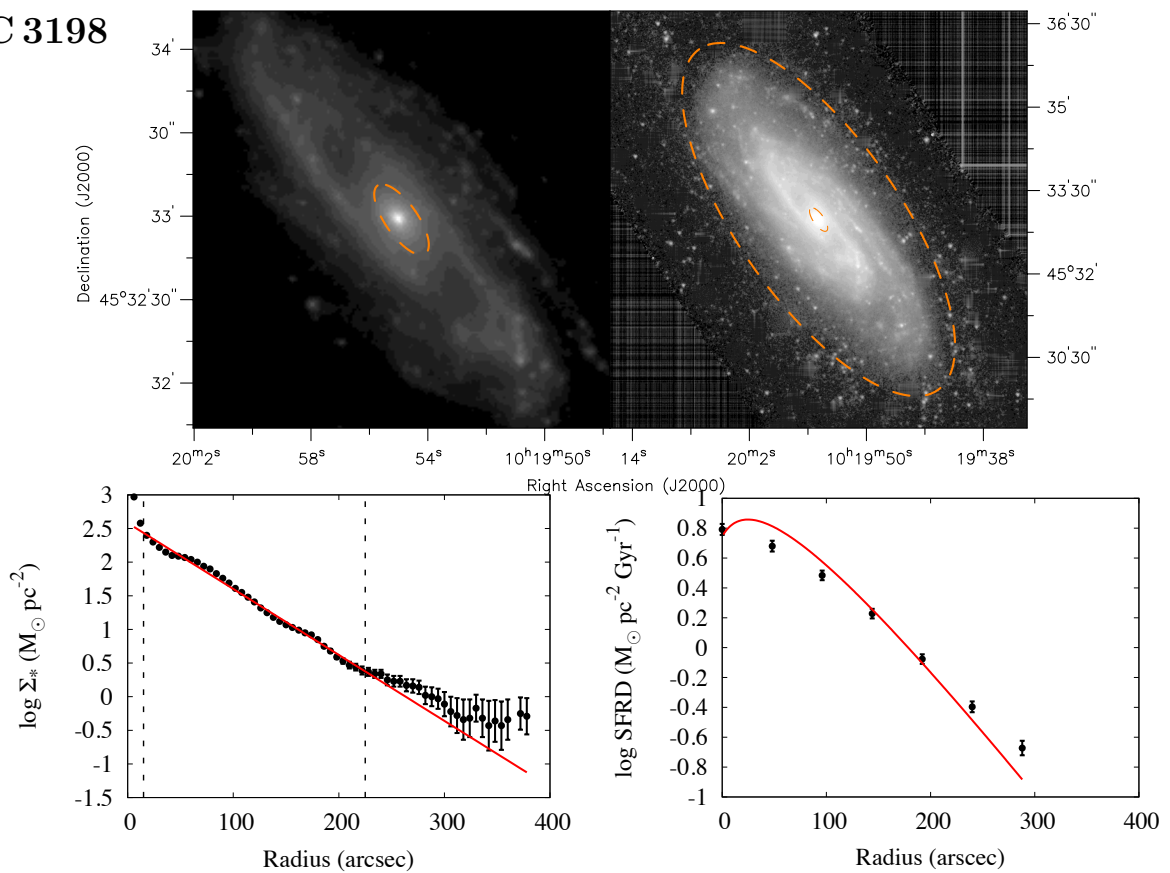
NGC 3031. 3.6 μm fit range: 213–783 arcsec; unweighted. The bulge is very prominent, but the disc-dominated region is clearly traced by the appearance of spiral arms.

NGC 3184



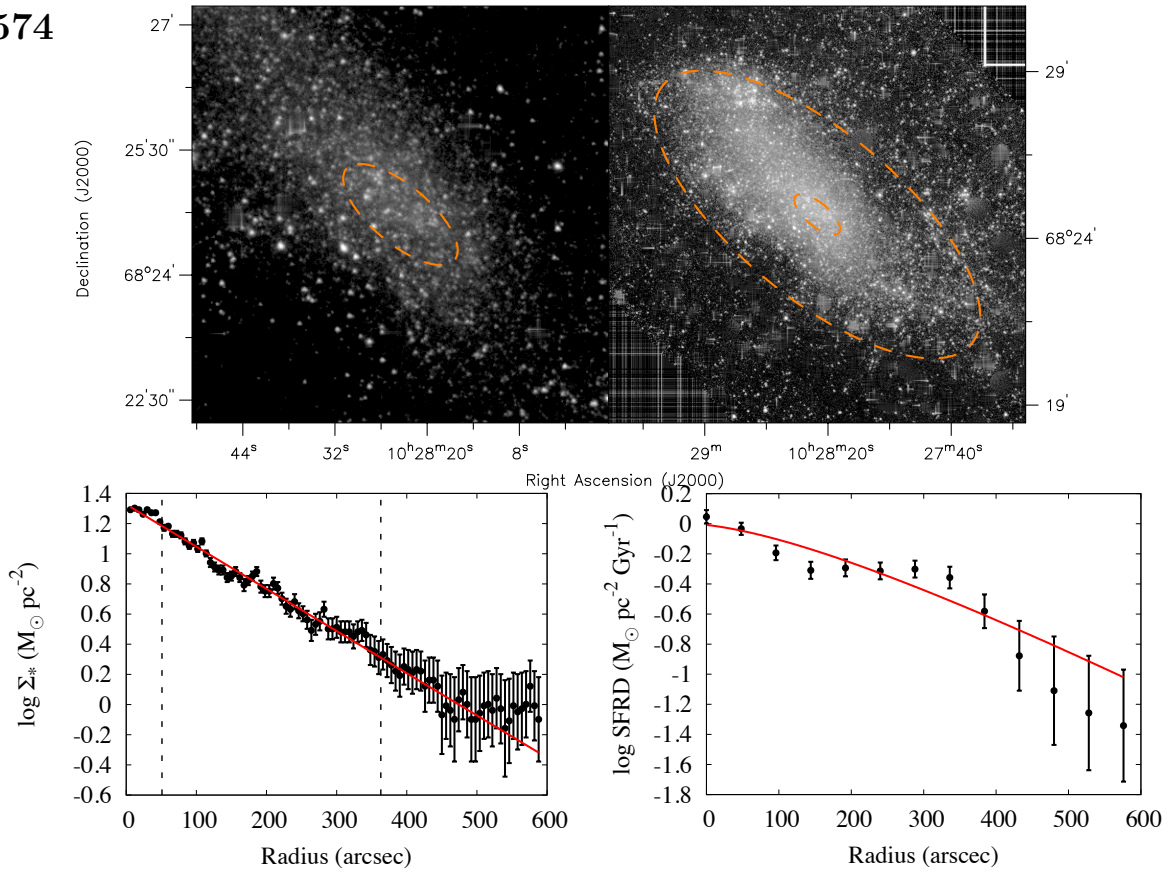
NGC 3184. $3.6 \mu\text{m}$ fit range: 21–213 arcsec; unweighted. As for NGC 3031, the disc-dominated region is readily recognized thanks to the prominent spiral structure.

NGC 3198



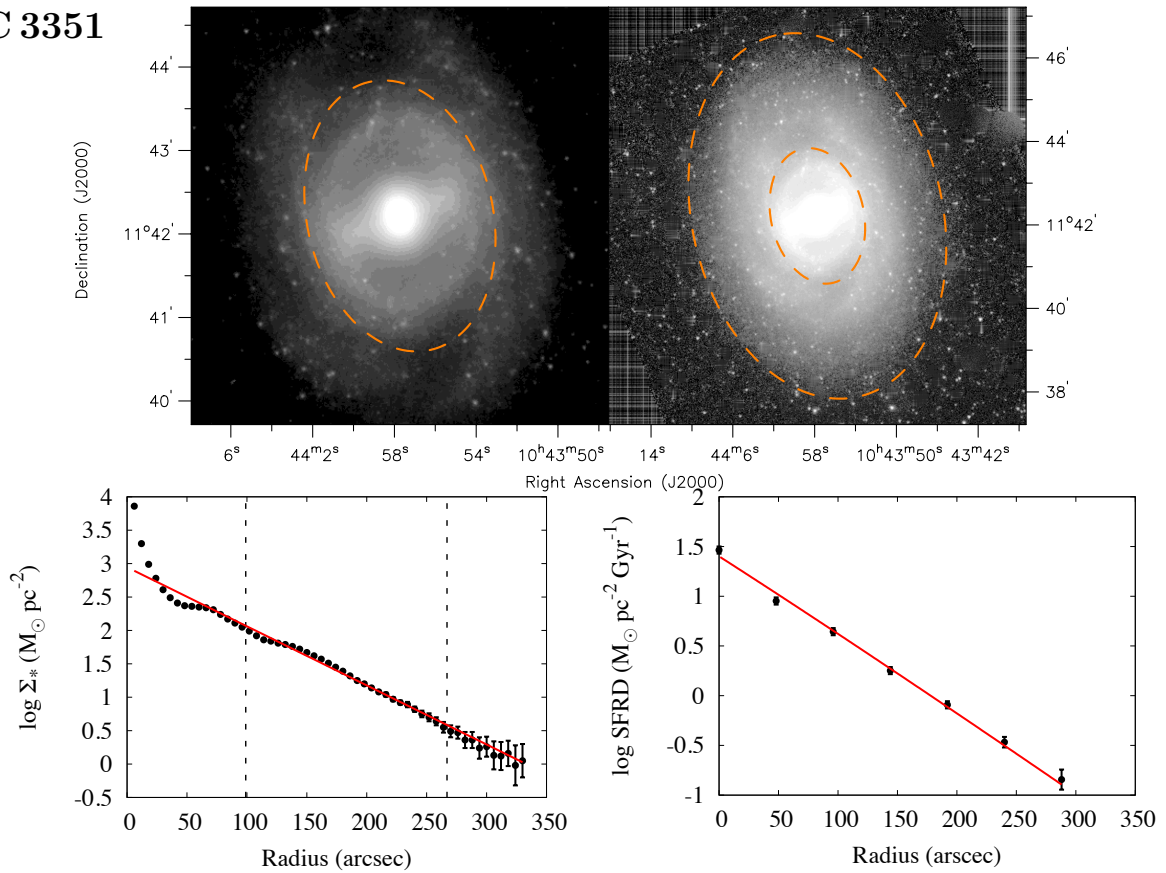
NGC 3198. $3.6 \mu\text{m}$ fit range: 15–225 arcsec.

IC 2574



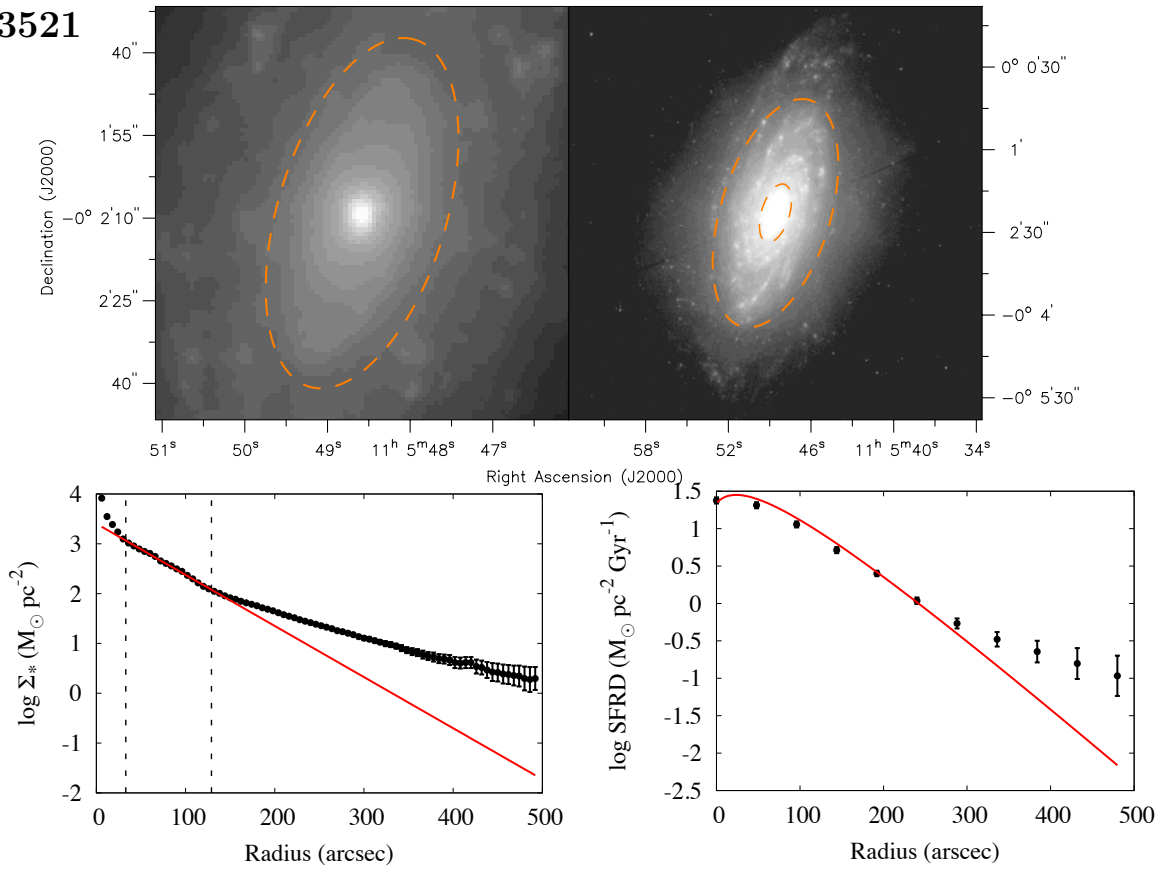
IC 2574. $3.6 \mu\text{m}$ fit range: 51–363 arcsec. The inner ellipse is chosen to compensate for a central offset. This is the nearest galaxy in our sample (just 4 Mpc from us), hence the possibility to see small scale oscillations in both profiles.

NGC 3351



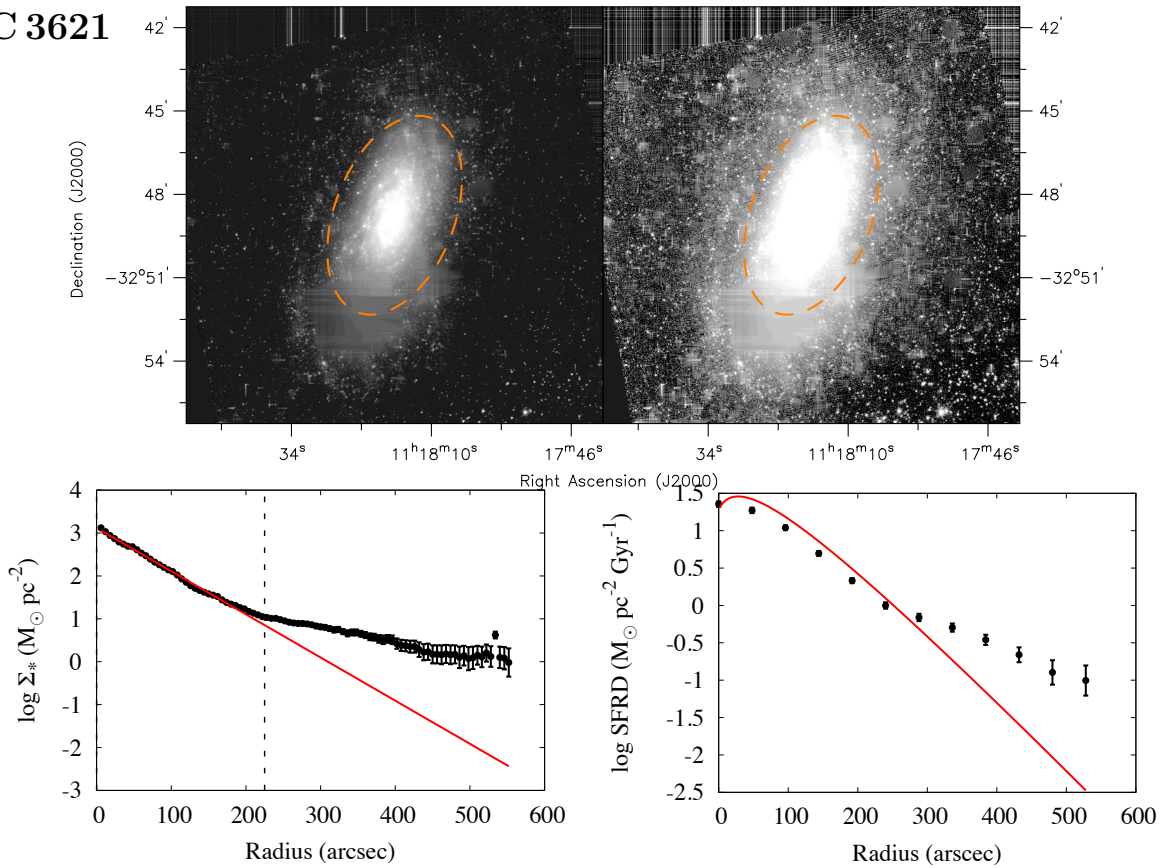
NGC 3351. $3.6 \mu\text{m}$ fit range: 99–267 arcsec unweighted. The inner ellipse encloses a prominent central ring.

NGC 3521



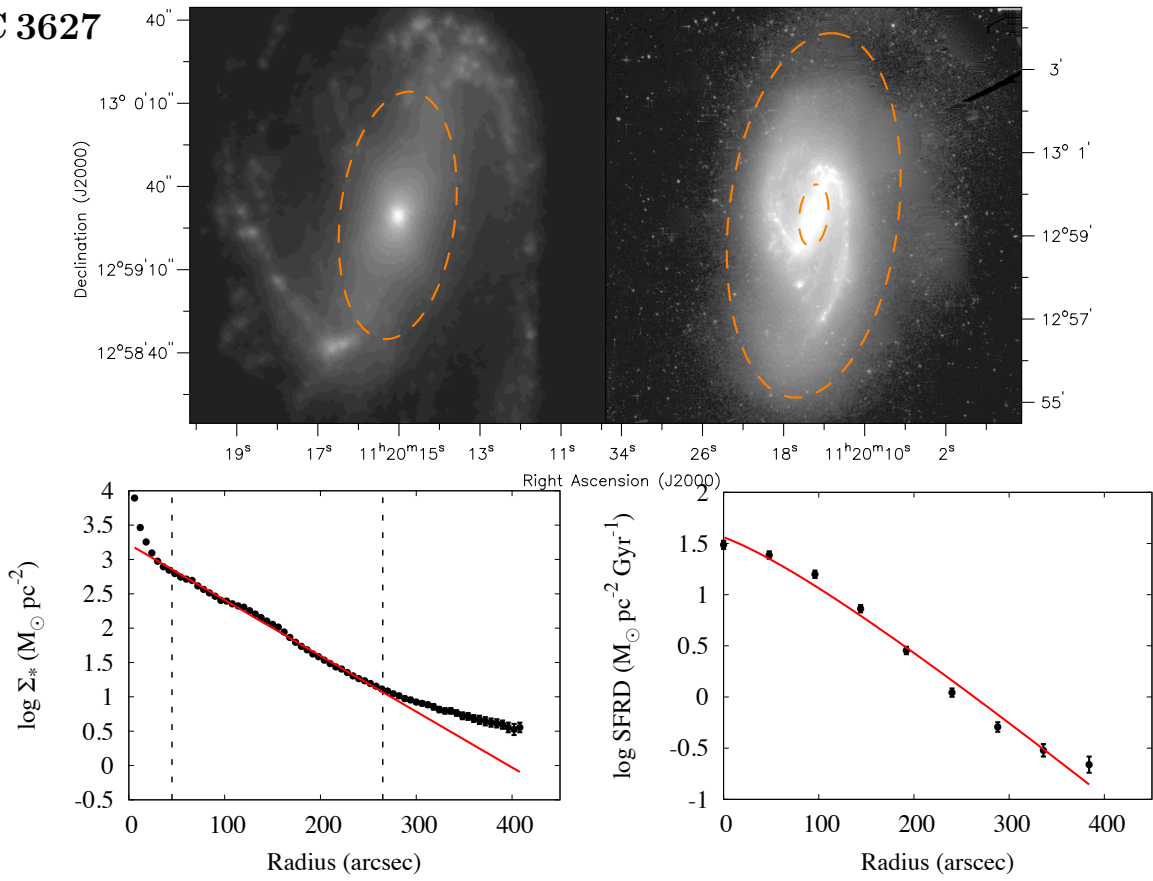
NGC 3521. $3.6 \mu\text{m}$ fit range: 33–129 arcsec. Out of 129 arcsec, the $3.6 \mu\text{m}$ profile suddenly becomes shallower and the isophotes assume a peculiar boxy shape. Note that the SFRD profile starts to flatten at much larger radii.

NGC 3621



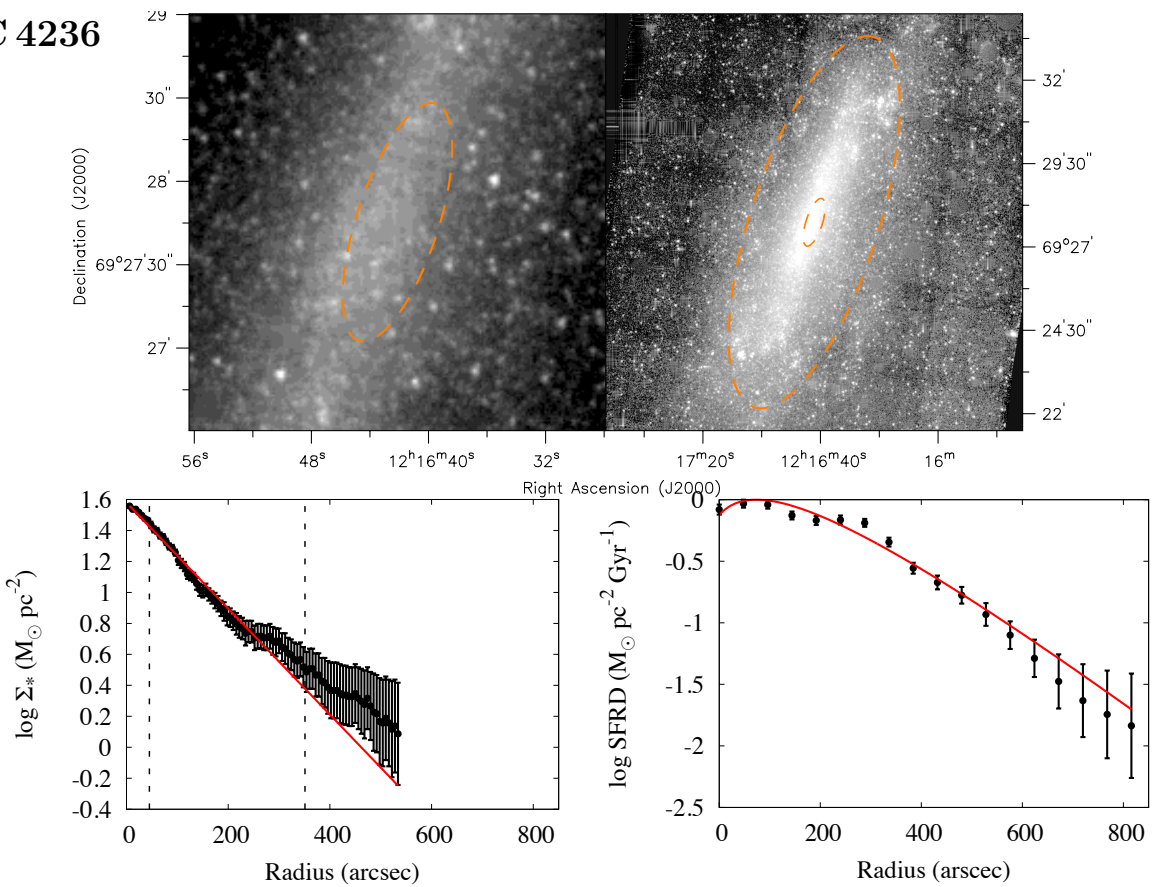
NGC 3621. $3.6 \mu\text{m}$ fit range: 0–225 arcsec. The ellipse at 225 arcsec is shown in both images, with the same scale but different contrast, to better show the emission of the inner disc (left) and the outer disc (right). Both profiles show an abrupt outer flattening starting from this radius.

NGC 3627



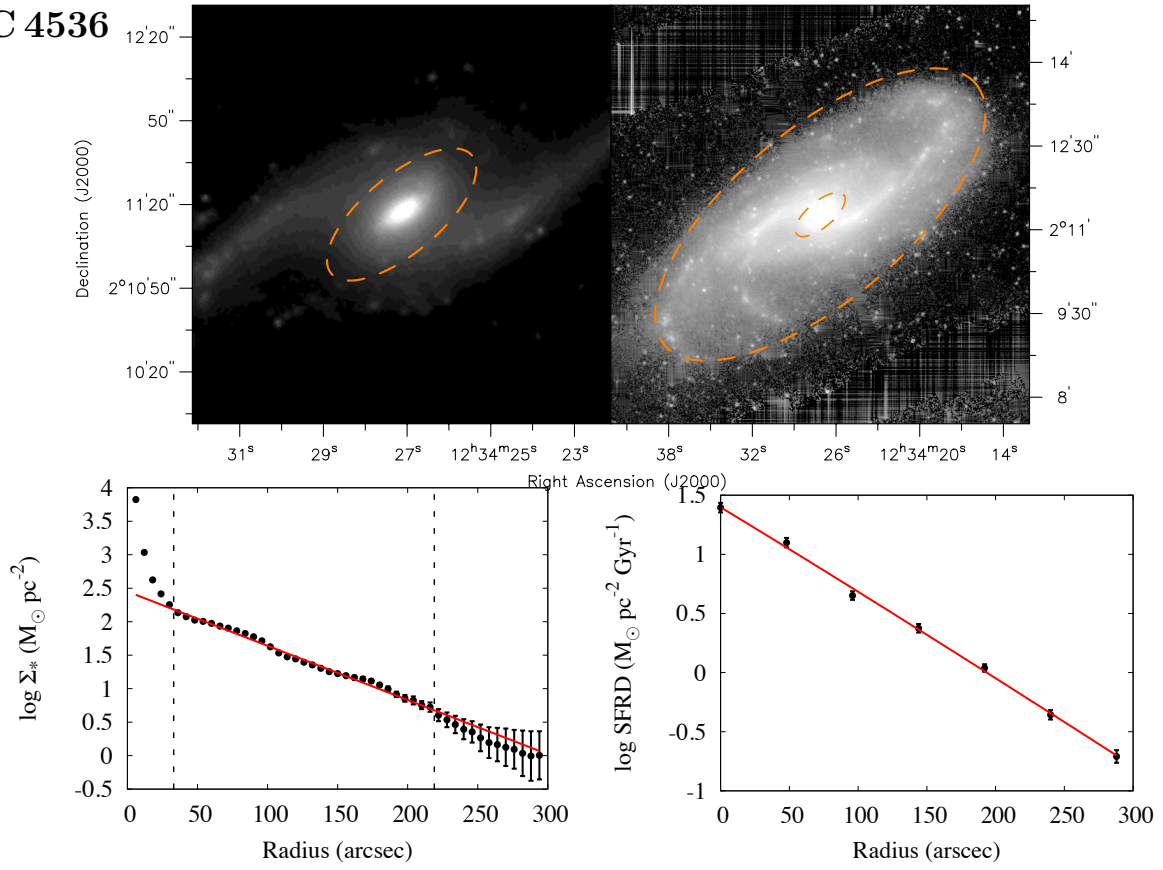
NGC 3627. $3.6 \mu\text{m}$ fit range: 45–265 arcsec.

NGC 4236



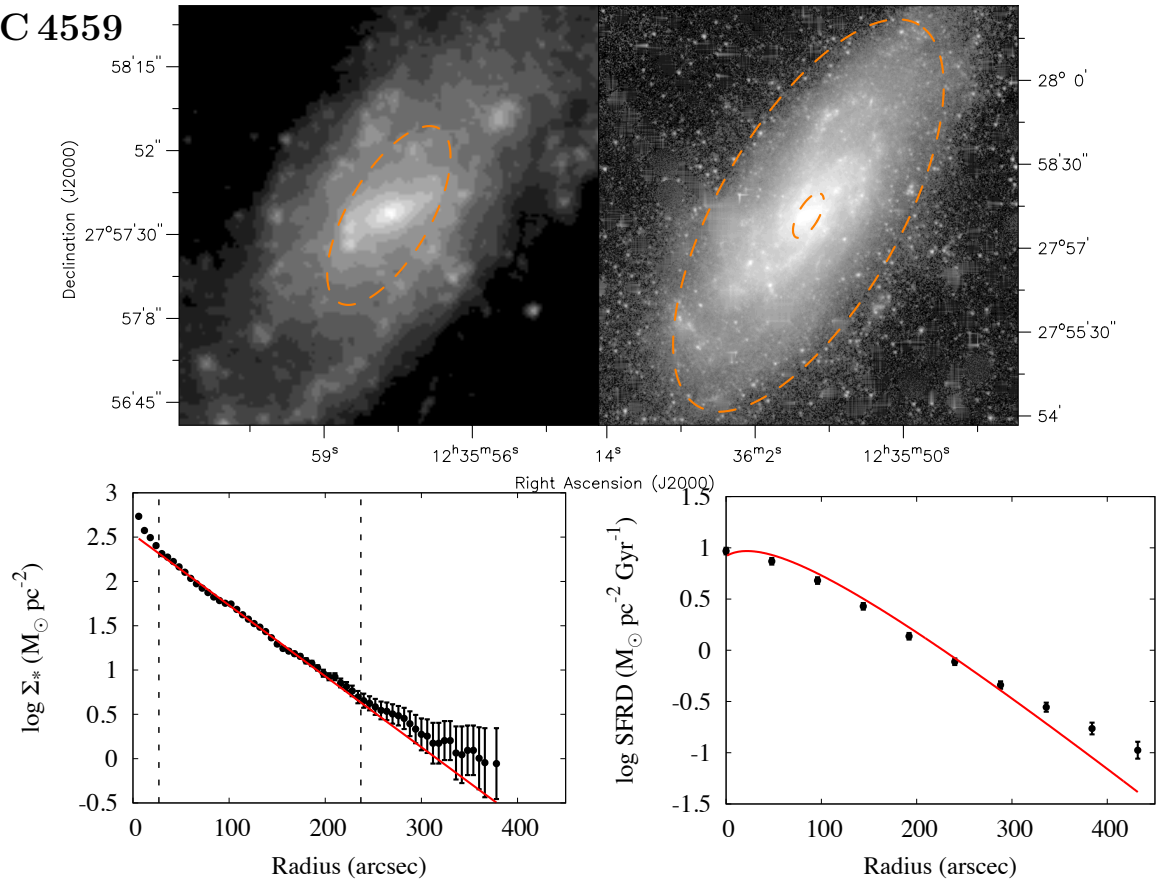
NGC 4236. $3.6 \mu\text{m}$ fit range: 45–351 arcsec. The inner ellipse is chosen to compensate for an offset in the centre position.

NGC 4536



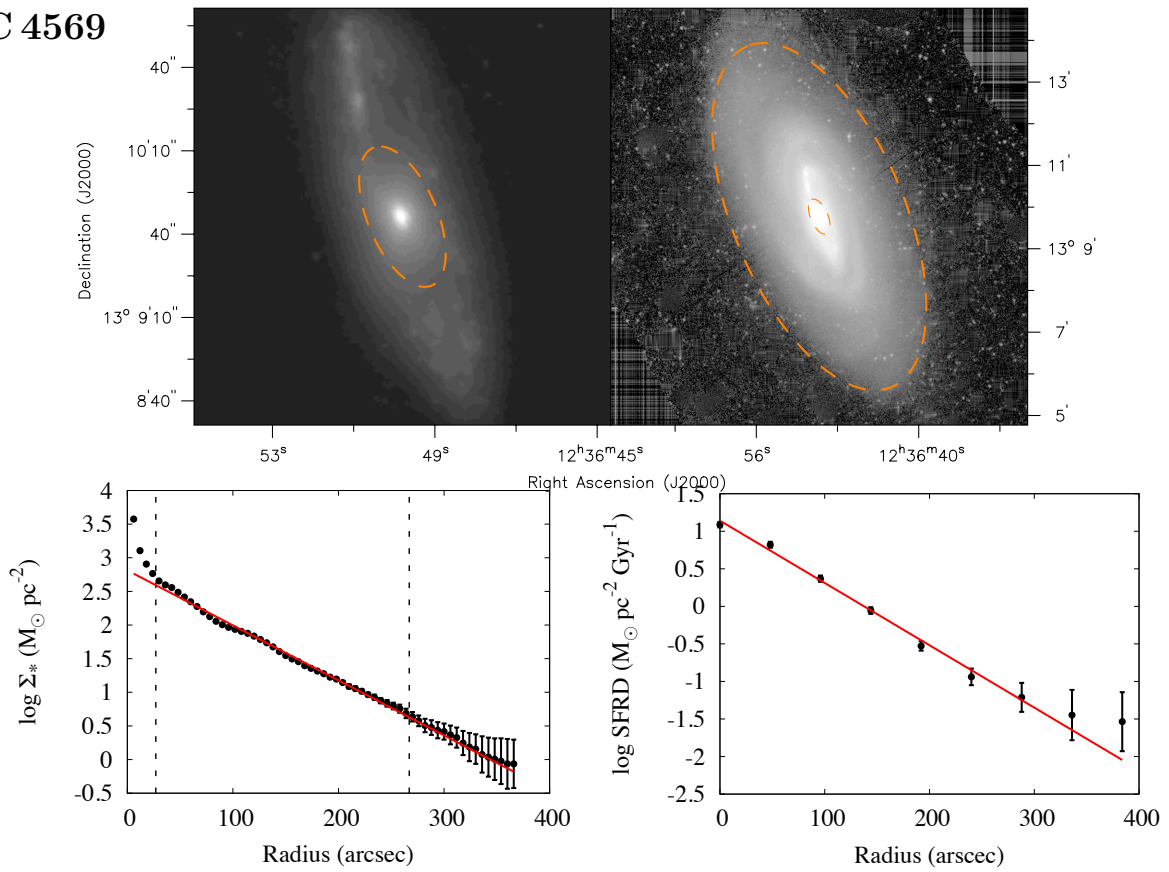
NGC 4536. 3.6 μm fit range: 33–219 arcsec.

NGC 4559



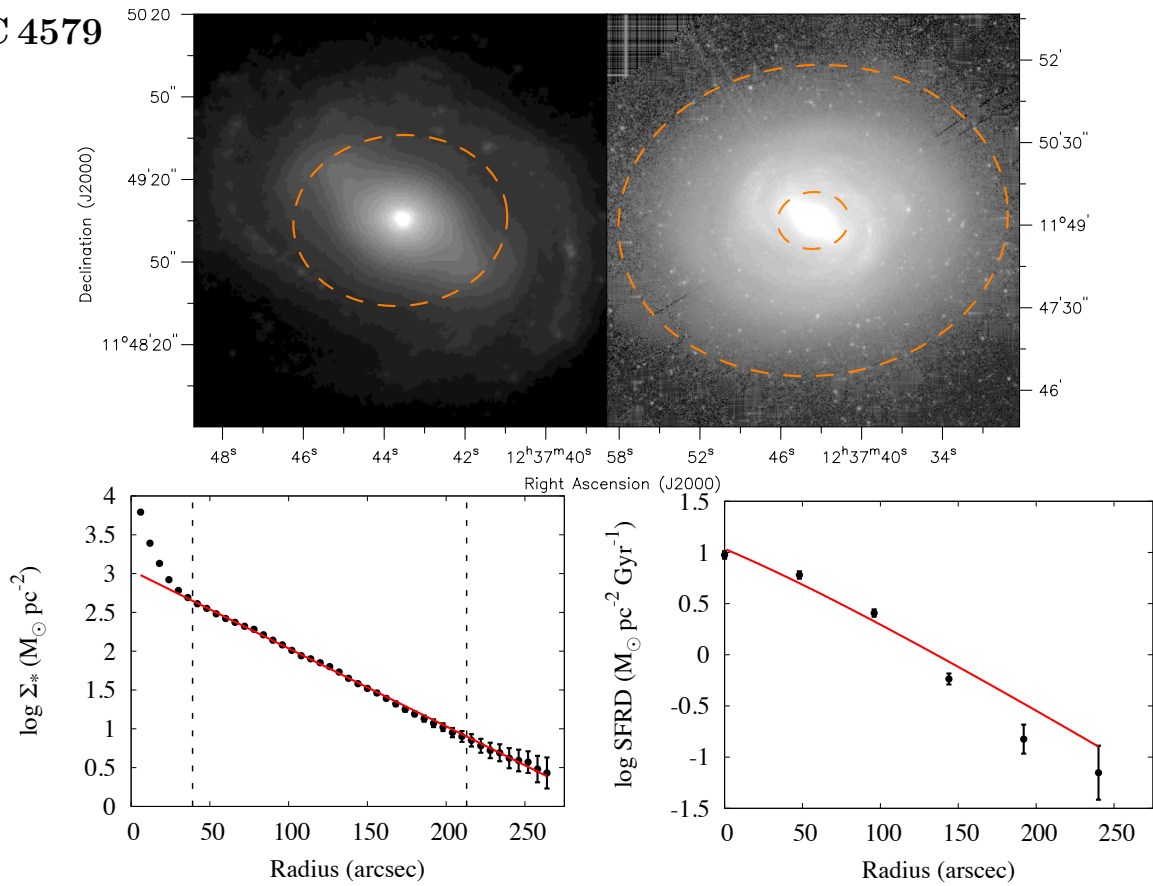
NGC 4559. 3.6 μm fit range: 27–237 arcsec.

NGC 4569



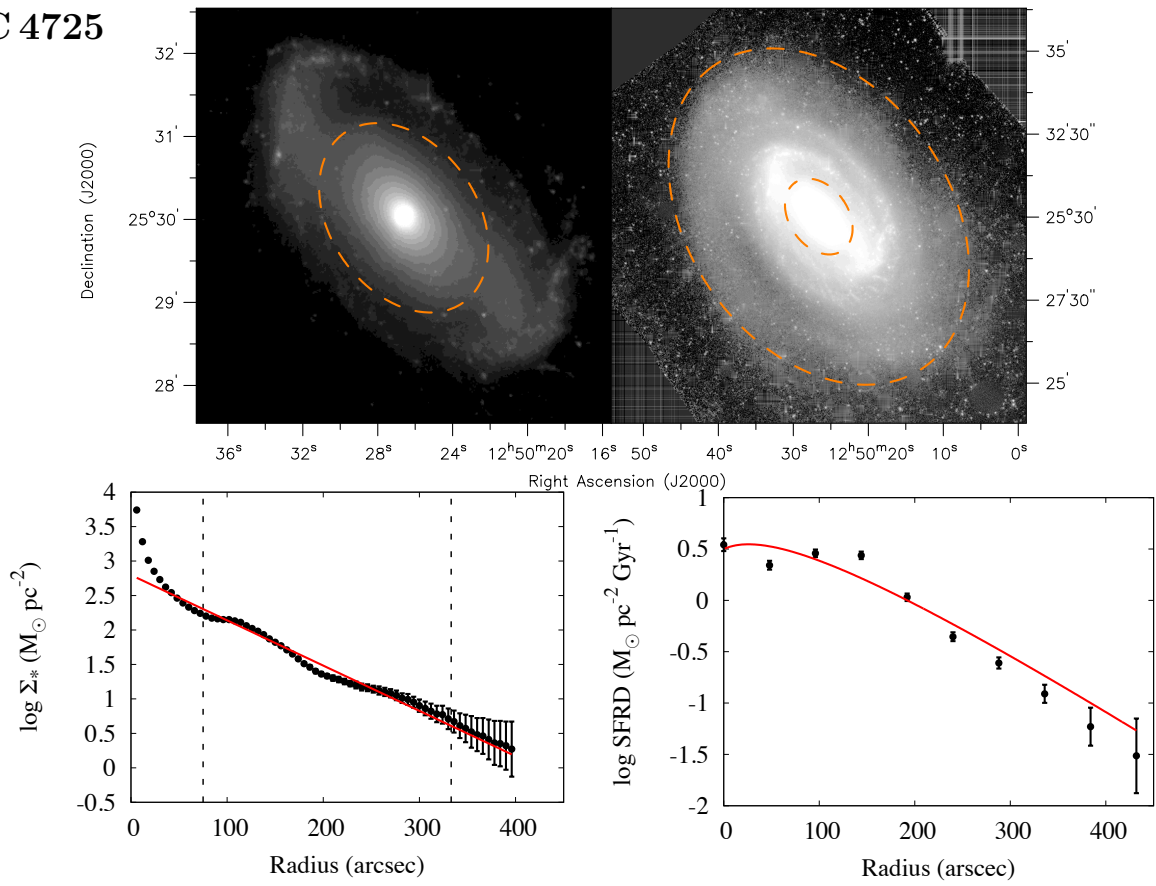
NGC 4569. $3.6 \mu\text{m}$ fit range: 27–267 arcsec; unweighted.

NGC 4579



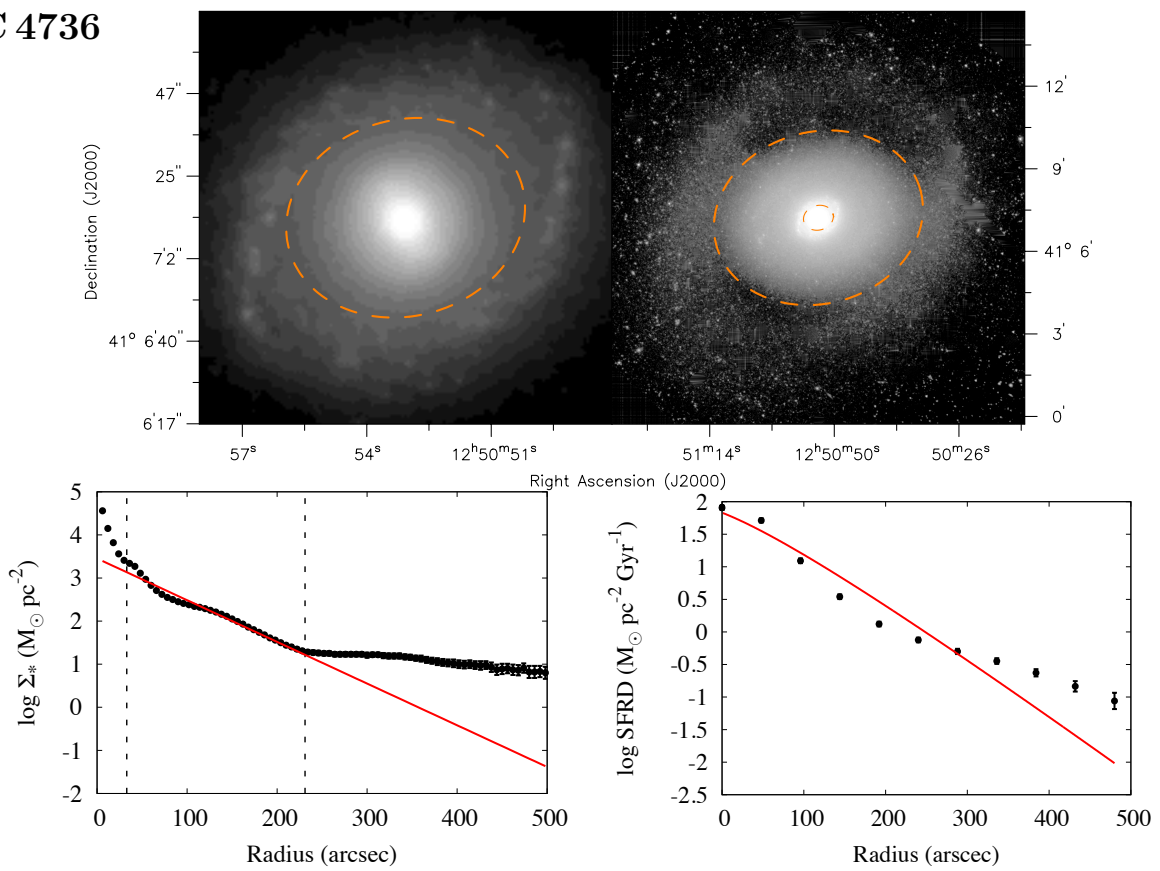
NGC 4579. $3.6 \mu\text{m}$ fit range: 39–213 arcsec.

NGC 4725



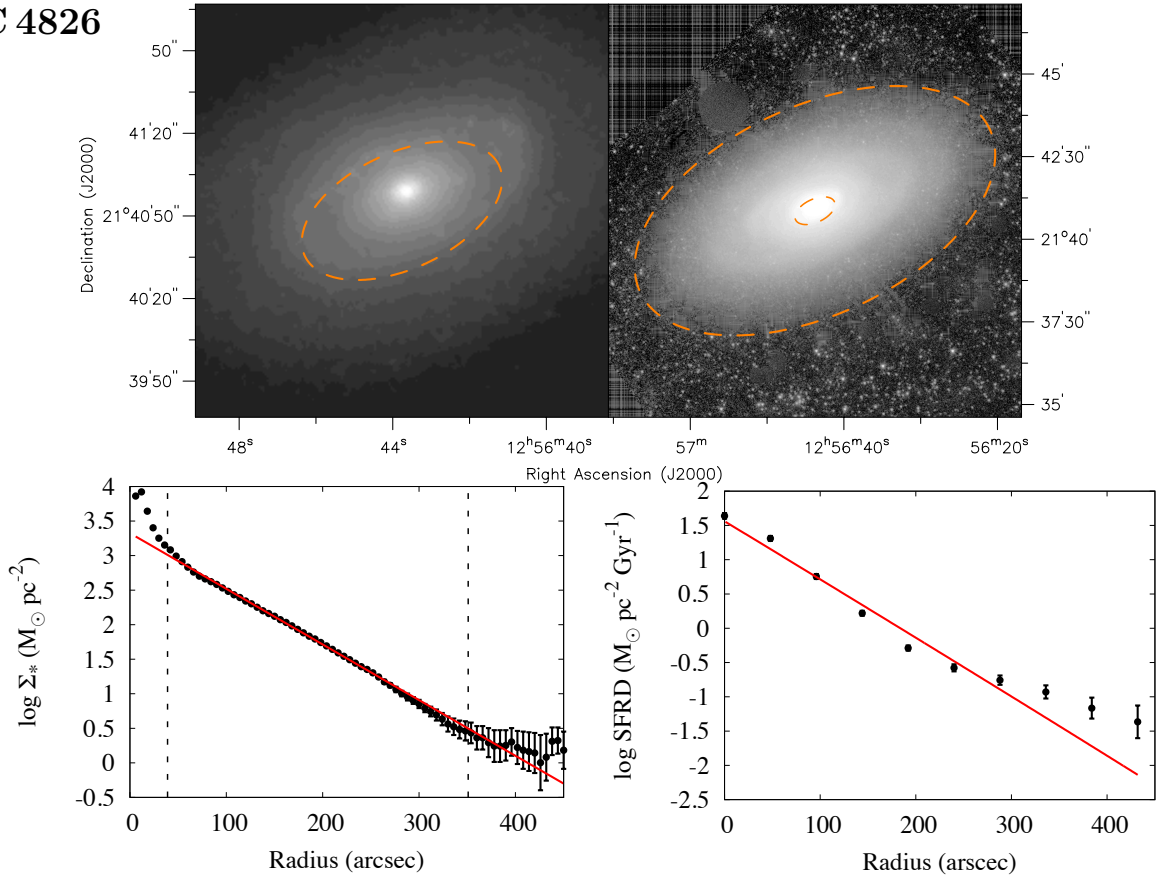
NGC 4725. $3.6 \mu\text{m}$ fit range: 75–333 arcsec.

NGC 4736



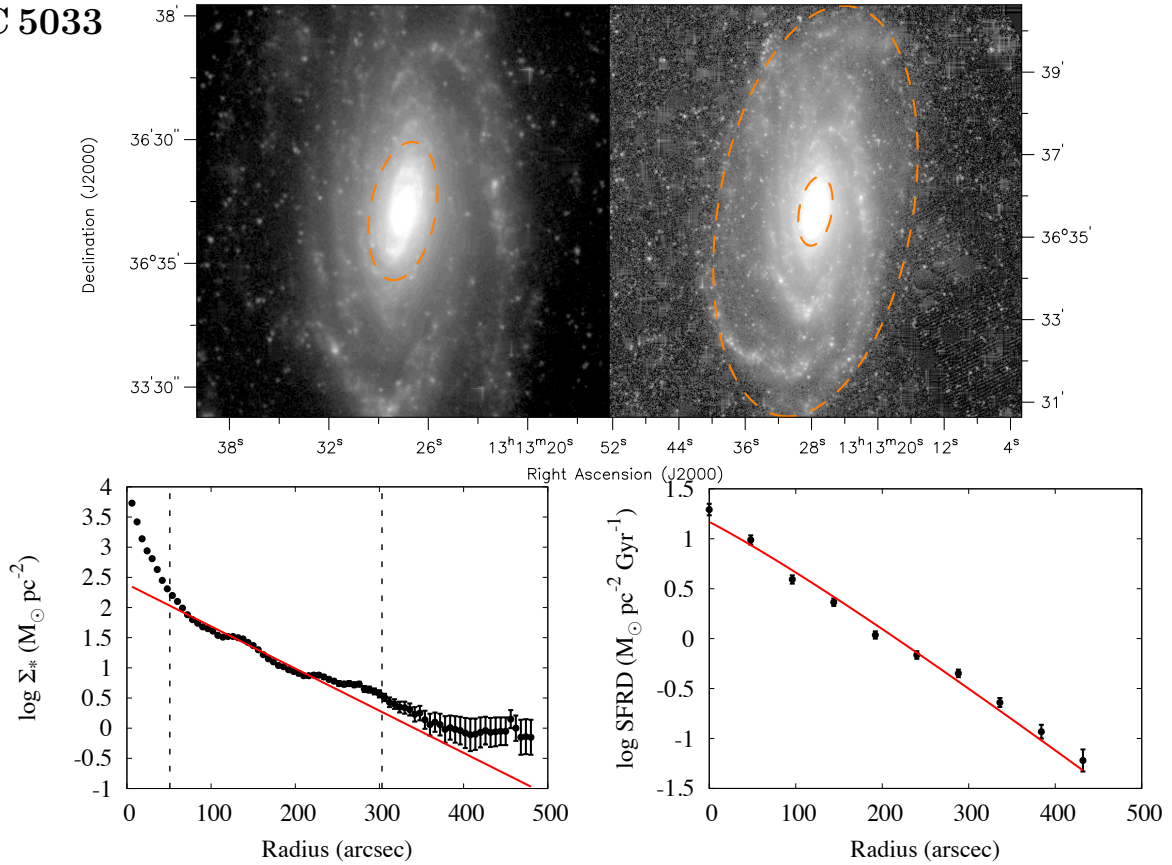
NGC 4736. $3.6 \mu\text{m}$ fit range: 33–231 arcsec. An extended ring is the probable origin of the outstanding outer flattening, which is also visible, though less prominent, in the SFRD profile.

NGC 4826



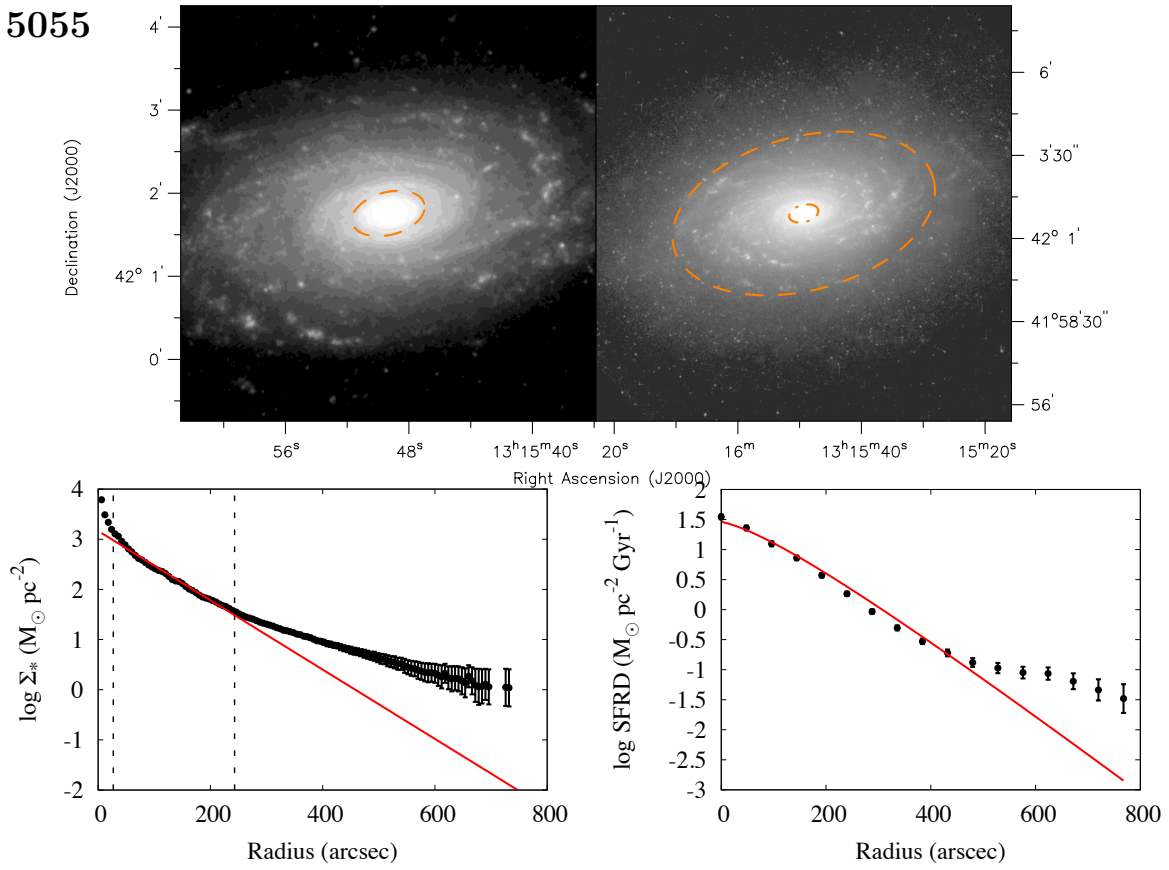
NGC 4826. $3.6 \mu\text{m}$ fit range: 39–351 arcsec. The inner ellipse is chosen both to comprise the bulge and to compensate for a central offset.

NGC 5033



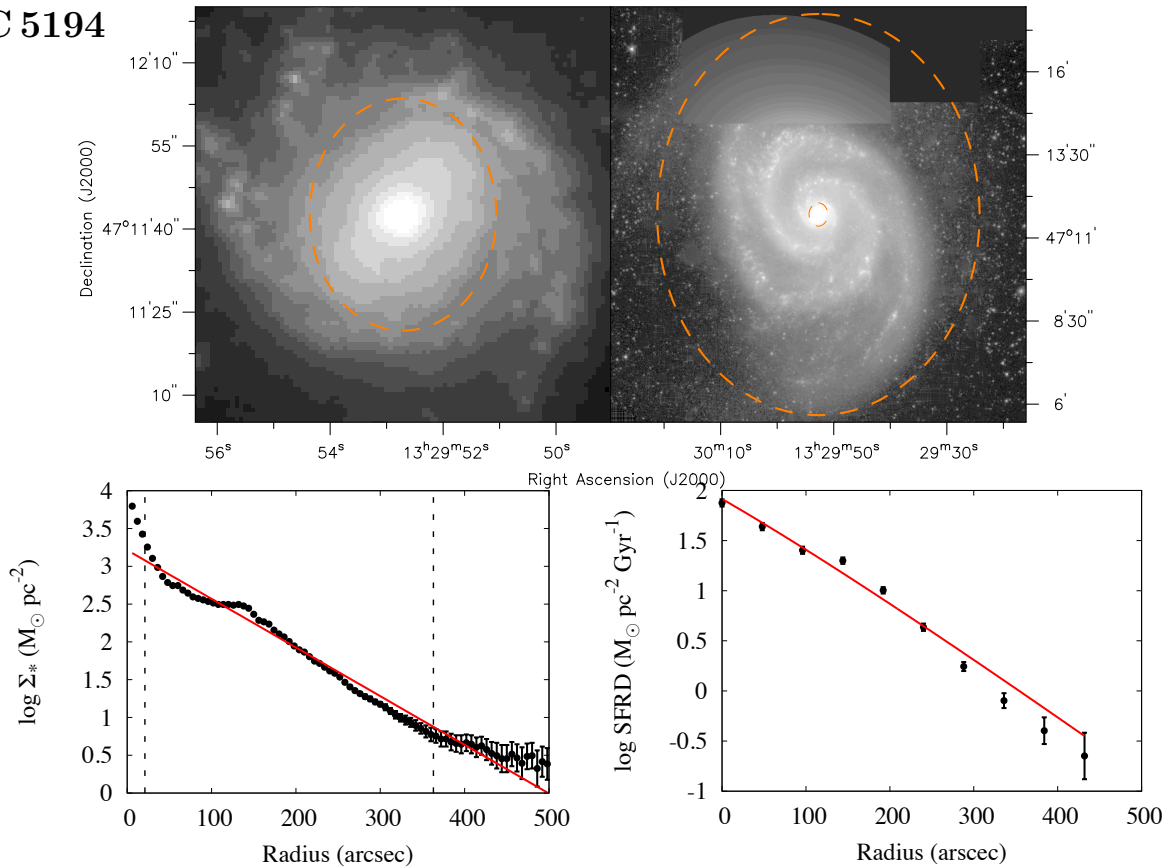
NGC 5033. $3.6 \mu\text{m}$ fit range: 51–303 arcsec. Even if spiral structure can be traced down to very small radii, the inner arms appear to be embedded into a bright spheroidal component, which we exclude from our fit of the disc.

NGC 5055



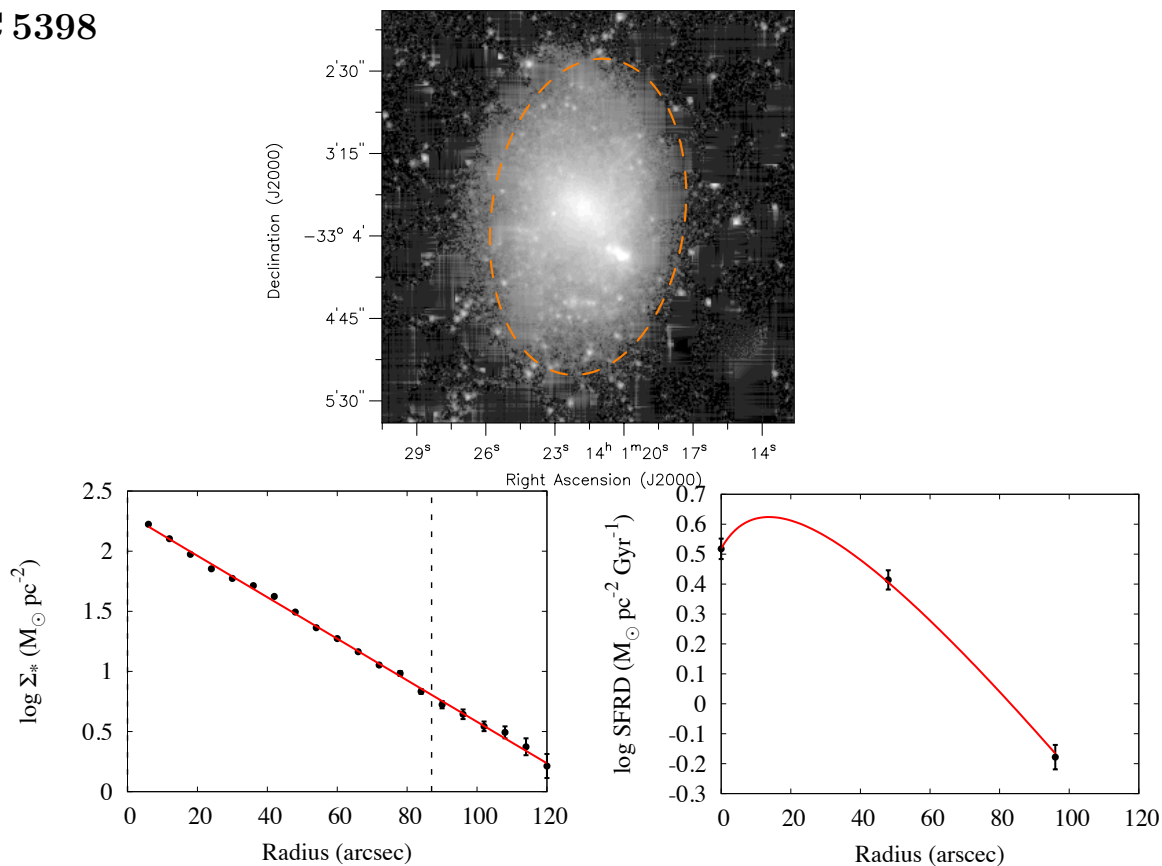
NGC 5055. $3.6 \mu\text{m}$ fit range: 27–243 arcsec. The disc region traced by spiral arms is well described by an exponential. A second disc component, with a greater scalelength and no prominent spiral structure, seems to be present at the periphery. The SFRD follows theoretical expectations out to a remarkably large radius and then in turn exhibits a flattening.

NGC 5194



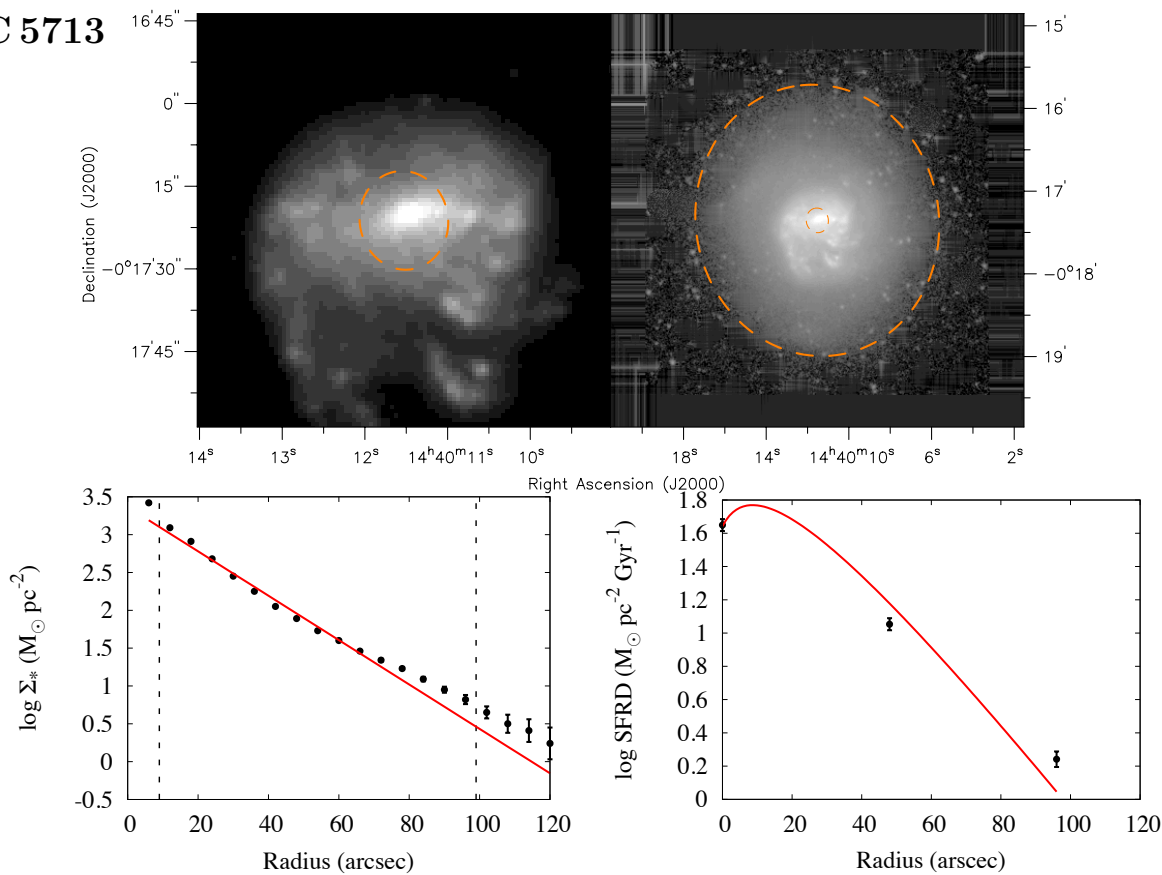
NGC 5194. $3.6 \mu\text{m}$ fit range: 21–363 arcsec. Considering its strong interaction with NGC 5195 (masked out in the northern region of the map), this galaxy shows a surprisingly regular behaviour.

NGC 5398



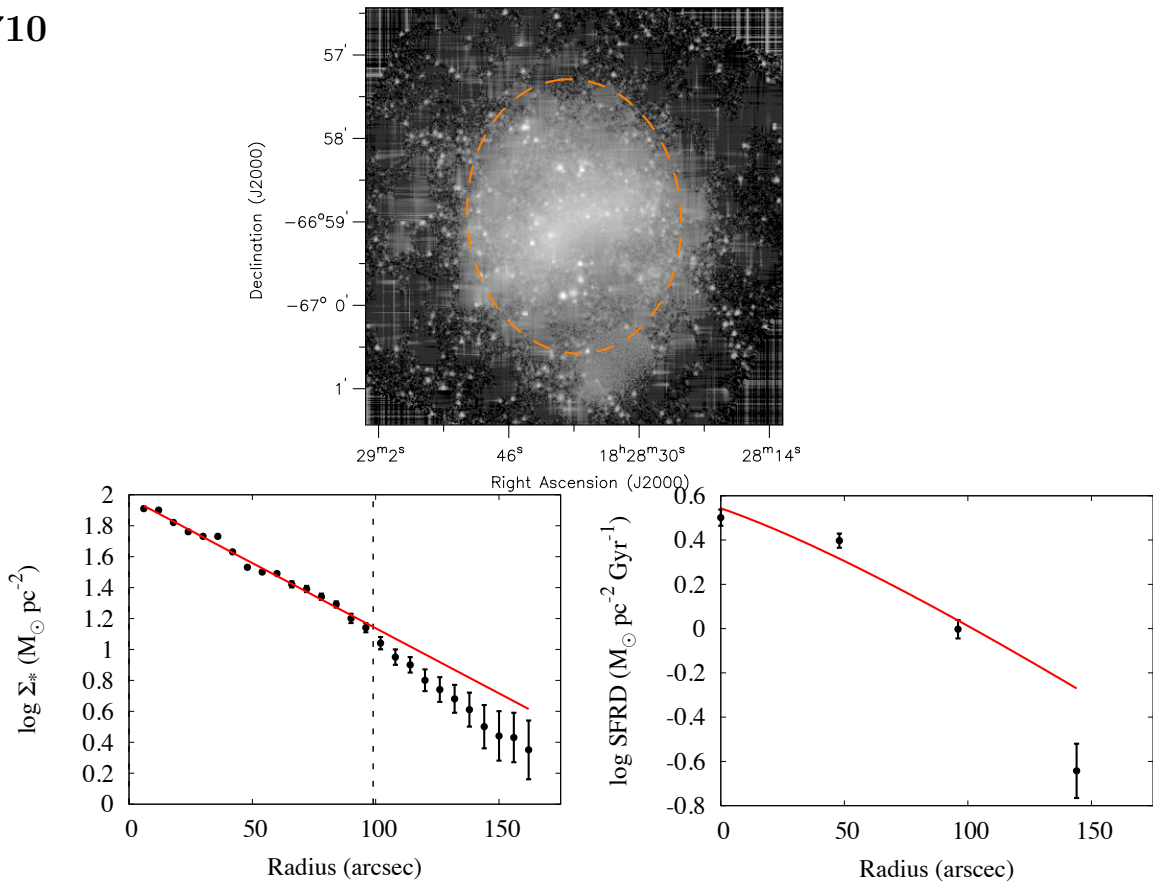
NGC 5398. 3.6 μm fit range: 0–87 arcsec.

NGC 5713



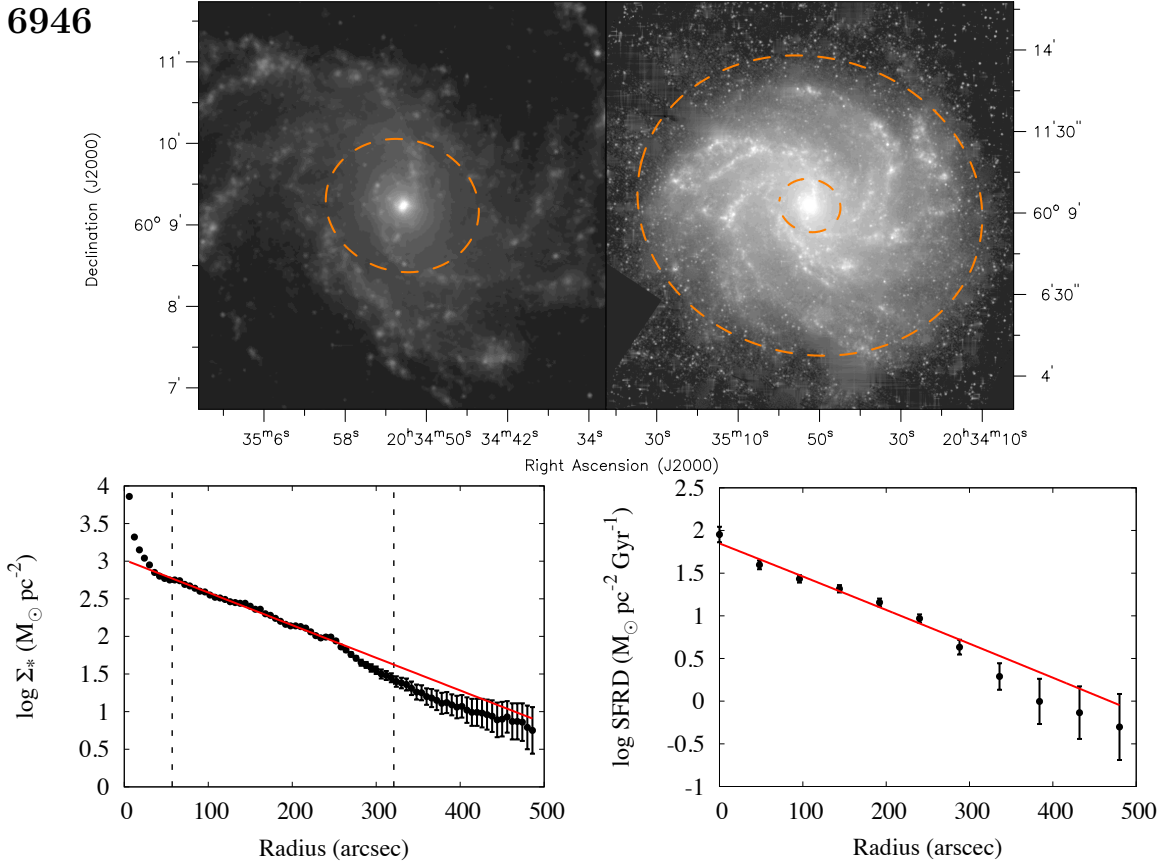
NGC 5713. 3.6 μm fit range: 9–99 arcsec.

IC 4710



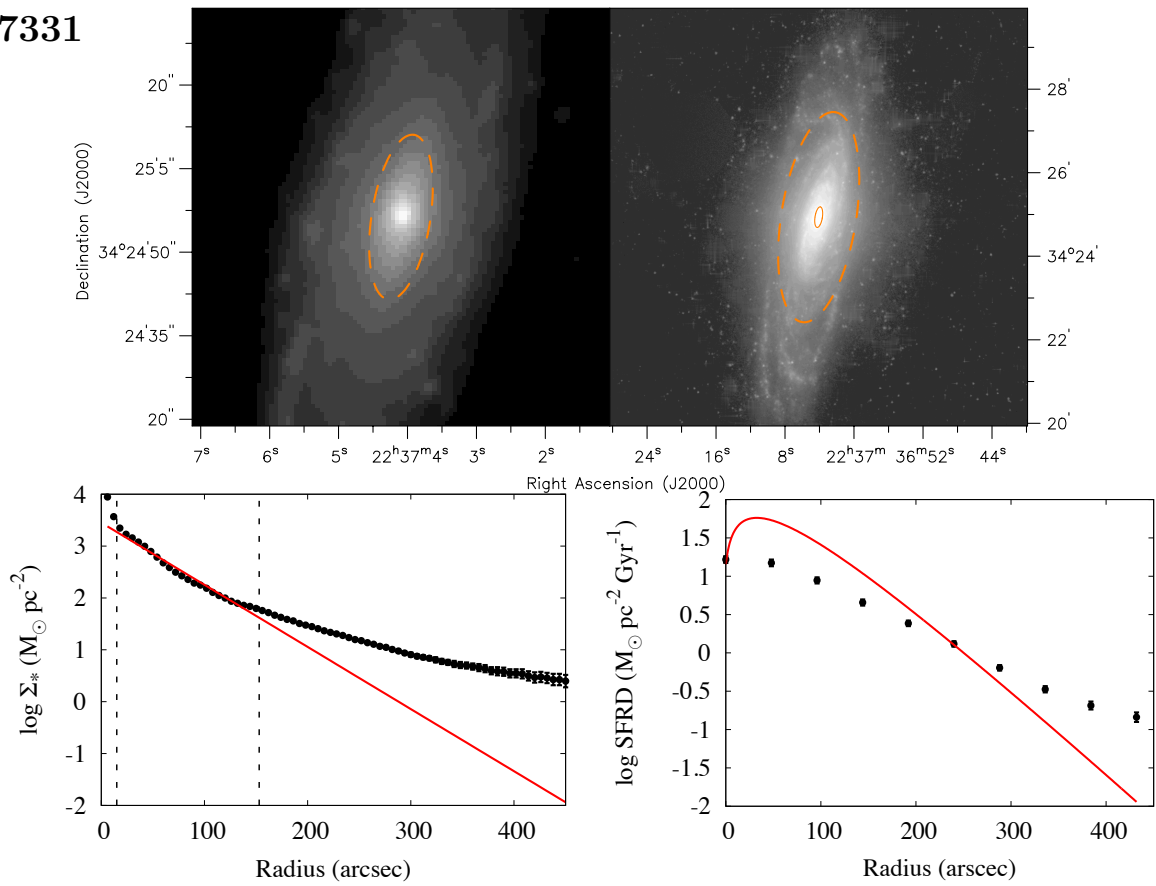
IC 4710. $3.6 \mu\text{m}$ fit range: 0–99 arcsec. A hint is present for a common downbending in both stellar mass and SFR surface densities.

NGC 6946



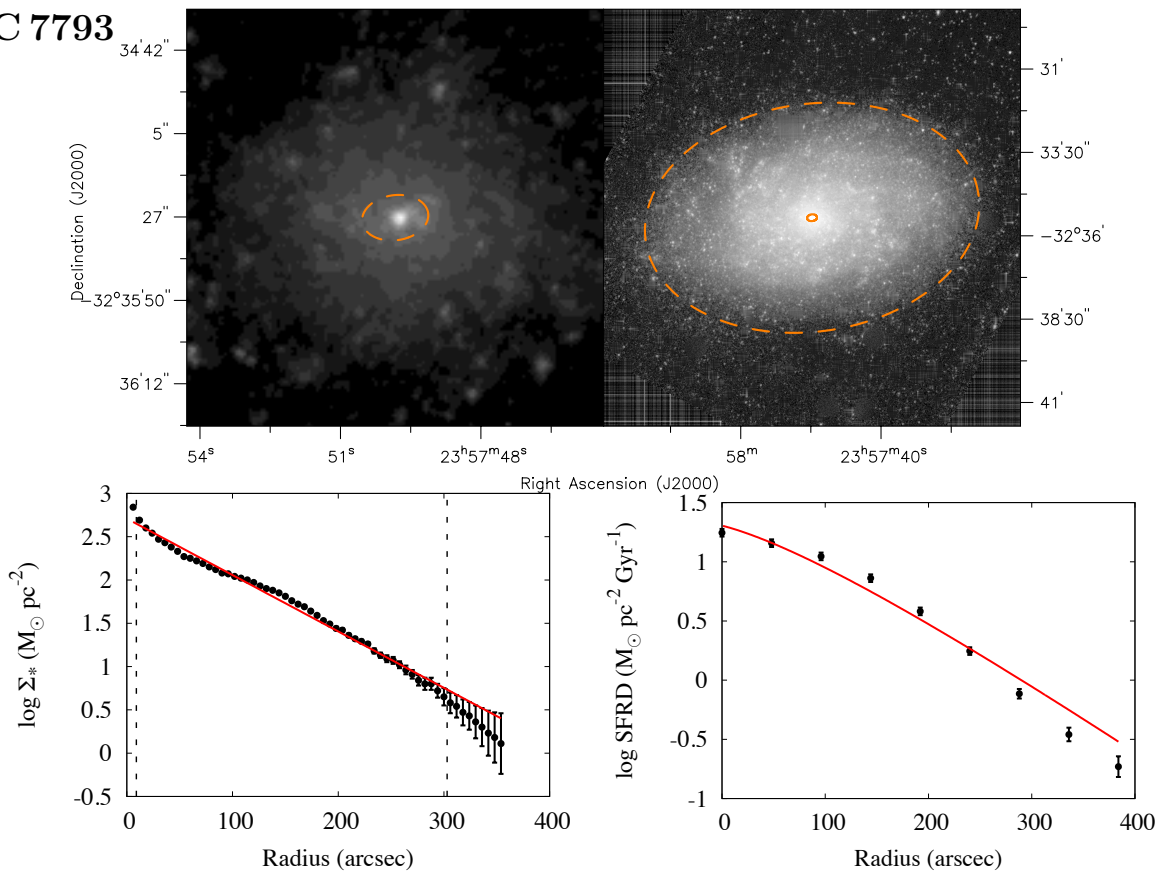
NGC 6946. $3.6 \mu\text{m}$ fit range: 57–321 arcsec.

NGC 7331



NGC 7331. $3.6 \mu\text{m}$ fit range: 15–153 arcsec. Out of 153 arcsec, the $3.6 \mu\text{m}$ profile abruptly flattens and the isophotes have a very peculiar geometry. The SFRD profile is nearly exponential out to very large radii, but our model fails to reproduce its large scalelength.

NGC 7793



NGC 7793. $3.6 \mu\text{m}$ fit range: 9–303 arcsec; unweighted.

Chapter 3

Accretion, radial flows and abundance gradients in spiral galaxies[†]

Abstract

In this Chapter, we consider the local aspects of the accretion of mass and angular momentum on the discs of spiral galaxies. The spatial distribution of mass and angular momentum accretion rates are of great importance for the evolution of discs, but still largely unknown. However, the physical connection between the two can be useful to reconstruct them indirectly. It is well known that even a very small angular momentum mismatch between the accreting gas and the disc inevitably drives radial gas flows within the disc itself. This effect has a large impact on the reconstruction of the mass accretion profile and on the prediction of chemical abundance gradients; since the latter are observable, they can be used to put constraints on the spatial structure and the dynamics of accretion on spiral galaxies. Here we provide a generalization of existing analytic techniques for the study of this problem and we apply them to the Milky Way and to a nearby spiral galaxy (NGC 628). We consider different models: with or without radial flows and including or not inside-out growth (cfr. Chapter 2). We find that models with neither radial flows nor inside-out growth compare very badly with observations. Inside-out growing models without radial flows perform better, but still fail to give the correct steepness of gradients. Radial flows, with or without inside-out growth, can explain the observed gradients if the metal-poor gas is accreted at large radii and rotates with $\sim 70 - 85\%$ of the rotational velocity of the disc.

3.1 Introduction

As we have seen in Chapter 1, continuous accretion of metal poor gas is known to be a crucial ingredient in the evolution of spiral galaxies, from a wide variety of evidence (e.g. Pagel & Patchett 1975; Fraternali & Tomassetti 2012; Zafar et al. 2013; Sánchez Almeida et al. 2014 and references therein), but, unfortunately, direct observations

[†]Based on G. Pezzulli & F. Fraternali, 2015, MNRAS, in press.

of the actual accretion process has proven to be very elusive (e.g. Sancisi et al. 2008, Di Teodoro & Fraternali 2014 and references therein), with the consequence that the spatial distribution of the accretion is largely unknown, even for our own Galaxy at the present time, let alone for external galaxies and on cosmological timescales. Hence, indirect inference from observed properties of galaxies is still necessary.

Models for the evolution of spiral galaxies, and of our own Galaxy in particular, have always taken great advantage from simple parametrizations of the accretion rate surface density as a function of time and radius (e.g. Pagel 2009; Matteucci 2012 and references therein). In order to constrain this function from observations, a powerful and widely used approach is the requirement, for every annulus with given galactocentric radius R , that the integral over time of the accretion rate surface density at R equals the total present-time observed baryonic surface density there.

One problem of the above method is that it implicitly assumes that the material accreting on a galaxy disc at some radius will keep staying there for the whole galactic history (the so-called *independent annuli* approach). This occurrence is in general very unlikely, being in contradiction with a basic dynamical requirement, namely angular momentum conservation. In fact, as it was first emphasized by Mayor & Vigroux (1981), whenever the specific angular momentum of the accreting material is not exactly equal to that of the disc in the point of impact (which would be a fine-tuned coincidence), radial flows will inevitably onset within the disc in order for total angular momentum to be conserved. This implies the break of the independent annuli assumption and, in particular, of the link between the total mass in a given annulus and the integral over time of the mass accretion rate there.

A direct detection of net radial motions in the gaseous discs of spirals would be very valuable, since it would give constraints on the dynamics of the accretion process onto spiral galaxies. Unfortunately, the velocities predicted as a consequence of the aforementioned effect are so low that they are barely measurable and, most importantly, it is still not clear how they could be observationally distinguished from spurious effects driven by non-axisymmetric disturbances (Wong, Blitz & Bosma 2004). Therefore, indirect methods are necessary, which are able to capture the integrated signal of such low velocities across the whole history of a galaxy disc. Chemical evolution provides the desired alternative, since, at any given time, the distribution of metals in the interstellar medium (ISM) depends on the whole history of enrichment and dilution that each gas element has undergone throughout its path across the galaxy.

A considerable amount of work has been devoted to the effect of radial flows on chemical evolution, and in particular on the development of abundance gradients (e.g. Lacey & Fall 1985; Goetz & Koeppen 1992; Portinari & Chiosi 2000; Cavichia et al. 2014; Kubryk, Prantzos & Athanassoula 2015, among many others), sometimes in conjunction with other mechanisms, like inside-out formation (cfr. Chapter 2) and radial variations (either smooth or discontinuous) in the normalization of the star formation law (e.g. Clarke 1989; Chamcham & Tayler 1994; Spitoni & Matteucci 2011), both in the Local Universe and at high redshift (Mott, Spitoni & Matteucci 2013). Several mechanisms can in principle contribute to the onset of ordered radial gas flows within the discs of spirals (e.g. Lacey & Fall 1985; Thon & Meusinger 1998) and turbulence can cause additional transport of metals (e.g.

Yang & Krumholz 2012; Petit et al. 2015), but order of magnitude estimates suggest angular momentum deficit in accretion to be the dominant process, or one of the dominant processes, in this respect (Bilitewski & Schönrich 2012). However, only few works, to our knowledge, have so far implemented radial flows that are consistent with angular momentum conservation.

In their seminal work, Mayor & Vigroux (1981) considered the extreme case of infall of gas completely devoid of angular momentum. Lacey & Fall (1985) improved the angular momentum equation allowing for non-vanishing rotation in the accreting material, but they did not use it in their models, preferring simpler parametrizations of the radial velocity.

Two major improvements came in the field with the work by Pitts & Tayler (1989), though both of them maybe received somewhat less consideration than they were worth of.

First, these authors introduced the fundamental concept of *effective accretion*, which is the amount of gas that has to come at a given annulus at a given time in order to sustain a given structural evolution. The effective accretion, rather than the accretion itself, is the quantity that can be directly constrained by the present-day structure of galaxies (e.g. its integral over time equals the present-day baryonic surface density) and which should, therefore, be preferentially chosen as a starting point for semi-analytic models of galaxy evolution. In general, the effective accretion needs to be decomposed in two contributions, direct accretion from the IGM and an internal contribution due to radial flows, a problem which we refer to as *mass flux decomposition*. To better appreciate the importance of this, it may be useful to consider that fixing an accretion profile, rather than the profile of effective accretion, in a set of models with radial flows, has the consequence that different models will have a different final structure (e.g. models with inward radial flows will be more centrally concentrated) and therefore they cannot all succeed in satisfying observational structural requirements (e.g. Lacey & Fall (1985); Tosi (1988a); Goetz & Koeppen (1992)). The approach based on effective accretion, instead, guarantees that all the models match the same structural constraints and therefore allows to validate or discard radial flow models on the basis of chemical information. Note that in this way the accretion profile is a prediction, rather than an input, of a model with radial flows.

As a second improvement, Pitts & Tayler (1989) provided some analytic solutions to the mass flux decomposition problem as a function of the angular momentum of the infalling material. Their solutions, however, were valid only for some very special values of the angular momentum and did not allow a continuum of models to be explored.

The mass flux decomposition problem has been recently reconsidered, from a numerical point of view, by Bilitewski & Schönrich (2012), who solved a discretized version of the equation of angular momentum conservation and were able to compute a fine grid of models. Implementing their technique into the detailed Milky Way evolution model by Schönrich & Binney (2009), they provided the current benchmark for the dynamical properties of accreting material on our own Galaxy.

In this work, we build upon the analytic approach of Pitts & Tayler (1989) and we generalize it. In Sec. 3.2 we discuss a minimal model for the evolution

of spiral galaxies and we investigate the consequences of the independent-annuli assumption on the chemical evolution of spiral galaxies. In Sec. 3.3 we give the general analytic solution to the mass flux decomposition problem as a function of the angular momentum of the accreting material. We also discuss its implications for the reconstruction of radial flows and accretion profiles, both in general and for a Milky-Way like example. In Sec. 3.4 we propose a novel method, based on characteristic lines, to compute chemical evolution in the presence of radial flows and we compare it with other computational techniques. We then discuss the impact of the angular momentum of the accreting material on gas-phase abundance gradients and we use observational data to put constraints on the dynamical properties of gas accretion onto the disc of the Milky Way. In Sec. 3.5 we combine our analysis with the results of Chapter 2. In particular, we show how structural and chemical information can be combined to disentangle the effects of inside-out growth and radial flows on the development of abundance gradients in spiral galaxies. Again, the application to the Milky Way is discussed in detail. In Sec. 3.6 we describe an application to the external spiral galaxy NGC 628, which is taken from the same sample analyzed in Chapter 2 and for which recent determinations of gas-phase abundances were available. We draw out our conclusions in Sec. 3.7.

In the Appendices, some more theoretical discussion can be found about angular momentum and accretion in a couple of very different scenarios (App. 3.A and 3.B), as well as some additional investigation about the effect of the metallicity of the IGM (App. 3.C).

3.2 A minimal model for the evolution of galaxy discs

Before looking at more complex situations, we consider in this Section the simplest possible model for the evolution of a galaxy disc. We just make elementary assumptions, based on few general properties of the discs of spiral galaxies and simple enough to allow for an analytic description. We use dimensionless units when possible, but also give an illustrative example with parameters chosen to be plausible for the Milky Way.

3.2.1 Exponential discs obeying the Kennicutt-Schmidt law

As basic structural requirements, we ask that stellar discs have an exponential radial mass distribution (cfr. (2.1)):

$$\Sigma_{\star}(t, R) = \frac{M_{\star}(t)}{2\pi R_{\star}^2} e^{-\frac{R}{R_{\star}}} \quad (3.1)$$

and form stars according to the Kennicutt-Schmidt law:

$$\dot{\Sigma}_{\star} = A \Sigma_{\text{g}}^N \quad (3.2)$$

The fiducial parameters of the Kennicutt-Schmidt law are $N = 1.4$ and $A = 0.11375$, if surface densities are measured in $\text{M}_{\odot} \text{pc}^{-2}$ and times in Gyr. These

values are taken from Kennicutt (1998), with A corrected for a helium factor equal to 1.36 and then multiplied by a factor $(1 - \mathcal{R})$, with an assumed *return fraction* $\mathcal{R} = 0.3$, to take into account material returned from stars to the ISM during stellar evolution. Note that this implies that our $\dot{\Sigma}_\star$ represents the net (or *reduced*) star formation rate surface density, rather than the instantaneous one.

Equations (3.1) and (3.2) imply that also the gas distribution is exponential:

$$\Sigma_g(t, R) = \frac{M_g(t)}{2\pi R_g^2} e^{-\frac{R}{R_g}} \quad (3.3)$$

with a scalelength that is larger than the one of the stars, according to:

$$R_g = NR_\star$$

while the total gas mass M_g is linked to the global star formation rate \dot{M}_\star by the equation:

$$\dot{M}_\star = \hat{A}M_g^N \quad (3.4)$$

with:

$$\hat{A} := \frac{A}{N^2(2\pi R_g^2)^{N-1}} \quad (3.5)$$

Equation (3.4) resembles in form the Kennicutt-Schmidt law, with the important differences that it refers to masses, rather than surface densities, and its normalization \hat{A} is not universal, but a function of the scalelength. For a fiducial stellar scalelength $R_\star = 2.5$ kpc, which should be similar to the value appropriate for our Galaxy, it is $R_g = 3.5$ kpc (see also Schönrich & Binney 2009) and therefore $\hat{A} = 0.16187$, if masses are measured in units of $10^9 M_\odot$ and times in Gyr.

Finally, we consider the simple case of an exponentially declining star formation history:

$$\dot{M}_\star(t) = \frac{M_{\star,\infty}}{t_\star} e^{-\frac{t}{t_\star}} \quad (3.6)$$

where $M_{\star,\infty}$ is the asymptotic value of the stellar mass and t_\star is the star formation decline timescale. Equations (3.6) and (3.4) imply that the gaseous mass is also exponentially declining with time, but with a larger timescale $t_g = Nt_\star$ and an initial value $M_{g,0}$ linked to the other parameters by the relation:

$$M_{\star,\infty} = \hat{A}M_{g,0}^N t_\star \quad (3.7)$$

The two independent parameters of the model, $M_{\star,\infty}$ and t_\star , can be uniquely constrained, for a given galaxy, from the global properties of that galaxy at the present time. In particular, the quantity $x = t_0/t_\star$, t_0 being the age of the disc, can be inferred from observations by inverting the relation:

$$\frac{x}{e^x - 1} = \frac{t_0 \hat{A} M_g^N(t_0)}{M_\star(t_0)} \quad (3.8)$$

and $M_{\star,\infty}$ can then be found by the means of (3.7). In our fiducial example, we consider a 12 Gyr aged disc with a stellar mass $M_\star = 4 \times 10^{10} M_\odot$ and a gaseous

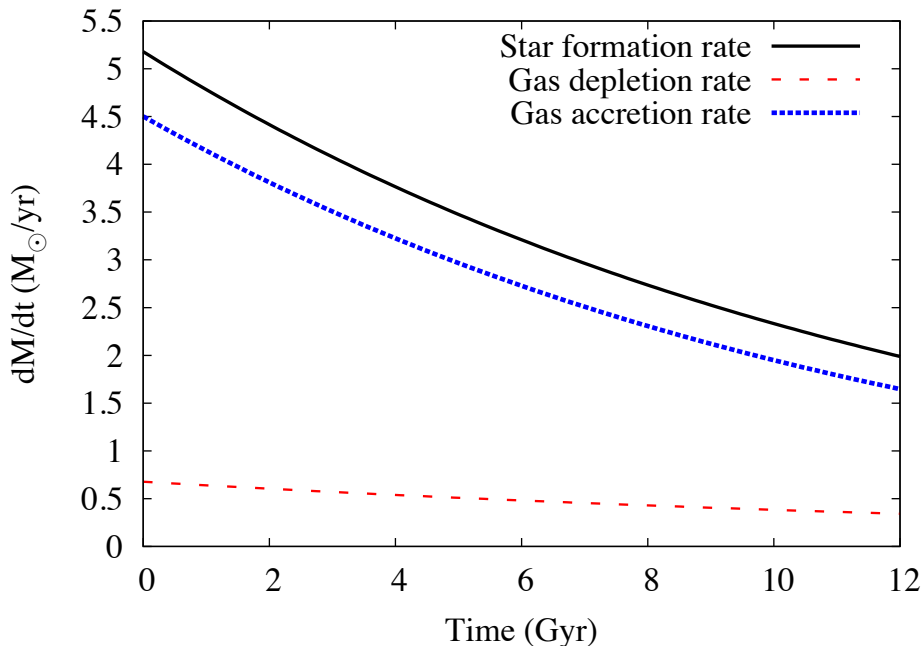


Figure 3.1: The global star formation rate \dot{M}_* (solid black line), gas consumption rate ($-\dot{M}_g$) (dashed red line) and gas accretion rate \dot{M}_{acc} (dotted blue line) for our fiducial model of the Milky Way. Note the relatively slow decline of all these quantities and the similar evolution of the star formation rate and the gas accretion rate.

mass $M_g = 6 \times 10^9 M_\odot$. The resulting parameters of the model are $t_* = 12.5$ Gyr and $M_{*,\infty} = 6.5 \times 10^{10} M_\odot$.

In Fig. 3.1 we show the resulting predicted star formation history, together with the gas consumption rate and the accretion rate implied by the other two. Note that the star formation rate and the accretion rate follow a very similar evolution and are only mildly declining with time, in agreement with the findings by Fraternali & Tomassetti (2012).

3.2.2 Effective accretion rate surface density

Following Pitts & Tayler (1989), we define the *effective* accretion rate surface density as:

$$\dot{\Sigma}_{\text{eff}}(t, R) := \frac{\partial}{\partial t}(\Sigma_* + \Sigma_g)(t, R) \quad (3.9)$$

which is the amount of gas that is needed at a given time t and a given radius R in order to sustain a given structural evolution. This material can either directly come from the IGM, or through the disc via radial flows, or, in general, from a combination of the two routes (Pitts & Tayler 1989, Schönrich & Binney 2009). This fact is conveniently formalized by the equation of conservation of mass. If, in the evolution of the gas component, a sink term $\dot{\Sigma}_*$ and a source term $\dot{\Sigma}_{\text{acc}}$ are accounted for, to describe star formation and accretion, respectively, then the

continuity equation can be written:

$$\dot{\Sigma}_{\text{eff}} = \dot{\Sigma}_{\text{acc}} - \frac{1}{2\pi R} \frac{\partial \mu}{\partial R} \quad (3.10)$$

where:

$$\mu := 2\pi R \Sigma_{\text{g}} u_R \quad (3.11)$$

is the radial gaseous mass flux, u_R being the net radial velocity of the gas.

If an independent annuli approach is adopted, then radial flows are neglected, the second term in the r.h.s. of (3.10) vanishes and therefore $\dot{\Sigma}_{\text{acc}} = \dot{\Sigma}_{\text{eff}}$. In general, however, a different accretion profile is needed, a problem which we will come back to in Sec. 3.3.2.

All the considerations above are fully general and do not depend on the particular structural evolution model under consideration. In the particular case of an exponential disc obeying the Kennicutt-Schmidt law (Sec. 3.2.1), equation (3.9) reads:

$$\dot{\Sigma}_{\text{eff}} = \frac{\dot{M}_{\star}(t)}{2\pi R_{\star}^2} e^{-\frac{R}{R_{\star}}} + \frac{\dot{M}_{\text{g}}(t)}{2\pi R_{\text{g}}^2} e^{-\frac{R}{R_{\text{g}}}} \quad (3.12)$$

where all the functions and parameters are as specified in Sec. 3.2.1. If radial flows are neglected, (3.12) gives the accretion profile at any time in our minimal model.

3.2.3 Metallicity evolution with independent annuli

In a model with independent annuli, the metallicity evolution of each annulus is governed by the equation:

$$\frac{\partial \tilde{X}_i}{\partial t} = \frac{\dot{\Sigma}_{\star}}{\Sigma_{\text{g}}} - \tilde{X}_i \frac{\dot{\Sigma}_{\text{acc}}}{\Sigma_{\text{g}}} \quad (3.13)$$

where $\tilde{X}_i = X_i/y_i$ is the abundance by mass of an element i , normalized on its yield y_i . Strictly speaking, equation (3.13) is an approximation, because, consistently with our treatment of star formation (see Sec. 3.2.1), it assumes instantaneous recycling. For this reason, it can be considered reliable only to predict the abundances of α elements, which are produced by short-lived stars. Furthermore, (3.13) can only be straightforwardly applied to abundances in the ISM; the spatial distribution of stellar abundances, in fact, is known to be severely affected by stellar radial migration (e.g. Schönrich & Binney 2009; Kubryk, Prantzos & Athanassoula 2013; Minchev, Chiappini & Martig 2014). However, restricting our attention to α elements in the ISM will not prevent us to draw significant conclusions.

If $\tilde{X}_i = 0$ at $t = 0$, the explicit solution for (3.13) is:

$$\tilde{X}_i(t, R) = e^{-\sigma(t, R)} \int_0^t e^{\sigma(t', R)} \frac{\dot{\Sigma}_{\star}}{\Sigma_{\text{g}}}(t', R) dt' \quad (3.14)$$

where we introduced the dimensionless coordinate:

$$\sigma(t, R) := \int_0^t \frac{\dot{\Sigma}_{\text{acc}}}{\Sigma_{\text{g}}}(t', R) dt' \quad (3.15)$$

Notice that σ increases with time at different rates with varying R , implying different timescales for chemical evolution at different radii.

3.2.4 Independent-annuli chemical evolution of exponential discs

The independent-annuli metallicity evolution of the minimal model of Sec. 3.2.1 is conveniently computed in terms of the dimensionless time and space coordinates:

$$\tau := \frac{t}{t_1} \quad \rho := \frac{R}{R_1} \quad (3.16)$$

where:

$$t_1 := \frac{N}{N-1} t_\star \quad R_1 := \frac{N}{N-1} R_\star \quad (3.17)$$

In our fiducial model, $t_1 = 43.8$ Gyr and $R_1 = 8.75$ kpc.

Under the independent-annuli assumption, $\dot{\Sigma}_{\text{acc}}$ is given by (3.12) (see Sec. 3.2.2), and therefore the coordinate σ defined in (3.15) is:

$$\sigma(\tau, \rho) = q_0 e^{-\rho} (1 - e^{-\tau}) - \frac{\tau}{N-1} \quad (3.18)$$

where $q_0 = \hat{A} t_1 M_{\text{g},0}^{N-1} / N^2$, which is a dimensionless parameter. In the fiducial model, $q_0 = 37.5$

Note that the coordinate (3.18) is time-increasing (and thus, well defined) for $\tau + \rho < \ln((N-1)q_0)$. The reason is that outside this domain (3.12) formally describes an effective wind and therefore cannot be used as an accretion term into (3.13) anymore. Our fiducial model matches the requirement for its present age out to more than 20 kpc, which is large enough for a comparison with observations. Within this domain, the metallicity evolution (3.14) reads:

$$\tilde{X}_i(\tau, \rho) = q_0 e^{-\sigma(\tau, \rho) - \rho} \int_0^\tau e^{\sigma(\tau', \rho) - \tau'} d\tau' \quad (3.19)$$

with σ given by (3.18).

Equation (3.19) gives the general evolution of the abundance profiles for an exponential disc obeying the Kennicutt-Schmidt law with an exponentially declining SFH, in the absence of radial flows. It provides a family of self-similar solutions for each value of the dimensionless parameter q_0 .

In Fig. 3.2 we show, for the fiducial value $q_0 = 37.5$, the resulting profile, in dimensionless units, for some values of the dimensionless time τ . In the units of the fiducial model, the maximum radius shown is $R_{\text{max}} = 17.5$ kpc, while the present time is $\tau = 0.27$, corresponding to a profile between the solid blue line and the dashed black line.

As a consequence of the exponential structure of the disc and of the Kennicutt-Schmidt law, chemical enrichment in this model proceeds on longer timescales at larger radii (formally, σ increases with τ more rapidly for smaller values of ρ , see (3.18)). As shown in Fig. 3.2, the inner regions relatively quickly tend towards an approximately common equilibrium, while enrichment at the periphery proceeds much slower, with the outermost annuli being progressively less evolved and more metal-poor. As a result, this class of models predicts, at early times, a negative abundance gradient throughout the disc and, at late times, a progressive flattening

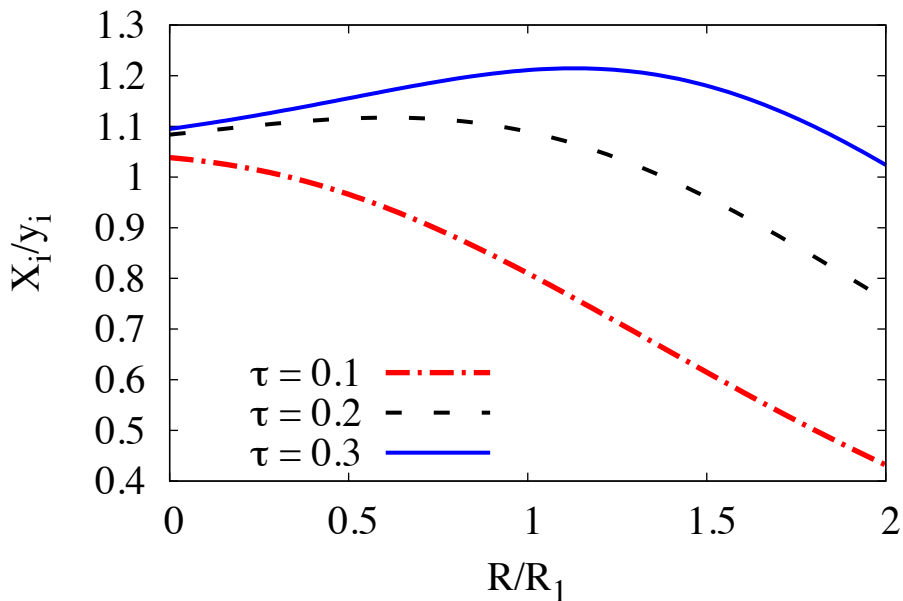


Figure 3.2: Evolution of abundance profiles, in dimensionless units, for an exponential disc forming stars according to the Kennicutt-Schmidt law. The scaling for the Milky Way is $R_1 = 8.75$ kpc and $\tau = 0.27$. Progressive flattening and even gradient inversion occur at late times, contrary to observations. No radial flows, nor inside-out formation, are included in this model.

in the inner regions and even the development of an inverted gradient there. This prediction is at strong variance with the observed properties of spiral galaxies today (e.g. Moustakas et al. 2010; Sánchez et al. 2014) and suggests that a major revision of one or more of our hypotheses is necessary.

The most arbitrary of our assumptions is probably equation (3.6). However, we repeated our calculations with a very different star formation history (vanishing, rather than peaking, for $t = 0$) and we verified that this does not significantly alter the behaviour shown in Fig. 3.2, which is more likely driven by the radial structure of the disc and of the accreting material.

More effective, in this sense, is to remove the hypothesis, implicit in Sec. 3.2.1, that the stellar scalelength R_* is constant with time. This route is tightly linked to the inside-out formation scenario (e.g. Larson 1976), which predicts a rather different distribution of accretion (and therefore of metal dilution) and is indeed the most commonly invoked mechanism to explain abundance gradients in spiral galaxies (e.g. Matteucci & Francois 1989; Mollá, Ferrini & Díaz 1997; Boissier & Prantzos 1999; Chiappini, Matteucci & Romano 2001; Naab & Ostriker 2006; Pilkington et al. 2012). The other way to significantly alter the accretion profile is the removal of the independent-annuli assumption (see Sec. 3.1). This is the main topic of this work and will be discussed in detail in Secs. 3.3 and 3.4. Our combined approach to inside-out growth and radial flows will be discussed in Sec. 3.5.

3.3 Angular momentum, accretion and radial flows

3.3.1 General context and basic equations

The classical theory of galaxy formation (White & Rees 1978) predicts that spiral galaxies accrete a substantial part of their mass from the cooling of large and hot gas reservoirs (*coronae*), which have been detected in X-ray emission around local spiral galaxies, including the Milky Way (Anderson, Bregman & Dai 2013; Bogdán et al. 2013a; Bogdán et al. 2013b; Miller & Bregman 2015). Due to their large (close to virial) temperatures, these structures likely have a non-negligible pressure support against gravity and therefore they are expected to rotate at less than the centrifugal speed at each point; this results in a local angular momentum deficit at the moment of accretion on the centrifugally-supported disc. Other channels, like accretion from filaments (Dekel & Birnboim 2006) or minor mergers (Di Teodoro & Fraternali 2014) can bring some cold gas directly to the disc; material accreted in these ways is not even expected to always rotate in the same sense of the galaxy. An average local angular momentum deficit in accretion is therefore a quite general expectation.

The basic equation describing the dynamical consequences of accretion onto a rotating disc has been first introduced, in the context of galaxy evolution, by Mayor & Vigroux (1981) and then improved by Lacey & Fall (1985). For our purposes, it can be conveniently rewritten, in terms of the radial mass flux μ defined in (3.11), as:

$$\mu = -2\pi\alpha R^2 \dot{\Sigma}_{\text{acc}} \quad (3.20)$$

where we introduced the dimensionless parameter α , which is a measure of the local angular momentum deficit of the infalling material with respect to the disc:

$$\alpha := \frac{l_{\text{disc}} - l_{\text{acc}}}{R \frac{\partial l_{\text{disc}}}{\partial R}} \quad (3.21)$$

Since $\partial l_{\text{disc}}/\partial R$ is always positive, the parameter α is positive whenever $l_{\text{acc}} < l_{\text{disc}}$ and the radial mass flux is therefore directed inwards. In the typical case of a flat rotation curve, (3.21) reduces to:

$$\alpha = 1 - \frac{V_{\text{acc}}}{V_{\text{disc}}} \quad (3.22)$$

The simplest situation in which a prediction for α can be made is the case of accretion from an isothermal corona in a logarithmic potential, for which we have:

$$\alpha = 1 - \sqrt{1 - \delta \frac{c_s^2}{V_{\text{disc}}^2}} \quad (3.23)$$

where c_s is the isothermal sound speed of the hot gas and δ is the logarithmic derivative of the equatorial density of the corona:

$$\delta = -\frac{\partial \ln \rho}{\partial \ln R} \quad (3.24)$$

We will address this topic in much more detail in Chapter 4¹. We can notice here that, already in the ideal case described by (3.23) and (3.24), α is constant with R only if the coronal density follows a power-law along the equator, which in general will not be true. Furthermore, the shape of the function α can be altered by hydrodynamical interactions between the lower layer of the hot corona and the cold extraplanar gas that circulates near the disc in the so-called *galactic fountain* (Marinacci et al. 2010a; Marasco, Fraternali & Binney 2012). We discuss this specific problem in some more detail in Appendix 3.A. In Appendix 3.B, we propose instead some back-of-the-envelope calculations to gain some insight on the more complex problem of cold-mode accretion. In general, however, α is likely a non-trivial function of both space and time; while more theoretical and observational efforts are still required to deepen our understanding in this respect, it is useful to develop a method to evaluate the impact on galaxy evolution of the local angular momentum of the accreting material, under general conditions.

3.3.2 The general mass flux decomposition

As already mentioned (Sec. 3.1, Sec. 3.2.2), the observed structural properties of spiral galaxies do not give us direct constraints on the accretion rate surface density $\dot{\Sigma}_{\text{acc}}$, but just on the effective accretion rate $\dot{\Sigma}_{\text{eff}}$, which should then be decomposed in two contributions: direct accretion from IGM $\dot{\Sigma}_{\text{acc}}$ and a radial mass flux μ (the *mass flux decomposition* problem).

If the equation of angular momentum conservation (3.20) is taken into account, the continuity equation (3.10) becomes a linear differential equation for the unknown μ , whose solution is:

$$\mu(t, R) = \frac{1}{h(t, R)} \left(\mu_0 - 2\pi \int_{R_0}^R R' h(t, R') \dot{\Sigma}_{\text{eff}}(t, R') dR' \right) \quad (3.25)$$

where h is the dimensionless auxiliary function:

$$h(t, R) = \exp \left\{ \int_{R_0}^R \frac{dR'}{R' \alpha(t, R')} \right\} \quad (3.26)$$

while R_0 is an arbitrary radius and $\mu_0 = \mu(R_0)$ is an integration constant. We recall that $\dot{\Sigma}_{\text{eff}}$ is specified by the considered structural evolution model, according to (3.9), while α describes the angular momentum of the accreting material, according to (3.21). Once the radial mass flux μ is known from (3.25), the accretion rate surface density $\dot{\Sigma}_{\text{acc}}$ is readily computed from (3.20):

$$\dot{\Sigma}_{\text{acc}} = -\frac{\mu}{2\pi\alpha R^2} \quad (3.27)$$

while the radial velocity u_R immediately comes from equation (3.11):

$$u_R = \frac{\mu}{2\pi R \Sigma_g} \quad (3.28)$$

¹See, for instance, the lower-right panel of Fig. 4.2

This completes the solution of the mass flux decomposition problem.

Note that, imposing the condition that the total accretion rate is finite, it follows from (3.20) that the radial mass flux must vanish both at the origin and at infinity, provided that α is a limited function there; in particular, in all but pathological cases, it is safe to assume $R_0 = 0$ and $\mu_0 = 0$ ². We can also see as a consequence, by integrating the continuity equation (3.10), that the total accretion rate:

$$\dot{M}_{\text{acc}} = \int_0^{+\infty} 2\pi R \dot{\Sigma}_{\text{acc}} dR$$

always equals the total effective accretion rate. In other words, taking the detailed angular momentum distribution of accreting material into account does not alter the total needed amount of accretion from the IGM, but it affects the way such accretion is distributed in space.

The solution given by (3.25) and (3.26) can be applied to all galaxy models where the net (azimuthally averaged) radial gas flows are dominated by accretion and angular momentum conservation; it provides the mass flux decomposition (and in particular the correct accretion profile) for any desired structural evolution (encoded in $\dot{\Sigma}_{\text{eff}}$) and dynamical properties of accreting material (encoded in α), by the means of explicit quadrature formulae.

3.3.3 Particular cases

A particularly simple case is the one where α is a function of time only. This encompasses the majority of the cases considered so far in the literature, which effectively assume α to be constant with both time and space. If α does not depend of radius, the solution (3.25), (3.26) reads:

$$(-\mu)(t, R) = 2\pi R^{-\frac{1}{\alpha(t)}} \int_0^R R'^{1+\frac{1}{\alpha(t)}} \dot{\Sigma}_{\text{eff}}(t, R') dR' \quad (3.29)$$

An interesting property of (3.29) is that, whenever the effective accretion rate $\dot{\Sigma}_{\text{eff}}$ is (or can be approximated by) an analytic function of radius:

$$\dot{\Sigma}_{\text{eff}} = \sum_k a_k R^k \quad (3.30)$$

then the derived accretion rate $\dot{\Sigma}_{\text{acc}}$ is an analytic function of radius as well:

$$\dot{\Sigma}_{\text{acc}} = \sum_k \frac{a_k}{1 + (k+2)\alpha} R^k \quad (3.31)$$

For the simple exponential model described in Sec. 3.2.1, (3.29) becomes:

$$(-\mu)(t, R) = \dot{M}_*(t) f\left(\frac{1}{\alpha(t)}, \frac{R}{R_*}\right) + \dot{M}_g(t) f\left(\frac{1}{\alpha(t)}, \frac{R}{R_g}\right) \quad (3.32)$$

²Note that, if α is limited near the origin, the definition of h (3.26) is formally singular for $R_0 = 0$; however, notice also that R_0 can be kept arbitrary (and finite) here, since the dependence on it cancels out in (3.25) for $\mu_0 = 0$.

where f is derived from the lower incomplete Euler gamma function γ :

$$f(a, x) := x^{-a}\gamma(2 + a, x) = \sum_{k=0}^{\infty} \frac{(-1)^k}{k!} \frac{x^{k+2}}{a + k + 2} \quad (3.33)$$

while the accretion rate surface density is given by:

$$\dot{\Sigma}_{\text{acc}}(t, R) = \frac{\dot{M}_{\star}(t)}{2\pi R_{\star}^2} g\left(\frac{1}{\alpha(t)}, \frac{R}{R_{\star}}\right) + \frac{\dot{M}_{\text{g}}(t)}{2\pi R_{\text{g}}^2} g\left(\frac{1}{\alpha(t)}, \frac{R}{R_{\text{g}}}\right) \quad (3.34)$$

with:

$$g(a, x) := ax^{-(2+a)}\gamma(2 + a, x) = \sum_{k=0}^{\infty} \frac{(-1)^k}{k!} \frac{a}{a + k + 2} x^k \quad (3.35)$$

The expressions above further simplify for some particular integer values of a , or particular fractional values of α . Completely obvious is the case $\alpha = 0$ (i.e. $a \rightarrow \pm\infty$), where it is $\mu = 0$ and $\dot{\Sigma}_{\text{acc}} = \dot{\Sigma}_{\text{eff}}$, as expected. Less trivial particular cases are essentially those originally found and described by Pitts & Tayler (1989)³. Our approach allows us to explore, with the same simplicity coming from an analytic formulation, the whole continuum of possible values of α .

There are of course other cases admitting a simplified treatment. For instance, the one where α is a linear function of radius:

$$\alpha(R) = \alpha_0 \left(1 + \frac{R}{R_{\alpha}}\right) \quad (3.36)$$

corresponds to the following simple form for the auxiliary function:

$$h(R) = K \left(1 + \frac{R_{\alpha}}{R}\right)^{-\frac{1}{\alpha_0}} \quad (3.37)$$

where K is a constant such that $h(R_0) = 1$. Note that the coefficients α_0 and R_{α} can be a function of time. Note also that R_{α} can be negative, but in this case there is a critical radius $|R_{\alpha}|$, where corotation occurs, out of which a separate solution is formally needed, associated to an outward radial flow.

3.3.4 Application to the minimal galaxy evolution model

As an illustrative example, we discuss here the application of our analytic mass flux decomposition to the fiducial model of Sec. 3.2.1.

Fig. 3.3 reports the accretion profile (upper panel), the inward radial mass flux ($-\mu$) (middle panel) and the inward radial velocity ($-u_R$) (lower panel), computed at the present time for some values of the angular mismatch parameter α , assumed to be constant with R ⁴.

The case $\alpha = 0$ is for fine-tuned local angular momentum balance between accretion and the disc. In this case, there are no radial flows and the accretion rate

³Some differences arise not from the decomposition, but from the details or their assumed $\dot{\Sigma}_{\text{eff}}$.

⁴Note that no assumption is necessary here about the dependence of α on time.

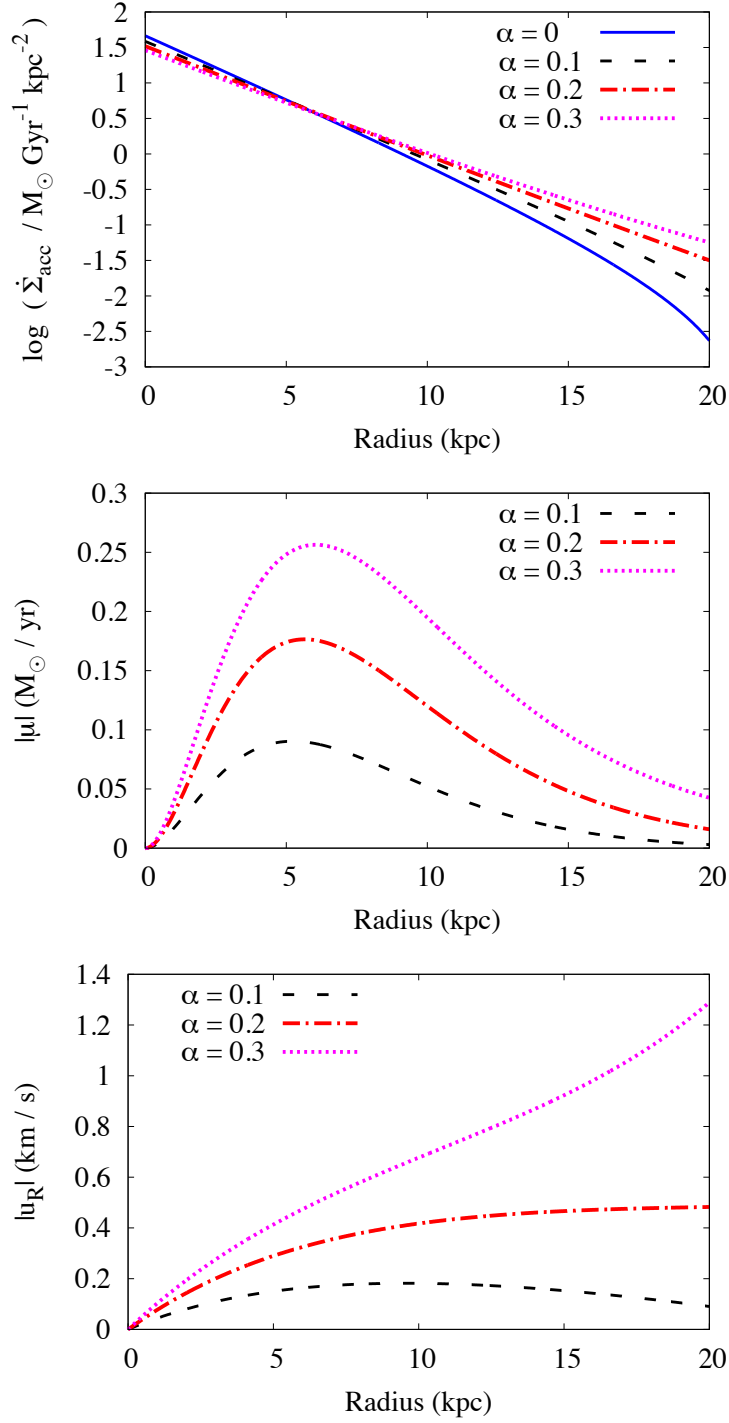


Figure 3.3: Illustrative mass flux decomposition for the fiducial model (Sec. 3.2.1), at the present time, for different values of the angular momentum mismatch parameter α . *Upper panel:* accretion rate surface density (in logarithmic scale). *Middle panel:* inward radial mass flux. *Lower panel:* inward radial velocity. For $\alpha = 0$, there are no radial flows and accretion coincides with the effective accretion. For larger α , accretion from the IGM preferentially occurs in the outer regions, from which the gas is then brought inwards by radial flows.

surface density (solid blue line) is equal to the effective accretion rate surface density (3.12).

Slightly larger values of α already have a significant impact on the shape of the accretion profile. The qualitative effect is a depletion of the needed accretion in the inner regions and a corresponding enhancement in the outskirts. This is a redistribution effect, since the total accretion rate is independent of α (see Sec. 3.3.2). The magnitude of the effect rapidly increases with increasing α : already for $\alpha = 0.2$ (corresponding, for a flat rotation curve, to material accreting with 80% of the rotational velocity of the disc), the needed accretion at 20 kpc is increased by more than one order of magnitude.

The increasing change in the shape of the accretion profile is associated to the onset of an increasingly large inward radial mass flux: the material falling down in the outskirts then travels radially within the disc, to reach the inner regions where it is needed to sustain the structural evolution of the disc. While the overall shape of the radial mass flux profile is mainly dictated by general boundary condition requirements (see Sec 3.3.2), the precise position of the peak is in general a function of α . However, it always coincides with the boundary between the inner region, where accretion is depleted with respect to the effective accretion, and the outer one, where it is enhanced. This fact is completely general, being an obvious consequence of the continuity equation (3.10).

The predicted radial velocity pattern is a non-trivial function of both radius and α (besides, of course, of time, as all the involved quantities), implying that the full calculation is always required for a model with radial flows to be compatible with angular momentum conservation. The predicted magnitude of radial velocities is very low, of the order of 1 km/s or less, which is not directly accessible to observations, but important for chemical evolution (see Sec. 3.1 and the next Section).

All the trends reported in Fig. 3.3 are in very good agreement with the ones found by Bilitewski & Schönrich (2012) by means of numerical techniques.

3.4 Chemical evolution with radial flows

In the presence of radial flows, equation (3.13) is no longer valid and it has to be replaced with the following equation:

$$\frac{\partial \tilde{X}_i}{\partial t} + u_R \frac{\partial \tilde{X}_i}{\partial R} = \frac{\dot{\Sigma}_\star}{\Sigma_g} - \tilde{X}_i \frac{\dot{\Sigma}_{\text{acc}}}{\Sigma_g} \quad (3.38)$$

This is a partial differential equation, the solution of which is usually approached by the means of numerical finite-difference techniques. Equation (3.38), however, has the special property of being linear in the unknown \tilde{X}_i . This allows it to be solved in a much simpler, more stable and less numerically demanding way, which is the method of characteristics.

3.4.1 The method of characteristics

The method of characteristics consists of the reduction of a linear partial differential equation into a combination of two sets of ordinary differential equations. The first

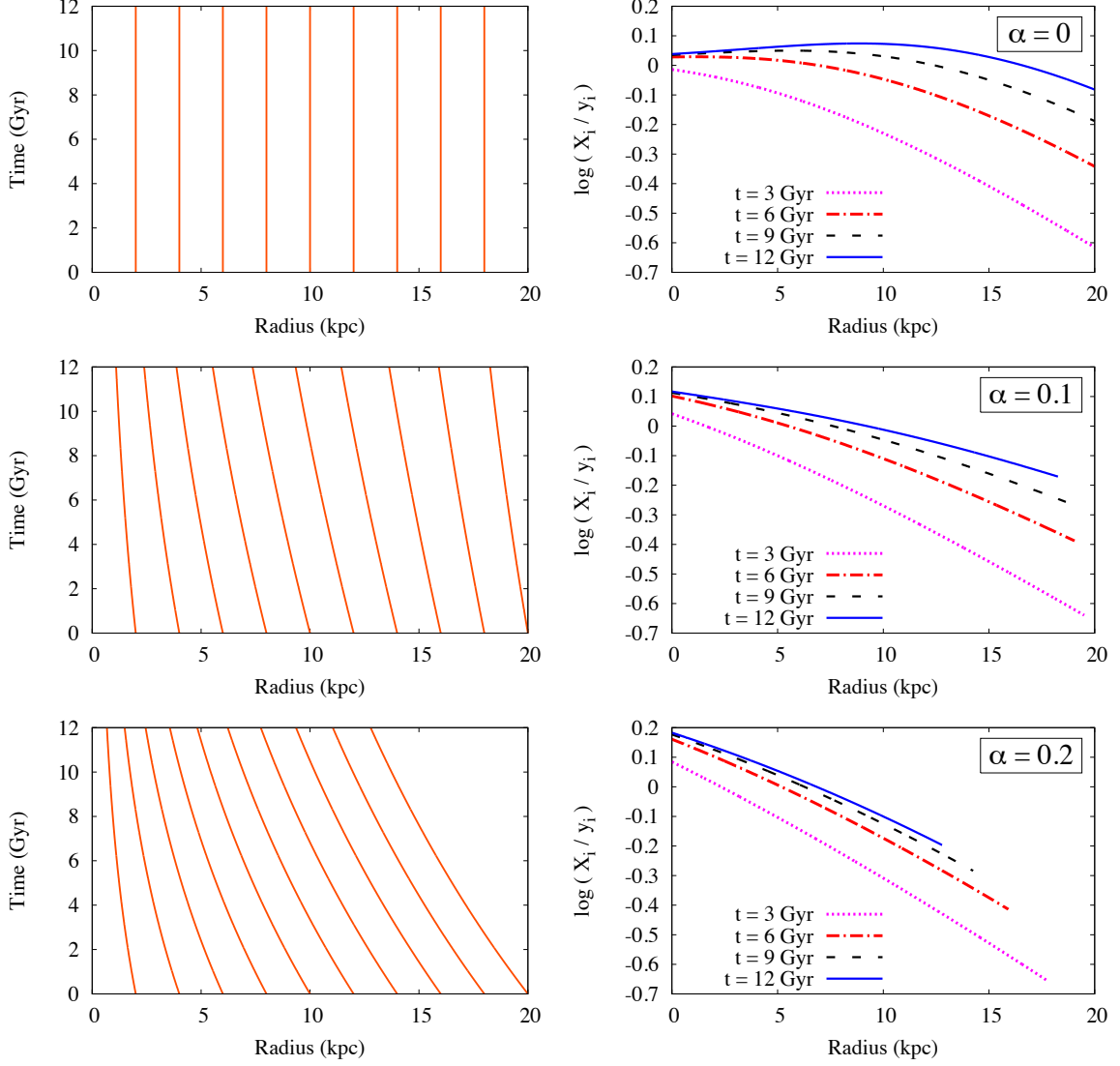


Figure 3.4: Illustrative application of the method of characteristics to the fiducial model of Sec. 3.2.1, when radial flows are included as in Sec. 3.3.4. *Left panels:* The characteristic lines, along which metallicity evolution can be computed independently. *Right panels:* The resulting logarithmic abundance profiles, at different epochs; the solid blue line is for the present time. Different rows are for different values of the angular momentum mismatch parameter: $\alpha = 0$ (*upper panels*), $\alpha = 0.1$ (*middle panels*) and $\alpha = 0.2$ (*lower panels*). The case $\alpha = 0$ (no radial flows) is equivalent to the independent-annuli assumption (cfr. Fig. 3.2). Negative gradients are already predicted for small, but non vanishing, values of α .

set defines characteristic lines, which are the loci, in the computational domain, along which the information propagates that is relevant to the solution of the problem. The second set encodes such an information propagation and describes the evolution of the unknown field along individual characteristic lines.

In our particular case, characteristic lines, in the (t, R) computational plane, are the integral curves of the radial velocity field u_R : that is, they are the solutions of the equation:

$$\frac{dR_{\text{char}}}{dt} = u_R \quad (3.39)$$

The left-hand side of (3.38) is easily recognized as the total time derivative of \tilde{X}_i along the characteristic lines defined by (4.52). This implies that, when restricted along characteristics, (3.38) formally reduces to (3.13) and therefore that the metallicity evolution along each characteristic can be independently computed by the means of the explicit quadrature formulae (3.14) and (3.15).

In this way, the problem of including radial gas flows into chemical evolution is reduced to replacing a model with independent annuli with a model with independent characteristics, essentially keeping the same computational difficulty. Note, however, that the independence of characteristic lines strictly relies on our simplifying assumptions and in particular on the instantaneous recycling approximation (Sec. 3.2.3). For our approach to be extended to elements produced by long-lived stars (among all, iron), some interaction should be accounted for between different lines, within a distance given by $|u_R|$ times the relevant stellar lifetimes; furthermore, the distance travelled by the stars themselves, due to stellar radial migration, should be taken into account as well in this case.

From a mathematical point of view, our approach is similar to the one by Edmunds & Greenhow (1995), although these authors did not include any accretion term in their equations, neither as a dynamical driver of radial flows, nor as a source for dilution of metals, while our formalism includes both effects in a natural way.

Physically, characteristics may be regarded as shrinking gaseous rings (for $\alpha > 0$), though attention should be paid to the fact that the matter they are constituted of is not fixed but continuously changing with time: at each radius, novel material is acquired from the IGM, while some other mass is left behind, deposited into the stellar component due to star formation.

3.4.2 Application to the minimal model

In Fig. 3.4 we illustrate the application of the method of characteristics to the chemical evolution of the minimal model of Sec. 3.2.1, with radial flows induced by a local angular momentum mismatch, as described in Sec. 3.3.4, assuming some values of α , which we take here to be constant with both space and time, increasing from $\alpha = 0$ (upper panels) to $\alpha = 0.2$ (lower panels). In the left panels, the characteristic lines are drawn in the (t, R) plane, while the right panels show the computed logarithmic abundance profiles, as a function of radius R , for different times.

For $\alpha = 0$, there are no radial flows ($u_R = 0$ everywhere) and therefore, according to (4.52), characteristic lines are lines of constant radius. This case is, of course,

coincident with the independent annuli model. In fact, the abundance profile shown in the upper right panel is just the same as Fig. 3.2, but with dimensional units for space and time and a logarithmic scale for the abundances. As already pointed out, the predicted abundance profile at the present time (the solid blue line) is in very strong disagreement with observations.

For $\alpha = 0.1$ and $\alpha = 0.2$, small, but non-negligible, inward radial gas flows onset (cfr. Fig. 3.3, lower panel). Accordingly, characteristic lines now connect radii that are no more constant, but decreasing with time. From the right panels, we see that even a small deviation from perfect corotation between the accreting material and the disc has a dramatic impact on the predicted abundance profiles. A very small value of the angular momentum mismatch parameter $\alpha = 0.1$ is already able to completely remove the inner gradient inversion, which was plaguing the independent annuli model. Furthermore, the steepness of the resulting profile is strongly dependent on α .

3.4.3 Origin of the steepening effect

Both the mathematical and the physical origin of the described behaviour can be relatively easily understood (see also Chamcham & Tayler 1994 on this).

From a mathematical point of view, the origin is two-fold. First, as described in Sec. 3.3.4 (Fig. 3.3, upper panel) increasing α implies a modification of the accretion profile. Depleted accretion in the inner regions means a reduced dilution and therefore higher metallicity there, while the opposite is true in the outskirts, going in the direction of creating or steepening abundance gradients. Furthermore, radial flows tend to bring inwards metals produced at large radii, further increasing the enrichment of the inner regions at the expenses of the outer ones.

From a physical point of view, the two effects are tightly linked to each other and they can be understood altogether. In our approach, in fact, all the models share the same structural evolution and therefore the same amount of gas arriving at each radius and time. The only difference is in the path that is followed by gas elements to come to their present position: directly from the IGM, and therefore unpolluted, in the case $\alpha = 0$, or through a more complex path, in the other cases, including a travel within the disc, where primordial material gets mixed with higher metallicity gas and polluted by ongoing star formation.

3.4.4 The role of boundary conditions

A major feature of Fig. 3.4 is that, when $\alpha \neq 0$, the domain where abundances are predicted appears to be shrinking with time. Such a behaviour is a logical outcome of our chosen computational method: at each time, the maximum radius where abundances are predicted is the one reached, at that time, by the outermost considered characteristic: in the shown example, the one starting at $t = 0$ from a radius $R_{\max} = 20$ kpc. Points lying, in the (t, R) plane, above and to the right of such a line are not reached by any characteristic and therefore the information needed to compute the metallicity evolution is not available there.

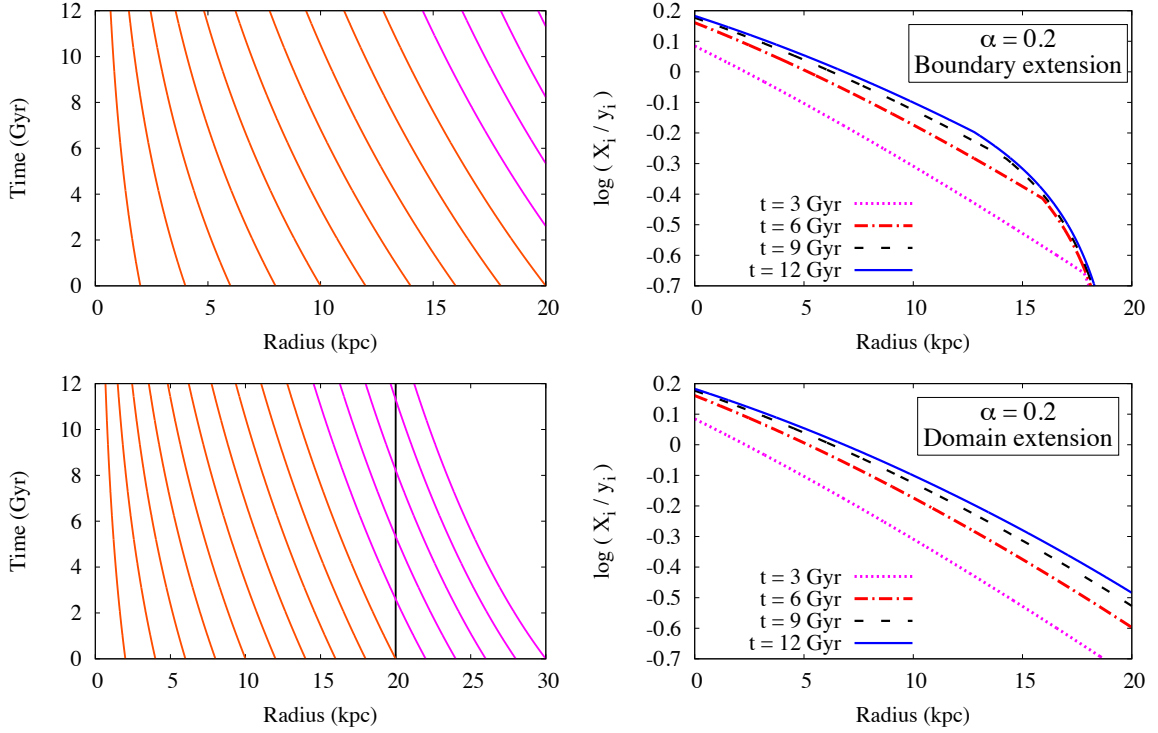


Figure 3.5: Similar to Fig. 3.4, but showing the two alternative strategies to extend the predicted abundance profiles to the whole computational domain, in the illustrative case $\alpha = 0.2$. *Upper panels:* The boundary-extension strategy, where the (t, R) plane is filled with additional characteristics starting from the maximum radius R_{\max} at different times; this is equivalent to the classical approach, with radial accretion of primordial material from the outer boundary, and predicts a sharp steepening of gradients at the disc periphery. *Lower panels:* The domain-extension strategy, where the additional characteristics start at the initial time $t = 0$, but from larger radii; the outer profiles in this case are the smooth continuation of the ones in Fig. 3.4. Note that the characteristics of the boundary extension strategy are the same of the domain-extension strategy, but cut along the vertical black solid line (lower-left panel).

A simple solution to this drawback is to fill the gap in the (t, R) plane with additional characteristics, as shown, for the illustrative case $\alpha = 0.2$, in the upper-left panel of Fig. 3.5. At variance with the lines already shown in Fig. 3.4, lower-left panel, all of which start at the same time $t = 0$ but from different radii, these additional lines all start from the same radius $R = R_{\max}$ but at different times. This method, which we refer to as the *boundary-extension* strategy, allows the full calculation of the metallicity evolution, provided that some value is chosen for the normalized abundance \tilde{X}_i at the starting point of the added lines, which coincides with the outermost considered radius R_{\max} . This strategy is the equivalent, within the characteristic framework, of the one adopted in classical finite-difference calculations, where some boundary condition needs to be stated for the metallicity of the material incoming from the chosen outer edge of the model.

The upper-right panel of Fig. 3.5 shows the predictions of the boundary-extension strategy, if accretion of primordial material is allowed to occur at $R = R_{\max}$. Profiles computed in this way show a sharp steepening in the outer regions. The illustrative example shown here is an extreme case, the effect being milder for a non-primordial composition of the IGM. For instance, if we assumed $\tilde{X}_{i,\text{IGM}} = 0.1$, all predicted abundances would be slightly higher and the profiles in the upper-right panel of Fig. 3.5 would tend, for $R \rightarrow R_{\max}$, to $\log(\tilde{X}_i) = -1.0$ instead of $\log(\tilde{X}_i) = -\infty$.

The solution discussed above is not the only possibility. The precise location and extent of the information gap in the (t, R) plane clearly depends on the choice of the initial radius for the outermost characteristic R_{\max} . Since this is in general largely arbitrary, it is useful to look at the results for different choice of R_{\max} . In particular, a suitably large value of R_{\max} should in principle allow to fill any desired region of the (t, R) plane in a natural way. This is shown in the lower-left panel of Fig. 3.5, where characteristics start from radii as large as $R_{\max} = 30$ kpc and allow predictions out to $R = 20$ kpc at $t = 12$ Gyr, without the need of particular assumptions on boundary condition ⁵.

The abundance profiles predicted by this *domain-extension* strategy are reported in the lower right panel of Fig. 3.5. In this case, the predicted abundance profiles are a smooth continuation of the one in Fig. 3.4 (lower-right panel) and no steepening is predicted in the outer regions.

The difference between the predictions of the two methods, which may be thought of as the extremes of a continuum of intermediate possibilities, can be very clearly understood by looking at the corresponding characteristic line diagrams. Comparing the two left panels of Fig. 3.5, in fact, we see that the set of characteristics used in the boundary-extension method are the same of the domain-extension one, but cut along the line of constant radius $R = 20$ kpc. This has the consequence of ignoring the initial metallicity evolution, occurring along the cut portion of the lines, and therefore of underestimating the metallicity in the outer regions.

We cannot say that one method is definitely better than the other, since we do not know, in general, whether and how much radial accretion, in real galaxies,

⁵The reader may remember from Sec. 3.2.4 that our fiducial model without radial flows formally develops a wind outside 20 kpc. When radial flows are considered, however, the accretion profile remains positive out to large radii already for small values of α and can therefore be safely used in (3.13) and in (3.15).

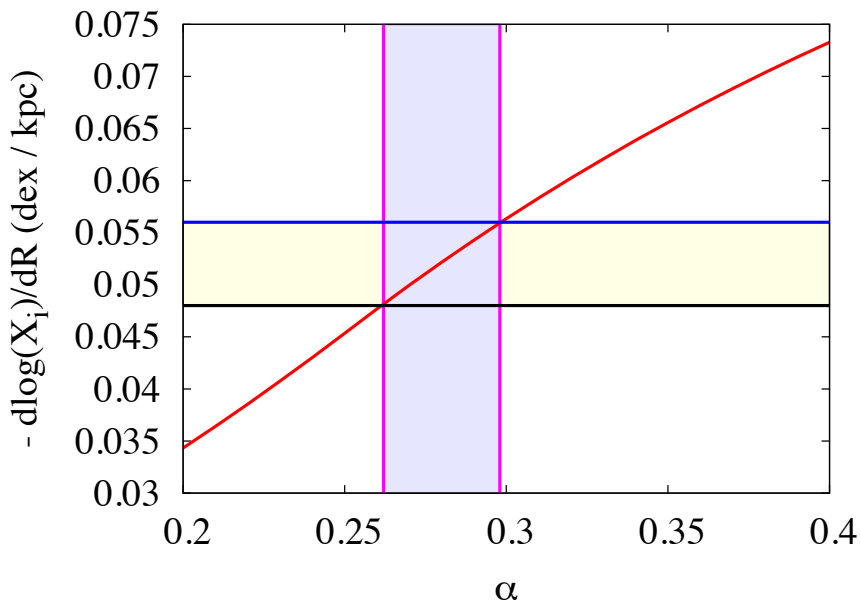


Figure 3.6: Abundance gradients, in the fiducial model, as a function of the angular momentum mismatch parameter α . Horizontal lines are Milky Way measurements for oxygen (upper line) and magnesium (lower line) in Cepheids (Luck & Lambert 2011). The predicted gradient (solid red line) is very sensitive to the rotational velocity of accreting gas; observations constrain it in a quite narrow range, of about $(72 \pm 2)\%$ of the rotational velocity of the disc.

directly occurs from an outer boundary. However, irrespectively of the adopted choice, it should be emphasized that the method of characteristics is the simplest way to clearly identify the region where predictions on abundance profiles, in a given galaxy evolution model, are dominated by effects associated with the choice of boundary conditions. This is potentially of great importance in the modelling of the outskirts of spiral galaxies, where theoretical predictions often disagree with each other and with observations.

3.4.5 Calibration from observed gradients

For a quantitative comparison with observations, we consider the domain extension technique, so that predictions do not depend on the choice of R_{\max} , provided that it is large enough. In our application, we never found an extension to be necessary farther out than 40 kpc.

In Fig. 3.6 the predictions are shown (solid red curve) of our fiducial model for the present-day abundance gradient, computed between 5 and 17 kpc, as a function of the angular momentum mismatch parameter α . We compare our predictions with the observed gradient, measured in the same radial range by Luck & Lambert (2011) for two representative α elements, oxygen and magnesium, in Cepheid stars in the Milky Way ⁶. Being very young stars, Cepheids are a fair tracer of ISM

⁶These values are also in agreement with the recent findings by Genovali et al. (2015), who unfortunately did not measure oxygen abundances, but report abundance gradients of various

abundances, while oxygen and magnesium are among those elements that are predominantly produced by Type II supernovae (SN) and therefore they are negligibly affected by time-delay effects, which are not included in our calculations. Besides observational uncertainties, the difference between the observed gradients for oxygen and magnesium may be partially due to a different dependence of the stellar yields on metallicity. Since our formalism does not take these details into account, our predictions can just be compared with the finite-width range defined by the two observed values. However, the predicted gradient is so sensitive to the angular momentum of accreting material that α is nonetheless constrained in a very narrow range, between 0.26 and 0.30. In the approximation of a flat rotation curve, (equation (3.22)), this means that metal-poor gas is accreted onto the Milky Way with an average rotational velocity equal to 70 – 74% the rotational velocity of the disc, in very good agreement with the estimate by Bilitewski & Schönrich (2012). Inverting (3.23), this would correspond to a coronal temperature $T_{\text{corona}} \sim 1.8/\delta \times 10^6$ K, where δ is defined as in (3.24) assuming a circular speed $V_{\text{disc}} = 220$ km/s and a mean molecular weight $\mu_{\text{m}} = 0.6$.

3.5 Inside-out models with radial flows

3.5.1 Structural constraints to inside-out growth

Radial flows are not the only possibility to explain abundance gradients in spiral galaxies, the main alternative being inside-out growth of discs (see references in Sec. 3.2.4).

As we have extensively discussed in the previous Chapters, the angular momentum build-up of galaxies, predicted by the theory of tidal torques (Peebles 1969; White 1984) is believed to be a major ingredient in determining the structure of galaxy discs (Fall & Efstathiou 1980; Mo, Mao & White 1998), which are generally expected to grow in size with time (e.g. Firmani & Avila-Reese 2009; Brooks et al. 2011), though the details depend on the particular accretion and merger histories of individual galaxies (Aumer, White & Naab 2014). On the other hand, the angular momentum assembly of spiral galaxies is also expected to drive radial flows within the disc, if the local aspects of angular momentum accretion are taken into account (Sec. 3.3.1). It is therefore likely that inside-out growth and radial flows, rather than being alternative, are both at work in real galaxies. However, the problem arises of how to break the degeneracies of a combined approach and to tell what contribution to the development of abundance gradients comes from inside-out growth and radial flows separately.

In close resemblance to what we have done in Sec. 3.2 for a simpler model, we propose to constrain the structural evolution (in this case, the inside-out growth) of a spiral galaxy by making use of its observed structural properties (e.g. the present-day distribution of gas, stars and star formation rate). As we have seen in Chapter 2, the radial profile of the star formation rate surface density (SFRD) is a particularly good tracer of inside-out growth. We can therefore use it to fix the relevant parameters

α -elements with a median value of -0.05 dex kpc^{-1} .

independently of chemical information and, in this way, we can fix the contribution of inside-out growth to the development of abundance gradients with no further freedom. In the following, we apply this idea to case of the Milky Way, while in Sec. 3.6 we discuss an application to the external galaxy NGC 628. For the case of the Milky Way, in order to facilitate the comparison with previous work on the subject, we will first adopt a formalism inspired by the classical semi-analytic models of inside-out growth (e.g. Matteucci & Francois 1989, Boissier & Prantzos 1999, Chiappini, Matteucci & Romano 2001), while in Sec. 3.5.4 we will consider a formalism more adherent to our own findings of Chapter 2.

Following the classical works mentioned above, we assume the effective accretion rate surface density to be an exponentially decreasing function of time, but with a timescale that is an increasing function of radius:

$$\dot{\Sigma}_{\text{eff}}(t, R) = \frac{\Sigma_{\infty}(R)}{t_{\text{acc}}(R)} \exp\left(-\frac{t}{t_{\text{acc}}(R)}\right) \quad (3.40)$$

where Σ_{∞} is the asymptotic total (baryonic) mass surface density of the disc and t_{acc} is the radially dependent accretion timescale. To parametrize Σ_{∞} , we require the total baryonic mass of the disc to have an exponential radial distribution at late times and therefore:

$$\Sigma_{\infty}(R) = \frac{M_{\infty}}{2\pi R_{\infty}^2} e^{-\frac{R}{R_{\infty}}} \quad (3.41)$$

while for the accretion timescale t_{acc} we choose, as customary, a linearly increasing function of radius:

$$t_{\text{acc}}(R) = t_{\text{acc},0} \left(1 + \frac{R}{R_{\text{acc}}}\right) \quad (3.42)$$

This model has 4 parameters ($M_{\infty}, R_{\infty}, t_{\text{acc},0}, R_{\text{acc}}$), which we constrain making a fit to observed properties of the Galactic disc today.

Our main observational constraint is the present-day SFRD profile of the Milky Way, as traced by the distribution of SN remnants (Case & Bhattacharya 1998). Since this is only given in dimensionless units, we scale it to the solar value, which we estimate applying the Kennicutt-Schmidt law (3.2) to a gas surface density of $10 \text{ M}_{\odot} \text{ pc}^{-2}$ (Binney & Merrifield 1998, note that we included a correction for helium). The SFRD profile derived in this way is also consistent with several other estimates of the SFRD in our Galaxy (e. g. Fraternali & Tomassetti 2012 and references therein)⁷. We also require that the mass surface density of stars at the solar radius ($R_{\odot} = 8.5 \text{ kpc}$), is $\Sigma_{\star}(R_{\odot}) = (37.1 \pm 1.2) \text{ M}_{\odot} \text{ pc}^{-2}$ (Read 2014) and that the stellar scalelength today is $R_{\star} = (2.5 \pm 0.25) \text{ kpc}$. This last constraint is chosen in such a way that the nominal 2σ interval coincides with the range of possible values $2 \div 3 \text{ kpc}$ quoted by Binney & Tremaine (2008).

For each set of parameters, equations (3.40) and (3.2) can be integrated in time, yielding the surface density of stars and gas (and thence of star formation rate) at each time and radius. Then, by the means of χ^2 minimization, we select the model that better matches the observational requirements. In Fig. 3.7 the comparison is

⁷Note, however, that the Case & Bhattacharya (1998) profile has been recently questioned by Green (2015), who propose a more centrally concentrated distribution.

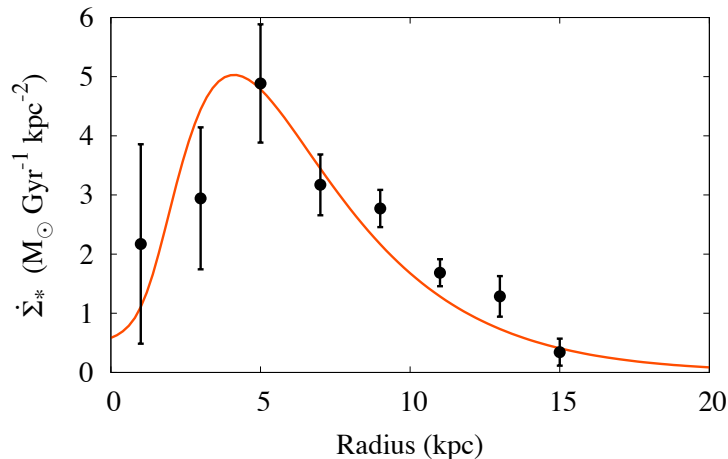


Figure 3.7: Calibration of the inside-out growth parameters on the observed SFRD profile. Points with error bars are measurements for the Milky Way based on the distribution of SN remnants (Case & Bhattacharya 1998). The solid line is our model. See text for further details.

shown between the model and observed SFRD profile at the present time. The model present-day stellar mass surface density at the solar radius is $\Sigma_*(R_\odot) = 36.0 M_\odot \text{ pc}^{-2}$, while the present-day stellar scalelength is $R_* = 2.9 \text{ kpc}$. The inferred infall timescale virtually vanishes at the origin (formally, $t_{\text{acc},0} = 22 \text{ Myr}$) and then linearly increases with radius with a slope of 1.1 Gyr/kpc .

Note that with the formalism adopted here the stellar disc is only approximately exponential at any given time. In Sec. 3.5.4 we will present a treatment where the stellar disc is strictly exponential at all times, built upon the theory presented in Chapter 2. Another alternative, adopted by Bilitewski & Schönrich (2012), is to assume that the disc of gas (rather than stars) is exponential at all times; in this case the SFRD is exponential as well (because of the Kennicutt-Schmidt law) and in particular there can never be a depletion of star formation at small radii.

3.5.2 Accretion and radial flows in an inside-out model

In Fig. 3.8, the mass flux decomposition, computed as described in Sec. 3.3.2, is reported as a function of the angular momentum mismatch parameters α (3.21), in a similar fashion to Fig. 3.3, but now for the inside-out growing model derived above.

The upper panel shows the predicted present-day accretion profiles for different values of α (assumed to be constant with radius). The first thing to be noticed is that accretion in this case always peaks at a finite galactocentric radius (at variance with the non inside-out case, where it always had its maximum at the origin, cfr. Fig. 3.3, upper panel). This is a distinctive feature of an inside-out growing model, which is also clearly reflected in the observed star formation rate surface density profile (Fig. 3.7). Furthermore, the radius where maximum accretion occurs is an increasing function of α . This is because, when some local angular momentum deficit is taken into account, accretion preferentially occurs at large radii, from which fresh

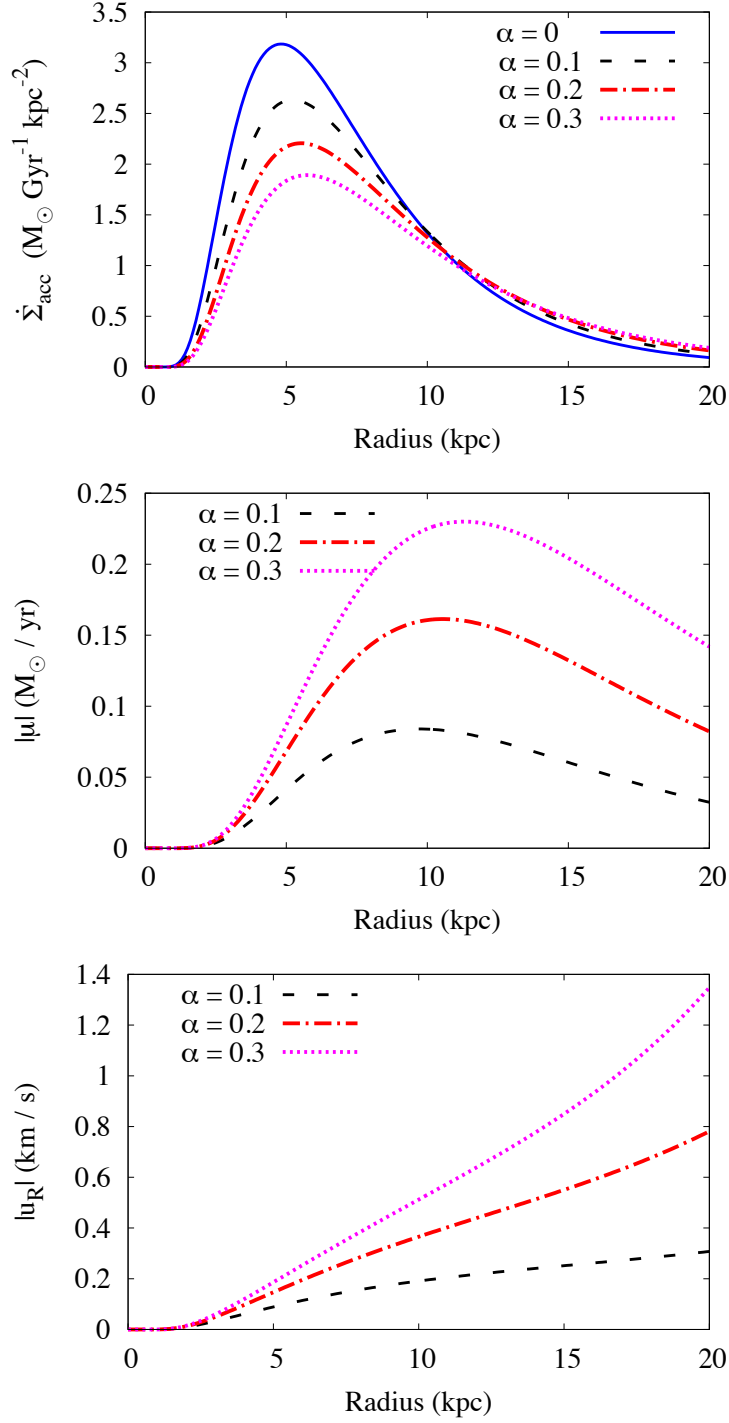


Figure 3.8: Similar to Fig. 3.3, but for an inside-out model of the Galaxy (Sec. 3.5.1). Note that a linear scale is adopted here for all the plots. The accretion profile has a marked peak at a finite radius, like the profile of star formation (Fig. 3.7). With increasing α , the peak of accretion moves outwards and progressively strong radial flows develop at large radii, bringing the gas, accreted in the outskirts with low angular momentum, towards the inner star formation peak.

gas is then brought inwards by radial flows.

The inwards radial mass flux ($-\mu$), consistently predicted by the mass-flux decomposition, is shown in the middle panel of Fig. 3.8. According to the general property pointed out in Sec. 3.3.4, the position of the peak of ($-\mu$) coincides with the radius outside which the predicted accretion is enhanced with respect to the effective one. The peak radius is larger now with respect to the non inside-out growing case: radial flows in this model bring inwards material that has been accreted, with relatively low angular momentum, at very large radii.

Finally, in the lower panel of Fig. 3.8 the predicted present-day patterns are reported for the inward radial velocity of gas, as a function of radius, for different values of α . Again, these show a non-trivial trend, which is also strongly varying with α and it is different from the one predicted in the non inside-out model (Fig. 3.3), especially in the inner and outer regions. This indicates that each particular structural evolution model requires its own mass flux decomposition, for radial flows to be compatible with angular momentum conservation; such a decomposition can always be easily achieved by means of the explicit formulae given in Sec. 3.3.2.

3.5.3 Abundance gradients in inside-out models with radial flows

We finally apply the methods described in Sec. 3.4 to compute the abundance gradients in an inside-out model in the presence of accretion-induced radial flows. We adopt the domain-extension strategy and we assume α to be constant with both space and time.

A technical digression is due here for completeness. Since our inside-out model has a formally vanishing gas density at the disc birth, then (3.11) formally implies infinite radial velocities at $t = 0$, which is obviously unphysical. Pitts & Tayler (1996) studied this problem with hydrodynamical simulations and concluded that, when very strong accretion occurs onto a disc with very low surface density, centrifugal equilibrium is rapidly, but not immediately, achieved, with the consequence that the physically motivated radial mass flux is smaller than the one predicted by (3.20). In our models, these conditions occur only at very early times and at very large radii and are thus expected to have a very limited impact (see also Chamcham & Tayler 1994). We performed several experiments, adopting different strategies to ensure a physically meaningful velocity field, and we verified that the results that we provide in the following are insensitive to the details of the adopted scheme.

As in Sec. 3.4.5, we compare the model predictions with the observed present-day α -element abundance gradient in Cepheid stars. Fig. 3.9, which is the analogue of Fig. 3.6, reports this comparison for the inside-out case. With respect to the previous model, the model with inside-out growth predicts a steeper gradient for any given value of α . This is because inside-out growth itself has the well known effect of steepening abundance gradients. As a consequence, the range for the parameter α inferred from observations is shifted towards lower, but still non vanishing, values for the angular momentum mismatch parameter. The derived interval is $0.19 \leq \alpha \leq 0.26$, corresponding, in the approximation of a flat-rotation curve for the disc, to cold gas accreting on the disc of the Galaxy with 74 – 81% of the rotational velocity

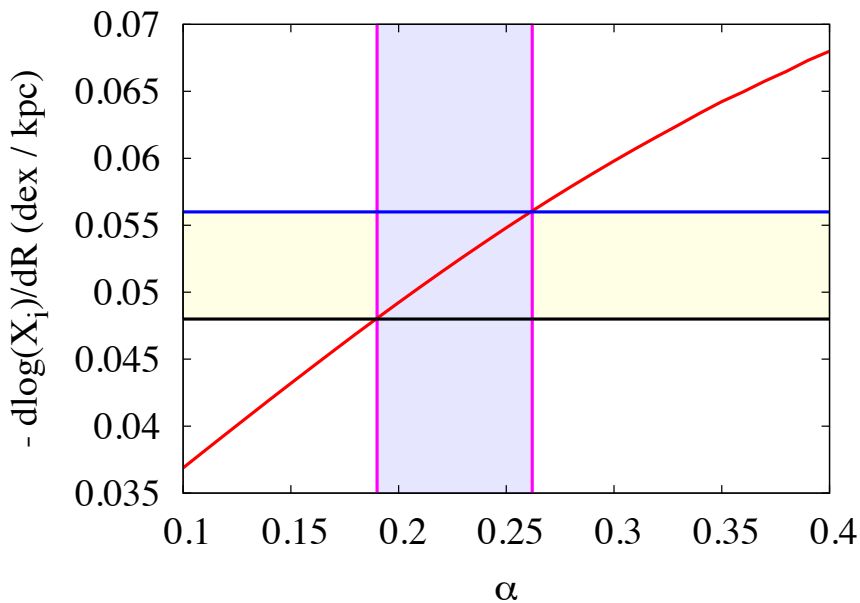


Figure 3.9: Similar to Fig. 3.6, but for an inside-out model of the Galaxy (Sec. 3.5.1). Slightly lower values of α are needed in this case to explain the observed abundance gradients, corresponding to accreting material rotating with as much as 81% of the rotational velocity of the disc.

of the disc. Also this finding is in very good agreement with Bilitewski & Schönrich (2012), despite their very different approach to inside-out growth.

3.5.4 The effect of the inside-out growth parametrization

We consider here how the results of the previous Section are affected by the details of the parametrization of the inside-out growth and of the SFRD profile. To this purpose, we adopt here the novel approach that we have introduced in Chapter 2. Furthermore, we replace the SFRD profile by Case & Bhattacharya (1998) with a more recent determination, based on the revision of the distribution of Galactic supernova remnants, proposed very recently by Green (2015). His new data and updated analysis indicate that the inner shape of the SFRD profile of the Milky Way is very well described by a linear radial increase, followed by an exponential decline. This is in excellent agreement with the expectation for an exponential disc with a time-increasing scalelength (cfr. equation (2.5) in Chapter 2). The central value of the SFRD is not easy to determine with precision, because the central region of the Milky Way can only be observed in projection, together with material lying at all galactocentric distances between $R = 0$ and $R = R_{\odot}$. As shown by Green (priv. comm.), the observed longitudinal distribution is compatible with a range of possibilities, which, in terms of our parametrization (2.5), correspond to with ν_R/ν_M being comprised between 0.35 and 0.5. For our simple application here, we adopt the value 0.43, in the middle of the allowed range. With this choice, the distribution of SNR is reproduced by our theoretical SFRD profile (2.5) if $R_{\star} = 2.43$ kpc, which is in turn in the middle of the allowed range for the scalelength

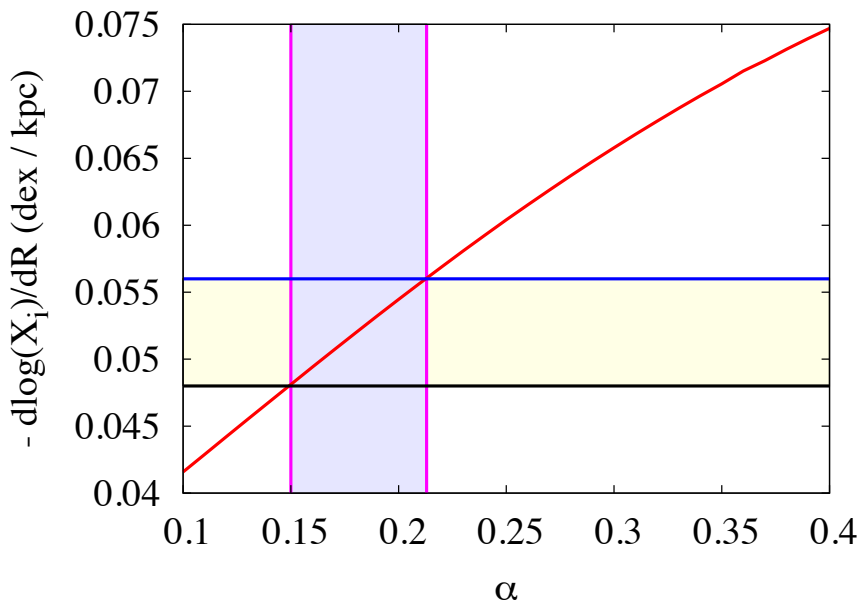


Figure 3.10: Similar to Fig. 3.9, but adopting the revised SFRD profile of Green (2015) and the parametrization of inside-out described in Chapter 2. The allowed values of α are slightly smaller in this case than in the model of Sec. 3.5.3.

of the Milky Way. Adopting the same stellar mass and global star formation rate of Sec. 3.2.1, the specific mass and radial growth rates are $\nu_M = 5 \times 10^{-2} \text{ Gyr}^{-1}$, $\nu_R = 2.15 \times 10^{-2} \text{ Gyr}^{-1}$, respectively, which are similar to the values measured in external galaxies (cfr. Table 2.2).

To compute a chemical evolution model, we adopt here the same star formation history of the fiducial model (see Sec. 3.2.1), while to describe the radial growth we assume that the ratio between ν_M and ν_R is constant and equal to the present-day value. In Fig. 3.10, predicted gradients are given for this model as a function of the angular momentum mismatch parameter. The allowed values of α are in this case $0.15 < \alpha < 0.21$, slightly smaller than those found in Sec. 3.5.3 and corresponding to a rotational velocity of the accreting material between 79 – 85% of the rotational velocity of the disc. We can therefore conclude that even significant changes in the adopted SFRD profile and in the parametrization of the inside-out growth have a limited impact on the inferred angular momentum of the material accreting on the disc the Milky Way.

3.6 Application to NGC 628

As we have shown in Chapter 2, the external perspective that we have of nearby spiral galaxies allows us to have a much cleaner view of their global structure, compared to our own Milky Way (see also Sec. 3.5.4). This allows a much easier determination of the parameters of inside-out growth. On the other hand, gas-phase abundance gradients of external galaxies are more difficult to determine with accuracy. In fact, as we have discussed in Sec. 1.1.1, direct measurements are possible

only in few cases, while indirect measurements can be subject to calibration issues.

For an illustrative application of our methods, we consider here the case of NGC628 (M74), for which we have measured the inside-out growth parameters in Chapter 2 (cfr. Fig. 2.2 and Table 2.2), while direct measurements of gas-phase abundances have been published for this galaxy by Berg et al. 2015 in the context of the CHAOS project.

For the present application, we adopt the distance $D = 7.2$ Mpc determined by Dyk, Li & Filippenko (2006). According to Sec. 2.4.4, this implies a revision of the mass to $M_\star = 2 \times 10^{10} M_\odot$ and of the scalelength $R_\star = 2.4$ kpc, while the specific mass and radial growth rate remain unaffected and equal to $\nu_M = 8.22 \times 10^{-2} \text{ Gyr}^{-1}$, $\nu_R = 2.87 \times 10^{-2} \text{ Gyr}^{-1}$, respectively (Table 2.2). Following the same treatment described in Sec. 3.2.1, we adopt an exponentially declining SFH. This turns out to be virtually constant with time: the formally derived timescale is $t_\star = 440$ Gyr, as derived from (3.8), assuming an age $t_0 = 12$ Gyr and requiring the right hand-side to be equal to $t_0 \nu_M = 0.9864$, as implied by (3.4) and the definition of ν_M (2.3). Finally, as we did in Sec. 3.5.4 for the Milky Way, we parametrize the growth of the stellat scalelength with time by assuming that the ratio ν_M/ν_R is constant and equal to the measured value.

In Fig. 3.11, we show, for this model, the predicted present-day abundance profiles for different values of the angular momentum mismatch parameter α , overlaid on the empirical determinations by Berg et al. (2015). The vertical scale of theoretical profiles is set for an oxygen yield $y = 0.005$. Datapoints have a large scatter at any given radius, which, as suggested Berg et al. (2015), may be due to residual uncertainties in the determination of electron temperatures. Despite this limitation, we can recognize a slight preference for models with a positive value of α , tentatively indicating that gas can be accreting on this galaxy with a local rotational velocity as low as 60% of the one of the disc.

3.7 Summary

The gas accreting onto the discs of spiral galaxies is likely to rotate, on average, at a lower speed with respect to the disc itself. This is especially true if the accretion comes from a hot reservoir, which must rotate more slowly than the disc, because of its partial pressure support against gravity. We will discuss this effect in much more detail in Chapter 4 (see also Appendix 3.A below). A similar effect is also likely for cold-mode accretion, based on geometrical grounds (see for instance Appendix 3.B below). The local angular momentum mismatch in accretion drives inward radial flows within the disc, due to angular momentum conservation, with at least two important consequences on structural and chemical evolution models. First, the accretion profile, as indirectly inferred from the observed structure of discs, is severely altered, in the sense of an enhancement of the required accretion in the outer regions and a corresponding depletion in the inner ones. Second, the spatial distribution of heavy elements is profoundly affected, in the sense of the creation or a strong steepening of abundance gradients. Abundances are observable and can be used to shed light on accretion and radial flows, which are still not (see Sec. 3.1). In this Chapter, we addressed the computation of accretion profiles, radial flows

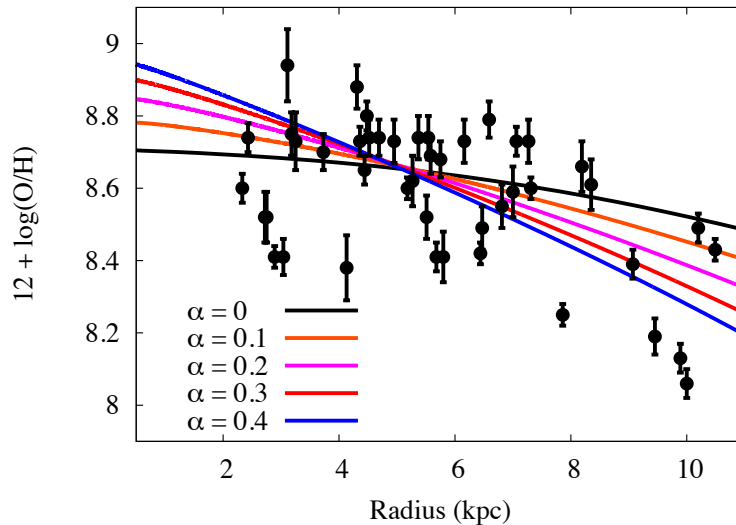


Figure 3.11: Comparison of predicted and the observed radial profiles of the abundance of α -elements in the ISM of NGC 628. Inside-out growth parameters have been fixed to those required to reproduce the SFRD profile of this galaxy (cfr. Fig. 2.2). Different lines are for some different values of the angular momentum mismatch parameter α ; data-points are direct measurements of oxygen gas-phase abundances by Berg et al. (2015). Observations suggest a preference for $\alpha > 0$ and therefore some angular momentum deficit in accretion, though the large scatter of datapoints at fixed radius does not allow firm conclusions to be drawn.

and abundance gradients, as a function of the angular momentum of the accreting material, from an analytic point of view.

The advantages of an analytic treatment come at the cost of simplifying assumptions. In particular, we assumed metallicity-independent yields and the instantaneous recycling approximation; we also did not address stellar radial migration and mechanisms of radial mixing other than those due to angular momentum conservation. These simplifications limit the predictive power of our chemical analysis to the abundance profile of α -elements in the interstellar medium. However, this observable is so remarkably sensitive to the angular momentum of the infalling material that it is very useful to extract the associated information by means of a simple and easily controllable machinery.

Our work and findings can be summarized as follows.

1. We considered the simplest possible model for the evolution of a galaxy disc – namely an exponential disc, with constant scalelength, obeying the Kennicutt-Schmidt law – and we have shown that, as long as radial gas flows are neglected, it is incompatible with the observed abundance gradients of spiral galaxies.
2. We provided the general exact solution to the problem of decomposing the gas flows, needed to sustain galaxy evolution, into direct accretion from the IGM and radial flows within the disc (equations (3.25) to (3.28)), which can be applied to any axisymmetric, non-viscous model for the structural evolution of a disc and to any angular momentum distribution of the accreting material;

we emphasize that with this approach both the accretion profile and the radial velocity pattern are model predictions, rather than model assumptions.

3. We proposed a novel method, based on characteristic lines, to solve the equation of metallicity evolution in the presence of radial flows, which makes the computation of gas-phase α -element abundance profiles very easy and allows the influence of boundary conditions on the steepness of outer gradients to be traced straightforwardly.
4. We suggested a strategy to disentangle the contributions of inside-out growth and radial flows in determining the steepness of abundance gradients: inside-out growth parameters can be fixed to those required to reproduce non-chemical observables and in particular the shape of the SFRD profile, which is particularly sensitive to the structural evolution of the disc; the contribution of inside-out growth to abundance gradients is thus fixed and residual discrepancies with observations, if present, can then be used to constrain the needed amount of radial flows.

Given their simplicity and generality, these methods can be readily applied to any future model of the evolution of our Galaxy or of external spiral galaxies, provided that radial flows are dominated by angular momentum conservation.

Simple illustrative models, calibrated on the Milky Way, require, to match observations, a rotational velocity for the accreting material comprised between 70% and 85% of the rotational velocity of the disc, in very good agreement with previous estimates. Once this effect is taken into account, a picture emerges in which a significant part of the accretion of cold gas occurs in the outskirts of the disc and it is then brought inwards by radial flows, towards the inner regions where it is required to sustain star formation.

We have also presented an application to the nearby external spiral galaxy NGC 628, taking advantage of our own measurement of the inside-out growth parameters of this galaxy, as derived in Chapter 2. The results are compatible with those that we have found for the Milky Way, though with a larger uncertainty, mainly due to issues in the observational determination of gas-phase abundances.

APPENDICES

3.A Angular momentum and radial flows in fountain-driven accretion

We briefly sketch here the basic ingredients for the study of accretion-induced radial flows in the context of the theory of fountain-driven accretion (Marinacci et al. 2010a; Marinacci et al. 2011; Marasco, Fraternali & Binney 2012).

In this scenario, clouds of cold gas are ejected out of the plane of the disc as a consequence of star formation feedback and then fall back onto the disc, attracted by its gravity (the mechanism of *galactic fountain*, e.g. Melioli et al. 2008). During their orbit, fountain clouds necessarily interact with the corona. The velocity difference

between the two media drive the onset of the Kelvin-Helmholtz instability and the creation of a turbulent wake, where mixing between cold fountain gas and hot coronal gas occurs. The resulting mixture has an intermediate temperature and metallicity between the disc and the corona and, because of the dependence of the cooling function from these quantities, this implies a reduction of the cooling time of coronal gas, which is therefore able to cool and accrete onto the disc.

Fig. 3.12 is a diagram of the involved phases and processes. Three regions are considered: the disc, the (upper) corona and an intermediate layer, where the interaction between the two occurs, the thickness of which is set by the vertical extent of the galactic fountain. In the intermediate layer, we distinguish two spatially mixed phases: a cold clumpy phase, constituted of fountain clouds together with coronal material condensing on them (this phase is observed in HI as extraplanar gas), and a hot diffuse phase, which is the lower part of the corona, in direct contact and interaction with the cold clouds. Thin black arrows indicate mass exchanges between different phases; to each of them a (not shown) advective angular momentum exchange is also associated, equal to the mass flux multiplied by the specific angular momentum of the upstream region: for instance, the net angular momentum gain of the disc is $\dot{L}_{\text{disc}} = (\dot{M}_{\text{out}} + \dot{M}_{\text{acc}})l_{\text{cold}} - \dot{M}_{\text{out}}l_{\text{disc}}$. In addition, there is a non advective angular momentum exchange, marked with a thick magenta arrow, between the cold and the hot phase in the intermediate layer: this is predicted by the Marinacci et al. (2011) theory and its outcome is to set an equilibrium angular momentum difference between the cold and the hot phase:

$$l_{\text{cold}} - l_{\text{hot}} = (\Delta l)_{\text{eq}} \quad (3.43)$$

which allows the condensation of coronal gas on fountain clouds to become effective. Here $(\Delta l)_{\text{eq}} = R(\Delta V)_{\text{eq}}$, where R is the galactocentric radius of the considered region and $(\Delta V)_{\text{eq}} \simeq 75$ km/s is the equilibrium velocity lag predicted by the theory. The mass flux from the upper corona to the lower corona is the one required to balance mass loss suffered by the hot phase as a consequence of fountain-driven accretion (in practice, it is driven by the imbalance between pressure and gravity due to the disappearance of part of the underlying hot material). According to Fraternali & Binney (2008), the angular momentum exchange between the cold and the hot phase is very efficient and it brings the system towards an approximate equilibrium in few dynamical times. During this time, we may assume that the fountain ejection rate \dot{M}_{out} does not change very much, nor the mass reservoir of the upper corona will be significantly eroded and therefore an approximately stationary state is a reasonable assumption on such timescales. Angular momentum balance for the hot and cold phases therefore give:

$$\begin{cases} \dot{M}_{\text{acc}}l_{\text{corona}} + \dot{L}_{\text{int}} = \dot{M}_{\text{acc}}l_{\text{hot}} \\ \dot{M}_{\text{out}}l_{\text{disc}} + \dot{M}_{\text{acc}}l_{\text{hot}} = \dot{L}_{\text{int}} + (\dot{M}_{\text{out}} + \dot{M}_{\text{acc}})l_{\text{cold}} \end{cases} \quad (3.44)$$

which, together with (3.43), can be solved for $l_{\text{cold}}, l_{\text{hot}}, \dot{L}_{\text{int}}$. In particular, we find:

$$l_{\text{cold}} = \frac{\dot{M}_{\text{out}}l_{\text{disc}} + \dot{M}_{\text{acc}}l_{\text{corona}}}{\dot{M}_{\text{out}} + \dot{M}_{\text{acc}}} \quad (3.45)$$

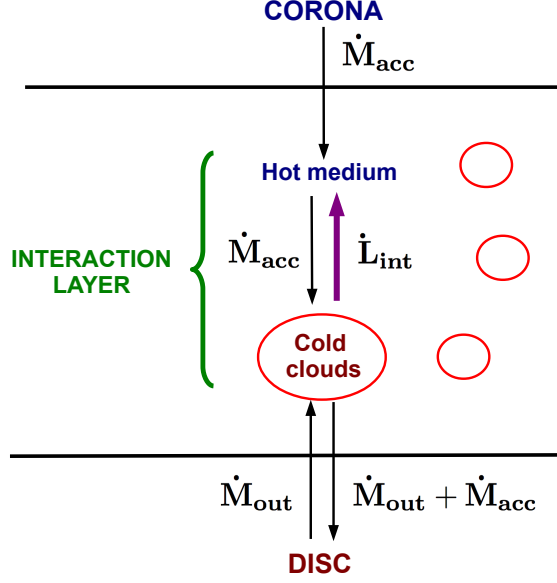


Figure 3.12: Schematic diagram of the accretion of coronal material onto the disc, according to the theory of Marinacci et al. (2011). After an initial transfer of angular momentum, the interaction with cold fountain clouds triggers the condensation of a part of the hot medium.

Note that the angular momentum of the cold accreting gas does not depend on the equilibrium lag $(\Delta l)_{\text{eq}}$, which, however, sets the rotation velocity of the lower corona and the magnitude of non-advective angular momentum exchanges within the interacting layer.

In the approximation of a flat rotation curve (3.22), the angular momentum mismatch parameter reads:

$$\alpha_{\text{cold}} := 1 - \frac{l_{\text{cold}}}{l_{\text{disc}}} = \frac{\eta}{1 + \eta} \alpha_{\text{corona}} \quad (3.46)$$

with obvious meaning of α_{corona} , while

$$\eta := \dot{M}_{\text{acc}} / \dot{M}_{\text{out}} \quad (3.47)$$

depends on the condensation efficiency and on the orbital time of the fountain clouds. Note that η can vary with position within the disc. More in general, all the discussion above is radial dependent and all masses and angular momenta should be accordingly translated into the corresponding surface densities.

According to (3.20), the radial mass flux is therefore given by:

$$\mu = -2\pi R^2 \alpha_{\text{cold}} (\dot{\Sigma}_{\text{out}} + \dot{\Sigma}_{\text{acc}}) \quad (3.48)$$

which, considering (3.46) and (3.47), can also be written:

$$\mu = -2\pi R^2 \alpha_{\text{corona}} \dot{\Sigma}_{\text{acc}} \quad (3.49)$$

Therefore, despite the fact that cold material accretes onto the disc with a specific angular momentum that can be very different from the one of the upper corona (equation (3.46)), the induced radial flows within the disc are nonetheless the same that one would have if the coronal material was accreting onto the disc directly (equation (3.49)), with the galactic fountain basically acting as a catalyst for accretion.

This conclusion is just a first approximation, the validity of which is limited by our numerous simplifying assumptions. Among them, we underline that our basic diagram (Fig. 3.12) can be read locally (as we did) only provided that the orbital radial excursion of each fountain is small compared with its starting radius. While this is nearly correct for moderate ejection velocities (Fraternali & Binney 2006; Spitoni, Recchi & Matteucci 2008), it will not be true in detail (Marasco, Fraternali & Binney 2012) and it will fail for a very powerful fountain, so that some level of distortion to (3.49) is indeed expected in general, the magnitude of which requires a dedicated study. The key prediction remains, however, that the main regulator for the radial flows in the disc has to be looked for in the angular momentum distribution of the upper corona, which is the ultimate source of mass and angular momentum in the model, but of which we still have a rather scant knowledge. To deepen our understanding of this important topic will be the main aim of Chapter 4 of this Thesis.

3.B Angular momentum accretion on a disc from random orbits

We consider here an extremely idealized description of angular momentum and accretion in a *cold mode* scenario. While a realistic description would be much more complex than, the treatment below can be useful to gain some insight on the basic geometrical ingredients that are relevant to this problem.

Let us consider a disc on which particles are accreting, coming from infinity from all possible directions, but globally carrying a net angular momentum in the ‘vertical’ direction orthogonal to the disc. We want to study how this angular momentum is deposited on the disc at different radii. In particular, we ask how does the average specific vertical angular momentum of particles, impacting the disc at some radius, compare with the value appropriate for centrifugal balance there ⁸.

We make the very crude approximation of keeping, for the gravitational field, the monopole term only and we approximate particle trajectories with parabolic orbits in a Keplerian potential. These can be written as:

$$R = \frac{l^2}{GM(1 + \cos(\theta - \psi))} \quad (3.50)$$

where (R, θ) are polar coordinates in the plane of the orbit, centered on the focus, where the attracting mass M lies, l is the modulus of the angular momentum vector

⁸We will omit the attribute ‘specific’ from now on, for brevity. Note that the proper angular momentum of particles can be replaced by the specific one in all the averages, provided that the particles share the same mass.

and G is the gravitational constant. Without loss of generality, we can assume θ to increase with time in $]\psi - \pi, \psi + \pi[$ ⁹. The orientation parameter $\psi \in [-\pi, \pi[$ sets the location of the vertex with respect to a reference direction where $\theta = 0$.

To identify an orbital plane, we can use the couple (u, χ) with $\chi \in [0, \pi[$ giving the direction of the line of nodes, while $u \in [-1, 1]$ is defined by:

$$u := \frac{l_z}{l} \quad (3.51)$$

where l_z is the vertical component of the angular momentum. Note that $|u|$ is equal to the cosine of the inclination of the orbital plane with respect to the disc and that changing the sign of u is equivalent to changing the direction of motion of a particle within an orbit. Also note that there is a one-to-one relation between the angular momentum vector and the set (l, u, χ) . For each angular momentum vector, we define a polar coordinate system in the orbital plane as described above, fixing, as the reference direction $\theta = 0$, an arbitrary orientation of the line of nodes. Then the generic orbit is fully specified by the 4 parameters (l, u, χ, ψ) . Of these, l sets the scale of the orbit, while the 3 coordinates (u, χ, ψ) together determine the radiant position and the initial projected motion of a particle.

The distribution f of the infalling particles is conveniently given as a function of (l, u, χ, ψ) . We assume that it can be written as:

$$f(l, u, \chi, \psi) = \frac{f_0(l)f_1(u)}{2\pi^2} \quad (3.52)$$

where f_0 is some normalized function ($\int_0^{+\infty} f_0(l)dl = 1$), while:

$$f_1(u) = \begin{cases} 0 & \text{if } -1 < u < 0 \\ 1 & \text{if } 0 < u < 1 \end{cases} \quad (3.53)$$

This choice for f is the appropriate one for particles that arrive at random from all possible radiants with all possible directions, while carrying a positive vertical angular momentum. In other words, for any given angular momentum l , we give equal weight to all possible orbits, but allow them to be followed in one sense only. Of course, other choices for f are possible, if one wants to allow for anisotropic accretion or for some particles having $l_z < 0$. We discuss anisotropic accretion in the end. On the other hand, counter-rotating accretion is hardly avoided in realistic situations and, if accounted for, it would even reinforce our final result, as it can be easily verified.

We now consider how does a particle distribution look like from the point of view of the disc. From (3.50), individual particles impact the disc at a radius:

$$R = \begin{cases} \frac{l^2}{GM(1 + \cos(\pi + \psi))} & \text{if } -\pi < \psi < 0 \\ \frac{l^2}{GM(1 + \cos \psi)} & \text{if } 0 < \psi < \pi \end{cases} \quad (3.54)$$

⁹In other words: we look at the orbital plane from the semispace containing the angular momentum vector and we adopt an angular coordinate increasing counterclockwise as usual.

so that specular orbits, with orientation parameters ψ differing by π , meet the disc in specular positions and thus at the same radius R . Taking this duplication into account, we equivalently choose one or the other of equations (3.54) to define, in the particle parameter space, a coordinate change $(l, u, \chi, \psi) \rightarrow (l, u, \chi, R)$ which then induces the density transformation:

$$f \rightarrow f' = 2 \frac{\partial \psi}{\partial R} f$$

The transformed density f' is the distribution of particles having the angular momentum vector associated to (l, u, χ) and impacting the disc at the radius R . With our position (3.52), it reads:

$$f'(l, u, \chi, R) = \frac{f_0(l)f_1(u)}{\pi^2 R} \sqrt{\frac{l^2}{GMR}} \left(2 - \frac{l^2}{GMR}\right)^{-\frac{1}{2}}$$

if $l^2 < 2GMR$ and vanishes otherwise. Averaging over (l, u, χ) and using (3.51) and (3.53), we can finally compute the average vertical angular momentum of particles joining the disc at radius R :

$$\frac{\langle l_z \rangle (R)}{l_{\text{circ}}(R)} = \frac{\int_0^2 f_0(\sqrt{GMRx}) \sqrt{\frac{x}{2-x}} dx}{2 \int_0^2 \frac{f_0(\sqrt{GMRx})}{\sqrt{2-x}} dx} \quad (3.55)$$

where in the integrals I made the variable change $x = l^2/GMR$ and $l_{\text{circ}}(R) = \sqrt{GMR}$ is the angular momentum of a particle on a circular orbit at radius R .

The ratio (3.55) depends on the angular momentum distribution f_0 . To provide an application, we again consider here the simplest possible situation, in which f_0 is uniform as well, up to some maximum angular momentum l_{max} , that is:

$$f_0(l) = \frac{1}{l_{\text{max}}}$$

for $0 < l < l_{\text{max}}$ and vanishing elsewhere. Then (3.55) greatly simplifies, at least for small enough radii $R < R_{\text{max}} = l_{\text{max}}^2/2GM$:

$$\frac{\langle l_z \rangle (R)}{l_{\text{circ}}(R)} = \frac{\int_0^2 \sqrt{\frac{x}{2-x}} dx}{2 \int_0^2 \frac{1}{\sqrt{2-x}} dx} = \frac{\pi}{4\sqrt{2}} < 1$$

The ratio for $R > R_{\text{max}}$ is even lower than this (we do not report the details here, for the sake of brevity).

As a minimal robustness test, we can also consider another simple angular momentum distribution:

$$f_0(l) = \frac{2l}{l_{\text{max}}^2}$$

for $0 < l < l_{\text{max}}$ and vanishing otherwise. The choice of a distribution biased towards high angular momenta is made to go in the direction that might be expected

according to the theory of inside-out growth of galaxy discs. The result in this case, again for small enough radii, is:

$$\frac{\langle l_z \rangle}{l_{\text{circ}}} = \frac{\int_0^2 \frac{x}{\sqrt{2-x}} dx}{2 \int_0^2 \sqrt{\frac{x}{2-x}} dx} = \frac{4\sqrt{2}}{3\pi}$$

which is again less than unity.

Finally, as an extreme case, we can consider the result for a simple anisotropic distribution, which is also biased towards low orbit inclinations and high values of l_z , obtained replacing (3.53) with:

$$f_1(u) = \begin{cases} 0 & \text{if } -1 < u < 0 \\ 2u & \text{if } 0 < u < 1 \end{cases}$$

With this choice, the ratio $\langle l_z \rangle / l_{\text{circ}}$ further increases by a factor 4/3, still not enough to make it greater than unity.

It is probably not worth to insist too much on the details of the angular momentum distribution, since there are more relevant reasons why the presented model cannot be directly applied to galaxies (most obviously, the choice of the potential). However, the elementary calculations above suggest that, at least in simple situations, material accreting on to a disc from independent orbits locally rotates, on average, slower than what needed for centrifugal balance, with the consequence that inward radial motions will be necessary, after accretion, if equilibrium is to be reached. This situation, which is a natural outcome of hot mode accretion (see Chapter 4), might then be appropriate to the cold scenario as well, with accreting particles finding their way towards the disc without interacting with each other.

3.C The effect of the IGM metallicity

We briefly consider here what is the impact, on predicted abundance profiles, of assuming a non-vanishing metallicity of the IGM. This is easily included by replacing (3.14) with:

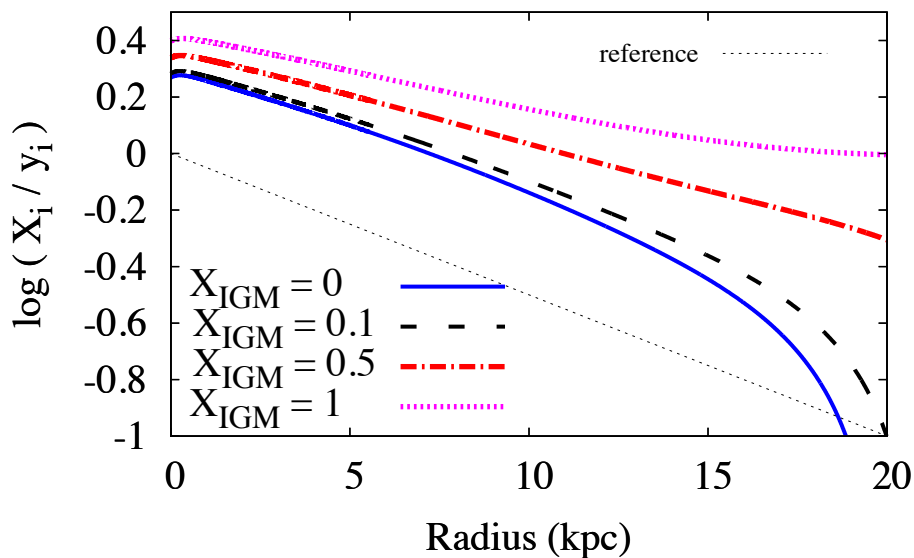
$$\tilde{X}_i(t, R) = e^{-\sigma(t, R)} \int_0^t e^{\sigma(t', R)} \left(\frac{\dot{\Sigma}_\star}{\Sigma_g}(t', R) - \tilde{X}_{\text{IGM}}(t') \frac{\dot{\Sigma}_{\text{acc}}}{\Sigma_g}(t', R) \right) dt' \quad (3.56)$$

In Fig. 3.13 the resulting predictions are reported for the inside-out model for the Milky Way described in Sec. 3.5.4, with $\alpha = 0.2$. The normalized IGM metallicity \tilde{X}_{IGM} is assumed to linearly increase with time, up to a maximum value between 0 (primordial composition) and 1 (pre-enrichment equal to the integrated yield). The upper panel and lower panel are for models computed with the domain extension strategy and the boundary extension strategy, respectively (Sec. 3.4.4).¹⁰

A non vanishing metallicity of the IGM has the obvious effect of increasing the general level of chemical enrichment in the ISM, but it also has some impact on the

¹⁰Note that assuming \tilde{X}_{IGM} to be different from zero already at $t = 0$ would induce a discontinuity in the profiles computed with the boundary extension strategy. This would be both unphysical and in disagreement with observations.

Boundary extension



Domain extension

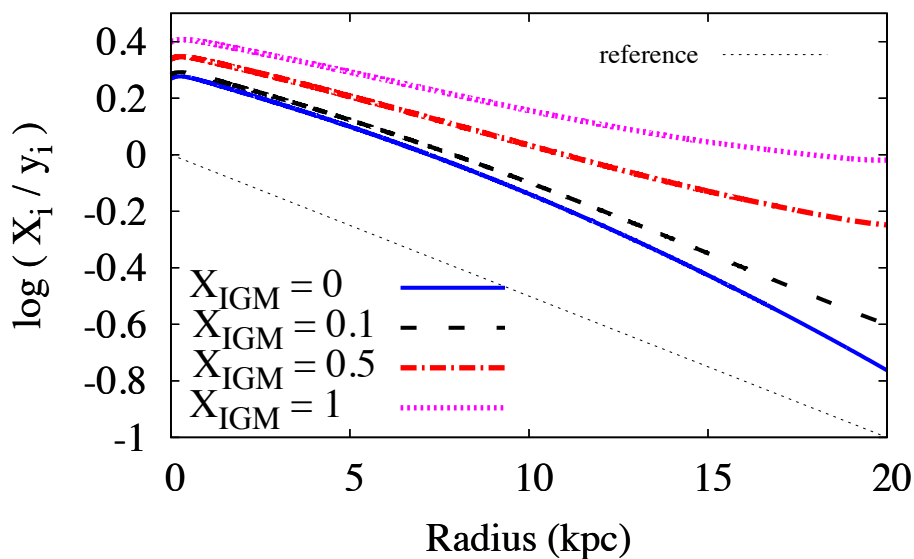


Figure 3.13: Dependence of abundance profiles on boundary conditions, for an inside-out model of the Milky Way with $\alpha = 0.2$ (see Sec. 3.5.4). Predictions are given obtained with the domain extension strategy (*upper panel*) and the boundary extension strategy (*lower panel*). Different lines are for different metallicities of the IGM (normalized to the yield). The ‘reference’ straight line, put to guide the eye, has a slope of -0.05 dex/kpc, equal to the median abundance gradient of α -elements in Milky Way Cepheid stars, mostly at galactocentric distances between 5 and 15 kpc (Genovali et al. 2015).

shape of metallicity distributions. With the domain extension strategy, abundance profiles always gently decline with radius, with the tendency to become shallower with increasing X_{IGM} . In contrast, models computed with the boundary extension strategy show a wider variety of behaviours, ranging from a very strong steepening (for primordial IGM composition) to an outer flattening (for high enough IGM metallicity).

Note that the enrichment of the accreting gas can be partially due to mixing of the IGM with metals produced in the disc itself and then ejected in the halo by AGN or supernova feedback.

Chapter 4

Angular momentum and entropy in models of rotating coronae[†]

Abstract

In the last part of this Thesis, we attempt a modeling of the likely source of both the mass and the angular momentum of galaxy discs, which, for massive galaxies like the Milky Way, should be an extended corona of gas with a large (nearly virial) temperature. Theory (cfr. Chapter 1) provides predictions for the angular momentum distribution of these structures, while comparison with observations requires the knowledge of their density distributions and rotation curves. In this Chapter, we address for the first time the problem of reconstructing the structure and the rotation of a hot gas, in equilibrium in a given gravitational potential, from the knowledge of its angular momentum distribution. We first consider the idealized case of an isothermal gas in a logarithmic potential, for which we derive the general solution as well as physically interesting special cases. We find that, already in this very crude approximation, a cosmologically motivated angular momentum distribution, scaled to parameters plausible for the Milky Way, produces models compatible with a scenario in which the accretion of coronal material can sustain both the inside-out growth of the disc (cfr. Chapter 2) and the radial gas flows required to explain the observed abundance gradients (cfr. Chapter 3). We then consider the more general case of baroclinic equilibria in a generic axisymmetric potential. We describe a novel parametrization for baroclinic equilibria as well as a new class of self-similar solutions. We show that baroclinic equilibria can be reconstructed from the knowledge of the joint angular momentum/entropy distribution, provided that suitable boundary conditions are known either on the vertical axis or on the equatorial plane.

4.1 Introduction

According to the standard theory of galaxy formation (Rees & Ostriker 1977; White & Rees 1978), massive galaxies should be surrounded by large and massive haloes

[†]A significant part of this work has been carried out during a visiting period at the Rudolf Peierls Centre for Theoretical Physics, University of Oxford, under the supervision of James Binney and Ralph Schönrich.

of ionized gas (*coronae*), with very low density and a temperature close to the virial value (cfr. Chapter 1). These *coronae* are expected to form out of primordial gas that has been shock-heated after accretion on massive dark matter haloes. Because of its very large cooling time (comparable to the Hubble time), the coronal gas around a Milky-Way sized spiral galaxy can cool and accrete onto the central disc only very slowly and only if aided by physical processes whose nature is still debated, like some form of thermal instability (e.g. Maller & Bullock 2004, though see Binney, Nipoti & Fraternali 2009 and Nipoti & Posti 2014), or some form of positive star formation feedback (Marinacci et al. 2010a).

Besides being predicted by the theory, coronae have been recently observed around spiral galaxies (e.g. Anderson, Bregman & Dai 2013). However, their detailed structure and kinematics are still out of reach of the current instrumentation. As a consequence, only crude models have been used to interpret the data, based on very simple assumptions, in particular spherically symmetric hydrostatic equilibrium, in the absence of rotation (e.g. Gatto et al. 2013; Miller & Bregman 2015). While these simplifications are justified, from an observational point of view, by the lack of kinematical data, there are strong reasons to believe that coronae should contain a large amount of angular momentum as well. According to the theory discussed in Chapter 1, hot extended coronae should be made of material that has been accreted on the halo more recently with respect to the already assembled disc and therefore, following the theory of tidal torques (Peebles 1969; White 1984), they should have a larger amount of specific angular momentum. Furthermore, if coronae are the mass sources of the disc (as expected by the *hot-mode* accretion scenario, cfr. Chapter 1), they must also be sources of their angular momentum, in order to sustain the observed inside-out growth of star-forming discs (cfr. Chapter 2 and references therein). Since angular momentum growth is a key ingredient to understand the evolution of spiral galaxies (both from a theoretical and observational point of view), it is important to develop theoretical models and testable predictions for the angular momentum content of galactic coronae.

Models of rotating coronae can be divided in two categories, whose general properties have been extensively described in the more general context of rotating hydrostatic equilibria (e.g. Tassoul 2000). *Barotropic* models (e.g. Marinacci et al. 2011) are those relying on the hypothesis that pressure and density are stratified on the same surfaces (this is, for instance, the case of an isothermal gas). These models are appealing because of their simplicity and of several mathematical advantages (for instance, the possibility to define an *effective potential* to describe the centrifugal force in a locally rotating frame). However, they are forced to obey special properties, like the independence of the rotation velocity on the vertical coordinate (*rotation on cylinders*). In contrast, *baroclinic models* are those where density and pressure are allowed to be stratified independently. This is a very broad class, out of which only few cases have been described in detail (e.g. Amendt, Lanza & Abramowicz 1989). In the context of applications to hydrodynamics of galaxies, a great improvement has come with the work of Barnabè et al. (2006), whose models produce a vertical rotational velocity gradient similar to those observed in the gaseous haloes of nearby spiral galaxies (e.g. Oosterloo, Fraternali & Sancisi 2007)¹. They also pro-

¹Note however that, as Barnabè et al. (2006) point out, the observed cold extraplanar gas

posed a method to compute generic baroclinic equilibria, which however produces both meaningful and meaningless solutions (e.g. solutions with imaginary rotation velocity), which need to be distinguished *a posteriori*.

Irrespective of being barotropic or baroclinic, all the above models are built by deriving the density from the kinematics, or viceversa. Density and kinematics, in turn, allow to compute the angular momentum distribution by mass $\psi \equiv dM/dl$. This quantity is very important, for the theoretical study of coronae, because it is supposed to be conserved during the slow evolution of these structure (*detailed angular momentum conservation*, e.g. Mestel 1963). Furthermore, it is believed to reflect the angular momentum distribution of the dark matter (Fall & Efstathiou 1980), which is known a priori, from tidal torque theory and numerical simulations (Bullock et al. 2001; Sharma & Steinmetz 2005).

It would therefore be useful to make the inverse exercise, namely deriving the density distribution and the kinematics of a rotating corona from the assumption of a given angular momentum distribution. This would help in bridging the gap between the predictions of Cosmology (Chapter 1) and observational indications of angular momentum assembly coming from galaxy evolution studies (cfr. Chapters 2 and 3). In Sec. 4.2 we will attempt a solution of this *inversion problem*, in the very simple case of an isothermal (and therefore barotropic) corona in a logarithmic potential.

A formally similar exercise was the one developed by Kaiser & Binney (2003). These authors studied non-rotating, spherically symmetric hydrostatic equilibria of hot gas in the potential well of a galaxy cluster. Instead of working with radial profiles only, these authors built their solutions in terms of the entropy distribution by mass (specific entropy as a function of enclosed mass). If cooling occurs on timescales longer than the sound crossing timescale, then the evolution can be computed as a succession of quasi-static equilibria, each identified by a different entropy distribution. Having solved the *inversion problem* (from entropy distribution to spatial structure) allowed the authors to give a simple analytic description of cooling flows. Similarly, solving our inversion problem (from angular momentum distribution to coronal structure and kinematics) could be relevant to study the evolution of rotating gas undergoing viscous friction (and therefore angular momentum redistribution) on long timescales.

In the general baroclinic context, the degrees of freedom are too many for the inversion problem to be correctly defined in terms of just one function of one variable and it requires instead to be formulated in terms of the joint angular momentum/entropy distribution. This is the ideal generalization of the two simple one-dimensional inversion problems: the non rotating case of Kaiser & Binney (2003), based on the entropy distribution, and the barotropic rotating case based on the angular momentum distribution. Solving this problem would in principle allow the study of the quasi-static evolution of a rotating corona subject to quite general processes, including cooling, viscous transport and mass exchanges with the ambient medium (accretion from the IGM and condensation onto the disc).

cannot be in hydrostatic equilibrium, because of its relatively low temperature and also because of the details of its kinematics (see also Marinacci et al. 2010b); therefore, it is rather likely to be interacting with a hot medium in rotating baroclinic equilibrium.

We attempt some steps in this direction by considering baroclinic models in two steps. First, in Sec. 4.3 we give a general parametrization of physically meaningful baroclinic rotating equilibria in terms of a suitably chosen function of two variables (the specific angular momentum as a function of position in the meridional plane). As a second step, in Sec. 4.4 we discuss how an algorithm can be devised to reconstruct a general baroclinic equilibrium given the knowledge of its joint angular momentum/entropy distribution, supplemented by suitable boundary conditions. Finally, the results of this work are summarized in Sec. 4.5.

4.2 Isothermal equilibria

4.2.1 Basic equations

Let us consider an isothermal gas, with sound speed c_s , in rotating equilibrium in a fixed, spherically symmetric, gravitational potential. In this Section, we will assume for simplicity, a logarithmic potential:

$$\Phi(r) = V_d^2 \ln \left(\frac{r}{\tilde{r}} \right) \quad (4.1)$$

where V_d is the (constant) rotational velocity of a disc in centrifugal equilibrium within it and \tilde{r} an arbitrary radius. Of course, in cylindrical coordinates (R, z) , (4.1) reads:

$$\Phi(R, z) = V_d^2 \ln \left(\frac{\sqrt{R^2 + z^2}}{\tilde{r}} \right) \quad (4.2)$$

If the volume density in the equatorial plane at some cylindrical radius R is equal to $\rho_0(R)$, then, from isothermality and the vertical hydrostatic equilibrium, we have:

$$\rho(R, z) = \rho_0(R) e^{-\frac{\Phi(R, z) - \Phi(R, 0)}{c_s^2}} = \rho_0(R) \left(1 + \left(\frac{z}{R} \right)^2 \right)^{-\frac{a}{2}} \quad (4.3)$$

where:

$$a := \left(\frac{V_d}{c_s} \right)^2 \quad (4.4)$$

is the square of the Mach number of the disc with respect to the corona and it is inversely proportional to the temperature of the corona. The surface density at radius R is given by:

$$\Sigma(R) = 2 \int_0^{+\infty} \rho(R, z) dz = 2kR\rho_0(R) \quad (4.5)$$

with k given by:

$$k = \int_0^{+\infty} (1 + x^2)^{-\frac{a}{2}} dx \quad (4.6)$$

It should be noted that k (and thence the surface density at any specified radius) is finite provided that $a > 1$, that is when the disc is supersonic with respect to the corona. This sets an upper limit to the temperature of the corona in order for

isothermal solutions to exist; however, a more stringent limit is set by the requirement that the mass be finite in the radial direction, as we discuss in the following.

The coronal mass enclosed inside a cylindrical surface of radius R obeys the equation:

$$\frac{dM}{dR}(R) = 2\pi R\Sigma(R) = 4\pi kR^2\rho_0(R) \quad (4.7)$$

The specific angular momentum l of the corona is a function of radius R only, because of isothermality². Such a function also determines the local shape of the equatorial density distribution ρ_0 by means of the Euler radial equation in the equatorial plane, which can be written:

$$\frac{d\ln\rho_0}{d\ln R}(R) = a \left(\left(\frac{l(R)}{RV_d} \right)^2 - 1 \right) \quad (4.8)$$

In particular, we see that the corona rotated slower than the disc any time its equatorial density is a decreasing function of radius. Taking (4.7) and (4.8) into account, mass convergence at large radii requires:

$$-3 > \lim_{R \rightarrow \infty} \frac{d\ln\rho_0}{d\ln R}(R) \geq -a \quad (4.9)$$

which implies $a > 3$. Note that the definition (4.4) can also be expressed, in a more common notation, as:

$$a = \frac{3T_{\text{vir}}}{T} \quad (4.10)$$

where T is the temperature of the corona and T_{vir} is the *virial temperature*, commonly associated to the velocity scale V_d according to:

$$\frac{3}{2}k_B T_{\text{vir}} = \frac{1}{2}\mu_m m_p V_d^2 \quad (4.11)$$

where k_B , μ_m and m_p are the Boltzmann constant, the mean molecular weight and the mass of the proton, respectively. The condition $a > 3$ is therefore equivalent to $T < T_{\text{vir}}$. Also note that k monotonically decreases from 1 to 0 as a increases from 3 to $+\infty$ (that is, as the temperature decreases from T_{vir} to 0). We therefore see from (4.7) that the mass within the cylindrical radius R never exceeds the one comprised, within an equal *spherical* radius, by an ideal spherical distribution with radial profile ρ_0 (with equality holding for the virial temperature).

Mass convergence at small radii, instead, sets a lower limit to the rotation velocity of the corona $V(R) \equiv l(R)/R$, in the proximity of the origin:

$$\frac{V(0)}{V_d} = \lim_{R \rightarrow 0} \frac{l(R)}{RV_d} \geq \sqrt{1 - \frac{3}{a}} \quad (4.12)$$

which is always well defined and never vanishing, because of the constraint we have just derived on a ³.

²This is a consequence of the *Poincaré-Wavre theorem*, which we will discuss in some more detail in Sec. 4.3.4

³Note that velocities lower than this are actually expected in the very central regions, where the gravitational potential significantly deviates from our logarithmic approximation (e.g. Marinacci et al. 2011). The lower limit above is therefore better understood, in realistic cases, as a minimum amplitude for the initial rise of the rotation curve of the corona.

4.2.2 Dimensionless variables

The problem we are considering has so far just one physical scale (the velocity scale V_d set by the the gravitational potential (4.1)). It can therefore be put in dimensionless form if other two independent physical scales are introduced. A very natural choice is to fix some mass and angular momentum scales M_1 and L_1 and in particular to choose them equal to the total mass and angular momentum of the corona, respectively ⁴. Note that the total mass and angular momentum are related to the angular momentum distribution

$$\psi \equiv dM/dl \quad (4.13)$$

by:

$$\begin{cases} M_1 = \int_0^{+\infty} \psi(l)dl \\ L_1 = \int_0^{+\infty} l\psi(l)dl \end{cases} \quad (4.14)$$

Once M_1 and L_1 are fixed, we can define some scales for the specific angular momentum, length and density:

$$l_1 := \frac{L_1}{M_1} \quad R_1 := \frac{l_1}{V_d} \quad \rho_1 := \frac{M_1}{4\pi k R_1^3} \quad (4.15)$$

and the corresponding dimensionless variables:

$$\lambda := \frac{l}{l_1} \quad s := \frac{R}{R_1} \quad y := \frac{\rho_0}{\rho_1} \quad (4.16)$$

Note that the mass contained within the dimensionless radius s is:

$$\frac{M(s)}{M_1} = \int_0^s \hat{s}^2 y(\hat{s}) d\hat{s} \quad (4.17)$$

Note also that l_1 is the average specific angular momentum of the corona, while R_1 is the radius where the disc has a specific angular momentum equal to this value. To have a better idea of the physical scale associated to R_1 , one can consider that (as it is easily seen) an exponential disc with a flat rotation curve has an average specific angular momentum $l_d = 2V_d R_d$, where V_d and R_d are the rotational velocity and the scalelength of the disc, respectively. We therefore have:

$$\frac{R_1}{2R_d} = \frac{l_1}{l_d} \quad (4.18)$$

Obviously, the average angular momentum of the disc can grow with time only if the galaxy accretes material with an angular momentum greater than l_d . Therefore, the ratio (4.18) has to be greater than unity, if the corona has to sustain the inside-out

⁴Note that fixing M_1 and L_1 to the total mass and angular momentum of the corona is a convenient and physically meaningful, but not mandatory, choice. We will always adopt it, from now on, if not explicitly stated otherwise. However, keeping this freedom of choice in mind will be useful to give the correct interpretation to some of our solutions in Sec. 4.2.6.

growth of the disc (cfr. Chapters 2 and 3). At the same time, it cannot be larger than a few, because of the normalization of the Fall relation and the relatively small spin parameters that are expected as an outcome of cosmological tidal torques (e.g. Romanowsky & Fall 2012; Dutton & van den Bosch 2012). These considerations will be of much help for the discussion of our simple coronal models in the context of cosmology and galaxy evolution (Secc. 4.2.3 and 4.2.7).

4.2.3 A class of simple truncated models

To gain some insight on the relation between structure, kinematics and angular momentum distribution of the corona, under our simple hypotheses, we consider here the simplest possible situation, where the corona has the following properties (easily seen to be equivalent):

- i) a flat rotation curve
- ii) a power law density distribution, truncated at a maximum radius R_{\max}
- iii) a power law angular momentum distribution, truncated at a maximum radius l_{\max}

In formulae:

$$\begin{aligned}
 V(R) &= wV_d \quad \forall R \\
 \rho_0(R) &= \begin{cases} \rho_{0,1} \left(\frac{R}{R_1}\right)^{-q} & R < R_{\max} \\ 0 & R > R_{\max} \end{cases} \\
 \psi(l) &= \begin{cases} \psi_1 \left(\frac{l}{l_1}\right)^p & l < l_{\max} \\ 0 & l > l_{\max} \end{cases}
 \end{aligned} \tag{4.19}$$

Once the temperature parameter a is specified ⁵, the parameter p , describing the shape of the angular momentum distribution, determines the value of all the other involved quantities:

$$\left\{ \begin{aligned}
 q &= 2 - p \\
 w &= \frac{V}{V_d} = \sqrt{1 - \frac{p-2}{a}} \\
 s_{\max} &= \frac{R_{\max}}{R_1} = \frac{2+p}{1+p} \frac{1}{w} \\
 \lambda_{\max} &= \frac{l_{\max}}{l_1} = \frac{2+p}{1+p} \\
 y_1 &= \frac{\rho_{0,1}}{\rho_1} = \frac{(1+p)^{2+p}}{(2+p)^{1+p}} w^{1+p} \\
 \frac{\psi_1 l_1}{M_1} &= \frac{(1+p)^{2+p}}{(2+p)^{1+p}}
 \end{aligned} \right. \tag{4.20}$$

⁵Note that the solutions of this family formally exist also for $1 < a < 3$ (i.e. for $T_{\text{vir}} < T < 3T_{\text{vir}}$). This is possible because of the radial density truncation.

where R_1 , l_1 and ρ_1 are as in (4.15)

Note that it has to be $p > -1$ to ensure that the integral of ψ gives a finite mass. Models with $-1 < p < 2$ have $q < 0$ and therefore the density diverges near the origin (of course, in an integrable way), while $w < 1$, which means sub-centrifugal rotation. As an opposite case, models with $p > 2$ have a vanishing central density (and pressure) and super-centrifugal rotation (these are *vortex*-like solutions). The dividing value $p = 2$ is for a corona with uniform equatorial density and in perfect corotation with the disc everywhere.

Besides being very simplistic, the above models also have other potential problems, if applied to real galaxies, when the cosmological context (Chapter 1), evidence for inside-out growth (Chapter 2) and chemodynamical arguments (Chapter 3) are taken into account. As we have seen in Chapter 1, cosmological theory and observations suggest that the coronae around spiral galaxies are much larger than the embedded discs. Combined with the expectation that the ratio (4.18) is of the order of unity (Sec. 4.2.2), we infer $R_{\max}/R_1 \gg 1$ and therefore, from the third of (4.20), $w \ll 1$.

If the disc has a maximum radius $R_{d, \max}$, then the material accreting on it from the corona will have an average specific angular momentum

$$l_{\text{acc}} < l(R_{d, \max}) = V R_{d, \max} = w V_d R_{d, \max} \quad (4.21)$$

which compares with the average specific angular momentum of the disc as:

$$\frac{l_{\text{acc}}}{l_d} < \frac{w R_{d, \max}}{2 R_d} \quad (4.22)$$

If $w \ll 1$ and the disc extends for a few scalelengths, this will not be enough to sustain inside-out growth of the disc (cfr. Chapter 2).

Furthermore, $w \ll 1$ implies $\alpha = 1 - w \sim 1$, where α is the angular momentum mismatch parameter discussed in Chapter 3. As we discussed there, much smaller values ($0.2 \lesssim \alpha \lesssim 0.3$) are required to explain abundance gradients in the Milky Way. Given the strong dependence of gradients on this parameter, values as large as $\alpha \sim 1$ are likely incompatible with observations. Moreover, the inferred radial flows could become large enough to be incompatible with the relatively regular rotation commonly observed in the outer HI discs of massive star forming spirals (Pitts & Tayler 1996).

4.2.4 Coronal structure for a given angular momentum distribution

In order to consider more complex situations, we want to solve the inversion problem of deriving the structure and kinematics of the corona from an arbitrary angular momentum distribution ψ .

The equations (4.7) and (4.8) can be rewritten as:

$$\begin{cases} \frac{dl}{dR}(R) = 4\pi k R^2 \frac{\rho_0(R)}{\psi(l(R))} \\ \frac{d\rho_0}{dR}(R) = a \frac{\rho_0(R)}{R} \left(\left(\frac{l(R)}{R V_d} \right)^2 - 1 \right) \end{cases} \quad (4.23)$$

This system of two ordinary differential equations has to be supplemented by two boundary conditions $l(0) = 0$ and $l(R_{\max}) = l_{\max}$. Note that the two obvious boundary conditions on the mass ($M(R)$ vanishing for $R = 0$ and being equal to the total mass for $R = R_{\max}$) are then recovered automatically, from the definition of ψ (4.13). While the simple, but somewhat artificial, examples of Sec. 4.2.3 relied on finite values of R_{\max} and l_{\max} , we will focus, if possible, on the more natural choice $l(R) \rightarrow +\infty$ for $R \rightarrow +\infty$.

To put the problem in dimensionless form, we introduce, in addition to (4.16), a dimensionless version of the (multiplicative) inverse of ψ :

$$g(\lambda) := \frac{M_1}{l_1 \psi(l_1 \lambda)} \quad (4.24)$$

This allows (4.23) to be written:

$$\begin{cases} \frac{d\lambda}{ds}(s) = s^2 y(s) g(\lambda(s)) \\ \frac{dy}{ds}(s) = a \frac{y(s)}{s} \left(\left(\frac{\lambda(s)}{s} \right)^2 - 1 \right) \end{cases} \quad (4.25)$$

The second equation of (4.25) is singular in the origin ⁶. This issue needs to be addressed with an asymptotic analysis of the equations near the origin.

4.2.5 Asymptotic analysis near the origin

We start by isolating the behaviour of the function g near the origin ⁷:

$$g(\lambda) = g_1 \lambda^{-p} G(\lambda) \quad (4.26)$$

$g_1 \neq 0$ and $G(0) = 1$.

We look for a solution of (4.25) in the form:

$$\begin{cases} \lambda(s) = \lambda_1 s^\alpha A(s) \\ y(s) = y_1 s^\beta B(s) \end{cases} \quad (4.27)$$

with $\lambda_1 \neq 0$, $y_1 \neq 0$, $A(0) = 1$ and $B(0) = 1$. Substituting in the first equation of (4.25) and reading the limit for $s \rightarrow 0$ gives:

$$\begin{cases} \beta = (1+p)\alpha - 3 \\ y_1 = \frac{\alpha \lambda_1^{1+p}}{g_1} \end{cases} \quad (4.28)$$

while from the second we have:

$$\lambda_1^2 \lim_{s \rightarrow 0} s^{2(\alpha-1)} = 1 + \frac{(1+p)\alpha - 3}{a} \quad (4.29)$$

⁶Note that a singularity is implied by the l^2/R^3 term in the radial Euler equation already. This is therefore a quite general fact, independent of our particular choice of the potential.

⁷Note that the sign of the parameter p is chosen to be consistent with the particular case of Sec. 4.2.3. Note also that the condition $p > -1$ for the convergence of mass holds in the general case as well, since it only depends on the behaviour of ψ for small values of l .

Formally, (4.29) can be satisfied for $\alpha \geq 1$. However, the case $\alpha > 1$ can be discarded for giving rise to the following absurd:

$$0 = 1 + \frac{(1+p)\alpha - 3}{a} > 1 - \frac{3}{a} > 0 \quad (4.30)$$

where the first inequality comes from $p > -1$ (which is required by the convergence of mass for low angular momentum) and the second from $a > 3$ (from mass convergence at large radii).

We are therefore left with the case $\alpha = 1$, implying:

$$\lambda_1 = \sqrt{1 + \frac{p-2}{a}} \quad (4.31)$$

which is always well defined, since it is always $p-2 > -3$ and $a > 3$. The system (4.27) is reduced to:

$$\begin{cases} \lambda(s) = \lambda_1 s A(s) \\ y(s) = \frac{\lambda_1^{1+p}}{g_1} s^{p-2} B(s) \end{cases} \quad (4.32)$$

with $A(0) = B(0) = 1$.

The rotation curve of the corona is given by:

$$\frac{V(R)}{V_d} = \frac{l(R)}{RV_d} = \frac{\lambda(s)}{s} = \lambda_1 A(s) \quad (4.33)$$

In particular the central rotation velocity is $V(0)/V_d = \lambda_1$, which is given by (4.31) and, of course, satisfies the already established inequality (4.12). Note, from (4.31) and (4.32), that the dependence of the central properties of the corona on the parameter p is the same as described in Sec. 4.2.3.

To compute the full structure of the corona we need to find and solve the equations for the functions A and B . These can be found by inserting (4.26) and (4.32) into (4.25):

$$\begin{cases} \frac{dA}{ds}(s) = \frac{1}{s} (B(s)A^{-p}(s)G(\lambda_1 s A(s)) - A(s)) \\ \frac{dB}{ds}(s) = (a+p-2)\frac{B(s)}{s}(A^2(s) - 1) \end{cases} \quad (4.34)$$

Note that the singularities in the right hand side of (4.34) are only apparent and that the following limits can be found for $s \rightarrow 0$, by means of a first order Taylor expansion:

$$\begin{cases} A'(0) = \frac{G'(0)\lambda_1}{6-p-2a} \\ B'(0) = \frac{2(a-p-2)G'(0)\lambda_1}{6-p-2a} \end{cases} \quad (4.35)$$

apart in the very special case $a = (6-p)/2$, which can arise for $-1 < p < 0$ and which we will just ignore in the following, for simplicity.

For each value of $a \neq (6-p)/6$, the system (4.34), regularized by (4.35), together with the initial conditions $A(0) = B(0) = 1$, correctly defines a Cauchy problem and

therefore admits a unique solution, which can be computed by means of a numerical integration. Substituting the solution in (4.32) determines the density and angular momentum of the corona in the equatorial plane and thence everywhere. Note that the boundary condition $l(0) = 0$ is automatically satisfied, while the other one ($l(R) \rightarrow +\infty$ for $R \rightarrow +\infty$) in general will not; this last criterion can be used to select, among the possible models, the physically meaningful ones (see next two Sections for some examples).

4.2.6 The exponential angular momentum distribution

A simple class of angular momentum distributions is the one of exponentially truncated power-laws:

$$\psi(l) = \frac{M_1 (1+p)^{1+p}}{l_1 \Gamma(1+p)} \left(\frac{l}{l_1}\right)^p \exp\left\{- (1+p) \frac{l}{l_1}\right\} \quad (4.36)$$

where the Γ is the complete Euler function. The distribution (4.36) differs from the power-law distributions discussed in Sec. 4.2.3 for having a smooth, rather than abrupt, cut-off for large values of the angular momentum. Besides their elegance and simplicity, these distributions are also of cosmological interest, having been found to describe both dark matter and baryons in non-radiative cosmological simulations (Sharma & Steinmetz 2005)⁸.

To provide a simple illustrative application of the methods introduced in Sec. 4.2.5, we consider here the elementary case $p = 0$, which, for its simplicity, is very useful to gain insight into our methods and their outcome. Furthermore, this value is among the most common ones found in the simulations by Sharma & Steinmetz (2005) and coincides with the asymptotic behaviour of ψ seen in the simulations of Bullock et al. (2001). For $p = 0$, (4.36) just reduces to an exponential angular momentum distribution:

$$\psi(l) = \psi_0 e^{-\frac{l}{l_1}} \quad (4.37)$$

with $\psi_0 = M_1/l_1$.

Following the notation of Sec. 4.2.5, we need to solve:

$$\begin{cases} \frac{dA}{ds}(s) = \frac{1}{s} (B(s)e^{\lambda_1 s A(s)} - A(s)) \\ \frac{dB}{ds}(s) = (a-2) \frac{B(s)}{s} (A^2(s) - 1) \end{cases} \quad (4.38)$$

where $\lambda_1 = \sqrt{1 - 2/a}$ (from (4.31)), while the limits for $s \rightarrow 0$ are:

$$\begin{cases} A'(0) = -\frac{\lambda_1}{2(a-3)} \\ B'(0) = -\lambda_1 \frac{a-2}{a-3} \end{cases} \quad (4.39)$$

⁸While the non-radiative assumption is a very crude approximation for baryons in general, it should provide a reasonable description for coronal gas, which, by definition, has not undergone significant cooling yet.

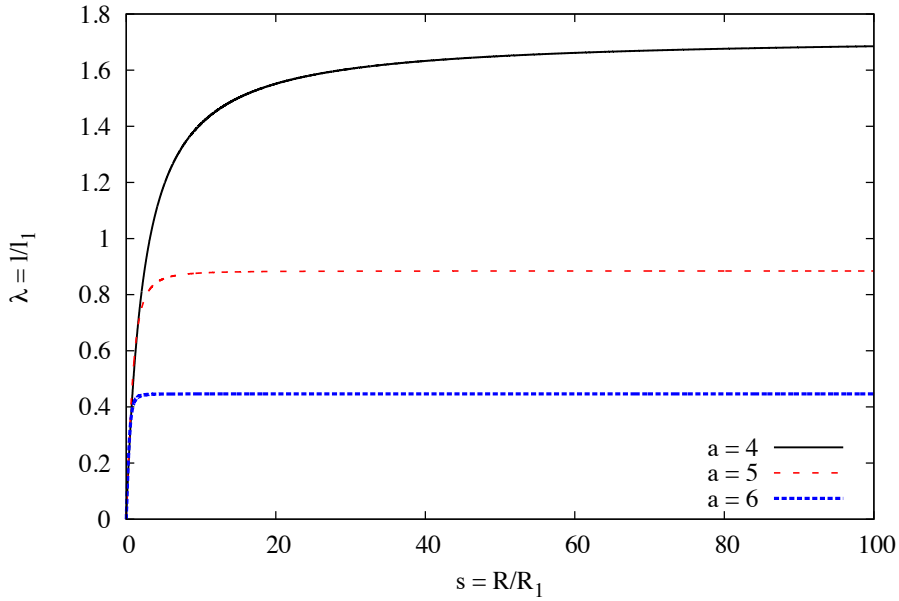


Figure 4.1: Dimensionless radial profile of specific angular momentum for the exponential angular momentum distribution (4.37). The three lines are for different values of the temperature parameter $a = 3T_{\text{vir}}/T$. All the models tend to a horizontal asymptote, instead of approaching infinity: this is a model inconsistency, indicating that the angular momentum distribution must be truncated at some value l_{max} .

which are well defined and negative for all allowed values of $a > 3$. The system (4.38) has to be integrated, as usual, with the initial conditions $A(0) = B(0) = 1$ and then converted into physical quantities according to (4.32), with $p = 0$ and $g_1 = 1$ (from (4.24) and (4.26)).

In Fig. 4.1 the resulting solutions are reported for the radial profiles of specific angular momentum of the corona, for three allowed values of the parameter a (which is related to the coronal temperature by (4.10)). A very clear property of these models is that they fail to match the boundary condition $l(R) \rightarrow +\infty$ for $R \rightarrow +\infty$, instead displaying a horizontal asymptote at a finite value l_{max} . This is an internal inconsistency of the model (4.37): it is not compatible with the total mass and the average specific angular momentum being equal to M_1 and l_1 , respectively. A reasonable way to interpret this finding is that the computed solutions are associated to an angular momentum distribution that is equal to (4.37) for low values of l , but it is then truncated at some maximum value l_{max} . Since this implies a modified normalization for both mass and angular momentum, the re-interpretation is only possible at the cost of a suitable re-scalings (see footnote 4, Sec. 4.2.2), which we describe in detail the next Section. Note that the existence of a maximum angular momentum l_{max} is physically sensible (it would be equal to the specific angular momentum imprinted by cosmological tidal torques on the last ‘shell’ of accreted material) and compatible with what suggested by the simulations of Bullock et al. (2001). Formally, a truncated exponential model is intermediate between the model (4.37) and the model (4.19) with $p = 0$.

Table 4.1: Dimensionless parameters for our illustrative coronal models with a truncated exponential angular momentum distribution (4.40).

a	$\frac{T}{T_{\text{vir}}}$	ξ	ω	$\frac{l_{\text{max}}}{l_1}$	$\frac{\psi_0 l_1}{M_1}$
4	0.75	1.69	0.62	2.74	0.76
5	0.6	0.88	0.38	2.34	0.64
6	0.5	0.45	0.21	2.16	0.57

4.2.7 Truncated exponential angular momentum distributions

The general truncated exponential angular momentum distribution reads:

$$\psi(l) = \begin{cases} \psi_0 \exp\left(-\omega \frac{l}{l_1}\right) & l < l_{\text{max}} \\ 0 & l > l_{\text{max}} \end{cases} \quad (4.40)$$

The three parameters ψ_0 , ω and l_{max} are subject to the constraint that the total mass is M_1 and the average specific angular momentum is l_1 , which leave just one degree of freedom. The resulting one-dimensional family of models is conveniently parameterized by the quantity $\xi \equiv \omega l_{\text{max}}/l_1$, in terms of which the three parameters can be written as:

$$\begin{cases} \omega & = 1 - \frac{\xi e^{-\xi}}{1 - e^{-\xi}} \\ \frac{l_{\text{max}}}{l_1} & = \frac{\xi(1 - e^{-\xi})}{1 - (1 + \xi)e^{-\xi}} \\ \frac{\psi_0 l_1}{M_1} & = \frac{1 - (1 + \xi)e^{-\xi}}{(1 - e^{-\xi})^2} \end{cases} \quad (4.41)$$

The parameter ξ can assume all non-negative real values. When ξ varies from 0 to $+\infty$, ω increases from 0 to 1, l_{max}/l_1 from 2 to $+\infty$, and $\psi_0 l_1/M_1$ from 1/2 to 1. Note that the limits $\xi \rightarrow 0$ and $\xi \rightarrow +\infty$ correspond, respectively, to the uniform distribution discussed in Sec. 4.2.3 (with $p = 0$) and the non-truncated exponential of Sec. 4.2.6, as expected.

Comparing (4.40) with (4.37), we see that the models of Sec. 4.2.6 can be translated into physically meaningful ones by means of the rescaling $l_1 \rightarrow l_1/\omega$, which, because of (4.16), also implies the rescaling of both axes of Fig. 4.1 $\lambda \rightarrow \omega\lambda$ and $s \rightarrow \omega s$. The scaling factor ω appropriate to each model can be computed, through the first of (4.41), from the appropriate value of ξ , which, in turn, is directly readable from the horizontal asymptote in Fig. 4.1, since $\lambda_{\text{max}} \rightarrow \omega\lambda_{\text{max}} = \xi$. In this way, each temperature is associated to one of the models from the family of truncated exponentials (see Table 4.1). The radial profiles of some relevant properties of these models are plotted, after rescaling in Fig. 4.2, while a two-dimensional map of the

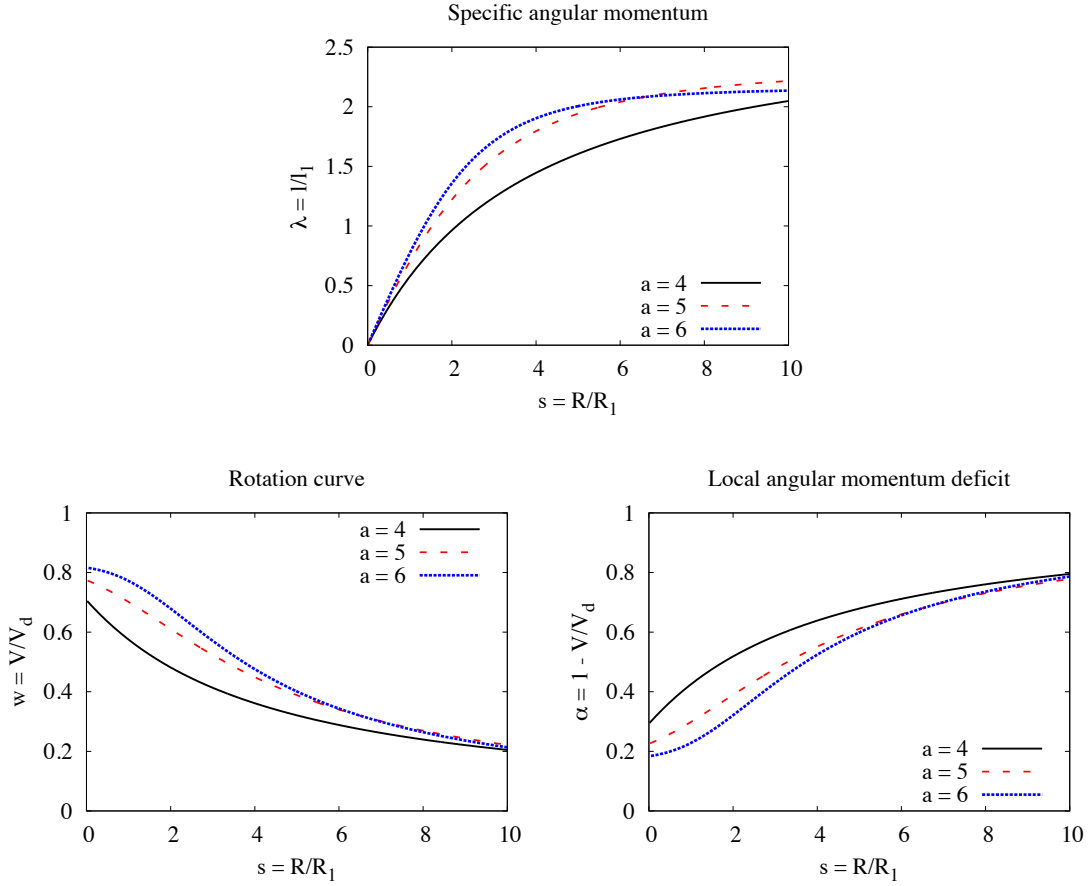


Figure 4.2: Illustrative models of isothermal coronae with a truncated exponential angular momentum distribution. Model parameters are as in Table 4.1 and the physical scales R_1 and l_1 as in Sec. 4.2.2. *Upper panel:* the specific angular momentum of the corona in units of its global average. *Lower-left panel:* The rotational velocity of the corona, in units of the one of the disc. *Lower-right panel:* The local angular momentum mismatch of the corona with respect to the disc $\alpha = 1 - V/V_d$, which is relevant for its dynamical and chemical consequences on the disc, as discussed in Chapter 3 (this is just a “mirror” version of the previous plot).

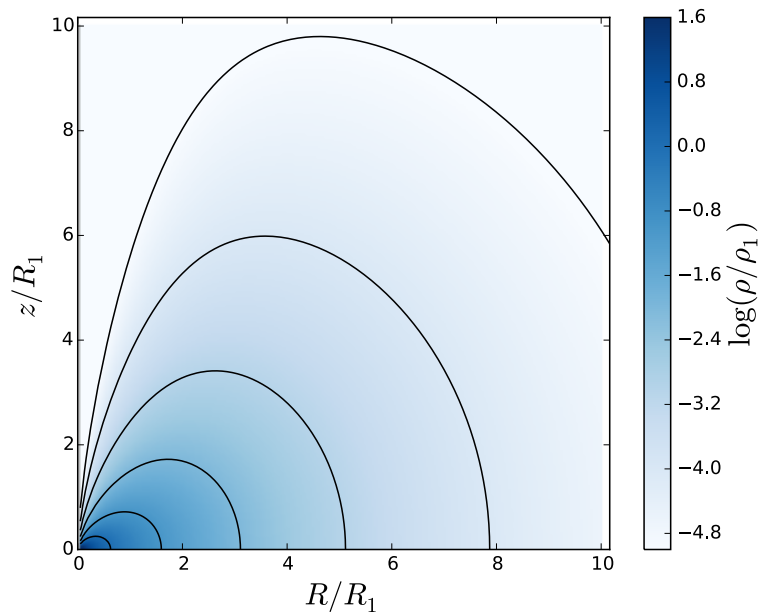


Figure 4.3: Two-dimensional map of the density in the meridional plane for our model of isothermal equilibrium with an exponentially truncated angular momentum distribution and a temperature equal to one half of the virial value. Contours of $\log(\rho/\rho_1)$ are shown from -5 to 0 in steps of 1. Pressure and entropy (not shown) are stratified on the same surfaces, as a consequence of the isothermal assumption.

density⁹ can be found in Fig. 4.3, for the case $a = 6$.

The models presented here show several improvements, if compared with the simpler ones of Sec. 4.2.3, as it can be qualitatively seen from Fig. 4.2. Since the rotation curve is not flat (lower-left panel), the specific angular momentum profile has a more complex behaviour than a mere linear increase (upper-panel). More precisely, l increases more rapidly in the inner regions than in the outskirts: this makes it possible for the disc (which resides at small radii) to be in contact with (and possibly accrete) coronal material with relatively high angular momentum, as needed to explain inside-out growth. For the same reason, the parameter $\alpha = 1 - V/V_d$ (lower-left panel), which sets the magnitude of the radial flows induced within the disc as a consequence of accretion (cfr. Chapter 3), has now much smaller values, at small R , than in the model of Sec. 4.2.3, possibly preventing the dynamical and chemical issue that we have mentioned there. A more quantitative discussion of these aspects is attempted in the next Section.

4.2.8 A tentative Milky-Way-like scaling

Putting our self-similar models on a precise physical scale requires the knowledge of the total mass and angular of the corona, both of which are generally poorly constrained. With this *caveat* in mind, it is nonetheless interesting to attempt a physical scaling that may be plausible for the Milky-Way.

For the spatial scaling, we assume a disc scale-length $R_d = 2.5$ kpc (Jurić et al.

⁹The density is rescaled according to $y \rightarrow ((1 - e^{-\xi})/\omega^3)y$.

2008) and a corona with twice the specific angular momentum of the disc (that is, of the same order of the specific angular momentum of the dark matter halo, e.g. Dutton & van den Bosch 2012 and references therein). From (4.18) we thence derive $R_1 = 10$ kpc and therefore the maximum displayed radius in Fig. 4.2 would be 100 kpc, or about one half of the virial radius (Dehnen, McLaughlin & Sachania 2006). For comparison, the disc extent that we considered in our chemical models of Chapter 3 is $2R_1 = 20$ kpc. The upper panel of Fig. 4.2 shows that the specific angular momentum of the corona in this region (and therefore, the one of possibly accreting material) easily reaches values that are larger than the global average of the disc (in our scaling, $l_d/l_1 = 0.5$), implying that accretion from the corona is, at least in principle, able to sustain the inside-out growth of the disc. At the same time, we see from the lower-right panel that, within the same region, the predicted values of the angular momentum mismatch parameter α (cfr. (3.22)) are remarkably similar to those required to explain the abundance gradients in the disc of the Milky Way (cfr. Fig. 3.9).

Assuming $V_d = 220$ km s⁻¹ (e.g. Koposov, Rix & Hogg 2010), the average specific angular momentum of the corona would therefore be $l_1 = R_1 V_d = 2.2 \times 10^3$ km s⁻¹ kpc, which is very similar to what expected for Milky-Way sized haloes (Romanowsky & Fall 2012). Assuming a halo mass $M_h \sim 1.5 \times 10^{12} M_\odot$ (e.g. Piffi et al. 2014 and references therein), the mass of the corona is:

$$M_1 = 2.3 f_c \times 10^{11} M_\odot \quad (4.42)$$

if it contains a fraction f_c of the of the baryons nominally associated to the halo (defined by the cosmological parameter $\Omega_n/\Omega_m = 0.15$, Planck Collaboration 2014). For the density scaling (expressed in particle number density), (4.15) gives:

$$n_1 = \frac{\rho_1}{\mu_m m_p} = 2.1 f_c \text{ cm}^{-3} \quad (4.43)$$

where $\mu_m = 0.6$ is the mean molecular weight, m_p the mass of the proton and we have used $k = 0.59$, as appropriate for $a = 6$ (or $T = 0.5T_{\text{vir}}$), according to (4.6). A comparison of this number with observations is not trivial, since the data are usually interpreted assuming spherical symmetry, in contrast with our model. To circumvent this limitation, we can compute our models at an intermediate height of 45° above the equatorial plane¹⁰. At $R = z = 5R_1 = 50$ kpc, corresponding to a spherical radius $r \sim 70$ kpc, we obtain the particle number density of:

$$n = 2.1 \times 10^{-4} f_c \text{ cm}^{-3} \quad (4.44)$$

Interestingly, if the corona approximately contains the baryons nominally associated to its dark matter halo ($f_c \sim 1$), the value above is very near to the estimate derived by Gatto et al. (2013) for this galactocentric distance.

We have therefore found that a model based on very simple assumptions agrees surprisingly well with a variety of theoretical and observational requirements, ranging from the expected mass and angular momentum content of the corona, to chemodynamical constraints associated to inside-out growth and abundance gradients, to

¹⁰An average would be a natural alternative. This, however, would be affected by the severe density drop near the vertical axis (see Fig. 4.3), a feature that, as we will show in Sec. 4.3.4, is mainly due to our simplifying assumption of isothermality.

independent estimates of the density of the coronal density of the Milky Way. We recognize, however, that our models are very simple in many respects and several refinements (like the inclusion of a more realistic gravitational potential and the relaxation of the isothermal assumption) would be useful to draw more firm conclusions.

4.3 Baroclinic equilibria

4.3.1 A constructive approach to the general baroclinic equilibrium

I look for a general solution of the system:

$$\begin{cases} -\frac{l^2}{R^3} &= -\frac{1}{\rho} \frac{\partial P}{\partial R} - \frac{\partial \Phi}{\partial R} \\ 0 &= -\frac{1}{\rho} \frac{\partial P}{\partial z} - \frac{\partial \Phi}{\partial z} \end{cases} \quad (4.45)$$

with 3 unknowns (l, ρ, P) of two variables (R, z) , the gravitational potential Φ being fixed.

I start allowing the specific angular momentum l to be an arbitrary function of (R, z) . Then I define the effective gravitational field G :

$$\begin{cases} G_R := -\frac{\partial \Phi}{\partial R} + \frac{l^2}{R^3} = g_R + \frac{l^2}{R^3} \\ G_z := -\frac{\partial \Phi}{\partial z} = g_z \end{cases} \quad (4.46)$$

$g = -\nabla\Phi$ being the usual gravitational field. We can notice that the field G is conservative (and hence it admits an effective potential) if and only if l is a function of R only (rotation on cylinders). Also, the effective potential can be written in the usual way $\Phi_{\text{eff}} = \Phi + l^2/(2R^2)$ in the even more particular case that l is a global constant. However, here we are interested in the general case in which l is arbitrary, G is not conservative and the effective potential does not exist.

Equation (4.45) can be rewritten as:

$$\nabla P = \rho G \quad (4.47)$$

Let us think of it as an equation for P and look for a condition on ρ in order for a solution to exist. Given that the meridional plane is simply connected, the necessary and sufficient condition is that the two-dimensional field ρG is closed. This turns into one equation on one unknown ρ , which we discuss in detail in the next Section. Besides providing the density field ρ , solving this equation guarantees that the equation (4.47) for the pressure P can be solved by integration along arbitrary paths in the meridional plane, thus completing the solution of the problem (4.45). The problem of choosing boundary conditions and of selecting physically meaningful solutions is addressed in Sec. 4.3.3.

4.3.2 Construction of the density and pressure fields

The closure condition for the field ρG reads:

$$F_R \frac{\partial \rho}{\partial R} + F_z \frac{\partial \rho}{\partial z} = \rho \left(\frac{\partial G_R}{\partial z} - \frac{\partial G_z}{\partial R} \right) \quad (4.48)$$

where the vector field F is defined by:

$$\begin{cases} F_R := G_z \\ F_z := -G_R \end{cases} \quad (4.49)$$

In the usual view of the meridional plane, F is just the effective gravitational field G rotated by $\pi/2$ clockwise.

Equation (4.48) can be simplified dividing by ρ , defining $\chi := \ln \rho$ and noting that the contribution of the gravitational potential Φ cancels out in the explicit calculation of the right hand side. The result is:

$$F_R \frac{\partial \chi}{\partial R} + F_z \frac{\partial \chi}{\partial z} = A(R, z) \quad (4.50)$$

where

$$A(R, z) := \frac{1}{R^3} \frac{\partial l^2}{\partial z}(R, z) \quad (4.51)$$

is a scalar field completely defined by the scalar field l ; we also notice that it identically vanishes in (and only in) the case of rotation on cylinders.

The characteristic lines for equation (4.50) are the integral curves of the field F , that is, they are the tracks of the solutions of the equation:

$$\begin{cases} \frac{dR}{dt}(t) = F_R(R(t), z(t)) \\ \frac{dz}{dt}(t) = F_z(R(t), z(t)) \end{cases} \quad (4.52)$$

Note that the characteristic lines are completely determined by the knowledge of the potential Φ and the angular momentum field l . If χ is known to be equal to some $\chi_0 = \ln \rho_0$ at some point (R_0, z_0) in the meridional plane, then the field χ is known along the whole characteristic passing through that point. More precisely, if we choose a solution of (4.52) that passes through (R_0, z_0) for $t = 0$, then the value of χ at any other point of the same characteristic line is given by:

$$\chi(R(t), z(t)) = \chi_0 + \int_0^t A(R(\hat{t}), z(\hat{t})) d\hat{t} \quad (4.53)$$

or, which is the same:

$$\rho(R(t), z(t)) = \rho(R(0), z(0)) \exp \left(\int_0^t A(R(\hat{t}), z(\hat{t})) d\hat{t} \right) \quad (4.54)$$

If the density is constructed in this way, then the closure condition (4.48) guarantees that the pressure field can be consistently computed by integrating (4.45)

along arbitrary paths in the meridional plane. However, the integration along characteristic lines is by far the most convenient choice. In fact, from equation (4.47) and since F is orthogonal to G , characteristics are also lines of constant pressure (*isobaric lines*):

$$P(R(t), z(t)) = P(R_0, z_0) \quad \forall t \quad (4.55)$$

Equations (4.54) and (4.55) allow the reconstruction of the pressure P and density ρ across the whole meridional plane, provided that *boundary conditions* for them are assigned along some suitable reference *non-characteristic* line¹¹. The same equations also guarantee that if the pressure and the density are positively defined along the reference line, than they automatically have the same property in the whole plane. This greatly simplifies the task of checking the physical meaningfulness of the formal solutions built with the described strategy. However, the two fields cannot be chosen independently, since they are related by the projection of (4.47) along the reference line. We will address this point further in the next Section.

4.3.3 Entropy, hydrostatic potential and the choice of boundary conditions

Consider the a change of thermodynamic variables $(P, \rho) \rightarrow (S, Q)$, defined as:

$$\begin{cases} S & := & \ln\left(\frac{P}{k\rho^\gamma}\right) \\ Q & := & \frac{\gamma}{\gamma-1}k^{\frac{1}{\gamma}}P^{\frac{\gamma-1}{\gamma}} \end{cases} \quad (4.56)$$

With a suitable choice of γ ($\gamma = 5/3$ for an ideal gas), S is the dimensionless specific entropy (just *entropy*, from now on), while k is an arbitrary constant with suitable physical dimensions¹². We can call the quantity Q *hydrostatic potential*, because it has the same dimensions of the gravitational potential and, with the positions (4.56), the equation of hydrostatic equilibrium (4.47) can be re-written:

$$\nabla Q = e^{-\frac{S}{\gamma}} G \quad (4.57)$$

The key points of Sec. 4.3.2 can be easily translated in the novel notation. For instance, the evolution of the entropy along an isobaric line is:

$$S(R(t), z(t)) = S(R_0, z_0) - \gamma \int_0^t A(R(\hat{t}), z(\hat{t})) d\hat{t} \quad (4.58)$$

while, since characteristics and isobars coincide, equation (4.50) reads:

$$\left(g_R + \frac{l^2}{R^3}\right) \frac{\partial S}{\partial z} - g_z \frac{\partial S}{\partial R} = \frac{\gamma}{R^3} \frac{\partial l^2}{\partial z} \quad (4.59)$$

which is equivalent to the so-called *thermal wind relation* (e.g. Tassoul 2000).

¹¹That is a line not parallel to F , i.e. non orthogonal to G .

¹² $k = P_0 \rho_0^{-\gamma}$ where (P_0, ρ_0) is a thermodynamic state belonging to the adiabat where the entropy has been arbitrarily chosen to vanish.

The coordinates (4.56) are especially useful in the choice of the boundary conditions. Let $s \mapsto x(s) = (R(s), z(s))$ be a parametrization of the reference line. Then the hydrostatic equilibrium (4.57) projects on this line as:

$$\frac{dQ}{ds}(s) = \exp\left(-\frac{S(s)}{\gamma}\right) G_p(s) \quad (4.60)$$

where $G_p(s) := \langle G(x(s)), x'(s) \rangle$ is the projection of the effective gravitational field along the reference line¹³. Note that G_p never vanishes on the reference line¹⁴ and therefore it has a constant sign along it. This implies that Q has its minimum value at one extreme of such a line (which may be at infinity). If a non-negative initial condition for Q is assigned at that end of the line, then (4.60) can be integrated, yielding a solution for Q that is non-negative everywhere. By inverting (4.56), we eventually find density and pressure fields that are well defined along the reference line and therefore, because of what we have seen in Sec. 4.3.2, in the whole meridional plane. This completes the construction of the general physically meaningful solution to the system (4.45).

4.3.4 Geometry and rotation

We make here a brief digression on the link between rotation and the geometry of isobaric lines, in a couple of relevant situations.

For simplicity, we consider here only the “upper” half of the meridional plane ($z \geq 0$); specular considerations clearly hold for $z < 0$. We also assume that Φ increases with both R and z and that g_z vanishes only for $z = 0$. I will call *equatorial line* the locus of the meridional plane defined by $z = 0$, the revolution of which is the *equatorial plane*.

Sub-centrifugal rotation

We will say that a configuration for l is of *sub-centrifugal rotation* if the condition:

$$l^2 < -R^3 g_R \quad (4.61)$$

holds everywhere. From (4.49) and (4.46), this implies that $F_z > 0$ and therefore, from (4.52), that the height z can be used as a coordinate along each characteristic line.

With this choice, the equation (4.52) for the shape of characteristics can be written:

$$\frac{dR}{dz} = \frac{F_R}{F_z} = -\frac{G_z}{G_R} = -\frac{g_z}{g_R + l^2/R^3} \leq 0 \quad (4.62)$$

where the equality holds only for $z = 0$. Note that characteristics start from the equatorial line being orthogonal to it and then bend inwards, with a monotonic increase in z and decrease in R ¹⁵.

¹³Angle parentheses denote here the ordinary scalar product.

¹⁴The reference line is non-characteristic by definition, cfr. footnote 11, Sec. 4.3.2.

¹⁵It can also be shown that, for potentials that are spherically symmetric or flatter, all these lines end on the vertical axis at a finite value of z and hence they have a finite length.

According to (4.54), the density changes along characteristic as:

$$\frac{d \ln \rho}{dz}(z) = -\frac{\frac{\partial l^2}{\partial z}(R, z)}{R^3 g_R(R, z) + l^2(R, z)} \quad (4.63)$$

Note that the equatorial line is non-characteristic and therefore suitable for the definition of boundary conditions.

Rotation on cylinders

The *Poincaré–Wavre theorem* (e.g. Tassoul 2000) states that a perfect gas in rotating equilibrium in a static axisymmetric gravitational potential has an angular velocity (as well as rotational velocity and specific angular momentum) that is independent on height z (*rotation on cylinders*) if and only if it is in a *barotropic* configuration (that is, with pressure and density stratified on the same surfaces); furthermore, this is the necessary and sufficient condition for the existence of the effective potential:

$$\Phi_{\text{eff}}(R, z) = \Phi(R, z) - \int \frac{l^2(\hat{R})}{\hat{R}^3} d\hat{R} \quad (4.64)$$

which is then stratified on the same surfaces as well.

It is interesting to notice how our geometrical perspective offers an alternative proof of this well-known theorem. From (4.54) and (4.51), in fact, it immediately follows that ρ is constant along characteristic (isobaric) lines if and only if l is independent of z . Furthermore, from (4.52) and (4.49), characteristics are also everywhere orthogonal to the effective gravitational field, which is the gradient of the effective gravitational potential (4.64) (with changed sign), implying that the latter is constant along isobaric lines as well.

Rotation on cylinders is an interesting example where the sub-centrifugal condition (4.61) is, in general, not satisfied everywhere. In fact, at a fixed radius R , the specific angular momentum l is independent of height, by definition, while the angular momentum of centrifugal equilibrium is:

$$l_{\text{eq}}(R, z) = \sqrt{-R^3 g_R(R, z)} = \sqrt{R^3 \frac{\partial \Phi}{\partial R}(R, z)} \quad (4.65)$$

which, in the majority of physically interesting potentials, goes to zero as $z \rightarrow +\infty$. There will therefore be some critical height $z_c(R)$ above which the fluid will start rotating faster than the centrifugal balance requires. From (4.52), (4.49) and (4.46), we see that the crossing point $(R, z_c(R))$ is also a point of maximum height for the characteristic line passing through it, after which that line (which is also an isobaric and equidensity line) turns down to lower R and z .

The isothermal case discussed in Sec. 4.2 is an obvious example of barotropic model. The discussion above therefore explains the shape of isobaric lines that we have seen in Fig. 4.3 and clarifies that this is a general property of barotropic models¹⁶. We will see in Sec. 4.3.6 example baroclinic models with a very different shape of the isobars.

¹⁶Note, however, that the precise shape of the central cavity does depend of the choice of the potential. Note also that in systems with a sharp spatial edge, the effect can formally occur outside the physical boundary of the object, therefore effectively disappearing. These include, for instance, some barotropic models of rotating stars.

4.3.5 A class of models rotating on spheres

Consider a rotating ideal gas in (baroclinic) equilibrium in a spherical potential:

$$\Phi(R, z) = \Phi_0(\sqrt{R^2 + z^2}) \quad (4.66)$$

and suppose it is rotating with a constant fraction \sqrt{c} of the local centrifugal velocity:

$$l^2(R, z) = cR^3 \frac{\partial \Phi}{\partial R}(R, z) = cR^4 \left(\frac{\Phi_0'(r)}{r} \right)_{|r=\sqrt{R^2+z^2}} \quad (4.67)$$

with $0 < c < 1$. It is readily seen that the angular velocity $\omega = l/R^2$ is constant on spherical surfaces (which are also equipotentials).

From (4.62) and (4.66), the characteristic (isobaric) lines are easily identified by solving:

$$\frac{dR}{dz}(z) = -\frac{\frac{\partial \Phi}{\partial z}(R, z)}{\frac{\partial \Phi}{\partial R}(R, z) - \frac{l^2(R, z)}{R^3}} = -\beta \frac{z}{R} \quad (4.68)$$

with:

$$\beta = \frac{1}{1-c} > 1 \quad (4.69)$$

Characteristics are a family of homotetic ellipses, parametrized by the semi-major axis (or elongation along the equator) R_0 and described by:

$$R^2 + \beta z^2 = R_0^2 \quad (4.70)$$

Correspondingly, the isobaric surfaces are oblate ellipsoids¹⁷. Thanks to (4.63), the density along each characteristic line obeys:

$$\frac{d \ln \rho}{dz}(z) = -(\beta - 1)z \left(\frac{h(r)}{r^2} \right)_{|r=\sqrt{R^2+z^2}} \quad (4.71)$$

where h is a dimensionless function, dependent on the choice of the potential:

$$h(r) = 1 - \frac{r \Phi_0''(r)}{\Phi_0'(r)} \quad (4.72)$$

Because of their shape (4.70), characteristic lines are also suitably parametrized by the spherical radius r , as an alternative to the height z ¹⁸:

$$r = \sqrt{R^2 + z^2} = \sqrt{R_0^2 - (\beta - 1)z^2} \quad (4.73)$$

With this choice, (4.71) simplifies in:

$$\frac{d \ln \rho}{dr}(r) = \frac{h(r)}{r} \quad (4.74)$$

The density field is therefore given by:

$$\rho(R, z) = \rho_0(R_0) \exp \left(- \int_r^{R_0} \frac{h(x)}{x} dx \right) \quad (R_0 = \sqrt{R^2 + \beta z^2}; r = \sqrt{R^2 + z^2}) \quad (4.75)$$

where $\rho_0(R) := \rho(R, 0)$ is the equatorial density profile.

¹⁷They would have been hyperboloids in the case (which I do not develop here) $f > 1$, corresponding to the gas rotating faster than centrifugal equilibrium everywhere.

¹⁸Note that r decreases with increasing z .

Particular cases

For some choices of the potential, the function h turns out to be a constant, so that (4.75) further simplifies in:

$$\rho(R, z) = \rho_0(\sqrt{R^2 + \beta z^2}) \left(\frac{R^2 + z^2}{R^2 + \beta z^2} \right)^{\frac{h}{2}} \quad (4.76)$$

To this class belong the logarithmic potential (particularly simple, with $h = 2$) and all potentials proportional to some power of the spherical radius (e.g. the Keplerian potential, with $h = 3$).¹⁹

We also give the function h computed for the NFW potential (Navarro, Frenk & White 1997):

$$\Phi_0(r) = -V_0^2 \left(\frac{r}{r_s} \right)^{-1} \ln \left(1 + \frac{r}{r_s} \right) \quad (4.77)$$

$$h(r) = 3 - \left\{ \frac{y^2}{(1+y)[(1+y)\ln(1+y) - y]} \right\}_{|y=\frac{r}{r_s}} \quad (4.78)$$

which is a positive increasing function of r within the limits:

$$\begin{aligned} \lim_{r \rightarrow 0^+} h(r) &= 1 \\ \lim_{r \rightarrow +\infty} h(r) &= 3 \end{aligned} \quad (4.79)$$

which are the values for a uniform gravitational field and the Keplerian field, respectively.

4.3.6 A self-similar family of rotating coronae in a logarithmic potential

We now apply the formalism of the previous Section to derive a simple self-similar (toy) baroclinic model of rotating coronae. We consider a logarithmic potential (4.1) and, using the notation of Sec. 4.3.3, we define on the equatorial line a simple scale-free boundary condition:

$$S(R) = \gamma A \ln \frac{R}{R_S} \quad (4.80)$$

with $A > 0$. The radius R_S is, in this self-similar model, an arbitrary choice: it does not fix any spatial scale, but just fixes the arbitrary constant in the definition of the entropy to be:

$$k = P_1 \rho_1^{-\gamma} \quad (4.81)$$

¹⁹Just as a curiosity, we notice that the harmonic potential (with $h = 0$) is the only one for which the density comes out to be stratified with the pressure, with the consequence that cylindrical rotation is in place. More precisely, a model like this rotates as a solid body, with an angular velocity proportional to the proper frequency of the oscillator.

with $P_1 = P(R_S)$ and $\rho_1 = \rho(R_S)$. Introducing the dimensionless variables $x = R/R_S$ and $q = Q/V_d^2$, the hydrostatic equilibrium on the equatorial plane (4.60) reads:

$$\frac{dq}{dx}(x) = -\frac{1}{\beta x^{1+A}} \quad (4.82)$$

with the trivial solution:

$$q(x) = \frac{1}{\beta A x^A} \quad (4.83)$$

where the integration constant has been chosen in such a way that the pressure vanishes at infinity. From (4.56), pressure and density along the equator are given by:

$$\frac{P(x)}{P_1} = \frac{\rho(x)}{\rho_1} = x^{-\frac{\gamma A}{\gamma-1}} \quad (4.84)$$

Note that the isothermal sound speed is constant along the equatorial plane, according to:

$$\frac{c_s^2}{V_d^2} = \frac{P(x)}{\rho(x)V_d^2} = \frac{P_1}{\rho_1 V_d^2} = \frac{\gamma-1}{\gamma} q(1) = \frac{\gamma-1}{\gamma \beta A} \quad (4.85)$$

where the third equality follows from (4.56) and (4.81), while the last one comes from (4.83). Combined with (4.4) and (4.10), (4.85) can be used to express the (constant) equatorial temperature T_1 in units of the virial temperature T_{vir} :

$$\frac{T_1}{T_{\text{vir}}} = \frac{3(\gamma-1)}{\gamma \beta A} \quad (4.86)$$

The equatorial temperature T_1 is therefore fixed by the rotation law (parametrized by β) and the shape of the entropy profile (parametrized by A). Note that the temperature is constant along the equator, but not in the whole space. Thermodynamic functions are easily computed in the whole meridional plane by means of (4.76) (with $h = 2$, as appropriate in this case):

$$\left\{ \begin{array}{l} P(R, z) = P_1 (R^2 + \beta z^2)^{-\frac{\gamma A}{2(\gamma-1)}} \\ \rho(R, z) = \rho_1 (R^2 + z^2) (R^2 + \beta z^2)^{-(1+\frac{\gamma A}{2(\gamma-1)})} \\ T(R, z) = T_1 \frac{R^2 + \beta z^2}{R^2 + z^2} \\ S(R, z) = \gamma \left[\left(1 + \frac{A}{2}\right) \ln(R^2 + \beta z^2) - \ln(R^2 + z^2) \right] \end{array} \right. \quad (4.87)$$

Note that isothermal lines in the meridional plane are straight lines through the origin, with the temperature increasing from the minimum value T_1 along the equator to the maximum value βT_1 on the vertical axis.

In Fig. 4.4, two-dimensional maps are represented for the model (4.87), computed with $A = 1$ and $\beta = 4/3$. According to (4.69), this is appropriate for $c = 1/4$ and $\sqrt{c} = 1/2$, that is for a corona that rotates at one half of the local centrifugal speed everywhere. Note the stratification of the temperature on straight lines (lower-right panel). In units of the virial value, the temperature increases from $0.9 T_{\text{vir}}$, on the

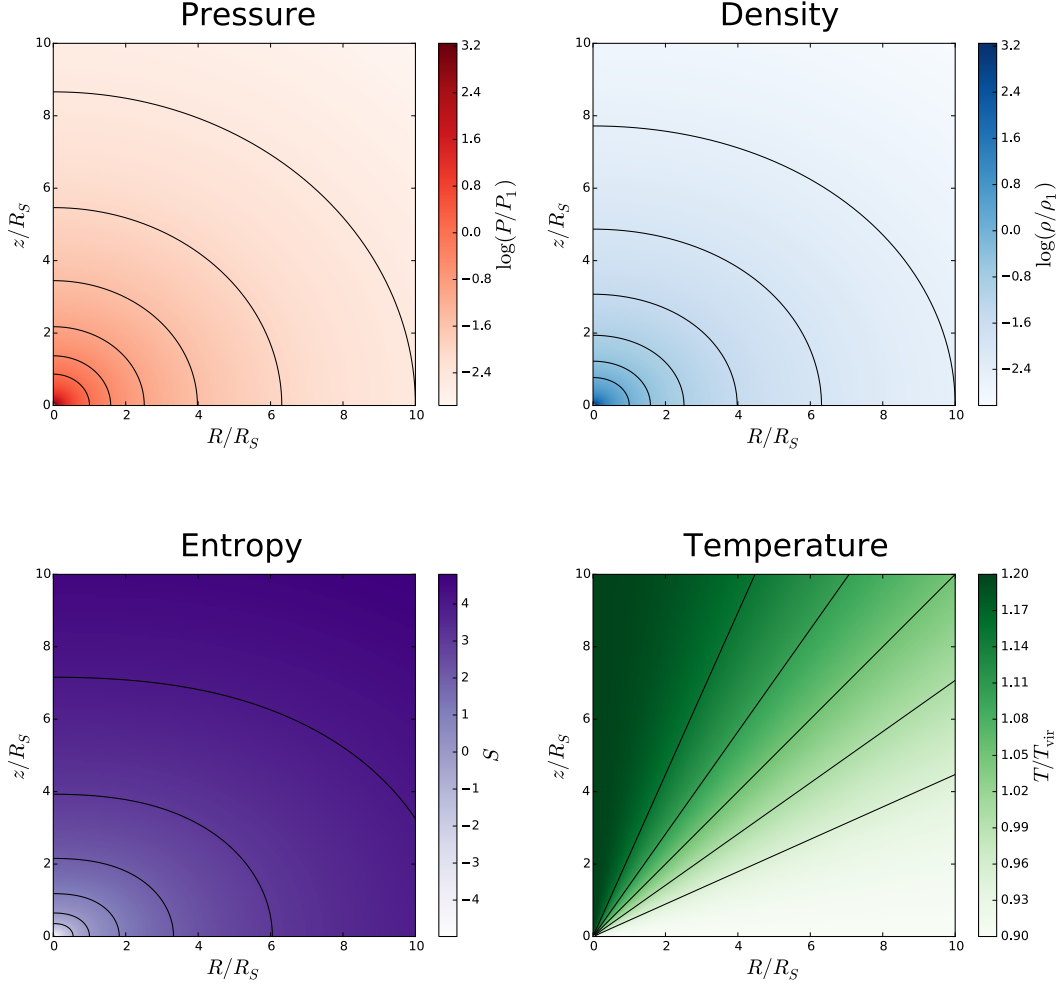


Figure 4.4: Two-dimensional maps for the self-similar model (4.87) of baroclinic equilibrium in a logarithmic potential. The example shown rotates at one half of the local centrifugal speed everywhere. *Upper left:* Pressure, in logarithmic units, with contours of $\log(P/P_1)$ shown from -2.5 to 0, in steps of 0.5. *Upper-right:* Density, in logarithmic units, with contours of $\log(\rho/\rho_1)$ from -2.5 to 0 in steps of 0.5. *Lower-left:* Entropy, in linear scale, with contours from -1 to 4 in steps of 1 (note that the entropy increases outwards). *Lower right:* Temperature, shown in linear scale, is stratified on straight lines and varies from from $0.9 T_{\text{vir}}$ (on the equator) to $1.2 T_{\text{vir}}$ (on the vertical axis); contours are drawn in equal steps of 0.05. Pressure, density and entropy are stratified on different surfaces, with an increasing flattening, in this order. The very small, but non vanishing, temperature gradient, has a dramatic impact on the shape of the model, especially near the vertical axis (cfr. Fig. 4.3).

equatorial plane, to $1.2 T_{\text{vir}}$, on the vertical axis, with a maximum contrast $\beta = 4/3$. A mild temperature gradient like this one already has a dramatic impact on the stratification of the other quantities, as it is clear from a comparison with isothermal models (cfr. Fig. 4.3 and Sec. 4.3.4)²⁰. Furthermore, because of the baroclinic nature of this model, pressure, density and entropy are stratified along different surfaces, with an increasing flattening going from pressure to density to entropy.

4.4 Rotating equilibria from angular momentum and entropy distributions

4.4.1 Problem statement

We address here the inverse problem of reconstructing the structure and kinematics of a rotating corona from its joint angular momentum and entropy distribution:

$$\Sigma = \frac{\partial^2 M}{\partial l \partial S} \quad (4.88)$$

More precisely, the *abstract density* Σ is defined by:

$$M(\Omega) := \int_{\Omega} \Sigma(l, S) dl dS \quad (4.89)$$

being the gaseous mass with angular momentum and entropy comprised within a given region Ω of the (l, S) plane. If (4.89) is re-written as an integral in the meridional plane and Ω is allowed to be an arbitrarily small domain, we find this useful expression for Σ ²¹:

$$\Sigma(l(R, z), S(R, z)) = \frac{2\pi R \rho}{\frac{\partial l}{\partial R} \frac{\partial S}{\partial z} - \frac{\partial l}{\partial z} \frac{\partial S}{\partial R}}(R, z) \quad (4.90)$$

where we took into account that the denominator is a positive quantity in every stable configuration²². The same stability requirement also implies that the entropy increases outwards, when evaluated along lines of constant angular momentum, and therefore, for each value of l , has its minimum on the equatorial line. In other words, Σ is non-vanishing only for $S > f(l^2)$ ²³, where f defines the relation between specific angular momentum and entropy of a particular equilibrium configuration:

$$S(R, 0) = f(l^2(R, 0)) \quad (4.91)$$

We will assume that both l and S increase with R and therefore that f is a monotonically increasing function of l^2 .

²⁰Note that only the shape of the lines is relevant in the comparison of Fig. 4.4 with Fig. 4.3. The normalization, in fact, has a very different meaning in the two cases, being based on the total mass, there, and on an arbitrary radius, here.

²¹The proper value of Σ is actually twice of this, for symmetry reasons. However, we will focus in the following only on the $z > 0$ half of the meridional plane, for simplicity.

²²Cfr. the second *Solberg-Høiland condition*, e.g. Tassoul (2000).

²³We use the angular momentum squared here for later convenience.

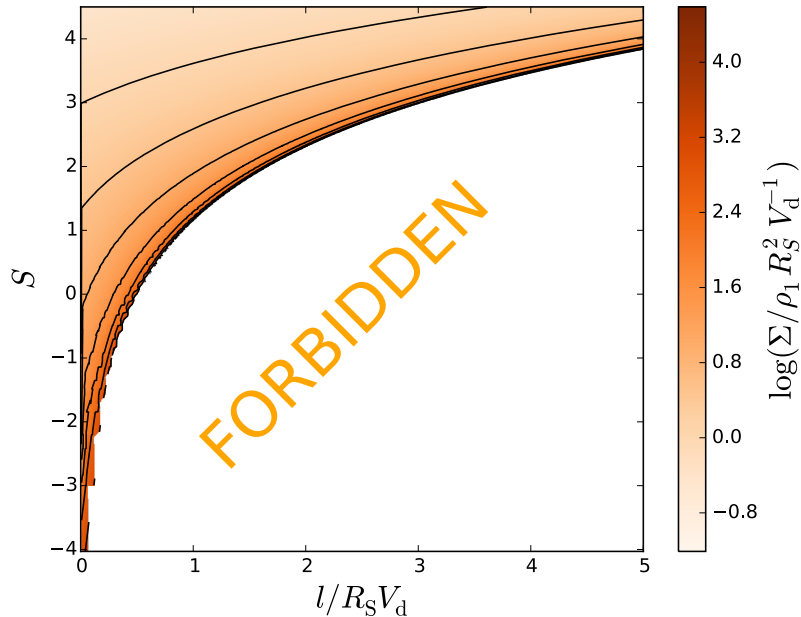


Figure 4.5: The *abstract* mass density Σ in the angular momentum-entropy (l, S) plane, for the same model of Fig. 4.4, with contours drawn that are equally spaced in logarithm. Notice the ridge line, dividing the plane in an allowed and a forbidden region, approaching which the abstract density Σ increases indefinitely.

As an example, we report in Fig. 4.5 the map of the abstract density Σ in the (l, S) plane for our toy baroclinic model of Sec. 4.3.6 and Fig. 4.4. Equation (4.91) identifies the locus where the equatorial line is mapped to in the (l, S) plane. Since, for any given l , the minimum entropy is the one attained on the equator, the abstract density Σ necessarily vanishes below this line. Note also that Σ appears to diverge when this line is approached from the allowed region. We will come back to this in Sec. 4.4.4.

Equation (4.90), together with the equations of hydrostatic equilibrium (4.45) and the first of (4.56), form a system of 4 equations in the 4 unknowns (P, ρ, S, l) , which should therefore be solvable, if suitable boundary conditions are defined.

4.4.2 An inductive reconstruction algorithm

We give here a sketch of how an algorithm can be devised to compute the solution by induction. We first consider the case where the fields (P, ρ, S, l) are known, as a function of R , at some given height z and show how they can be reconstructed in the rest of the meridional plane. Similar arguments hold if they are instead assigned as a function of z at given R .

Equation (4.90) can be combined with the thermal wind relation (4.59) to yield a linear system of two equations in the two unknowns $\partial l/\partial z$ and $\partial S/\partial z$, the solution

of which is:

$$\begin{cases} \frac{\partial l}{\partial z} = \frac{-l_1^2 C + l_2^2 l_R S_R}{2\gamma l l_R + l_1^2 S_R} \\ \frac{\partial S}{\partial z} = \frac{2\gamma l C + l_2^2 S_R^2}{2\gamma l l_R + l_1^2 S_R} \end{cases} \quad (4.92)$$

where (just to simplify the notation) we have been using the positions:

$$\begin{cases} C & := \frac{2\pi R\rho}{\Sigma} \\ l_1^2 & := -(R^3 g_R + l^2) \\ l_2^2 & := -R^3 g_z \\ l_R & := \frac{\partial l}{\partial R} \\ S_R & := \frac{\partial S}{\partial R} \end{cases} \quad (4.93)$$

By hypothesis, all these quantities are known at the height z . Therefore, equation (4.92) can be integrated to give l and S at the height $z + \Delta z$ (of course, with an accuracy that increases with decreasing Δz). The pressure and density fields can then be computed at $z + \Delta z$, by using the change of variables (4.56) and integrating the vertical component of the hydrostatic equilibrium:

$$\frac{\partial Q}{\partial z} = e^{-\frac{s}{\gamma}} g_z \quad (4.94)$$

Note that the radial component of the Euler equation:

$$\frac{\partial Q}{\partial R} = e^{-\frac{s}{\gamma}} \left(g_R + \frac{l^2}{R^3} \right) \quad (4.95)$$

should be satisfied automatically and can therefore be used to quantify the accuracy of the numerical solution throughout its construction.

For completeness, we report the equations for the alternative induction strategy, proceeding in the radial direction:

$$\begin{cases} \frac{\partial l}{\partial R} = \frac{C l_2^2 + l_1^2 l_z S_z + 2\gamma l l_z^2}{l_2^2 S_z} \\ \frac{\partial S}{\partial R} = \frac{2\gamma l l_z + l_1^2 S_z}{l_2^2} \end{cases} \quad (4.96)$$

with:

$$\begin{cases} l_z & := \frac{\partial l}{\partial z} \\ S_z & := \frac{\partial S}{\partial z} \end{cases} \quad (4.97)$$

In this case, (4.95) is used to update pressure and density, while (4.94) allows to keep track of the accuracy.

By definition, our induction strategy will be useful only after suitable boundary conditions have been assigned. The natural places for this assignment to be made are the equatorial line and the vertical axis. In both these *loci*, however, the relevant equations have a non-trivial behaviour, which we therefore address in some more detail in the following two Sections.

4.4.3 Asymptotic analysis near the vertical axis

Suppose that the sub-centrifugal hypothesis (4.61) holds and that the equilibrium angular velocity has a finite limit for $R \rightarrow 0$ ²⁴. Then the specific angular momentum can be expanded near the vertical axis, to the second order in R , as:

$$l(R, z) = R^2 \Omega_0^2(z) + O(R^3) \quad (4.98)$$

with:

$$\Omega_0^2(z) < \Omega_{0,\text{eq}}^2(z) := \lim_{R \rightarrow 0} \frac{1}{R} \frac{\partial \Phi}{\partial R}(R, z) \quad (4.99)$$

If we also assume the entropy field to be regular on the vertical axis, then its radial derivative must vanish there, implying that, for small R , S is of the form:

$$S(R, z) = S_0(z) + R^2 \sigma(z) + O(R^3) \quad (4.100)$$

Inserting (4.98) and (4.100) into (4.90), we obtain the limit for $R \rightarrow 0$ (and thence for $l \rightarrow 0$), of the abstract density Σ :

$$\Sigma(0, S(z)) = \frac{\pi \rho(0, z)}{\Omega_0^2(z) S_0'(z)} \quad (4.101)$$

while the limit of the thermal wind relation (4.59) is:

$$(\Omega_0^2 - \Omega_{0,\text{eq}}^2) S_0' - 2g_z \sigma = 2\gamma \Omega_0 \Omega_0' \quad (4.102)$$

Together with the vertical hydrostatic equilibrium (4.94), equations (4.101) and (4.102) constitute a set of 3 ordinary differential equations in the 4 unknown functions $(\Omega_0^2, S_0, \sigma, Q)$ of one variable z ²⁵. This leaves the freedom to arbitrarily assign, for instance, the entropy profile on the vertical axis S_0 . The other quantities are then determined by integration of the mentioned system, thus providing a suitable boundary condition for the induction to proceed in the radial direction, according to (4.96).

Of course, additional physical requirements (e.g. dynamical stability, or the sub-centrifugal rotation) are not automatically guaranteed everywhere and can be used *a posteriori*, if required, to select the physically interesting boundary conditions among the infinite possibilities.

²⁴Note that all spherically symmetric potentials satisfy this last condition, except, in some cases, in the origin.

²⁵Note that the density $\rho(0, z)$ appearing in (4.101) can be written in terms of $Q(0, z)$ and $S(0, z) = S_0(z)$ by inverting (4.56).

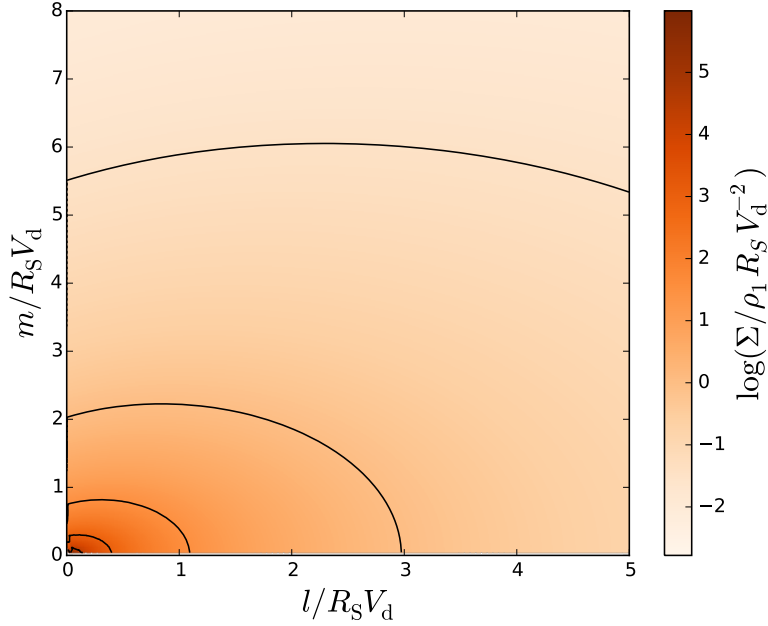


Figure 4.6: The abstract mass density $\Sigma_{(l,m)}$ in the novel coordinate system (l, m) . Note the much more regular behaviour, compared to Fig. 4.5, and in particular the absence of divergency near to the equatorial plane (mapped here into the horizontal axis $m = 0$).

4.4.4 Regularization in the proximity of the equatorial plane

If the entropy S and the specific angular momentum l are smooth functions of (R, z) and are symmetric with respect to the equator, then both $\partial l/\partial z$ and $\partial S/\partial z$ vanish for $z = 0$. This implies that the abstract density Σ is a divergent quantity for $z \rightarrow 0$ or (which is the same) when the ridge line in the (l, S) plane is approached from the allowed region (cfr. Fig. 4.5).

This problem can be circumvented with means of a suitable change of coordinates $(l, S) \mapsto (l, m)$. For instance, the new coordinate m can be defined with the same physical dimensions of l as:

$$m = \sqrt{f^{-1}(S) - l^2} \quad (4.103)$$

where f is as defined in (4.91)²⁶. With position (4.103), m is constant (in particular, it vanishes) for $z = 0$: as a consequence, its gradient is orthogonal (rather than parallel) to the equator and the new abstract density:

$$\Sigma_{(l,m)} = \frac{2\pi R \rho}{\frac{\partial l}{\partial R} \frac{\partial m}{\partial z} - \frac{\partial l}{\partial z} \frac{\partial m}{\partial R}} = 2m f'(l^2 + m^2) \Sigma \quad (4.104)$$

has (but in very peculiar conditions) a finite limit for $z \rightarrow 0$. As an illustration, we show in Fig. 4.6 the map of $\Sigma_{(l,m)}$ for the model of Sec. 4.3.6, which is clearly much more regular with respect to the one in the original (l, S) plane (Fig. 4.5).

By using the inverse of (4.103):

$$S = f(l^2 + m^2) \quad (4.105)$$

²⁶We recall that f is invertible by hypothesis.

the thermal wind relation (4.59) can be written in the new coordinates:

$$\left(R^3 g_R + l^2 - \frac{\gamma}{f'(l^2 + m^2)} \right) l \frac{\partial l}{\partial z} + (R^3 g_R + l^2) m \frac{\partial m}{\partial z} = R^3 g_z \left(m \frac{\partial m}{\partial R} + l \frac{\partial l}{\partial R} \right) \quad (4.106)$$

Equations (4.104) and (4.106) can finally be combined, as in Sec. 4.4.2 to obtain the analogs of (4.92), in the coordinates (l, m) :

$$\begin{cases} \frac{\partial l}{\partial z} = \frac{-l_1^2 C' m + l_2^2 l_R (ll_R + mm_R)}{(l_1^2 + l_3^2) ll_R + l_1^2 mm_R} \\ \frac{\partial m}{\partial z} = \frac{(l_1^2 + l_3^2) l C' + l_2^2 m_R (ll_R + mm_R)}{(l_1^2 + l_3^2) ll_R + l_1^2 mm_R} \end{cases} \quad (4.107)$$

with:

$$\begin{cases} C' & := \frac{2\pi R \rho}{\Sigma_{(l,m)}} \\ l_3^2 & := \frac{\gamma}{f'(l^2 + m^2)} \\ m_R & := \frac{\partial m}{\partial R} \end{cases} \quad (4.108)$$

while l_R , l_1^2 and l_2^2 are as in (4.93).

The system (4.107) allows the solution to be found by induction in the vertical direction, starting from boundary conditions defined on the equator. The latter are uniquely determined by the choice of the rotation curve (or the specific angular momentum profile) on the equator. In fact, the coordinate m is identically vanishing by definition, the entropy S comes from l by virtue of either (4.105) or (4.91) (which are equivalent, by construction), while the pressure can be computed, as usual, from the integration of (4.95) and the coordinate change (4.56). Mirroring the conclusions of Sec. 4.4.3, optional additional requirements (for instance, that a regular entropy field is recovered near the vertical axis), can help *a posteriori* to select the physically interesting solutions among all the possibilities.

4.5 Summary

In this Chapter, we have addressed the problem of how to reconstruct the structure and kinematics of a hot halo, in rotating equilibrium in a given gravitational potential, from the knowledge of its angular momentum and entropy distribution.

This problem has several potential applications to the study of hot coronae around spiral galaxies and in particular:

1. To link cosmological predictions, based on detailed angular momentum conservation, to the properties of the corona, which can be constrained observationally either directly (by future observations able to measure the rotation of these structures) or indirectly, through constraints on angular momentum accretion coming from structural and chemical evolution of spiral galaxies.
2. To predict the evolution of coronae as a consequence of slow processes like viscous transport, cooling and accretion from the IGM.

In the first part, we focused on isothermal models in a logarithmic potential. We have shown how the density and rotational velocity can be computed from the angular momentum distribution and temperature of the corona. Furthermore, we considered in some more detail a couple of interesting particular cases:

1. Polynomial distributions, which are associated to a flat rotation curve and need a sharp truncation both in the density and in the angular momentum distributions. If put in the context of cosmology and galaxy evolution, these models face several difficulties. In particular, they do not appear to be able to sustain the inside-out growth of spirals and would induce too large radial flows within the gaseous discs of spiral galaxies with respect to what suggested by observations.
2. Exponential distributions, similar to those suggested by numerical simulations, under the hypothesis of detailed angular momentum conservation. In order to be self-consistent, these models need to be truncated at a maximum specific angular momentum, which is a function of the coronal temperature. When put on scales that are plausible for a Milky-Way sized galaxy, a model like this shows a surprising agreement with several independent requirements, including the global mass and angular momentum content of the corona, its ability to sustain the inside-out growth of the disc and to induce radial flows compatible with the observed abundance gradients.

We then discussed more general baroclinic models. We have found a novel parametrization of the general barotropic equilibrium in a given static, axisymmetric gravitational potential, which is improved with respect to parametrizations by other authors in being always well-defined. We considered some special cases in more detail and in particular a new class of analytic self-similar baroclinic models in an arbitrary spherically symmetric potential. A comparison with isothermal models has shown that even moderate temperature gradients can have a significant impact on structure of the corona near the axis of rotation.

Finally, we have studied the properties of the joint angular momentum/entropy distribution of a gas in rotating equilibrium in a given potential. We have proposed an algorithm that allows the reconstruction of the structure and kinematics of a gas in rotating equilibrium, starting from the knowledge of its joint angular momentum/entropy distribution and of one boundary condition, defined either on the mid-plane or the vertical axis.

Chapter 5

Conclusions

Spiral galaxies like our own Milky Way continuously acquire gas from the intergalactic medium (IGM), which allows them to sustain significant levels of star formation throughout their histories. During this process, they also gain angular momentum, as predicted by the tidal torque theory and implied by observational indications of inside-out growth. In this Thesis, we have presented novel methods for the study of the accretion of mass and angular momentum onto the discs of spiral galaxies, both from the global and the local point of view, and we compared theoretical predictions with a variety of observational data.

If, as theory dictates, the average specific angular momentum of spiral galaxies is an increasing function of time, then their discs should grow in size, while they grow in mass (inside-out growth). In Chapter 2 we have presented a novel method for the measurement of the specific mass and radial growth rates of stellar discs, based on the comparison of their stellar mass surface density and star formation rate surface density (SFRD) profiles and on the assumption that stellar discs are well described by an exponential with a time-varying scalelength. We tested the validity of our theory on a sample of 35 nearby spiral galaxies, for which multiwavelength data, from FIR to FUV, were publicly available from the SINGS survey. For almost all galaxies in our sample, we have found a positive radial growth rate, which is the signature of ongoing inside-out growth. Only one object (NGC 1097) was found to be undergoing significant disc shrinking, which we interpret as a possible consequence of an ongoing merger event. The specific mass growth rates of our galaxies are similar to those reported by studies of the main sequence of star forming discs. Interestingly, we have found that also the specific radial growth rates lie on a sequence with a similar shape, but systematically shifted downwards by a factor of ~ 3 . This implies that galaxies, on average, grow in size at about one third of the rate at which they grow in mass. We have then shown that measurements like ours can be used to put tight constraints on a possibly ongoing evolution of the scaling relations of disc galaxies. Our results are compatible with independent measurements out to $z \sim 1$ and they agree very well with theoretical expectations if known scaling relations of disc galaxies are not evolving with time. We find instead a tension with simple models based on the assumption that galaxies evolve in lockstep with their dark matter haloes. This suggests that baryonic processes may be regulating the rate of mass and angular momentum accretion onto galaxy discs, at least at low redshift.

While the masses and radii of spiral galaxies are mainly determined by the global mass and angular momentum accretion rates, many important aspects of galaxy evolution, most notably chemical evolution, depend on local processes and in particular on how the accretion of mass and the accretion of angular momentum are distributed with galactocentric distance. Both these pieces of information are not directly accessible to observations yet. However, significant insights can be gained from structural and chemical observational constraints and from the physical link that must exist between the accretion of mass and angular momentum, on dynamical grounds. Accretion, in fact, induces radial gas flows within the disc, depending on the angular momentum of the accreting material, with observable consequences on the distribution of the heavy elements injected by stars into the interstellar medium (ISM). Conversely, the observed distribution of α -elements in the ISM, combined with the observed structural properties of discs, can be used to reconstruct radial flows, the accretion profile and the local angular momentum of the accreting material. In Chapter 3 we have presented novel methods to perform this reconstruction. Our improvements with respect to previous work include: i) a generalization of existing analytic solutions to arbitrary angular momentum distributions, ii) an improved treatment of boundary effects, which have a key role in shaping abundance gradients in the outskirts of spiral galaxies and iii) a prescription, based on the results of Chapter 2, to separate the effects of inside-out growth and radial flows on the steepness of abundance gradients. By applying our methods to the Milky Way, we have found that the material accreting on the disc of our Galaxy likely rotates at $\sim 70 - 85\%$ of the rotational velocity of the disc, in agreement with previous estimates. We also performed our analysis for one nearby spiral galaxy (NGC 628), finding similar results, though with larger uncertainties. Our findings are consistent with a scenario in which gaseous material is accreted onto the discs of spiral galaxies at relatively large radii and then travels inwards within the disc, to reach the inner regions where it is needed to sustain star formation. The local angular momentum deficit of the accreting material with respect to the disc is in agreement with general theoretical expectations, based on geometrical and hydrodynamical arguments. If the accretion originates from the cooling of a hot corona surrounding the disc, then the inferred deficit can be used to put some constraints on the temperature and the structure of the corona.

A coherent view of the local and global processes discussed in Chapters 2 and 3 requires the understanding of the ultimate source of mass and angular momentum of spiral galaxies. In the context of the hot-mode accretion scenario, which should hold for massive spirals like our own, this means modeling the mass and angular momentum content of hot coronae surrounding galaxy discs. According to the theory, these are the large-scale reservoirs where mass and angular momentum are stored after accretion from the cosmic web onto dark matter haloes and before condensation on star forming discs. Simple theoretical models predict that coronae around galaxies should have an angular momentum distribution very similar to the one of dark matter haloes, which is in turn a prediction of tidal torque theory. It is therefore very interesting to investigate the consequences of this assumption and to consider whether it is compatible with independent observational constraints on galaxy evolution. In Chapter 4 we have studied the theoretical problem of reconstructing the

structure and kinematics of the corona from the knowledge of its angular momentum distribution. We have first considered the idealized case of an isothermal equilibrium in a logarithmic potential, which is a very simple but reasonable first approximation to a realistic situation. After describing the general solution, we applied it to some particular angular momentum distributions. Interestingly, we have found that a cosmologically motivated model, scaled on parameters plausible for the Milky Way, shows an encouraging agreement with independent measurements of the coronal density and the angular momentum content of the corona. Moreover, the rotation curves predicted by our models are compatible with coronal accretion driving both the inside-out growth of the disc (cfr. Chapter 2) and the radial flows required to explain abundance gradient of the Milky Way (cfr. Chapter 3). We have also attempted a study of the more general case of baroclinic equilibria in an arbitrary axisymmetric gravitational potential. We have proposed a novel parametrization of the general baroclinic equilibrium and discussed some interesting particular cases. Finally, we have discussed a method for the reconstruction of the coronal structure and kinematics, which, in this case, relies on the knowledge of the joint angular momentum/entropy distribution. Further investigation on this subject will be useful to study the evolution of coronae under various physical processes including cooling, viscous friction, mass accretion from the cosmic web and partial condensation on the star forming disc.

Acknowledgements

I am very happy to acknowledge Samuel Boissier and Juan Carlos Muñoz-Mateos for a fruitful collaboration and for their always prompt and useful advices and suggestions. I am thankful to James Binney, Ralph Schönrich and to all the people at the Rudolf Peierls Centre for Theoretical Physics, University of Oxford, for hospitality during Summer 2014, when the majority of the work in Chapter 4 was done. I owe a special acknowledgement to James Binney, for encouraging me to study the joint angular momentum/entropy distributions of rotating equilibria and for several important suggestions on this and other topics. I wish to thank Aura Obreja for driving my attention on the work of Sharma & Steinmetz (2005) and Steve Balbus for underlying the importance of the thermal wind relation. I also thank Donatella Romano for useful discussion and Dave Green for kindly making some additional analysis of the longitudinal distribution of supernova remnants in the Milky Way.

I am grateful to Lorenzo Posti and Enrico Di Teodoro for generously sharing with me their knowledge, their skills and their insanity during these years together. Among all, I wish to express my gratitude to my supervisor Filippo Fraternali. Without his guidance, his friendship and, notably, his wisdom, this work would not have been possible (at least, not in less than one Hubble time).

Bibliography

- Abramson L. E., Kelson D. D., Dressler A., Poggianti B., Gladders M. D., Oemler, Jr. A., Vulcani B., 2014, *ApJL*, 785, L36
- Allen S. W., Evrard A. E., Mantz A. B., 2011, *ARA&A*, 49, 409
- Amendt P., Lanza A., Abramowicz M. A., 1989, *ApJ*, 343, 437
- Anderson M. E., Bregman J. N., 2010, *ApJ*, 714, 320
- Anderson M. E., Bregman J. N., 2011, *ApJ*, 737, 22
- Anderson M. E., Bregman J. N., Dai X., 2013, *ApJ*, 762, 106
- Aumer M., Binney J. J., 2009, *MNRAS*, 397, 1286
- Aumer M., White S. D. M., Naab T., 2014, *MNRAS*, 441, 3679
- Baldwin J. E., Lynden-Bell D., Sancisi R., 1980, *MNRAS*, 193, 313
- Barden M. et al., 2005, *ApJ*, 635, 959
- Barker M. K., Ferguson A. M. N., Cole A. A., Ibata R., Irwin M., Lewis G. F., Smecker-Hane T. A., Tanvir N. R., 2011, *MNRAS*, 410, 504
- Barnabè M., Ciotti L., Fraternali F., Sancisi R., 2006, *A&A*, 446, 61
- Barnes J., Efstathiou G., 1987, *ApJ*, 319, 575
- Begeman K. G., Broeils A. H., Sanders R. H., 1991, *MNRAS*, 249, 523
- Behroozi P. S., Conroy C., Wechsler R. H., 2010, *ApJ*, 717, 379
- Bell E. F., de Jong R. S., 2000, *MNRAS*, 312, 497
- Bell E. F., McIntosh D. H., Katz N., Weinberg M. D., 2003, *ApJS*, 149, 289
- Belli S., Jones T., Ellis R. S., Richard J., 2013, *ApJ*, 772, 141
- Benítez-Llambay A., Navarro J. F., Abadi M. G., Gottlöber S., Yepes G., Hoffman Y., Steinmetz M., 2015, *MNRAS*, 450, 4207
- Berg D. A., Skillman E. D., Croxall K. V., Pogge R. W., Moustakas J., Johnson-Groh M., 2015, *ApJ*, 806, 16

Bigiel F. et al., 2011, ApJL, 730, L13

Bilitewski T., Schönrich R., 2012, MNRAS, 426, 2266

Binney J., 1977, ApJ, 215, 483

Binney J., 2004, MNRAS, 347, 1093

Binney J., Merrifield M., 1998, Galactic Astronomy. Princeton University Press

Binney J., Nipoti C., Fraternali F., 2009, MNRAS, 397, 1804

Binney J., Tremaine S., 2008, Galactic Dynamics: Second Edition. Princeton University Press

Birnboim Y., Dekel A., 2003, MNRAS, 345, 349

Bland-Hawthorn J., Sutherland R., Agertz O., Moore B., 2007, ApJL, 670, L109

Blumenthal G. R., Faber S. M., Flores R., Primack J. R., 1986, ApJ, 301, 27

Bogdán Á., Forman W. R., Kraft R. P., Jones C., 2013a, ApJ, 772, 98

Bogdán Á. et al., 2013b, ApJ, 772, 97

Boissier S. et al., 2008, ApJ, 681, 244

Boissier S. et al., 2007, ApJS, 173, 524

Boissier S., Prantzos N., 1999, MNRAS, 307, 857

Boselli A., Boissier S., Cortese L., Gil de Paz A., Seibert M., Madore B. F., Buat V., Martin D. C., 2006, ApJ, 651, 811

Bothwell M. S., Maiolino R., Kennicutt R., Cresci G., Mannucci F., Marconi A., Ciccone C., 2013, MNRAS, 433, 1425

Braun R., Walterbos R. A. M., Kennicutt, Jr. R. C., Tacconi L. J., 1994, ApJ, 420, 558

Bregman J. N., 1980, ApJ, 236, 577

Bresolin F., Kennicutt R. C., Ryan-Weber E., 2012, ApJ, 750, 122

Briggs F. H., 1990, ApJ, 352, 15

Broeils A. H., Rhee M.-H., 1997, A&A, 324, 877

Brook C. B., Stinson G., Gibson B. K., Roškar R., Wadsley J., Quinn T., 2012, MNRAS, 419, 771

Brooks A. M. et al., 2011, ApJ, 728, 51

Bryan G. L., Norman M. L., 1998, ApJ, 495, 80

Buat V. et al., 2005, *ApJL*, 619, L51

Buitrago F., Trujillo I., Conselice C. J., Bouwens R. J., Dickinson M., Yan H., 2008, *ApJL*, 687, L61

Bullock J. S., Dekel A., Kolatt T. S., Kravtsov A. V., Klypin A. A., Porciani C., Primack J. R., 2001, *ApJ*, 555, 240

Case G. L., Bhattacharya D., 1998, *ApJ*, 504, 761

Cavichia O., Mollá M., Costa R. D. D., Maciel W. J., 2014, *MNRAS*, 437, 3688

Chamcham K., Tayler R. J., 1994, *MNRAS*, 266, 282

Chiappini C., Matteucci F., Romano D., 2001, *ApJ*, 554, 1044

Churchill C. W., Trujillo-Gomez S., Nielsen N. M., Kacprzak G. G., 2013, *ApJ*, 779, 87

Clarke C. J., 1989, *MNRAS*, 238, 283

Cole S., Lacey C., 1996, *MNRAS*, 281, 716

Cortese L., Boselli A., Franzetti P., Decarli R., Gavazzi G., Boissier S., Buat V., 2008, *MNRAS*, 386, 1157

Courteau S., Dutton A. A., van den Bosch F. C., MacArthur L. A., Dekel A., McIntosh D. H., Dale D. A., 2007, *ApJ*, 671, 203

Cowie L. L., Songaila A., Hu E. M., Cohen J. G., 1996, *AJ*, 112, 839

Dai X., Anderson M. E., Bregman J. N., Miller J. M., 2012, *ApJ*, 755, 107

Dalcanton J. J., 2007, *ApJ*, 658, 941

Dale D. A. et al., 2005, *ApJ*, 633, 857

de Vaucouleurs G., de Vaucouleurs A., Corwin, Jr. H. G., Buta R. J., Paturel G., Fouqué P., 1991, *Third Reference Catalogue of Bright Galaxies*. Springer-Verlag, New York

Dehnen W., McLaughlin D. E., Sachania J., 2006, *MNRAS*, 369, 1688

Dekel A., Birnboim Y., 2006, *MNRAS*, 368, 2

Dekel A. et al., 2009, *Nature*, 457, 451

Di Teodoro E. M., Fraternali F., 2014, *A&A*, 567, A68

Dressler A. et al., 1997, *ApJ*, 490, 577

Dutton A. A., Conroy C., van den Bosch F. C., Prada F., More S., 2010, *MNRAS*, 407, 2

- Dutton A. A., van den Bosch F. C., 2012, MNRAS, 421, 608
- Dyk S. D. V., Li W., Filippenko A. V., 2006, Publications of the Astronomical Society of the Pacific, 118, pp. 351
- Edmunds M. G., 1990, MNRAS, 246, 678
- Edmunds M. G., Greenhow R. M., 1995, MNRAS, 272, 241
- Edvardsson B., Andersen J., Gustafsson B., Lambert D. L., Nissen P. E., Tomkin J., 1993, A&A, 275, 101
- Eke V. R., Cole S., Frenk C. S., 1996, MNRAS, 282, 263
- Elbaz D. et al., 2011, A&A, 533, A119
- Elmegreen B. G., Elmegreen D. M., Vollbach D. R., Foster E. R., Ferguson T. E., 2005, ApJ, 634, 101
- Erwin P., Pohlen M., Beckman J. E., 2008, AJ, 135, 20
- Evoli C., Salucci P., Lapi A., Danese L., 2011, ApJ, 743, 45
- Fall S. M., 1983, in IAU Symposium, Vol. 100, Internal Kinematics and Dynamics of Galaxies, Athanassoula E., ed., pp. 391–398
- Fall S. M., 2002, in Astronomical Society of the Pacific Conference Series, Vol. 275, Disks of Galaxies: Kinematics, Dynamics and Perturbations, Athanassoula E., Bosma A., Mujica R., eds., pp. 389–396
- Fall S. M., Efstathiou G., 1980, MNRAS, 193, 189
- Fathi K., Gatchell M., Hatziminaoglou E., Epinat B., 2012, MNRAS, 423, L112
- Fillmore J. A., Goldreich P., 1984, ApJ, 281, 1
- Firmani C., Avila-Reese V., 2009, MNRAS, 396, 1675
- Fraternali F., 2009, in IAU Symposium, Vol. 254, IAU Symposium, Andersen J., Nordströara, m B., Bland-Hawthorn J., eds., pp. 255–262
- Fraternali F., Binney J. J., 2006, MNRAS, 366, 449
- Fraternali F., Binney J. J., 2008, MNRAS, 386, 935
- Fraternali F., Marasco A., Armillotta L., Marinacci F., 2015, MNRAS, 447, L70
- Fraternali F., Tomassetti M., 2012, MNRAS, 426, 2166
- Freeman K. C., 1970, ApJ, 160, 811
- Gallazzi A., Charlot S., Brinchmann J., White S. D. M., Tremonti C. A., 2005, MNRAS, 362, 41

García-Ruiz I., Sancisi R., Kuijken K., 2002, *A&A*, 394, 769

Gatto A., Fraternali F., Read J. I., Marinacci F., Lux H., Walch S., 2013, *MNRAS*, 433, 2749

Genel S., Fall S. M., Hernquist L., Vogelsberger M., Snyder G. F., Rodriguez-Gomez V., Sijacki D., Springel V., 2015, *ApJL*, 804, L40

Genovali K. et al., 2015, *A&A*, 580, A17

Gil de Paz A. et al., 2007, *ApJS*, 173, 185

Goddard Q. E., Kennicutt R. C., Ryan-Weber E. V., 2010, *MNRAS*, 405, 2791

Goetz M., Koeppen J., 1992, *A&A*, 262, 455

Gogarten S. M. et al., 2010, *ApJ*, 712, 858

González Delgado R. M. et al., 2014, *A&A*, 562, A47

Governato F. et al., 2010, *Nature*, 463, 203

Green D. A., 2015, *MNRAS*, 454, 1517

Guedes J., Callegari S., Madau P., Mayer L., 2011, *ApJ*, 742, 76

Gunn J. E., Gott, III J. R., 1972, *ApJ*, 176, 1

Higdon J. L., Wallin J. F., 2003, *ApJ*, 585, 281

Ibata R., Irwin M., Lewis G. F., Stolte A., 2001, *ApJL*, 547, L133

Ichikawa T., Kajisawa M., Akhlaghi M., 2012, *MNRAS*, 422, 1014

Jurić M. et al., 2008, *ApJ*, 673, 864

Kaiser C. R., Binney J., 2003, *MNRAS*, 338, 837

Kannappan S. J. et al., 2013, *ApJ*, 777, 42

Kaufmann T., Bullock J. S., Maller A. H., Fang T., Wadsley J., 2009, *MNRAS*, 396, 191

Kaufmann T., Mayer L., Wadsley J., Stadel J., Moore B., 2007, *MNRAS*, 375, 53

Kennicutt R. C., Evans N. J., 2012, *ARA&A*, 50, 531

Kennicutt, Jr. R. C., 1983, *ApJ*, 272, 54

Kennicutt, Jr. R. C., 1998, *ApJ*, 498, 541

Kennicutt, Jr. R. C. et al., 2003, *PASP*, 115, 928

Kobulnicky H. A., Kewley L. J., 2004, *ApJ*, 617, 240

Koposov S. E., Rix H.-W., Hogg D. W., 2010, *ApJ*, 712, 260

Kravtsov A. V., 2013, *ApJL*, 764, L31

Kroupa P., 2001, *MNRAS*, 322, 231

Kubryk M., Prantzos N., Athanassoula E., 2013, *MNRAS*, 436, 1479

Kubryk M., Prantzos N., Athanassoula E., 2015, *A&A*, 580, A126

Kudritzki R.-P., Urbaneja M. A., Bresolin F., Hosek, Jr. M. W., Przybilla N., 2014, *ApJ*, 788, 56

Lacey C. G., Fall S. M., 1985, *ApJ*, 290, 154

Lange R. et al., 2015, *MNRAS*, 447, 2603

Larson R. B., 1972, *Nature Physical Science*, 236, 7

Larson R. B., 1976, *MNRAS*, 176, 31

Lehner N., Howk J. C., 2011, *Science*, 334, 955

Lehner N. et al., 2013, *ApJ*, 770, 138

Leitner S. N., 2012, *ApJ*, 745, 149

Leitner S. N., Kravtsov A. V., 2011, *ApJ*, 734, 48

Lelli F., Verheijen M., Fraternali F., 2014a, *A&A*, 566, A71

Lelli F., Verheijen M., Fraternali F., 2014b, *MNRAS*, 445, 1694

Leroy A. K., Walter F., Brinks E., Bigiel F., de Blok W. J. G., Madore B., Thornley M. D., 2008, *AJ*, 136, 2782

Lilly S. J., Carollo C. M., Pipino A., Renzini A., Peng Y., 2013, *ApJ*, 772, 119

Lin D. N. C., Pringle J. E., 1987, *ApJL*, 320, L87

Lu Y., Mo H. J., Wechsler R. H., 2015, *MNRAS*, 446, 1907

Luck R. E., Lambert D. L., 2011, *AJ*, 142, 136

Ludwig J., Pasquali A., Grebel E. K., Gallagher, III J. S., 2012, *AJ*, 144, 190

Lynden-Bell D., 1967, *MNRAS*, 136, 101

Lynden-Bell D., Kalnajs A. J., 1972, *MNRAS*, 157, 1

Lynden-Bell D., Pringle J. E., 1974, *MNRAS*, 168, 603

MacArthur L. A., Courteau S., Bell E., Holtzman J. A., 2004, *ApJS*, 152, 175

Macciò A. V., Dutton A. A., van den Bosch F. C., 2008, *MNRAS*, 391, 1940

Maller A. H., Bullock J. S., 2004, MNRAS, 355, 694

Mannucci F., Cresci G., Maiolino R., Marconi A., Gnerucci A., 2010, MNRAS, 408, 2115

Mao S., Mo H. J., White S. D. M., 1998, MNRAS, 297, L71

Marasco A., Fraternali F., Binney J. J., 2012, MNRAS, 419, 1107

Marinacci F., Binney J., Fraternali F., Nipoti C., Ciotti L., Londrillo P., 2010a, MNRAS, 404, 1464

Marinacci F., Fraternali F., Ciotti L., Nipoti C., 2010b, MNRAS, 401, 2451

Marinacci F., Fraternali F., Nipoti C., Binney J., Ciotti L., Londrillo P., 2011, MNRAS, 415, 1534

Marino R. A. et al., 2013, A&A, 559, A114

Martig M., Bournaud F., Teyssier R., Dekel A., 2009, ApJ, 707, 250

Martin D. C. et al., 2005, ApJL, 619, L1

Matteucci F., 2012, Chemical Evolution of Galaxies. Springer-Verlag

Matteucci F., Francois P., 1989, MNRAS, 239, 885

Mayor M., Vigroux L., 1981, A&A, 98, 1

McGaugh S. S., 2012, AJ, 143, 40

McNamara B. R., Nulsen P. E. J., 2007, ARA&A, 45, 117

Meidt S. E. et al., 2012, ApJ, 744, 17

Meidt S. E. et al., 2014, ApJ, 788, 144

Melioli C., Brighenti F., D'Ercole A., de Gouveia Dal Pino E. M., 2008, MNRAS, 388, 573

Mestel L., 1963, MNRAS, 126, 553

Miller M. J., Bregman J. N., 2015, ApJ, 800, 14

Miller S. H., Bundy K., Sullivan M., Ellis R. S., Treu T., 2011, ApJ, 741, 115

Miller S. H., Ellis R. S., Sullivan M., Bundy K., Newman A. B., Treu T., 2012, ApJ, 753, 74

Minchev I., Chiappini C., Martig M., 2014, A&A, 572, A92

Mo H., van den Bosch F. C., White S., 2010, Galaxy Formation and Evolution

Mo H. J., Mao S., White S. D. M., 1998, MNRAS, 295, 319

- Mollá M., Díaz A. I., 2005, MNRAS, 358, 521
- Mollá M., Ferrini F., Díaz A. I., 1997, ApJ, 475, 519
- Mott A., Spitoni E., Matteucci F., 2013, MNRAS, 435, 2918
- Moustakas J., Kennicutt, Jr. R. C., Tremonti C. A., Dale D. A., Smith J.-D. T., Calzetti D., 2010, ApJS, 190, 233
- Muñoz-Mateos J. C., Boissier S., Gil de Paz A., Zamorano J., Kennicutt, Jr. R. C., Moustakas J., Prantzos N., Gallego J., 2011, ApJ, 731, 10
- Muñoz-Mateos J. C. et al., 2009a, ApJ, 701, 1965
- Muñoz-Mateos J. C., Gil de Paz A., Boissier S., Zamorano J., Jarrett T., Gallego J., Madore B. F., 2007, ApJ, 658, 1006
- Muñoz-Mateos J. C. et al., 2009b, ApJ, 703, 1569
- Naab T., Ostriker J. P., 2006, MNRAS, 366, 899
- Navarro J. F., Frenk C. S., White S. D. M., 1997, ApJ, 490, 493
- Navarro J. F., Steinmetz M., 1997, ApJ, 478, 13
- Navarro J. F., White S. D. M., 1994, MNRAS, 267, 401
- Nelson D., Vogelsberger M., Genel S., Sijacki D., Kereš D., Springel V., Hernquist L., 2013, MNRAS, 429, 3353
- Nicastro F., Mathur S., Elvis M., 2008, Science, 319, 55
- Nipoti C., Posti L., 2014, ApJ, 792, 21
- Oort J. H., 1970, A&A, 7, 381
- Oosterloo T., Fraternali F., Sancisi R., 2007, AJ, 134, 1019
- Oosterloo T. A., Morganti R., Sadler E. M., van der Hulst T., Serra P., 2007, A&A, 465, 787
- Pagel B. E. J., 2009, Nucleosynthesis and Chemical Evolution of Galaxies. Cambridge University Press
- Pagel B. E. J., Patchett B. E., 1975, MNRAS, 172, 13
- Pan Z., Li J., Lin W., Wang J., Kong X., 2014, ApJL, 792, L4
- Papastergis E., Cattaneo A., Huang S., Giovanelli R., Haynes M. P., 2012, ApJ, 759, 138
- Pedrosa S., Tissera P., 2015, ArXiv e-prints
- Peebles P. J. E., 1969, ApJ, 155, 393

Peng Y.-j. et al., 2010, ApJ, 721, 193

Peng Y.-j., Maiolino R., 2014, MNRAS, 438, 262

Penton S. V., Stocke J. T., Shull J. M., 2004, ApJS, 152, 29

Petit A. C., Krumholz M. R., Goldbaum N. J., Forbes J. C., 2015, MNRAS, 449, 2588

Phillipps S., Edmunds M. G., 1991, MNRAS, 251, 84

Piffi T. et al., 2014, A&A, 562, A91

Pilkington K. et al., 2012, A&A, 540, A56

Pilyugin L. S., 2007, MNRAS, 375, 685

Piontek F., Steinmetz M., 2011, MNRAS, 410, 2625

Pitts E., Tayler R. J., 1989, MNRAS, 240, 373

Pitts E., Tayler R. J., 1996, MNRAS, 280, 1101

Planck Collaboration, 2014, A&A, 571, A16

Pohlen M., Trujillo I., 2006, A&A, 454, 759

Portinari L., Chiosi C., 2000, A&A, 355, 929

Posacki S., Pellegrini S., Ciotti L., 2013, MNRAS, 433, 2259

Prochaska J. X., Weiner B., Chen H.-W., Mulchaey J., Cooksey K., 2011, ApJ, 740, 91

Putman M. E., Peek J. E. G., Joungh M. R., 2012, ARA&A, 50, 491

Randall S. W., Markevitch M., Clowe D., Gonzalez A. H., Bradač M., 2008, ApJ, 679, 1173

Ravindranath S. et al., 2004, ApJL, 604, L9

Read J. I., 2014, Journal of Physics G Nuclear Physics, 41, 063101

Rees M. J., Ostriker J. P., 1977, MNRAS, 179, 541

Regan M. W. et al., 2004, ApJS, 154, 204

Reichard T. A., Heckman T. M., Rudnick G., Brinchmann J., Kauffmann G., Wild V., 2009, ApJ, 691, 1005

Romanowsky A. J., Fall S. M., 2012, ApJS, 203, 17

Roškar R., Debattista V. P., Quinn T. R., Wadsley J., 2012, MNRAS, 426, 2089

Rubin K. H. R., Prochaska J. X., Koo D. C., Phillips A. C., 2012, ApJL, 747, L26

Rubin K. H. R., Prochaska J. X., Koo D. C., Phillips A. C., Martin C. L., Winstrom L. O., 2014, *ApJ*, 794, 156

Sánchez S. F. et al., 2014, *A&A*, 563, A49

Sánchez Almeida J., Elmegreen B. G., Muñoz-Tuñón C., Elmegreen D. M., 2014, *A&ARv*, 22, 71

Sánchez Almeida J. et al., 2015, *ApJL*, 810, L15

Sancisi R., Fraternali F., Oosterloo T., van der Hulst T., 2008, *A&ARv*, 15, 189

Schoenmakers R. H. M., 1999, PhD thesis, University of Groningen

Schönrich R., Binney J., 2009, *MNRAS*, 396, 203

Sellwood J. A., 2014, *Reviews of Modern Physics*, 86, 1

Sellwood J. A., Binney J. J., 2002a, *MNRAS*, 336, 785

Sellwood J. A., Binney J. J., 2002b, *MNRAS*, 336, 785

Sharma S., Steinmetz M., 2005, *ApJ*, 628, 21

Shen S., Mo H. J., White S. D. M., Blanton M. R., Kauffmann G., Voges W., Brinkmann J., Csabai I., 2003, *MNRAS*, 343, 978

Silk J., Wyse R. F. G., Shields G. A., 1987, *ApJL*, 322, L59

Simard L. et al., 1999, *ApJ*, 519, 563

Skillman E. D., 1998, in *Stellar astrophysics for the local group: VIII Canary Islands Winter School of Astrophysics*, Aparicio A., Herrero A., Sánchez F., eds., p. 457

Sommer-Larsen J., Gelato S., Vedel H., 1999, *ApJ*, 519, 501

Speagle J. S., Steinhardt C. L., Capak P. L., Silverman J. D., 2014, *ApJS*, 214, 15

Spitoni E., Matteucci F., 2011, *A&A*, 531, A72

Spitoni E., Recchi S., Matteucci F., 2008, *A&A*, 484, 743

Tassoul J.-L., 2000, *Stellar Rotation*. Cambridge University Press

Thilker D. A. et al., 2007a, *ApJS*, 173, 538

Thilker D. A. et al., 2007b, *ApJS*, 173, 572

Thon R., Meusinger H., 1998, *A&A*, 338, 413

Tinsley B. M., 1980, *Fundamentals of Cosmic Physics*, 5, 287

Tojeiro R. et al., 2013, *MNRAS*, 432, 359

Tosi M., 1988a, *A&A*, 197, 33

Tosi M., 1988b, *A&A*, 197, 47

Tremonti C. A. et al., 2004, *ApJ*, 613, 898

Trujillo I. et al., 2006, *ApJ*, 650, 18

Tully R. B., Fisher J. R., 1977, *A&A*, 54, 661

van den Bergh S., 1962, *AJ*, 67, 486

van den Bosch F. C., 2001, *MNRAS*, 327, 1334

van den Bosch F. C., Burkert A., Swaters R. A., 2001, *MNRAS*, 326, 1205

van der Hulst T., Sancisi R., 1988, *AJ*, 95, 1354

van der Kruit P. C., Freeman K. C., 2011, *ARA&A*, 49, 301

van Woerden H., Wakker B. P., 2004, in *Astrophysics and Space Science Library*, Vol. 312, *High Velocity Clouds*, van Woerden H., Wakker B. P., Schwarz U. J., de Boer K. S., eds., p. 195

Vilchez J. M., Esteban C., 1996, *MNRAS*, 280, 720

Vogt N. P. et al., 1997, *ApJL*, 479, L121

Voit G. M., Balogh M. L., Bower R. G., Lacey C. G., Bryan G. L., 2003, *ApJ*, 593, 272

von Weizsäcker C. F., 1948, *Zeitschrift für Astrophysik*, 24, 181

Wang J. et al., 2011, *MNRAS*, 412, 1081

White S. D. M., 1984, *ApJ*, 286, 38

White S. D. M., Rees M. J., 1978, *MNRAS*, 183, 341

Wilkins S. M., Trentham N., Hopkins A. M., 2008, *MNRAS*, 385, 687

Williams B. F., Dalcanton J. J., Dolphin A. E., Holtzman J., Sarajedini A., 2009, *ApJL*, 695, L15

Wong T., Blitz L., Bosma A., 2004, *ApJ*, 605, 183

Yang C.-C., Krumholz M., 2012, *ApJ*, 758, 48

Yoachim P., Roškar R., Debattista V. P., 2012, *ApJ*, 752, 97

Zafar T., Péroux C., Popping A., Milliard B., Deharveng J.-M., Frank S., 2013, *A&A*, 556, A141

Zaritsky D. et al., 2014, *AJ*, 147, 134